ABSTRACT

Title of Document: DEVELOPMENT OF MULTI-SCALE, MULTI-PHYSICS, ANALYSIS CAPABILITY AND ITS APPLICATION TO NOVEL HEAT EXCHANGER DESIGN AND OPTIMIZATION

Omar Abdelaziz Ahmed Abdelaziz, Doctor of Philosophy, 2009

Directed By: Reinhard Radermacher, Professor
Department of Mechanical Engineering

Heat exchanger development using enhanced heat transfer surface designs and optimization techniques is a continuing effort that is constrained by current state of the art technology. Assessment of novel geometries and concepts are currently limited to experimental and numerical investigations on discrete levels. This dissertation aims at the advancement of the heat exchanger technology through the development of multi-scale multi-physics simulation tools for conventional and novel heat exchanger designs.

A unified heat exchanger design and optimization framework was developed. This framework integrates the multi-scale multi-physics simulation capabilities with previously developed approximation assisted optimization techniques. The optimized designs are then interpreted in order to provide design guidelines for next generation air-to-water heat exchangers. These capabilities required the development of: (a)

generic $\varepsilon - NTU$ solver capable of analyzing the performance under geometrical variability, (b) systematic integration approach for CFD simulation at the segment level with the $\varepsilon - NTU$ solver at the heat exchanger level, (c) refrigerant distribution analysis tool. The developed simulation tools were verified numerically using systematic techniques adopted from literature and validated experimentally using measured data from a prototype heat exchanger. The structural integrity under conventional operating pressures of the novel heat exchanger design was analyzed using FEM for different tube materials and different wall thicknesses. Finally, existing single phase water flow in microtubes correlations were investigated numerically. The best matching correlation was selected for incorporation within the multi-scale simulation tool.

The approach described in this dissertation for the design and optimization of novel and conventional heat exchanger designs resulted in significant improvements over the current state of the art. Example performance improvements achieved in this dissertation show potential for 84 percent material savings and 61 percent volume savings for the same airside and refrigerant side pressure drop. The experimental investigations were in good agreement with the simulation results and demonstrated the superior performance of the novel design.

DEVELOPMENT OF MULTI-SCALE, MULTI-PHYSICS, ANALYSIS CAPABILITY AND ITS APPLICATION TO NOVEL HEAT EXCHANGERS DESIGN AND OPTIMIZATION

By

Omar Abdelaziz Ahmed Abdelaziz

Dissertation submitted to the Faculty of the Graduate School of the
University of Maryland, College Park, in partial fulfillment
of the requirements for the degree of
Doctor of Philosophy
2009

Advisory Committee:
Professor Reinhard Radermacher, Chair
Professor Avram Bar-Cohen
Professor Shapour Azarm
Professor Elias Balaras
Professor Gary Pertmer (Dean's Representative)

Dedication

To everyone who believed in me:

My family, mentors, teachers, friends and colleagues

Acknowledgements

The work presented in this dissertation is the result of my experience at the Center for Environmental Energy Engineering (CEEE). I am sincerely grateful to Dr. Radermacher for offering me the opportunity to work at CEEE. As my mentor, Dr. Radermacher provided me with continuing support, advice and guidance that shaped my research aptitude which resulted in the dissertation between your hands. I would also like to thank my dissertation committee members, Dr. Avram Bar-Cohen, Dr. Shapour Azarm, Dr. Elias Balaras, and Dr. Gary Pertmer (Dean's Representative) for their efforts, advice and support.

Working at CEEE under Dr. Radermacher' leadership was a unique experience; the right mix between academic and professional work environment. I would like to extend my gratitude to my current and former colleagues at CEEE namely Jon Winkler, Varun Singh, Abdullah Alabdulkarem, Khaled Saleh, Dr. Travis Horton, Lorie Hudson Puente, Mary Collins Baugher and Daniel Leighton. I am deeply grateful to Jan Muehlbauer who provided me with great support regarding my experimental testing and was a great source of ideas and innovative solutions. I am also especially thankful to Vikrant Aute for introducing me to the approximation assisted optimization field and lending me his programming, mathematical, and optimization expertise.

I thank my family for supporting and encouraging me. I am especially thankful to my parents for encouraging me to pursue my graduate degrees. My gratitude to my parents can not be expressed in words; they deserve all the credit for

my achievements. Also, I would like to thank my fiancée, Gannat Khowailed, for her support and understanding during the most stressful part of my Ph.D. program. Finally, I would like to extend my thanks to my friends for their support and encouragements; especially Hussein Ezzeldin and Tarek Massoud.

The work presented in this dissertation was supported in part through a grant from the U.S. Office of Naval Research, Grant # N000140710468. Such support does not constitute an endorsement by the funding agency of the opinions expressed in the dissertation.

Table of Contents

List of Tables

List of Figures

List of Acronyms

1D	One Dimensional
2D	Two Dimensional
3D	Three Dimensional
ACE	ACcumulative Error
ANN	Artificial Neural Network
BP	Back Propagation
CAD	Computer Aided Design
CEEE	Center for Environmental Energy Engineering
CFD	Computational Fluid Dynamics
DE	Differential Evolution
DOD	Department of Defense
DOE	Design Of Experiment
FEM	Finite Element Modeling
FPI	Fins Per Inch
GA	Genetic Algorithms
GB	Giga byte
GCI	Grid Convergence Index
HTC	Heat Transfer Coefficient
HTE	Heat Transfer Enhancement
HX	Heat eXchanger
HXD	Heat eXchanger Design
KBEM	Knowledge Based Evolutionary Method
LEM	Learnable Evolutionary Model
LHC	Latin HyperCube
LMTD	Log Mean Temperature Difference
MAE	Maximum Absolute Error
MAS	Metamodel Acceptability Score
MC	Monte Carlo
MCHX	Micro Channel Heat Exchanger
MED	Maximum Entropy Design
MFR	Mass Flow Rate
MOGA	Multi-Objective Genetic Algorithms
MOO	Multi-Objective Optimization
MSD	Maximin Scaled Distance
NGHX	Next Generation HX
NTU	Number of Transfer Units
PEC	Performance Enhancement Criteria
PMMA	Poly Methyl MethAcrylate
PPCFD	Parallel Parameterized CFD
PQSM	Progressive Quadratic response Surface Method
RAM	Random Access Memory
RE	Richardson Extrapolation

RMAE	Relative MAE
RMSE	Root Mean Squared Error
RNG	Renormalization Groups
RRMSE	Relative RMSE
RSS	Root Sum Square
RTD	Resistance Temperature Detector
SA	Simulating Annealing
SCFM	Standard Cubic Feet per Minute
SFCVT	Space Filling Cross Validation Tradeoff
SIMPLE	Semi Implicit Pressure Linking Equation
SIMPLEC	Semi Implicit Pressure Linking Equation Consistent
SS	Stainless Steel
TPD	Two Point Distribution
VFR	Volumetric Flow Rate

Nomenclature

A	Heat transfer area, m2
Br	Brinkman number: $\mathrm{Br} = \dfrac{\mu V^2}{k\left(T_w - T\right)}$
c	Specific heat, J/kgK
C	fluid thermal capacity, J/kg
C_2	Pressure jump coefficient
cp	Specific heat at constant pressure, J/kgK
C_R	Thermal heat capacity ratio
D	Diameter, m
E	Fluid Energy: sum of internal and kinetic energy, J/kg
e	error estimates
$\hat{e}$	approximated error
F	Body forces, N; correction factor
f	Friction factor; objective function
FFS	Free flow spacing
FS	Factor of safety
g	Gravitational acceleration; inequality constraint
Gz	Graetz number: $Gz = \dfrac{D_h}{L}\mathrm{Re}\,\mathrm{Pr}$
h	Enthalpy, J/kg; heat transfer coefficient, W/m^{2}K; representative mesh size, m; equality constraint
HS	Horizontal spacing
K	Pressure drop correlation parameter
i	Index
J	Species diffusion flux
k	Thermal conductivity, W/mK; turbulence kinetic energy, m^2/s^2
L	Length, m
M	Axial conduction number: $\dfrac{q_{axial\ conduction}}{q_{convection}}$; Mass
$\dot{m}$	Mass flow rate, kg/s
N	Number of mesh elements; Number

n	number of samples
Nu	Nusselt number: $Nu = \frac{hD_h}{k}$
P	Pressure, Pa; Probability
p	Observed convergence order
Pe	Péclet number (Re Pr)
Po	Poiseuille number (f Re)
Pr	Prandtl number: $\Pr = \frac{\mu cp}{k}$
Q, q	Heat transfer rate, W
q''	Heat flux, W/m^2
R	Thermal resistance, m^{2}K/W
r	polar r coordinate, mesh refinement ratio
Re	Reynolds number: $\frac{\rho vD}{\mu}$
S	Source term; space filling criterion
T	Temperature, K
t	Time, s; tube thickness, m
T	Temperature, K
U	Overall heat transfer coefficient, W/m^{2}K
v	Fluid velocity, m/s
V	Fluid velocity magnitude, m/s; volume, m^3,
VS	Vertical spacing
x	Cartesian x coordinate; design vector
X	statistical distribution value
$x+$	Dimensionless tube length: $x^+ = \frac{L}{\mathrm{Re}\, D_h}$
y	Cartesian y coordinate; true response
$\hat{y}$	Predicted response
z	Cartesian z coordinate

Greek Symbols

α	porous membrane permeability; slab inclination angle, °
Δ	Difference
δ	Offset

ε	Error, heat exchanger effectiveness; turbulent dissipation rate, m^2/s^3
ϕ	Key variable
η_o	Overall fin efficiency
ρ	Density, kg/m3
σ	Standard deviation
τ	Shear stress tensor, Pa
μ	Molecular viscosity, Pa-s

Subscripts

air	Air side
app	Apparent
avg	Average
b	bottom
c	Cold
crit	Critical
D	Hydraulic diameter
e	entrance length
eff	Effective
ext	Exact
f	fluid
fine	Fine mesh
Foul	Fouling
h	Heat, hot; hydraulic
H,i	header inlet
H,o	header outlet
i	Inlet; index
iH	inlet header
in	Inner
j	index
LOO	Leave One Out
m	Mass
max	Maximum
min	Minimum
o	Outlet

oH	outlet header
out	Outer
r, R	Relative
ref	refrigerant side
s	Solid
T	Total, tube
t	top
tube	tube side
w	Wall
water	Water side

Chapter 1: Introduction

This chapter describes the research motivation and the objectives of this dissertation. The research framework is briefly described followed by a summary of contributions in the field of air-to-water heat exchangers. This chapter ends with a brief description of the dissertation organization.

1.1. Motivation

Resource limitation and growing concern about sustainable development mandate the efficient anthropogenic use of material and energy. Improving material and energy use can be achieved via optimizing systems and components' design. In the refrigeration and air conditioning industry; Heat eXchangers (HX) affect system performance the most. Air-to-refrigerant HXs are widely used in this industry. Examples of such HXs are: condensers, gas coolers, radiators, and evaporators. Heat exchangers are essential in air-conditioning and refrigeration systems. There exist at least two heat exchangers in each vapor compression system, and with modern cycles incorporating secondary refrigerants at least one additional heat exchanger is added to the system.

The increase in concern about the environmental impact of heat transfer equipments requires the improvement of cycle efficiency while minimizing material used in manufacturing. A recent study (Westphalen et al. 2006) showed a potential of 0.7 to 1.1 quads of energy offset just by increasing the condensing units' Heat Transfer Coefficient (HTC) by 100 percent in the US market. This study shows the great impact of heat transfer improvement on energy savings.

The work presented in this dissertation is motivated by the complexity of novel HX performance prediction and the need to reduce the research and development cycle. Multi-scale multi-physics modeling capabilities for the design and optimization of the "next generation" air-to-refrigerant HX were developed, and applied to the design and optimization of a novel conceptual HX segment design. This tool provides a higher degree of model fidelity and accuracy. It can also evaluate the performance of novel HX designs targeting a new level of compactness with less flow impedance. In order to reduce the development cycle, the simulation tool is coupled with an approximation assisted optimization framework in order to find optimized HX designs at reduced computational time.

Prediction accuracy depends mainly on heat transfer and pressure drop correlations validity for both refrigerant and air sides of the HX. The conceptual design considerations presented later for the Next Generation of HXs (NGHX) suggest smaller channel dimensions for the refrigerant side and innovative design on the gas side to allow for compactness and heat transfer enhancement. The air side is usually of smaller densities and poor heat transfer coefficient compared to the refrigerant side and as such has higher improvement potential.

Available air side correlations validity for NGHX is questionable due to change in geometry and configuration. Therefore, heat transfer and pressure drop performance need to be evaluated through experimental or numerical investigations. Experimental investigations require the development of different prototype designs and time consuming experimental testing. On the other hand numerical investigations using Computational Fluid Dynamic (CFD) are proven to accurately evaluate the

thermal and hydraulic performance of enhanced surface designs (Sunden 2007, Nithiarasu 2005). CFD simulations require less time and are less expensive to conduct. This indicate the need to develop a multi-scale HX simulation tool that couples CFD simulations for thermal and hydraulic performance evaluation of the new surfaces with conventional HX models.

Conventional heat transfer and pressure drop correlations for single-phase refrigerant need to be investigated for the flow conditions at hand in order to ensure higher model fidelity. This investigation study was performed using verified and validated CFD simulations. The scope of the current research focuses on single-phase liquid refrigerant applications as these are widely used and can be seen as a pilot study for NGHXs.

The research presented here advances the air-to-water HX technology aiming at reducing the HX initial and operating costs. The initial cost reduction will be achieved through the optimized use of materials as well as optimized HX core volume. The operating cost reduction will be achieved through airside and refrigerant side pressure drop minimization resulting in minimized pumping power required for the same HX heat duty.

1.2. Objectives

This dissertation has three main objectives: (1) to develop accurate multi-scale multi-physics simulation tools coupled with previously developed approximation assisted optimization techniques, (2) to develop an integrated HX design and optimization framework for the development of next generation air-to-refrigerant heat

exchanger based on new heat exchanger geometries and materials, and (3) to develop design guidelines for next generation heat exchangers.

The multi-scale multi-physics heat exchanger simulation tool development encompasses: (a) development of a new generic ε-NTU solver that accounts for geometrical variability, (b) CFD simulation for segment level performance evaluation and development of an integrated approach with the previously developed ε-NTU solver, (c) investigation of available correlations validity for the operating range of interest, (d) numerical verification and experimental validations, and (e) multi-physics simulations to account for structural strength and refrigerant distribution analysis.

The heat exchanger design and optimization framework requires the development of new concept geometries to be studied, application of previously developed approximation assisted optimization techniques using the multi-scale multi-physics simulation tool, and assessment, verification and validation of the optimized results.

Finally, the development of next generation heat exchanger design guidelines requires thorough thermal and hydraulic analysis of the optimum results to identify the opportunities and limitations of the new heat exchanger concepts.

1.3. Dissertation Research Approach

Work presented in this dissertation aims at developing a new framework for HX design and optimization which depends on HX concept innovation. The flowchart of the developed framework is shown in Figure 1. First, the concept geometries are

compared against state of the art HX designs using first order analysis tools based on heat transfer area augmentation per unit HX volume and material, and overall thermal and fluid resistance. Second, potential geometries are further investigated through pilot CFD/FEM simulations to understand improvement potential, physics involved and gain experience required for batch evaluations. CFD simulations are verified using systematic procedures such as Grid Convergence Index (GCI) and Richardson Extrapolation (RE) to determine the simulation uncertainty. Third, the HX concept parameters are identified, and the CFD model and meshing strategies are developed based on experience from the second stage. Fourth, the multi-scale modeling approach is developed incorporating approximation techniques. Fifth, the approximation assisted multi-objective optimization coupled with multi-scale and multi-disciplinary modeling is used to optimize the conceptual NGHX design parameters. The optimization objectives include both HX volume and airside pressure drop; other objectives can be included based on the application at hand. Pareto solutions of the optimization problem are then used to demonstrate performance tradeoff and to understand performance improvement mechanisms. Finally, optimum solutions are verified using PPCFD simulations. Upon numerical verifications, potential prototype HX geometries are considered for prototyping, experimental validation and proof of concept.

Some preliminary work is required before this framework can be integrated. Such work includes: investigation of correlation validity, development of a multi-scale multi-physics HX modeling tool, and experimental test for CFD simulation validation. The investigation of correlation validity incorporates a CFD study on

single phase refrigerant flow in micro-tubes. CFD results are first verified and validated (American Institute of Aeronautics and Astronautics. 1998), then compared with conventional correlations for the specified operating conditions.

A new multi-scale CFD simulation approach is developed and used to minimize the computational time while maintaining an acceptable level of accuracy. In this approach, commercial CFD packages, Fluent® (Fluent 2007), is coupled with a developed segmented ε-NTU solver, CoilDesigner (Jiang et al. 2006), to simulate the overall HX performance. This coupling might be achieved online or offline. Online coupling requires a CFD simulation for a periodic HX segment to be evaluated for each configuration. Offline coupling requires several CFD simulations to be evaluated a priori. Results from CFD simulations are then used to construct a metamodel or a physics-based correlation that can later be used in the ε-NTU solver. For the offline coupling, either conventional or adaptive DOE methods are used to determine the sample of HX parameters to be evaluated.

The multi-scale simulation approach is verified using representative 3D CFD simulations. This tool is further extended to assemble HX of various segment designs in order to account for segment level geometrical variability due to manufacturing tolerances. An experimental test is carried out using a conceptual design to validate the multi-scale simulation tool. The prototyped HX is simplified based on the available manufacturing technologies and tube sizes.

Finally, the HX header design and performance evaluation tool is developed using CFD simulations for a simplified computational domain in order to reduce the computational expense. For these simulations, the porous jump boundary condition is

used to simulate the pressure drop through the HX flow channels in order to reduce the computational domain. This tool allows for batch evaluation; hence, it can be integrated with the multi-scale HX simulation tool to create a multi-physics HX simulation platform.

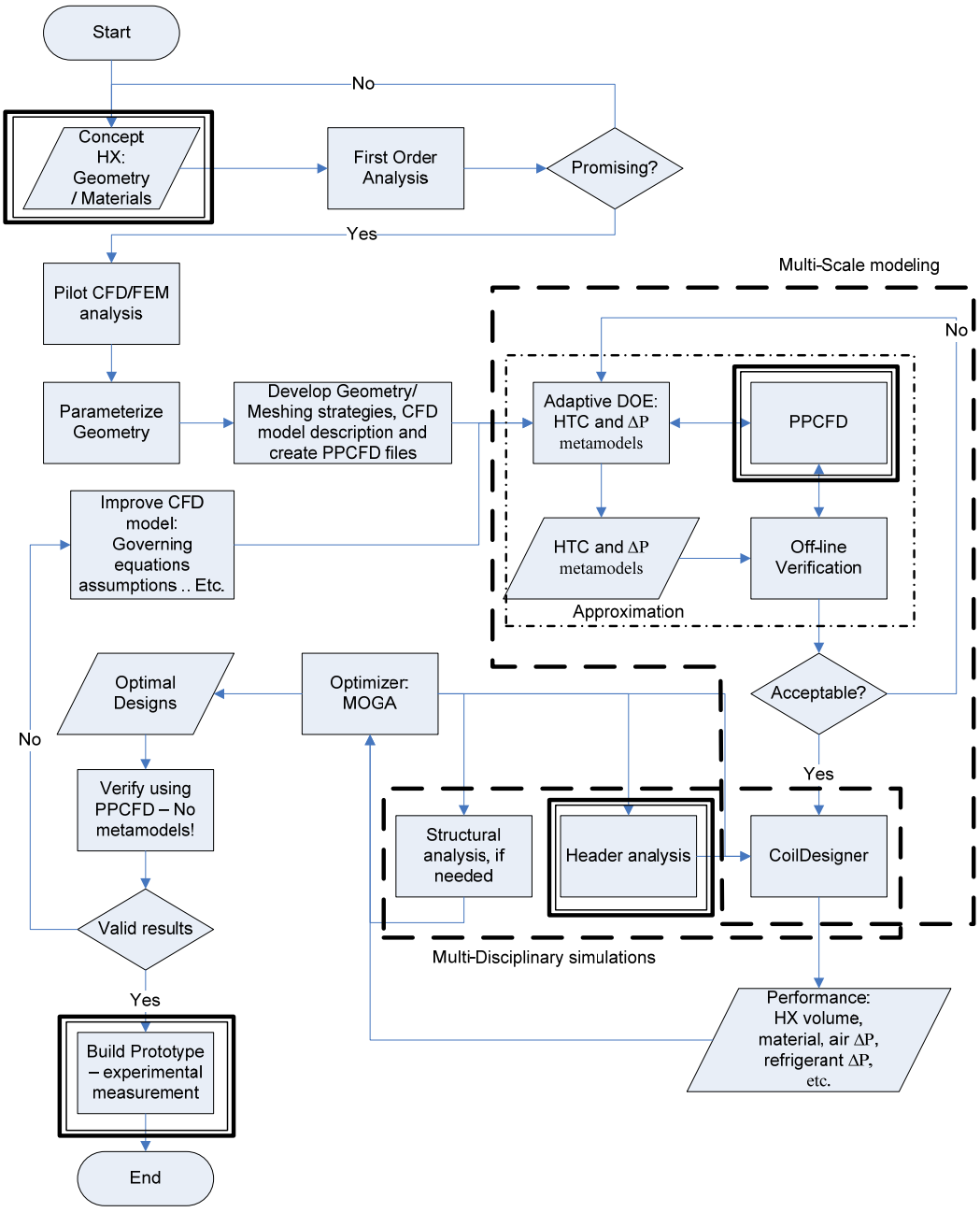

Figure 1: Proposed novel HX design and optimization framework

1.4. Contributions

This dissertation research aims at advancing the state of the art HX technology through development of a unified framework for novel HX design and optimization using advanced HX simulation tools and approximation assisted multi-objective optimization. Other major tasks include: investigation of conventional correlations validity for microscale flow, experimental investigation of novel HX designs, and development of novel header designs. Key contributions can be summarized as follows:

- Development, verification and validation of a multi-scale HX simulation capability.
- Development of a new ε-NTU solver capable of handling geometric and flow variability. Further, a new tool was developed for segment parameter distribution within a HX using Monte Carlo simulation approach.
- Header design and analysis model development.
- Development of design guidelines for a novel HX segment geometry based on results from approximation assisted optimization, header parametric studies and multi-scale simulation HX simulation under varying geometric and flow conditions.

1.5. Potential Compact HX Designs

After careful review of various heat transfer enhancement techniques discussed in section 2.1; it was decided to develop HX geometries to exploit some of

the passive techniques like extended surfaces, and secondary flows. Based on a thorough brainstorming session with sponsors, faculty and students at CEEE the following starting points were identified for potential novel designs:

- Refrigerant flow through thin fins: Eliminate bulky tubes obstructing the air flow.
- Implementations of enhanced fins concept such as slit and wavy fins.
- Removal of additional material.
- Bifurcation of refrigerant flow.
- Use of flexible tubes.
- Biologically inspired designs.
- Heat transfer surface augmentation.

A total of 22 geometries were proposed by CEEE faculty and students. These geometries were later used to stimulate discussions with CEEE consortium members (industrial, DOD, and Navy) who were invited for a day long workshop (Radermacher et al. 2007). The invited members provided comments about the approach and proposed geometries. Furthermore, the participants voted for geometry ranking in view of potential in development of the NGHX. The winning geometry was NGHX-13 shown in Figure 2. This concept geometry can have different port and tube configurations as described in (Abdelaziz et al. 2007). The work presented in this dissertation focus primarily on NGHX-13 with circular flow channels.

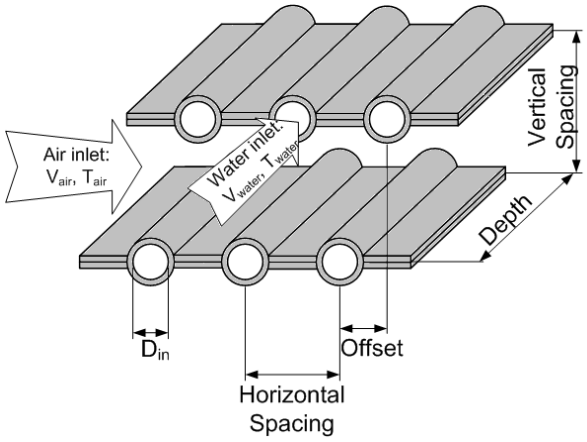

Figure 2: NGHX-13 geometry

1.6. Dissertation Organization

This dissertation is organized such that the literature review is presented in Chapter 2 with a summary of research guidelines, challenges and gaps in available literature that support the contributions claims listed earlier. Chapter 3 is dedicated to theoretical background regarding the techniques applied in this research. Chapter 3 provides the relevant background for heat exchanger simulations, CFD simulations, approximation techniques, and multi-objective optimization. Chapter 4 describes the development, verification and validation of the multi-scale simulation tool. Chapter 5 is dedicated for the header design and analysis and application to NGHX-13 header design. In light of the findings of Chapter 5 and the expected manufacturing challenges, the new ε-NTU solver is presented in Chapter 6 with case studies on three designs to reflect the baseline design impact. Chapter 7 presents methodologies and sample implementation of approximation assisted optimization to novel HX design optimization. In Chapter 8, the same approximation assisted optimization technique was applied to a conventional tube-fin A-type HX design. The experimental

investigations and the validation of the multi-scale simulation tool are presented in Chapter 9. Chapter 10 summarizes the main conclusions based on the research presented in this dissertation and provides design guidelines for NGHX. The dissertation concludes with recommendations for future work as presented in Chapter 11. First order analysis studies, structural analysis and single phase flow correlations validity investigations as well as first order header analysis problem description are listed in the appendices.

Chapter 2: Literature Review

This chapter provides a review of available literature related to the dissertation research. It summarizes the state of the art in Heat Transfer Enhancement (HTE), single phase flow in microtubes, CFD simulations of HXs, HX optimization and HX optimization using numerical methods.

2.1. Principles of Heat Transfer Enhancement

There exist numerous review publications on the topic of HTE. Over 9500 literature references are listed in (Webb and Kim 2005). According to (Webb and Kim 2005) HTE is classified into passive and active techniques as shown in Table 1. Other enhancement technique suited for mini and micro-scale transport phenomena such as: re-entrant obstruction, out of plane mixing, new surface treatment with alternating hydrophilic and hydrophobic sections, and variable roughness structures using micro-actuators are also listed in (Steinke and Kandlikar 2004).

Enhancement generally augment the product of heat transfer coefficient and the heat transfer surface area (hA) per unit base (hA) (Webb and Kim 2005). hA can be increased by increasing h, A or both. This leads to the increase of total HX UA value which can result in: (i) reduction in LMTD leading to better thermodynamic efficiency, (ii) reduction in size which can be translated into cost and weight reduction, or (iii) reduction in pumping power reflecting a reduction in the operating cost. Commercial development of enhanced heat transfer comes after several development phases (Webb and Kim 2005) which include: (1) basic performance "HTC and ΔP" correlations, (2) design and optimization methods, (3) manufacturing

technology and production cost, (4) pilot plant tests including long-term fouling and corrosion characteristics.

Table 1: HTE techniques

	Technique	Description
Passive	Surface coating	promote dropwise condensation "non-wetting coating", promote condensate drainage in evaporators "hydrophilic coating", enhance nucleate boiling "fin-scale porous coating"
	Rough surfaces	integral roughness – machining or non-integral – inserts: promote mixing in the boundary layer "single phase flow", induce nucleate boiling
	Extended surfaces	heat transfer area augmentation: external/internal
	Displaced inserts	indirectly improve energy transport at the heated surface
	Swirl Flow	create rotating or secondary flow: e.g. vortex generators
	Coiled tubes	higher heat transfer for the internal flow, higher heat transfer area per unit volume) "Channel Curvature"
	Surface tension	use surface tension forces to drain or transport liquid; film condensation coefficient is inversely proportional to the condensate film thickness
	Additives for liquids	solid particles/gas bubbles/liquid trace/nano composites
	Additives for gases	liquid droplets, solid particles – dilute-phase "gas-solid suspension" or dense-phase "packed tubes and fluidized beds"
Active	Mechanical aids	stir the fluid by mechanical means or rotate surface
	Surface vibration	low/high frequency – improve single-phase heat transfer
	Fluid vibration	low/high frequency
	Electrostatic fields	used with dielectric fluids leading to greater bulk mixing
	Injection	injecting secondary/upstream fluid to disrupt boundary layer
	Suction	vapor removal in nucleate film boiling, fluid withdrawal in single-phase flow through porous surface
	Jet impingement	impinging high velocity streams over the heat transfer surface

An example of heat transfer enhancement impact on energy efficiency is depicted in (Westphalen et al. 2006); authors showed that 100% increase in condenser

HTC can reduce the vapor compression cycle energy consumption by 10 to 15% which could provide about 0.7 to 1.1 quads of energy savings assuming no change in fan power. Furthermore, they listed the different challenges that face heat transfer enhancement as: tradeoff in energy savings versus cost, manufacturing techniques, fouling, as well as other case-by-case challenges. Their review showed that surface interruption techniques can achieve 50 to 100% HTE, surface roughness up to 300%, surface protuberances 50 to 500%, and boundary layer injection 50 to 500%.

Over the last 25 years, new compact HX surfaces have been introduced to provide better heat transfer rates, lower flow resistance, less weight, and lower cost alternatives. Multi-louver fin geometry is most common in auto industry heat exchangers, and offset strip fin geometry is common for aerospace and industrial heat exchanger applications (Shah 2006). Second-order improvement in single-phase convective heat transfer mechanisms may be achieved using offset strip fins and twisted tape inserts (Bergles 1997).

Vortex generation (swirl flow) is one of the actively researched HTE techniques (Jacobi and Shah 1995). Heat transfer enhancement associated with vortex generator depends on the location and number of the vortex generators “one or two delta wings” (O'Brien et al. 2004, O'Brien and Sohal 2005). For oval tubes, a single pair of winglets provides an average increase of 38% in heat transfer with less than 10% increase in friction factor. The numerical study of delta wing longitudinal vortex generators (Wu and Tao 2007) was used to identify the HTE mechanism associated with longitudinal vortices based on the field synergy principles (Guo et al. 1998, Tao et al. 2002). This study showed that longitudinal vortices improve the synergy

between velocity and temperature gradients. Dimpled surfaces may also be used to provide vortex generation for HTE (Ligrani et al. 2003). This concept was applied by (Chudnovsky and Kozlov 2006) for gas side heat transfer augmentation in fired process heaters. Their initial studies showed 30 to 40 % increase in heat transfer with acceptable pressure drop penalties. Furthermore, the suggested geometry was proven to be less prone to particulate fouling. Airside HTE was primarily sought by developing unsteady laminar flows through highly interrupted surface designs as smaller airside flow channels was not successful due to fouling problems and aspect ratio constraints (Jacobi and Shah 1998).

Reliable geometry optimization requires an understanding of the enhancement mechanism in order to exploit it to the extreme. Novel heat exchangers introduced recently rely mainly on smaller refrigerant flow channels (J. Pettersen et al. 1998, Saji et al. 2001, Kasagi et al. 2003b, Kasagi et al. 2003c) as well as new materials and flow structures (Gruss et al. 2005, Harris et al. 2000, C Harris et al. 2002, Li et al. 2004). Furthermore, there has been some efforts in incorporating porous metal medium instead of extended surfaces for flat tubes (Kim et al. 2000) showing comparable thermal performance to the louvered fins with a slight pressure drop increase.

Examples of continuing interest in heat transfer enhancement is witnessed by the large number of recent publications. In a review for the heat transfer literature in year 2000 (Goldstein et al. 2002), 23 papers addressed the issue of HTE. Those publications can be grouped into experimental and analytical studies. The experimental studies included extended surfaces, new tube designs, surface treatment

and the use of flow disturbance (inserts). The analytical studies focused on correlation development, visualization and numerical simulations, and validation of mathematical models. In the 2003 literature in heat transfer review (Goldstein et al. 2006), 38 publications were related to HTE. This shows an increasing trend in the work done in this field.

Another extensive review of HTE literature covering additional non-archival publications (Manglik and Bergles 2004) revealed that passive techniques are the most sought (70.9%) with emphasis on extended surfaces. They also suggest that fourth order heat transfer technology (Bergles 2002) evolved during 2001 where compound enhancement were introduced; e.g. rough surface tube with twisted tape inserts. This review also show the trend of investigating HTE on single phase flows during the initial development phase due to the large spectrum of applications.

The earlier transition from tube-fin design to microchannel design was based on smaller flow channel and the use of novel extended surfaces concepts such as louver and offset strip fins. Following the same line, NGHX would require further reduction in refrigerant channel dimensions and innovative design on the air side to allow for compactness and heat transfer enhancement.

2.2. Single Phase Liquid Flow in Microtubes

Interest in single phase heat transfer and pressure drop in circular microchannels has been increasing due to potential applications for heat exchanger performance improvement. Previous studies were mainly experimental in nature and focused on the higher end of the laminar Re as well as transition region. These studies

were driven by higher heat flux requirements as in the case of electronics cooling applications. The focus of this dissertation is to develop novel air-to-refrigerant heat exchangers. This application would have heat fluxes that are at least an order of magnitude less than typical microchannel application. As such, the available correlation validity is researched in order to find the best correlation for such application. Following is a critical review of previous work for liquid flow through microtubes.

Early work in pressure drop characteristic in microtubes showed a great deal of discrepancy due to overlooked physics and geometrical details relevant for microtubes (50 μm < D_h < 1 mm). This discrepancy is highlighted in (Judy et al. 2002, Koo and Kleinstreuer 2003, Hwang and Kim 2006). Careful analysis of measurement uncertainty found that error in tube diameter measurement had the highest impact on the overall uncertainty (Judy et al. 2002). Some of the relevant studies of pressure drop in microtubes are summarized in Table 2.

Earlier studies like (Mala and Li 1999) showed disagreement with conventional theory. Experimental results indicated higher friction factor as well as early laminar-to-turbulent transition. Viscous heating was not mentioned in their analysis; however they eliminated end effects by comparing pressure drop from 2 tubes of different length for each diameter. The disagreement was pronounced for smaller tubes and higher Re due to increased relative roughness and entrance length. A later study, (Judy et al. 2002), showed agreement with the Stokes flow theory after due considerations of entry length and temperature dependent viscosity effects (using the average viscosity in their data analysis). The work of (Li et al. 2003) showed that

laminar flow agree well with macroscale correlations for smooth flow; whereas for rough tubes this assumption does not hold true anymore. Ionic coupling and local viscosity changes were shown to increase the pressure drop in microtubes compared to conventional correlations (Brutin and Tadrist 2003); however, I believe that discrepancy in the results are due to the hydraulic entry length effects. (Koo and Kleinstreuer 2003) showed that entrance effects should be considered for all microfluidic systems whereas viscous heat dissipation should be considered for channel hydraulic diameters less than 100 μm. The same authors showed that viscous dissipation effects are pronounced for channel dimensions less than 50 μm hydraulic diameter in a later study (Koo and Kleinstreuer 2004). They concluded that both Br and Re determine whether or not viscous heating is significant and that the effect of property dependence on temperature increases especially in long channels with small D_h. This was also found in (Silber-Li and Cui 2005). The entrance type was shown to have no significant effect on the pressure drop as shown in (Campbell and Kandlikar 2004).

The heat transfer in microtubes has also been widely investigated before. Details of the experimental studies of relevant earlier work are summarized in Table 3. Results from these experiments varied between agreement and disagreement with conventional correlations. Experimental measurement of (Celata et al. 2002) showed disagreement with conventional correlations; disagreements were attributed to: higher measurement uncertainty at Re < 1000, axial conduction, viscous heating and the assumption of external wall temperature to be at steam condensing temperature. Variable Nu in the laminar region was reported in (Owhaib and Palm 2004); I believe

that this is mainly due to the thermal entry length. Based on REFPROP (Lemmon et al. 2007), R134a has a Pr of 3.423 (at 1.1 MPa pressure and 298.15K) which results in a thermal entrance length of 153 mm (~50% tube length) and 291 mm (~90% tube length) at Re of 1000 for the 0.8 mm and the 1.7 mm diameter tubes respectively. This effect was not pronounced in turbulent flow due to the small value of the thermally developing length (L_e/D_h ~ 20). Other experimental studies like (Kandlikar et al. 2003, Grohmann 2005, Celata et al. 2007) agreed with conventional correlations, e.g. (Gnielinski 1976) correlation, after accounting for surface roughness effects. Furthermore, the numerical investigations of (Lelea et al. 2004) were in good agreement with the (Shah and London 1978) correlations.

Axial conduction effects can be characterized by the dimensionless number M defined in equation (1). These effects can be neglected if M is less than 0.01 (Maranzana et al. 2004). This was also reflected in (Li et al. 2007) for both CFD simulations and experimental investigations.

$$M = \frac{q_{axial\ conduction}}{q_{convection}} = \frac{k_s \frac{A_s}{L}}{\rho c v A_f} \tag{1}$$

A recently developed technique by (Lin and Yang 2007) for local Nu measurement in microchannels using liquid crystal thermography was used for the heat transfer characterization of water flow in microtubes (Yang and Lin 2007). Thermal developing length was found to be longer than that predicted using the conventional correlation shown in equation (2).

$$L_e = 0.05 \,\mathrm{Re}\,\mathrm{Pr}\, D_i \tag{2}$$

Chronological order of published results shows better agreement due to advancement in micromachining, higher reliability and accuracy of recent experimental data, yet understanding the fluid flow and heat transfer mechanisms in microchannels has to be considered as an open scientific question (Morini 2004). Discrepancy in previous work might be attributed to surface roughness and experimental uncertainty (Celata 2004); in addition to viscous heating, thermal and hydraulic developing region effects and log mean temperature calculations (Palm and Peng 2004). After critical evaluation of the reported experimental studies, (Steinke and Kandlikar 2004) concluded that conventional theory is valid for microchannel and minichannel flows and found no evidence to an early laminar-to-turbulent transition. They suggest that reported discrepancies are due to: neglecting developing flows effect, fin efficiency, errors in channel geometry measurements as well as experimental uncertainties. Other reasons for discrepancy in previous results may be due to: experiment design flaws, surface roughness uncertainty, viscosity dissipation, and electric double layer theory (Shen et al. 2004). Finally, size effects leading to difference between micro and macro scale heat transfer and pressure drop where reviewed in (Guo and Li 2003). They attributed these effects to either gas rarefaction where the continuum assumptions is not valid – characterized by higher Knudsen number – and other factors like flow compressibility, surface roughness, surface forces having lower exponent dependence on length scale like viscous, surface tension and electrostatic forces, surface geometry, electrostatic charge, and axial conduction.

The debate on laminar single phase heat transfer and fluid flow in microtubes is moving towards accepting the fact that conventional theory is still valid for smooth tubes after due considerations to the hydraulic and thermal entry length as well as entrance conditions, transport property variations, viscous heating and axial conduction effects. Discrepancy in previous studies can be attributed to overlooked physics (e.g. entrance length, viscous heating, axial conduction, and property dependence) during data reduction and increased measurement uncertainties for lower Re and smaller tube diameters. Thus, the following points should be considered when studying fluid flow in microtubes:

- Measurement uncertainties over the entire experiment design space
- Entrance length effects based on theoretical boundary layer investigations
- Viscous heating effects should be judged based on Br and Re (Koo and Kleinstreuer 2004)
- Surface roughness measurements and their effect on pressure drop, heat transfer, and laminar to turbulent transitions
- Fluid transport property dependence on temperature
- Axial conduction effect (Maranzana et al. 2004)

Table 2: Summary of pressure drop experimental investigations

Reference:	D_i (μm)	Fluid tested	Tube material	Re	Results
Mohiuddin Mala and Li 1999	50 – 254	water	fused silica , SS	40 - 2100	Higher friction factor, dependence on Re
Celata et al. 2002	130	R114	SS	100 – 8000	good agreement for Re < 585, higher friction thereafter
Judy et al. 2002	15 – 150	water, methanol and isopropanol	fused silica and SS	8 – 2300	Agreement with theory
Li et al. 2003	79.9 – 205.3	deionized water	glass, silicon, SS	< 2500	Agreement for smooth tubes only
Brutin and Tadrist 2003	50 – 530	water	fused silica	NA	Higher friction factor
Campbell and Kandlikar 2004	457 – 1067	Water	NA	486 - 3952	No effect of entrance conditions
Silber-Li and Cui 2005	3 – 100	high pressure isopropanol	fused silica	0.1 - 1000	Higher effect of property dependence
Hwang and Kim 2006	244 – 792	liquid and two-phase R134a	SS	220 – 9300	8.9 % average deviation from Theory

Table 3: Summary of previous heat transfer experimental studies details

Reference:	D_i (μm)	Fluid tested	Tubes	Re	Results
Celata et al. 2002	130	R114	SS	100 – 8000	Lower heat transfer in the laminar regime, higher heat transfer in the turbulent regime
Kandlikar et al. 2003	620 – 1067	water	SS	500 – 3000	Agreement within experimental uncertainty. Increased surface roughness effects for small D_i
Lelea et al. 2004	125.4 – 500	water	SS	< 800	conventional theories are applicable for water flow through microchannel larger than 100 μm if entrance effects are included
Owhaib and Palm 2004	800 – 1700	R134a	SS	1000 – 17000	agreement with macroscale conventional correlations
Grohmann 2005	250 – 500	Argon	SS	400 – 20000	Superior performance in the developing region and agreement in the fully developed flow
Celata et al. 2006	120 – 528	water	glass	100 – 2300	Lower heat transfer, higher uncertainty for smaller D_i
Celata et al. 2007	120 – 528 146 – 440	demineralized water	glass, SS	50 – 3138 307–7025	Agreement with conventional correlations for SS
Lelea 2007	100 – 500	water	stainless steel	100 – 200	Numerical simulations agrees with conventional theory
Li et al. 2007	50 – 100 373 – 1570	Deionized water	fused silica, rough SS	20 – 2400	Agreement with conventional correlation for microtubes larger than 50 μm when surface roughness less than 1.5% Discrepancy in heat transfer results for Re < 100
Liu et al. 2007	243 – 520	Deionized water	quartz	100 – 7000	Rough agreement for laminar flow regime with Re > 100
Yang and Li 2007	123 – 962	water	SS tube bundle	80 – 23000	General agreement with conventional correlations, longer laminar $L_{e,th}$ for smaller D_i

2.3. CFD Simulations of Heat Exchangers

Traditional heat transfer and fluid flow performance prediction relied mainly on extensive experimental investigations. Based on those experimental results, performance data can be tabulated, plotted or correlated as in (Kays and London 1998). However, the increased computational capabilities allowed CFD simulations to be used more frequently. According to (Shah 2006), current industrial standard limits the role of CFD to just predicting the flow distribution in the headers and upstream of the HX as the accuracy of modern CFD simulation can't compete with experimental studies with its conventional acceptable accuracy of ±5%. He listed the use of CFD for HX as one of the future challenges and opportunities in the advancement of compact HX as they are required for the thermal and hydraulic prediction of new HX concepts (fluid flow/surface geometries). However, other researcher (Bergles 2002, Nithiarasu 2005) have suggested the use of numerical techniques for the prediction of heat transfer characterization of new geometries. CFD use in HX simulation can be categorized to two different approaches (Sunden 2007). In the first category, a large scale or relatively coarse computational meshes can be used along with local averaging or porous medium approach to predict the flow distribution upstream and within the HX by applying flow and thermal resistances. In the second category, periodic modules within the HX are identified and fine computational meshes are used to accurately simulate the heat transfer and skin friction. Accurate simulations depend on thorough understanding of the physics of transport phenomena and fundamentals of numerical algorithms. These CFD simulations could provide an insight into the heat transfer mechanism which helps

identify enhancement possibilities, e.g. (O'Brien et al. 2004). Examples of the second category of CFD use in HX simulation can be found in (Romero-Méndez et al. 2000, Li et al. 2006, Wu and Tao 2007, De Losier et al. 2007). There exist other studies in literature that used CFD for the thermal and hydraulic performance of new geometries (Xiong et al. 2005, Jing et al. 2005, Foli et al. 2006, Manzan et al. 2006, Malapure et al. 2007) showing acceptable validation to their CFD simulations with data from literature and experimental data. Further validation of other commercial CFD package for the thermal and hydraulic performance of HX can be found in (Van Der Vyver et al. 2003) and (Halbritter et al. 2004).

2.4. Modeling Heat Exchanger under Uncertainty

One of the earliest work in HX modeling under uncertainty was the work of (Haseler et al. 1983). They used the Root Sum Square (RSS) technique to propagate the effect of physical properties uncertainty, expressed in terms of error bounds, through the calculation of both HTC and total heat transfer area calculations. the RSS technique was used also to evaluate the confidence level in thermal design subject to HTCs and tube thickness uncertainties following a normal (Gaussian) distribution (Cho 1987). Other studies like (James et al. 1995) and (Bernier and Dinse 2002) also employed the RSS technique using error bounds to estimate HX performance uncertainties represented as error bounds. A two point distribution technique (TPD) (Rosenblueth 1981) was used by (Prasad et al. 2002) to estimate the temperature profile in counter flow concentric heat exchangers.

The other commonly used technique for modeling heat exchanger under probability is the use of Monte Carlo simulation. Normal distribution may well

represent HX geometrical parameter uncertainties whereas Weibull distribution is a better representation for the HTCs as suggested by (Badar et al. 1993). They used Monte Carlo simulation approach with 10,000 iterations to evaluate the required additional heat transfer area to achieve 80% and 99% confidence level in the thermal design of shell and tube heat exchangers used as oil coolers. Other examples of the recent use of Monte Carlo simulation for heat exchanger modeling under uncertainty can be found in (Clarke et al. 2001, Knetsch and Hauptmanns 2005, Pagani et al. 2005, Mackay et al. 2008). Studies mentioned hereinbefore are summarized in Table 4.

Heat exchanger analysis usually involves both thermal and hydraulic performance, all work presented earlier focused more on the thermal design with the exception of the work of (James et al. 1995). However, there exist other studies that focus mainly on the hydraulic performance such as the work of (Rodney L. Harris et al. 2002). They studied the water flow rate uncertainty in a fluidic system subject to design parameters (pump head, length, diameter, elevation, surface roughness, loss coefficients, and friction factor) and fluid properties (density, viscosity) following normal distributions using the advanced mean value plus iteration method. They validated the results using Monte Carlo simulation for few of their runs. The resulting mass flow rate followed a normal distribution as well.

Previous work relied mainly on the use of uncertainty bounds as in the case of analysis using RSS techniques or statistical distributions which was used along with RSS, TPD, and MC simulation techniques. The selection of the distribution type and parameter becomes a critical issue as these affect the response greatly. Selection of

input variable uncertainty should be based on sensitivity analysis and experts opinion (Pagani et al. 2005, Mackay et al. 2008). However, further investigations are needed to find the best way to represent actual variable uncertainties using statistical distributions.

2.5. Heat Exchanger Optimization

HX optimization is a traditional design problem. The first systematic HX optimization methodology was presented in (Fax and Mills 1957). They applied Lagrangian multipliers method (Deb 2001) in optimizing plate-fin gas-turbine heat exchanger based on analytical solutions. One of the earliest attempts for air-cooled HX optimization coupling analysis program to a numerical optimization scheme was presented in (Hedderich et al. 1982). However, typical HX optimization problem usually incorporates integer variables, e.g. the number of tubes, as well as continuous variables. For this type of problem, mixed variable optimization problem, conventional gradient based optimization techniques are limited. A mixed variable optimization problem can be solved by exhaustive search, branch and bound, relaxed discrete variables methods or heuristic approaches. Amongst the heuristic approaches, Genetic Algorithm (GA) (Deb 2001, Androulakis and Venkatasubramanian 1991) showed to be superior. This is depicted from the findings of (Tayal et al. 1999) where GA was able to provide multiple solutions of the same quality compared to Simulated Annealing (SA). Recent development in GA optimization include: Differential Evolution (DE) (Babu and Munawar 2007), GA coupled with Back Propagation (BP) Artificial Neural Network (ANN) (Peng and Ling 2008), and knowledge-based evolution method (KBEM) (Wu et al. 2008). DE was shown to be faster than

conventional GA which could be a potential source for accurate and faster optimization. GA with BPANN resulted in faster convergence than conventional GA.

Learnable Evolutionary Model (LEM) algorithm is a non-Darwinian evolutionary model. LEM attempts to model intellectual evolution; hence new populations are based on the results human designer's analysis of advantages and disadvantages of past populations through hypothesis formation and instantiation. This approach is proven to reduce evolution length as shown in (Cervone et al. 2000). A summary of relevant optimization studies is illustrated in Table 5 showing the optimization problem and optimization method for each study.

2.5.1. Heat exchanger optimization coupled with numerical simulation tools

CFD simulations of HX and optimization are discussed separately in previous sections. However, there exists a continuing effort in coupling HX optimization with CFD simulations for improved accuracy. This coupling is made possible due to the growing computational field and the introduction of approximation assisted optimization. In this section I will summarize some of the efforts undertaken in coupling HX optimization with CFD simulations as well as steps taken towards an integrated approximation assisted optimization framework.

Table 4: Summary of previous heat exchanger modeling under uncertainty

research group	uncertain parameters	method	Uncertainty distribution	Application	Evaluated performance
(Haseler et al. 1983)	physical properties	RSS	error bounds	shell and tube HX	U, A
(Cho 1987)	HTC, tube thickness	RSS	normal	shell and tube	confidence level
(Badar et al. 1993)	tube D, t, k, $HTC_{in,\ out}$	MC, 10000 trial	normal, log normal, Weibull	shell and tube oil cooler	U, A, confidence levels
(James et al. 1995)	49 parameter uncertainty: properties, dimensions and inlet conditions	RSS	error bounds	air to air cross flow heat exchanger	error bounds for Q, ΔP, T_{exit}
(Clarke et al. 2001)	gas fluid properties	MC (LHC Sampling) 1000 trial	normal distribution	hair pin HX (combustion gases to air)	U, A, T profiles
(Bernier and Dinse 2002)	soil temperature and thermal conductivity	RSS	error bounds	ground loop heat exchanger	L
(Prasad et al. 2002)	inlet temperature, overall HTC	TPD	NA	counter flow concentric tubes	T_{exit}
(Knetsch and Hauptmanns 2005)	$T_{i,\ gas}$, or VFR, and gas composition	MC 10000 trial, fitted data into the best possible statistical distribution	Truncated normal Lognormal Weibull Gamma Triangular Exponential	gas heater (using condensing steam on the hot side)	T_{exit} response subject to step input
(Pagani et al. 2005)	Power, P, T_{wall}, Nu, f	MC, 10000 trial	normal	Gas cooled fast reactor	probability of functional failure
(Mackay et al. 2008)	HTC, surface roughness, leakage, shaft moment of inertia	MC with LHC sampling	normal, log normal, exponential	decay heat removal heat exchanger	gas cooled reactor reliability: T_{max}

Table 5: Summary of Heat Exchanger Optimization Review

research group	optimization method	problem
(Bennett et al. 1994)	gradient based	minimizing the life-cycle cost of run-around heat exchangers subject to 9 constraints with 17 variables
(Chaudhuri et al. 1997)	SA with a black-box heat exchanger model	minimizing purchase cost subject to vibration constraints for shell and tube HX
(Litinetski and Abramzon 1998)	multistart adaptive random search	global constrained optimization with application to compact HX
(Reneaume and Niclout 2003)	relaxed discrete variables successive quadratic programming branch and bound SA approaches	plate fin HX design optimization
(Queipo et al. 1994)	GA	optimization of electronics components cooling
(Schmit et al. 1996)	GA	design of high intensity cooler
(Tayal et al. 1999)	SA and GA	large scale shell and tube heat exchanger design
(Wang et al. 2007)	GA	volume/weight minimization of a 100kW gas turbine recuperator under pressure drop constraints
(Babu and Munawar 2007)	DE	optimization of shell and tube heat exchangers
(Peng and Ling 2008)	GA with BPANN	minimization of plate fin heat exchangers volume and operating cost
(Wu et al. 2008)	KBEM	HX circuitry optimization
(Domanski et al. 2004, Michalski and Kaufman 2006)	LEM	HX circuitry optimization with non-uniform airflow distribution

Early work on HX optimization coupled with numerical simulation is shown in (Queipo et al. 1994). In this paper, GA optimization was coupled with a numerical solver for optimization of electronics cooling. GA was also used by (Fabbri 1997) in

longitudinal fin shape optimization using FEM resulting in new fin profiles that doubles the base heat flux. A simplified framework for shape optimization using CFD simulations (Guessous and Maddipatla 2002) was used to integrate Gambit and FLUENT with a 1D Golden-section unconstrained optimization method for minimization of flow non-uniformity in radiator headers. A graph based evolutionary algorithm was coupled with numerical simulation (Suram et al. 2006) for HX fin shape optimization. In an effort to reduce the optimization variables in fin shape optimization, the commercial FEM (FEMLAB) was coupled with a commercial multi-objective genetic algorithm optimization tool (modeFrontier) (Nobile et al. 2005, Nobile et al. 2006) to optimize the shape of wavy channels using the concept of NURBS (Farin 1999). A similar study with an automated and parallelized procedure was presented in (Hilbert et al. 2006) in order to reduce computational time.

HX geometry optimization extends beyond just fin shape optimization. (Foli et al. 2006) coupled a MOGA with a commercial CFD package in order to find the optimum geometrical parameters of a micro HX showing a trade-off between pressure drop and heat transfer coefficient. A systematic framework was presented in (Micheli et al. 2008) where a commercial process integration environment is used to integrate commercial CAD and CFD packages to solve the compact recuperator with design multi-objective optimization (MOO) problem using MOGA.

2.5.2. Approximation assisted Heat exchanger optimization

The increasing demand to reduce the computational time led to the application of approximation assisted optimization in HX design optimization. Early work in the approximation assisted optimization studies in HX, e.g. (Lee et al. 2001),

incorporated curve fitting to correlate the response obtained from a parametric CFD study with no DOE involved. A systematic procedure for the integration of DOE, meta-modeling, and optimization in thermo-sciences is illustrated in (Queipo et al. 2005) with a variety of DOE and metamodeling techniques. Latin HyperCube (LHC) DOE (McKay et al. 1979) and least squares response surface method were used in (Jing et al. 2005) for plate fins design optimization. The Progressive Quadratic Response Surface Method (PQSM) was used by (Park and Moon 2005) for heat sink optimization. Later, the same authors incorporated Kriging (Cressie 1993) metamodeling technique with LHC for DOE for the heat sink design optimization (Park et al. 2006).

2.6. Summary

The review of previous work in the fields of heat transfer enhancement, single phase flow in microchannels, CFD simulations of heat exchanger, and heat exchanger optimization revealed guidelines, challenges and gaps. In the sections below, the acceptable practices and guidelines are summarized followed by the challenges that face the heat exchanger developments and gaps that present opportunities for research.

2.6.1. Guidelines and acceptable practices

Available literature indicates that enhanced heat transfer continues to be an active area of research that requires more attention in order to develop better performance and optimized designs. Enhancement can be achieved passively through: novel area augmentation, improved mixing, composite material or actively through: vibration, electrostatic fields, suction or injection. Passive techniques are proven to be

more robust. Hence, this dissertation is focused on heat transfer improvement through area augmentation and boundary layer restarting.

Previous work in single phase liquid flow in microtubes showed a variation in experimental results that is largely due to experimental uncertainty; and that few reported simulation results verified that there is no additional physical phenomena observed down to a 100 μm tube diameter. There exists an agreement that conventional correlations can be used to predict the thermal and hydraulic performance of single phase flow in microchannels. The accuracy of CFD prediction is demonstrated in earlier studies through systematic grid refinement and validation against experimental data. And it was shown that CFD provides additional flow details which can help researchers gain more insight on the flow behavior and reasons for deviation from conventional and theoretical correlations.

As the above review shows, CFD simulation of heat exchanger is an established practice. Researchers were able to predict thermal and hydraulic performance accurately. Most of the previous work had been performed using commercial CFD packages such as Fluent®, StarCD® and CFX®. Both CFX® and Fluent® were used in the current work. However, Fluent® was proven to be easier to automate and had abundant validation studies. Hence, Fluent® was further employed for the CFD simulations of the HX elements.

Finally, HX optimization has been pursued extensively in previous studies. Previous research was either for segment optimization (employing CFD simulations) or for overall HX performance optimization (parameter selection and circuitry). These studies indicated that heuristic approaches, such as GA, are better suited for the

HX optimization problem since these problems usually involve both continuous and discrete variables. Several previous studies showed that CFD coupled optimization is possible. However, these studies proved to be computationally expensive. As such, approximation assisted optimization was introduced with focus on conventional DOE techniques and several metamodeling options.

2.6.2. Challenges

HX development targets heat transfer enhancement with minimum pressure drop penalty. Conventional practices indicate that higher heat transfer is usually associated with higher pressure drop due to increased diffusion. Hence, there would always be a tradeoff between heat transfer enhancement and pressure drop penalty. In this regards, the HX design optimization should be regarded as a multi-objective optimization problem. The relative increase in thermal performance should be measured against the added pressure drop. However, with systematic optimization, it is possible to find designs that provide superior thermal performance with lower pressure drop as shown in Chapter 7.

Computational time required to perform such optimization studies implies a great challenge. Hence, it is important to develop multi-scale simulation techniques that can reduce the computational time appreciably. To further reduce computational time, approximation techniques are required to be incorporated. Adaptive DOE methods can be used to efficiently select the designs required to develop the metamodels. This would ensure the efficient use of available computational time.

Another important challenge is to verify and validate analytical tools developed in order to ensure that only sound designs are selected for expensive, time consuming experimental investigations.

2.6.3. Gaps

Interest in heat transfer enhancement is a growing field of research. Conventional Performance Enhancement Criteria (PEC) provided limited impact on the overall performance of the HX. There is a need to develop multi-scale simulation capabilities for new design ideas that is capable of analyzing the performance improvement of the new designs over conventional or state of the art designs on the overall HX scale. This is important as circuitry and flow configurations affect the performance greatly. This was a great motivation to pursue the development of the multi-scale simulation tool, presented in Chapter 4, and verify the originality of such contribution.

The large body of literature in the field of single phase liquid flow in microtubes is limited on higher heat flux application in the range dictated by electronics cooling. These studies were performed with either constant wall temperature or constant heat flux. There were a limited number of studies that investigated convective boundary conditions. In the case of air to refrigerant heat exchangers the tubes are subject to convective boundary conditions with an order of magnitude lower heat flux than in the case of electronics cooling. As such further studies are required in order to determine the most suitable pressure drop and heat transfer correlations for low Re flow conditions subject to convective heat transfer.

This gap warrants the need for numerical investigations that are summarized in Appendix C.

The area of heat exchanger modeling under variability warrants additional investigations. Previous studies focused mainly on uncertainty in boundary conditions and the overall dimensions of the HX. Novel HX designs are expected to have smaller port diameters which render the tubes less rigid. This would introduce geometric and flow parameter variabilities within the HX. As such; there is a need to develop a tool that is capable of distributing the segment variability amongst the different segments within a HX. This would also require additional modifications to developed ε-NTU segmented solver to accommodate such variabilities.

There has not been previous work on optimizing a HX segment based on its impact on the overall HX performance using a detailed multi-scale HX simulation tool. Performing optimization employing CFD for segment performance evaluation and segmented HX simulation tool for the overall performance analysis has not been performed before. Such effort constitutes an original contribution as well. This technique was used as a case study for the space filling cross validation tradeoff developed adaptive DOE technique (Aute 2008).

Finally, there is a need to develop HX simulation capabilities that accounts for geometric and flow variability. This is especially important due to the challenges in associated with the manufacturing of compact heat exchanger of smaller length scales (Palm and Peng 2004). This would also reflect the need to understand the refrigerant flow distribution and the challenges associated with having a large number of parallel microtubes.

2.6.4. Closure

In summary, opportunities, challenges and gaps in the field of HX performance improvement warrants the additional research. This dissertation presents research work that capitalizes on the opportunities, fills some of the gaps in this field and overcome some of the challenges.

Based on the previous review of available literature the following are identified as key opportunities:

1. Passive techniques provide reliable means for heat transfer enhancement.
2. CFD simulations are capable of evaluating the thermal and hydraulic performance of new HX geometrical designs.
3. Heat transfer and pressure drop correlations for single phase liquid flow in microtubes are valid.
4. Adaptive DOE techniques provide an efficient use of computational resources.
5. Multi-Objective Genetic Algorithms are most suitable for HX design optimization problem.

The gaps and challenges described in the previous sections that are addressed in this work can be summarized as:

1. Need for a systematic coupling of CFD simulations of the HX segment with overall HX solver.
2. Need for a modified segmented ε-NTU model capable of accounting for geometric and flow variabilities within a HX.

3. Need for numerical verification and experimental validation of a proposed coupling approach.
4. Need for a modified HX solver that is capable to account for HX variability.
5. Need to account for refrigerant headers on the overall HX performance.
6. Need for the development of high fidelity, fast simulation approach to be incorporated in a systematic framework for design and optimization of new HX geometry.

Chapter 3: Theoretical Background

This chapter is intended to provide a review of thermal and fluid analysis incorporated in HX simulations as well as a review of the approximation assisted optimization techniques. First, the heat exchanger analysis methods are described with emphasis on the ε-NTU technique. Second, CFD simulation and verification methodologies are presented and followed by describing the approach used to perform parallel parameterized simulations. Third, approximation assisted optimization techniques are described with the 4 steps incorporated: design of experiment, metamodeling, verification and optimization.

3.1. Heat Exchanger Design

Heat exchanger design is a complex problem that requires thermal, hydraulic, geometrical, and structural analyses. HX design methodology can be divided into four inter-related categories: process specifications, thermal and hydraulic design, flow analysis and mechanical design, and processing (Shah and Sekulic 2003). This section focuses on the thermal and hydraulic design which depends on the thermo-physical properties of fluids and materials, surface characteristics and geometrical properties, and segment heat transfer, fin efficiency and pressure drop. The thermophysical properties of the working fluids were evaluated using NIST REFPROP 8.0 (Lemmon et al. 2007). Solid material properties are evaluated at an average temperature based on (Incropera and DeWitt 1996). The surface characteristics and geometry is dictated mainly by segment performance and HX constraints (heat duty, allowable pressure drop, geometrical and weight constraints).

Conventionally, heat transfer coefficient, fin efficiency and pressure drop are evaluated using correlations based on the prescribed boundary conditions and characteristic lengths. However, no valid correlations are available for new HX geometries; hence experiments or CFD simulations are required to estimate the heat transfer coefficient, fin efficiency and pressure drop.

There exist two techniques for heat exchanger design namely: *UA*-LMTD and ε-NTU. In the *UA*-LMTD technique, energy balance equations (3) and (4) are solved along the rate equation (5) according to the problem definition. *UA* and LMTD use in equation (5) are defined in equations (6) and (7) respectively for counter flow configuration, and *F* is the correction factor for other HX flow configuration. This technique is useful if all inlets and outlets conditions are known a priori.

$$Q = \dot{m}_h c_{p,h} \left(T_{h,i} - T_{h,o} \right) \tag{3}$$

$$Q = \dot{m}_c c_{p,c} \left(T_{c,o} - T_{c,i} \right) \tag{4}$$

$$Q = UA\left(F \times \mathrm{LMTD} \right) \tag{5}$$

$$UA = \left[\frac{1}{\left(\eta_o h A_T \right)_c} + R_{foul,c} + R_{contact,c} + R_{wall} + R_{contact,h} + R_{foul,h} + \frac{1}{\left(\eta_o h A_T \right)_c} \right] \tag{6}$$

$$\mathrm{LMTD} = \frac{\left(T_{h,i} - T_{c,o} \right) - \left(T_{h,o} - T_{c,i} \right)}{\ln\left(\dfrac{T_{h,i} - T_{c,o}}{T_{h,o} - T_{c,i}} \right)} \tag{7}$$

The ε-NTU technique relies on the definition of the HX effectiveness (ε), as shown in equation (8). ε depends on the flow geometry and passes arrangement. For a given HX configuration, ε is a function of NTU and C_R defined in equations (9) and (10) respectively. ε-NTU technique is superior to the *UA*-LMTD technique in HX

rating problem (when heat transfer rate and pressure drop for each stream are unknown). Both ε-NTU and *UA*-LMTD techniques inherently ensure that the second law of thermodynamics is not violated. However, the values of ε and NTU allow for physical interpretation of thermodynamics performance of the HX.

$$\varepsilon = \frac{Q}{Q_{\max}} = \frac{Q}{\left(\dot{m}c_p\right)_{\min}\left(T_{h,i} - T_{c,i}\right)} \tag{8}$$

$$\mathrm{NTU} = \frac{UA}{\left(\dot{m}c_p\right)_{\min}} \tag{9}$$

$$C_R = \frac{\left(\dot{m}c_p\right)_{\min}}{\left(\dot{m}c_p\right)_{\max}} \tag{10}$$

The use of LMTD provides a higher degree of accuracy; however the *UA*-LMTD cannot be used if both outlet temperatures are not known a priori as in the current situation. As such the ε-NTU approach was used. In this analysis, ε was evaluated based on correlations for unmixed-unmixed cross-flow HX (Shah and Sekulic 2003). The segmented HX model developed by (Jiang et al. 2006) was used to predict the overall HX performance. This model divides the heat exchanger into several cross-flow HX macro volumes (segments). For each segment, total heat transfer rate is first calculated from Equation (8), then Equations, (3) and (4) are solved to obtain the outlet temperature of both fluids. To allow for generalized circuitry, the model employs a junction-tube connectivity matrix which is used to track refrigerant flow from inlet to outlet of the HX. The computational sequence is generated at run-time based on heat exchanger circuitry. The model can be used to distribute mass flow rate through circuits of different length, based on pressure drop.

This model has been validated against experimental data from multiple sources, e.g. (Jiang et al. 2006, Wang 2008)

3.2. CFD Simulations

CFD simulations are based on numerical solutions of the fluid governing equations. The main governing equations are the continuity and momentum equations (Navier-Stokes equations) which describe the flow behavior. Other scalar transport governing equations, e.g. energy, species, and turbulent closure equations, describe the scalar transport within the flow field. The crucial step in CFD simulations is the pressure-velocity coupling. Earlier work was based on the semi-implicit-pressure-linking-equation (SIMPLE) techniques and its variants. Recently, FLUENT implemented a coupled pressure-based solver that improves convergence and model robustness greatly. Brief descriptions of the different governing equations (Patankar 1980, Versteeg and Malalasekera 1995, Fluent 2007) involved in the simulation of HX surface performance are illustrated below.

The general form of the continuity equation is shown in equation (11). In this equation, the first term can be neglected under the assumptions of incompressible steady state flow. Furthermore, the source term can be neglected since no mass source will be introduced in the current simulations.

$$\frac{\partial \rho}{\partial t} + \nabla \cdot \left(\rho \cdot \vec{v} \right) = S_m \qquad (11)$$

The conservation of momentum in an inertial (non-accelerating) reference frame may be described by equation (12). In this equation, P is the static pressure, $\bar{\bar{\tau}}$

is the stress tensor, $\rho\vec{g}$ is the gravitational body force and $\vec{F}$ is the external body forces. The stress tensor $\overline{\overline{\tau}}$ is defined as shown in equation (13).

$$\frac{\partial\left(\rho\vec{v}\right)}{\partial t}+\nabla\cdot\left(\rho\cdot\vec{v}\vec{v}\right)=-\nabla P+\nabla\cdot\left(\overline{\overline{\tau}}\right)+\rho\vec{g}+\vec{F} \qquad (12)$$

$$\overline{\overline{\tau}}=\mu\left[\left(\nabla\vec{v}+\nabla\vec{v}^{T}\right)-\frac{2}{3}\nabla\cdot\vec{v}I\right] \qquad (13)$$

The differential form of the energy equation can be written as shown in equation (14). Where: $\vec{J}_j$ is the diffusion flux of species j which is neglected in the current analysis. The first three terms on the right-hand side of equation (14) represent energy transfer due to conduction, species diffusion, and viscous dissipation, respectively. S_h includes the heat of chemical reaction, and any other volumetric heat sources defined in the flow model; heat sources are also neglected in HX simulation. E is the total energy of a fluid particle (control volume).

$$\frac{\partial}{\partial t}\left(\rho E\right)+\nabla\cdot\left(\vec{v}\left(\rho E+p\right)\right)= \nabla\cdot\left(k_{\text{eff}}\nabla T-\sum_{j}h_j\vec{J}_j+\left(\overline{\overline{\tau}}_{\text{eff}}\cdot\vec{v}\right)\right)+S_h \qquad (14)$$

The available CFD commercial package, Fluent®, used in the present work neglect the pressure work and kinetic energy in solving incompressible flow using a segregate solver, but these could be included intentionally if the flow physics warrants their importance. Similarly, the viscous heating is neglected by default when using segregate solver with incompressible flows as the Brinkman number (Br) will be typically less than unity. In case of Br greater than unity, the viscous heating should be accounted for in the solver controls.

As enhanced surfaces rely greatly on reducing the flow channel dimensions, normal flow conditions lie within the laminar flow regime. As such there was no need for turbulence models in the current situation. However, in some extreme cases the state of turbulence is declared, when flow Re is higher than the critical limit Re_{crit}. Turbulence state is associated with random flow field properties that affect all the flow parameters. Flow turbulence causes fluctuations that may be of small scale and high frequency; and as such is too computationally expensive to be directly simulated in practical engineering calculations. For this reason, the instantaneous governing equations are time-averaged, ensemble-averaged, or otherwise manipulated to remove the small scales, resulting in a modified set of equations that are computationally less expensive to solve (Bernard and Wallace 2002). However, the modified equations contain additional unknown variables, and turbulence models are needed to determine these variables in terms of known quantities. Turbulence model choice should be based on a case by case analysis. In this regard, for any novel HX geometry the best model should be sought during initial pilot studies.

3.2.1. CFD verification and validation

The problem of validation and verification has been thoroughly investigated. According to (American Institute of Aeronautics and Astronautics. 1998) "Verification is the process of determining if a computational simulation accurately represents the conceptual model, but no claim is made of the relationship of the simulation to the real world. Validation is the process of determining if a computational simulation represents the real world". The differences between verification and validation was further discussed in (Babuska and Oden 2004). CFD

verification and validation has been discussed in details in (Mehta 1996, Oberkampf and Blottner 1998, Stern et al. 2001). These studies identified the different physical and numerical modeling errors in CFD. They suggest the use of Grid Convergence Index, GCI (Roache 1997, Roache 1998), or Richardson Extrapolation, RE (Celik and Zhang 1995), to estimate the error associated with numerical simulations. These approaches were applied to a finite volume simulation for a steady state fluid flow and heat transfer problem with the suggestion of a new post processing tool for dynamic verifications (Cadafalch et al. 2002).

The status of numerical error assessment in CFD simulations was summarized in (Freitas 2002) with emphasis on the importance of considering the uncertainty analysis using RE or GCI for commercial code use. This study further suggests the use of tools that provide dynamic diagnostics of a given simulation. A five step procedure for the application of RE using the GCI in CFD is defined as follows (Freitas et al. 2003):

1. Calculate the representative mesh size is defined as shown in equation (15)
2. Use 3 different grid resolutions (grid refinement factor > 1.3: $h_{coarse}/h_{fine} \geq 1.3$) and run simulations to determine the value of key variables (ϕ)
3. Calculate the observed order, p, from equation (16)
4. Calculate the extrapolated value using equation (17)

5. Calculate and report error estimates according to equations (18) to (20) . A value of 1.25 for the Factor of Safety (FS) results in a GCI with a 95% confidence interval.

$$h = \sqrt[3]{\frac{\sum_{i=1}^{N} \Delta V_i}{N}} \tag{15}$$

$$p = \frac{1}{\ln(r_{21})}\left[\ln\left(\left|\frac{\varepsilon_{32}}{\varepsilon_{21}}\right|\right) + \ln\left(\frac{r_{21}^{p} - s}{r_{32}^{p} - s}\right)\right] \tag{16}$$

Where $h_1 < h_2 < h_3$, $r_{ij} = h_i / h_j$, $\varepsilon_{ij} = \phi_i - \phi_j$, and s is the sign of the ratio $\varepsilon_{32} / \varepsilon_{21}$.

$$\phi_{ext}^{21} = \frac{\left(r_{21}^{p}\phi_1 - \phi_2\right)}{r_{21}^{p} - 1}, \phi_{ext}^{32} = \frac{\left(r_{32}^{p}\phi_2 - \phi_3\right)}{r_{32}^{p} - 1} \tag{17}$$

$$e_a^{21} = \left|\frac{\phi_1 - \phi_2}{\phi_1}\right| \tag{18}$$

$$e_{ext}^{21} = \left|\frac{\phi_{ext}^{21} - \phi_1}{\phi_{ext}^{21}}\right| \tag{19}$$

$$GCI_{fine}^{21} = \frac{FS \times e_a^{21}}{r_{21}^{p} - 1} \tag{20}$$

The validation process can be done be comparing the CFD results with experimental measurement or analytical solutions. Fluent® solver has been widely validated. An example of such a validation work is shown in (Lee and Dimenna 2005). In this study, the code was benchmarked for a wide range of simple, classical, and complex physical problems. For simple physical problems, Fluent® results were compared against analytical solution and showed that the code predictions are within about 10% relative error. For the complex test problems, the code predictions agreed with the literature data within about 18% relative error. However, based on my

analysis of their work, better results could be achieved by implementing a higher order discretization schemes and improved meshing.

3.2.2. Parallel parameterized CFD simulations

The research framework presented in Figure 1 requires a large number of CFD simulations to be performed. As such, a new tool was developed to read a set of parameters for batch evaluation. This tool automatically generates Gambit® script files, Fluent® script files, runs the scripts and performs post processing to summarize the results in terms of relevant thermal and hydraulic performance indicators. The developed tool is named Parallel Parameterized CFD (PPCFD) simulations. The flow chart of PPCFD is shown in Figure 3.

Pilot CFD studies are required to build the required experience to develop meshing strategies, model limitations, boundary conditions, and parameters involved. Based on this experience, a code is developed to generate the required script files for different parametric values. PPCFD starts by reading the parametric values of all the CFD cases and then writing Gambit® and Fluent® journal files for each case. The tool generates batch process runners depending on the number of available processors (user specified) and run all batch files in parallel.

For each batch process, Gambit® reads the Gambit® journal and generates the mesh for each case. Fluent® then runs the Fluent® journal that reads the corresponding mesh, sets the model equation, boundary conditions, and solver settings and writes flux and surface integral reports for the boundaries of interest to an intermediate output file. Finally, PPCFD read the intermediate output file for each case and process it to find the overall heat transfer coefficient, airside pressure drop

as well as other key performance indicators that can be used for later analysis. As such, a consolidated output file is generated identifying each case parameters and performance indicators. This file has a unified format; the case name, pressure drop, heat transfer coefficient, air outlet temperature, Re, and number of iterations are written for each case. Other output values include CFD domain summary, air mass flow rates, air velocity, mass and energy balance errors, as well as details of the area-weighted average pressure at the inlet domain for the last 100 iterations (in case the maximum number of iterations are reached). The last four fields are: the average, maximum, minimum, and standard deviation of the inlet pressure over the last 100 iterations. If the maximum number of iterations are reached the solutions is only accepted if the inlet pressure shows a converged solution (e.g. the standard deviation is less than 0.5%).

3.3. Approximation Techniques

Approximation is a technique to replace time consuming function evaluation (physical or numerical experiments) using a metamodel or surrogate model (Simpson et al. 2001, Wang and Shan 2007). This is extremely important in the case of optimization since finding an optimum usually involve a large number of function evaluations ranging from hundreds to thousands based on the problem dimensions. Two types of responses are identified in approximation techniques: true response and predicted response. The true response is the output from an experiment or simulation while predicted response is the output of metamodel representing the experiment or the simulation. Approximation starts by the DOE stage (Giunta et al. 2003) to sample the design space and generate the response data, and then metamodeling tools are

used to build a metamodel based on DOE response data. The developed metamodel is then verified (Cressie 1993, Martin and Simpson 2005, Hamad 2006) for goodness assessment and is finally used for optimization or other parametric studies.

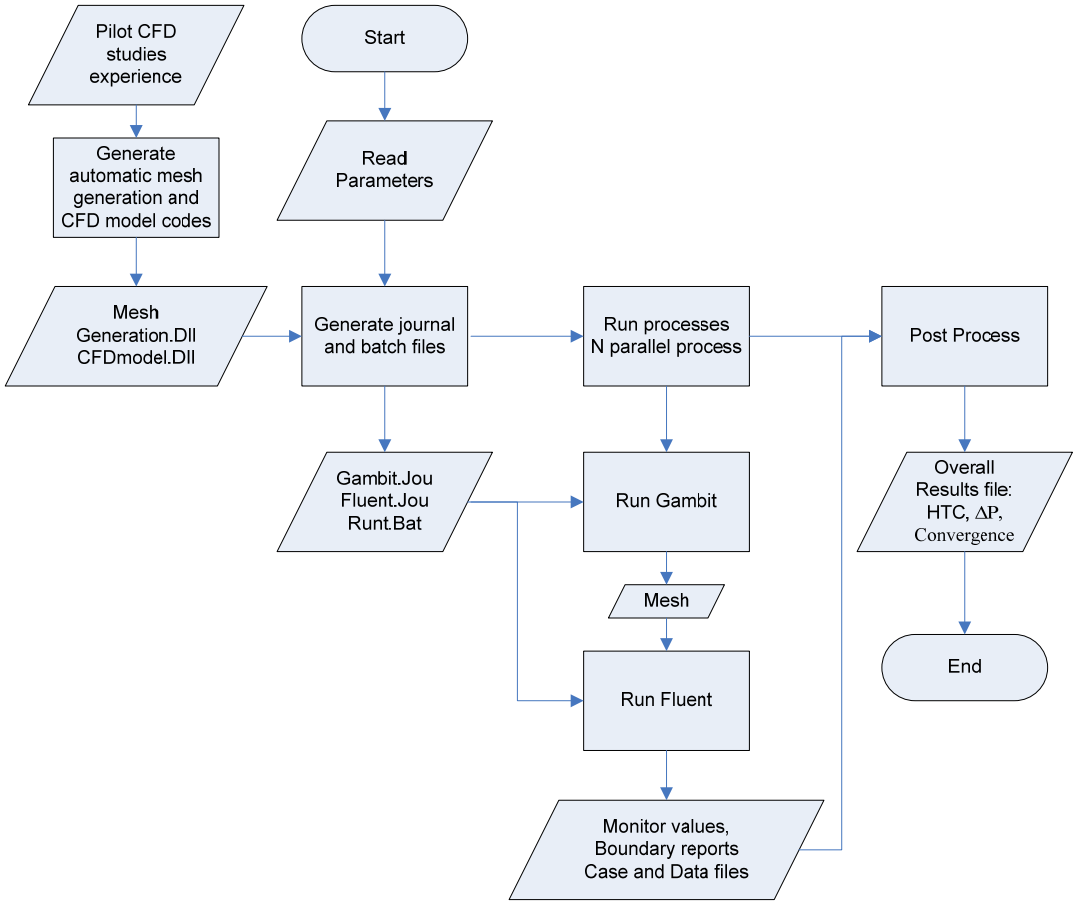

Figure 3: PPCFD flow chart

The three stages involved in approximation stated above are discussed below. The work presented in this dissertation is based on the SFCVT adaptive DOE technique with multi-objective formulation. Kriging (Cressie 1993) is used to develop the segment performance metamodels, and several verification metrics are employed to ensure metamodel accuracy.

3.3.1. Design of experiment

DOE is the step that involves the design space sampling. DOE methods can be broadly grouped as: classical methods, space filling methods and sequential or adaptive methods (Simpson et al. 2001). Classical designs, such as full and fractional factorial designs, central composite designs and Box-Behnken designs, tend to allocate points on or near the boundaries of the design space and leave a few points in the center (Myers and Montgomery 2002). Space filling designs such as LHC (McKay et al. 1979), Maximum Entropy Design (MED) (Shewry and Wynn 1987), mean squared error (Jin et al. 2002), integrated mean squared error (Sacks et al. 1989), maximin distance approach (Johnson et al. 1990), orthogonal arrays (Taguchi 1987, Owen 1992), Hammersley sequences (Kalagnanam and Diwekar 1997) also known as low discrepancy sequences (Wang and Shan 2007) and uniform designs (Fang et al. 2000) tend to fill the entire designs space instead of focusing only on the boundaries or at the center. None of these techniques is capable to detect the regions of large variations in the response functions. Hence, sample designs are not utilized efficiently.

Adaptive DOE methods are devised to retrieve maximum possible information about the behavior of the model being approximated while maintaining a manageable computational time for optimization of the model. Adaptive DOE utilize information from available function evaluations to find the next design sample. These methods can be formulated to develop either globally accurate metamodels or accurate metamodel near the optima as with the case of online approximation. The Maximin Scaled Distance (MSD) method (Jin et al. 2002) chooses the next sample as the point that is farthest from all points in the current design based on scaled distance

measures; this does not improve the sampling efficiency for functions with non-uniform response. ACcumulative Error (ACE) (Li et al. 2009), which is another adaptive DOE approach, develops a metamodel for leave one out cross validation errors (e_{LOO})using a simple isotropic correlation along with the use of a distance threshold to avoid clustering of points. The e_{LOO} measure ensures that new sample points are allocated in regions where the metamodel has lack of information (large variations in the response function). Hence, this method provides a more efficient way in sampling points where the information is most critical.

A recent development to the ACE approach was presented in (Aute et al. 2008, Aute 2008). The new approach selects new sample designs based on the tradeoff between cross validation error and the space filling criteria. The method is called Space Filling Cross Validation Tradeoff (SFCVT) technique. SFCVT can be developed to either develop single response models or multi-response models.

In a single-response SFCVT DOE approach new experiments are selected based on the trade-off between space-filling criterion and meta-model performance. The cross-validation and space filling objectives are conflicting since they compete for the available functions evaluations. Hence, multi-objective optimization is used to generate the tradeoff between space filling and cross validation. The problem can be simplified to a single objective optimization to find the design that maximizes the cross validation error subject to a space filling constraints. In this case, no tradeoff is generated and samples are selected one point at a time.

Multi-response SFCVT (MSFCVT) is an extension of the SFCVT approach. In this approach, the cross validation error for each response is set as an optimization

objective while the space filling criteria is set as a constraint. With this formulation, the next sample or samples selected within each step of the DOE can be selected from the Pareto. The larger the number of samples selected within each stage the lower the amount of information is retrieved; hence the approach becomes less efficient. However, with parallel computing capabilities, running 1 design or many design in parallel require the same clock time. This can be seen as an advantage of the MSFCVT since this architecture allows for parallel processing. Several selection criteria can be set for the sample selection from the Pareto front. For a single point at a time, the design is selected such that it is the closest to the ideal objective vector (Deb 2001). If more than one sample points are required per stage, both extreme designs should be selected. Figure 4 shows different design selections based on the number of points required at each stage for a 2 response DOE sampling problem. Figure 4 a) shows that a single design is selected such that it is closer to the ideal design point which represents a balance in the tradeoff between the 2 responses. Figure 4 b) shows that 2 designs are selected to represent maximum cross validation errors for each response. When more than 2 designs are required per stage, it is advised to select samples that provide more information for each response (corresponding to points of maximum e_{LOO}) for each response in addition to designs that presents a balanced tradeoff between metamodels performance as shown in Figure 4 (c) and (d).

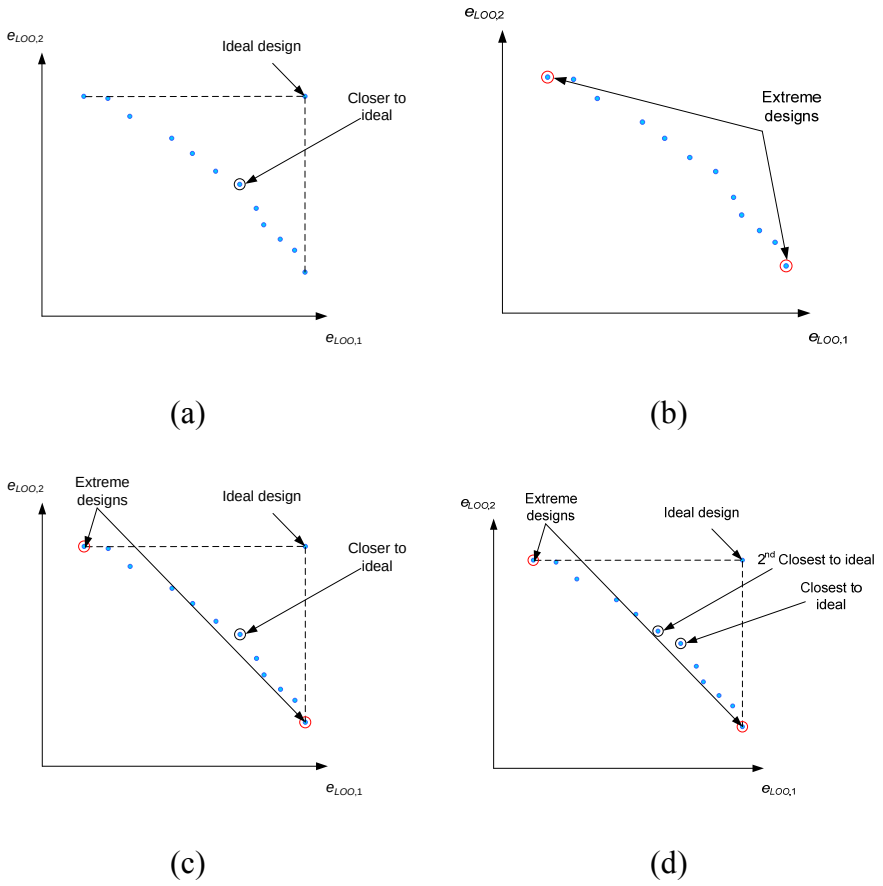

Figure 4: Example of different sample selections for MSFCVT: (a) 1 point per stage, (b) 2 points per stage, (c) 3 points per stage, (d) 4 points per stage.

3.3.2. Metamodeling

Metamodeling is a technique to correlate response at unobserved points to response from observed points. This technique evolved from the classical regression methodologies (Wang and Shan 2007). In classical approximation techniques, DOE was followed by an effort to correlate the data using least squares fitting methodologies. This classical approach required a functional form of the curve/surface/hypersurface fit. With deterministic computer simulations, such as the case with CFD simulations, the function form might not be known a priori. This led to a trial and error technique to develop the required correlation function. In this

regard, stochastic techniques have the advantage of not requiring a functional form. This imposes a great deal of flexibility and generality in representing response data (Sacks et al. 1989). Polynomial regression (linear, quadratic, or higher), splines regression (linear, cubic, NURBS (Farin 1999)), multivariate adaptive regression splines, Gaussian process, Kriging, radial basis functions, least interpolating polynomials, artificial neural networks, knowledge base, support vector machine, and hybrid models are examples of different metamodeling techniques (Simpson et al. 2001). Selecting the best metamodeling technique for use within the approximation approach is not conclusive. However, some techniques provide additional information or flexibility; hence the choice of the technique depends on the approximation assisted framework.

Kriging technique provides superior performance for nonlinear problems and shows a higher degree of flexibility and is recommended when the number of input variables is less than 50 (Wang et al. 2007). The basic idea behind Kriging is to use existing responses at some points x_i, where $i = 1$ to n, to predict the response at some unknown point x_0. Kriging also provide a standard error for its prediction; this is a significant advantage of Kriging over other metamodeling methods. Furthermore, Kriging does not require a functional form, though the choice of the correlation function is problem dependent.

As such Kriging was used in the current work due to its superior performance. Furthermore, Kriging can provide a measure of space filling criteria based on the variance associated with its prediction. Large variance in response prediction can be interpreted as large spacing between adjacent observed responses. An example of

Kriging prediction and the associated variance is shown in Figure 5. In this example, the values of the variance (error bars) of the predicted response are multiplied by 1000 in order to be noticeable. It is clear from Figure 5 that as the unobserved points are farther from the observed points, as in $x = 0.7$ and $x = 0.9$, the variance is much larger.

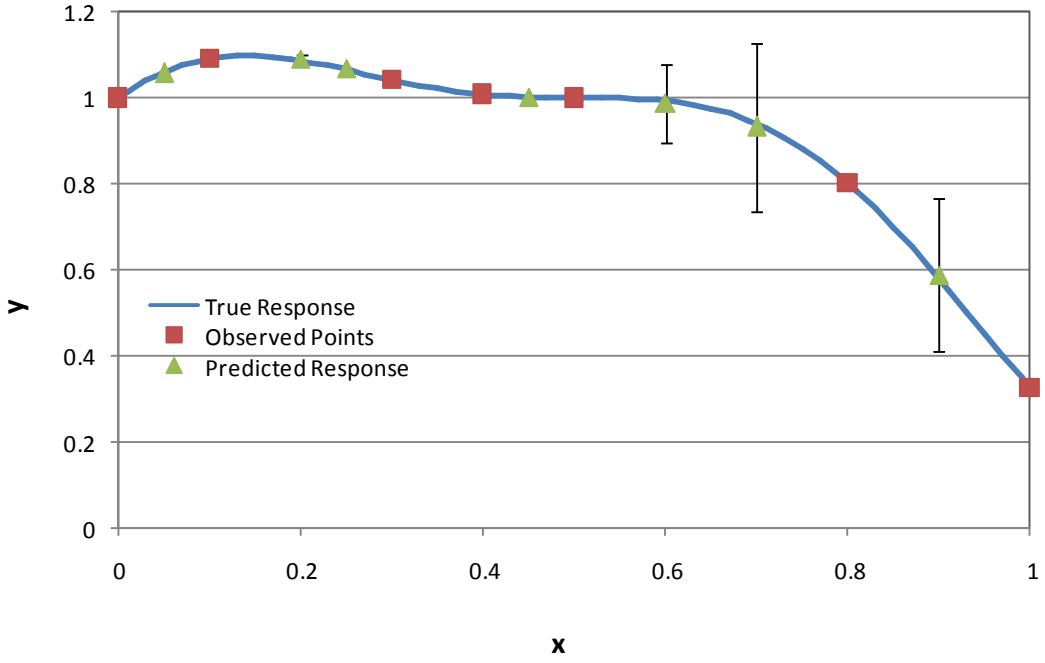

Figure 5: Kriging Example

3.3.3. Metamodel verification

There exist several measures of metamodel performance metrics. These measures compare the true value $y(x_i)$ with the value predicted by the metamodel $\hat{y}(x_i)$ of either a random or statistically distributed test samples. The Root Mean Squared Error (RMSE), Maximum Absolute Error (MAE), Relative RMSE, Relative MAE, defined in equations (21) through (24) are some of the widely used performance metrics.

$$\text{RMSE} = \sqrt{\frac{1}{n}\sum_{i=1}^{n}[y(x_i) - \hat{y}(x_i)]^2} \tag{21}$$

$$\text{MAE} = \max(|\, y(x_i) - \hat{y}(x_i)\,|), i = 1,...,n \tag{22}$$

$$\text{RRMSE} = \sqrt{\frac{1}{n}\sum_{i=1}^{n} e_i^2} \tag{23}$$

$$\text{RMAE} = \max(|\, e_i\,|) \tag{24}$$

Where

$$e_i = \frac{y(x_i) - \hat{y}(x_i)}{y(x_i)} \tag{25}$$

The Metamodel Acceptability Score (MAS) (Hamad 2006) is less sensitive to the sample size and is more intuitive in the context of the use of metamodels for global optimization. Prediction error for test sample is compared against acceptable error bounds as shown in Eq. (26). Test point response $\hat{y}(x_i)$ that satisfies Eq. (26) are said to be acceptable. The MAS is then defined as shown in Eq. (27)where n is the number of test samples and m is the number of acceptable responses.

$$\left(1 - \varepsilon_{\text{MAS}}\right) \le \left|\hat{y}_i / y_i\right| \le \left(1 + \varepsilon_{\text{MAS}}\right) \tag{26}$$

$$\text{MAS} = \frac{m}{n} \times 100 \tag{27}$$

3.4. Multi-Objective Optimization

Multi-Objective Optimization (MOO) problems involve *M* objective functions which are at least partly conflicting. The conflict in objective function results in a tradeoff in the performance. The result of a MOO is generally a set of tradeoff

designs referred to Pareto solutions. MOO problems are usually subject to equality and inequality constraints within a specified design space as shown in equation (28)

$$\begin{aligned} \underset{x}{\text{minimize}} \quad & f_i(x) && i = 1,...,M \\ \text{subject to:} \quad & g_j(x) \le 0 && j = 1,...,J \\ & h_k(x) = 0 && k = 1,...,K \\ & x_l^L \le x_l \le x_l^U && l = 1,...,d \end{aligned} \tag{28}$$

In equation (28) f_i refers to the i^{th} objective of the problem, x is a vector of d design variables, M is the number of minimization objectives, g_j represents the j^{th} inequality constraint, J is the number of inequality constraints, h_k is the k^{th} equality constraints and K is the number of equality constraints. HX optimization usually involves heat transfer enhancement and pressure drop minimization which are intrinsically conflicting. The vectors x_l^L and x_l^U indicate the lower and the upper bounds of the variable x_l respectively. In common engineering problems the equality constraints are replaced with inequality constraints representing the acceptable upper and lower bounds of the constrained value.

The work presented in this dissertation is based on the use of MOGA approach (Deb, 2001) to solve equation (28). The flow chart of MOGA as implemented in this work is shown in Figure 6.

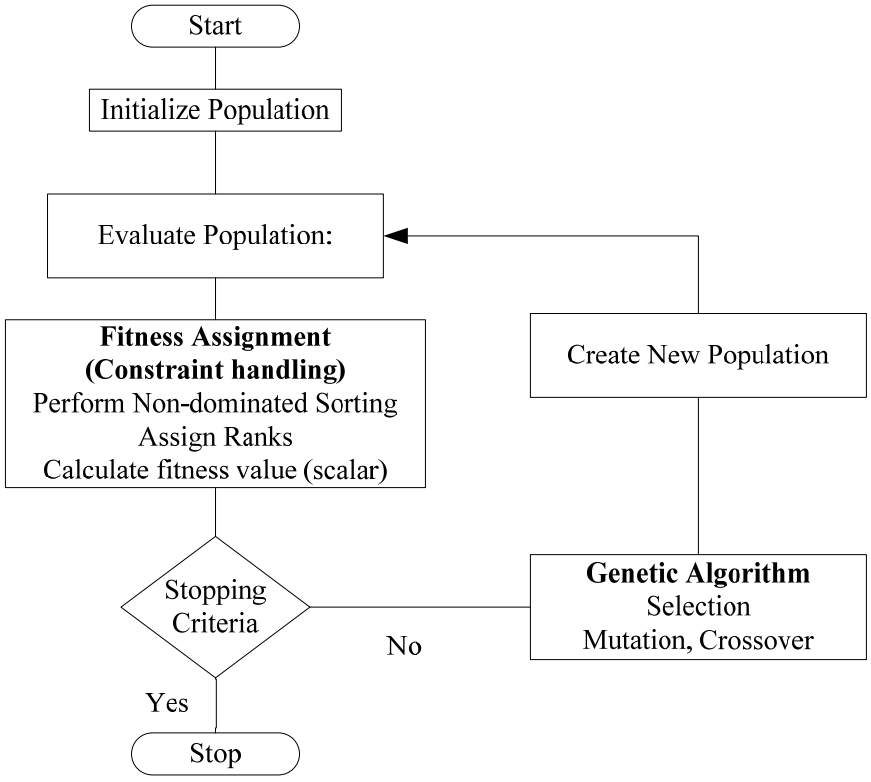

Figure 6: MOGA flow chart

Chapter 4: Multi-Scale HX Simulations: Development, Verification and Validation

Research in HX performance improvement is growing due to concerns on sustainability, energy efficiency, and economic feasibility. This chapter presents an effort to address computational challenges for the performance evaluation of innovative heat exchangers by replacing basic methodologies with a multi-scale simulation for the new geometries. This tool limits the CFD simulations to a periodic HX element and decouples the air side from the refrigerant side. This results in higher computational savings over the 3D CFD simulations of the entire HX.

4.1. Need for Multi-Scale Approach

The increased computational power that is offered by modern computing technologies allows for more complex simulations and comparison criteria. As such, enhanced surface performance improvement can be studied for an actual HX design which accounts for flow arrangement and circuitry using accurate segmented HX simulation tools, like CoilDesigner (Jiang et al. 2006). This can only be done if heat transfer and pressure drop performance of the enhanced surfaces are available; either in the form of correlation or predicted using CFD simulations. This multi-scale approach ensures that enhanced surfaces are compared against state of the art surfaces as part of the complete HX.

Multi-scale simulation enables efficient integration of the enhanced heat transfer segment performance prediction using CFD simulations with overall HX

performance prediction using segmented ε-NTU approach. In this case the multi-scale indicates that segment performance is evaluated at the finite volume length scale (discretized flow domain mesh characteristic length) and the HX performance is evaluated at the segment size. The expected length scale of the CFD simulations is $O(10^{-5}$ m) whereas the lengthscale involved in the segmented ε-NTU solver is $O(10^{-2}$ m) This multi-scale simulation definition bridges the need to discretize the entire HX for CFD simulations and hence provides significant computational savings.

CFD offers an accurate, reliable, and faster performance evaluation when compared to building a prototype and experimentally testing it. However, this does not eliminate the need for experimentation to validate the numerical results for promising designs. The use of CFD simulations in the prediction of enhanced heat transfer surface thermal and hydraulic performance was demonstrated in earlier work as summarized in section 2.3.

The multi-scale simulation approach provides a huge computational savings over CFD simulations of entire heat exchanger; which might require days of computational time. The multi-scale simulation approach described here reduces the simulation time by at least an order of magnitude. This is mainly because the CFD domain is limited to a periodic segment of the enhanced surface geometries for the evaluation of pressure drop and heat transfer coefficient on one or both sides.

Pilot studies using ANSYS CFX® ('ANSYS CFX' 2006) on a sample enhanced surface geometry, NGHX-13, were conducted for a 3D segment including air and water control volumes as shown in Figure 7. The study included the heat transfer coupling between the two fluid streams through the wall. The simulated tube

length was set to be 150% of the water side thermal entry length in order to model both developing and fully developed regions. The mesh generated for such tubes ranged from O (10^5) to O (10^6) finite volumes based on the different parameters involved. The simulation required a large number of iterations to converge due to the coupling between the two fluid streams. This computational complexity leads to prolonged computational time; in the order of hours for each configuration.

The pilot CFD simulations showed that side wall effects contribute to less than 1% of the tube length; Figure 8 shows practically no impact of the end walls on the wall heat flux. Pilot results also indicated that the third dimensional component velocity of air is practically zero as we move away from the header walls as shown in Figure 9. In addition, heat exchangers are known to be periodic in nature (e.g., symmetric tube arrangement, multiple parallel circuits, etc.) with the overall heat transfer coefficient limited by the highest thermal resistance. In air-to-refrigerant HX, the air side heat transfer is the dominant resistance (Shah and Sekulic 2003).

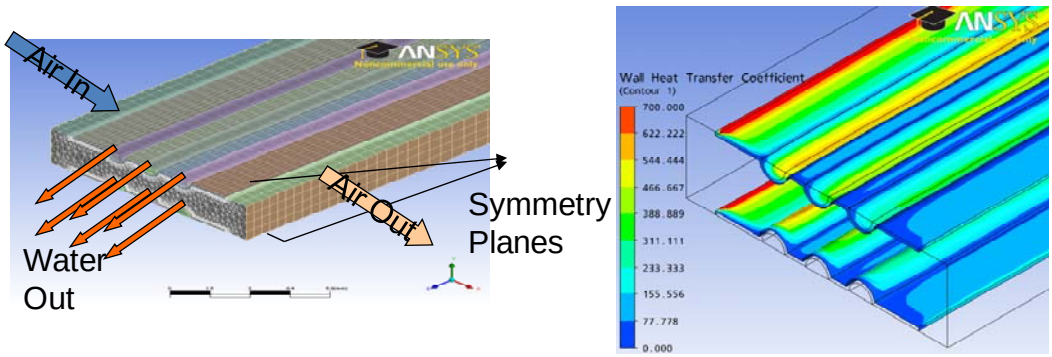

Figure 7: Pilot 3D CFD studies for the newly developed geometry

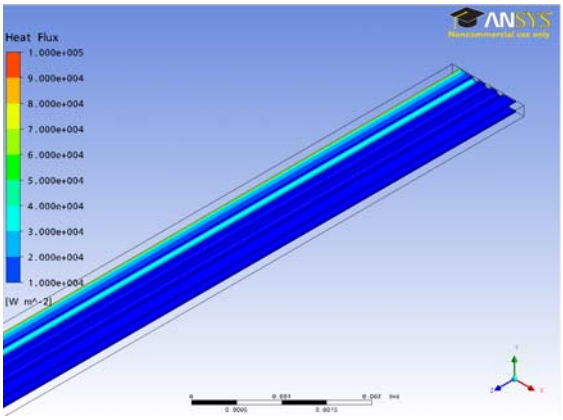

Figure 8: Wall heat flux

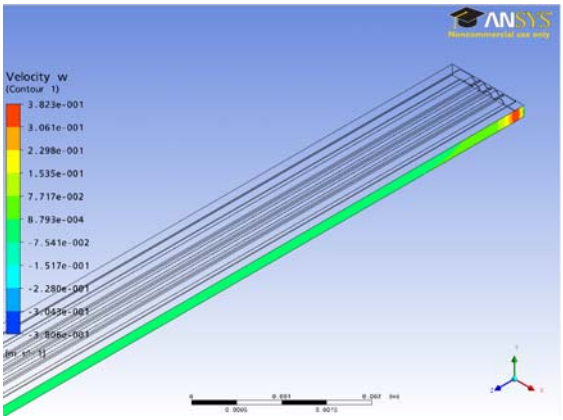

Figure 9: Air outlet z-component velocity

4.2. Approach

The approach used here integrates CFD simulations with a conventional segmented heat exchanger simulation tool to minimize the computational time while maintaining an acceptable level of accuracy. In this approach, the commercial CFD package, Fluent® (Fluent 2007) is coupled with an accurate segmented ε-NTU solver, CoilDesigner (Jiang et al. 2006), to simulate the overall HX performance. CFD simulations are used to evaluate the thermal and hydraulic performance of new enhanced surfaces and the resulting heat transfer coefficient and pressure drop values are used by the segmented HX solver to evaluate the overall performance.

The developed multi-scale simulation approach was based on the following observations and assumptions:

- Heat Exchangers are periodic in nature
- Symmetry planes could be identified
- Side wall effects contribute to less than 1% of the tube length
- The overall heat transfer coefficient is limited by the airside performance – weak coupling between fluid streams
- Constant water side temperature within each HX segment (equal water temperature for all ports)
- Constant air properties
- Constant water properties

The flow chart for the newly-developed multi-scale simulation approach is illustrated in Figure 10. First, the airside performance of the periodic heat exchanger segment is estimated using either 3D or 2D CFD simulations. The CFD simulation results are then processed to obtain the overall heat transfer coefficient between air stream and the tube inner wall temperature, i.e. including airside convection heat transfer coefficient and conduction through heat transfer surface walls, and the overall airside pressure drop. The segmented solver is then used to evaluate the refrigerant side performance using available correlations and solve for the segment outlet air and refrigerant conditions using the ε-NTU approach. The segmented solver is then used to propagate the air and refrigerant flow conditions along the HX based on the

refrigerant circuitry and HX configuration (tube banks, stagger, and cross, counter, or parallel flow configuration).

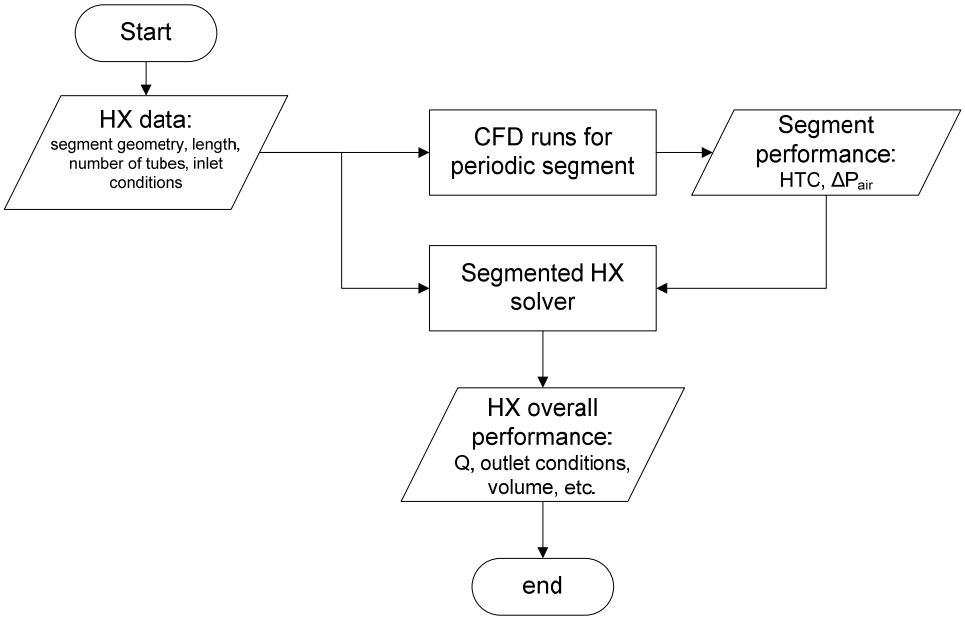

Figure 10: Multi-scale approach flowchart

4.3. Multi-Scale HX Simulation Sample Implementation

The multi-scale approach described above is applied to the NGHX-13 geometry. The assembled HX is shown in Figure 11 while the selected airside computational domain is illustrated in Figure 12. The HX element performance is evaluated at the finite level first and performance information is passed to the macro scale simulation tool to model the performance of the entire HX. The details of the CFD simulations and the overall HX performance evaluation are discussed in the following sections.

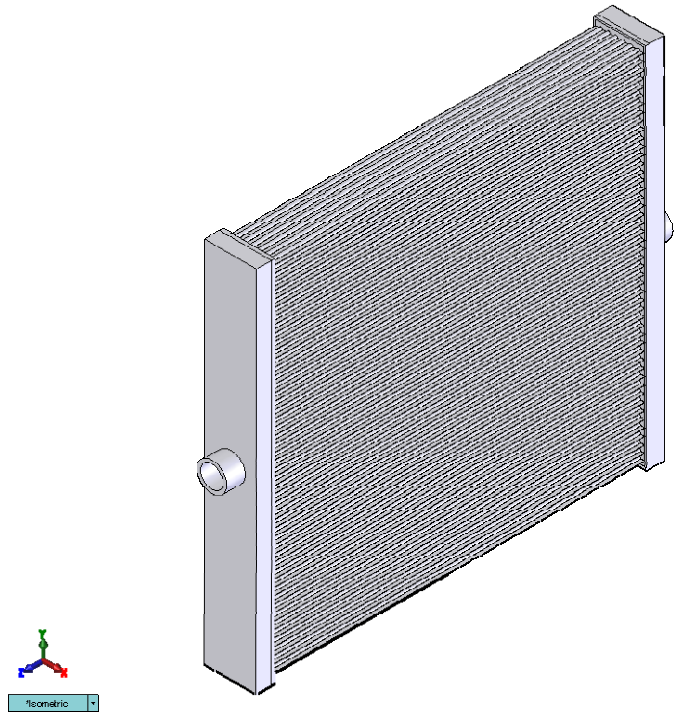

Figure 11: Assembled heat exchanger using the enhanced tubes

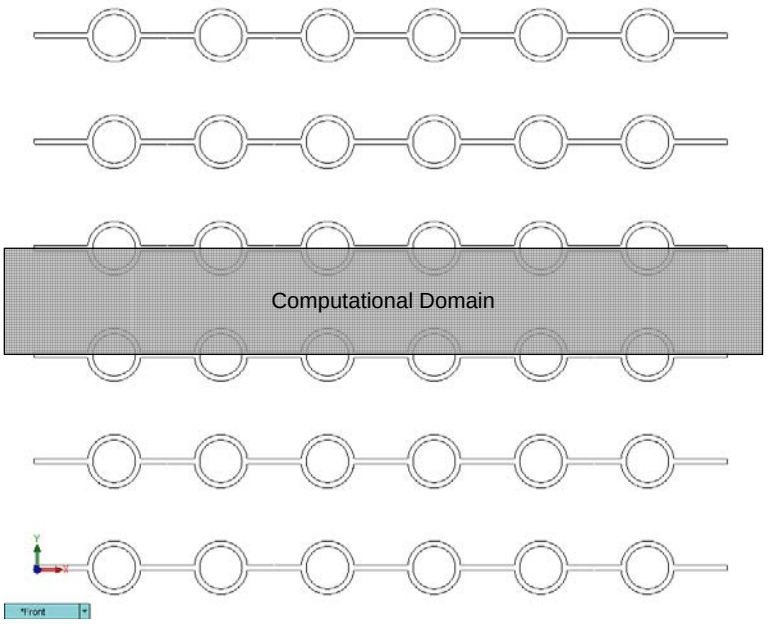

Figure 12: Cross-sectional view of enhanced surface showing airside computational domain

4.3.1. Heat exchanger segment airside CFD simulation

Airside CFD simulations were performed using the PPCFD tool described in section 3.2.2. PPCFD was used to generate Gambit® journal files based on the surface design values. Mapped triangular and quadrilateral meshes were used to discretize the domain as shown in Figure 13. However, triangular mesh was mainly used for the results reported in this thesis. The code is developed to generate three types of mesh: coarse, baseline and fine for verification purposes as illustrated in Figure 14. Also in this code, the mesh was carefully crafted to create fine structured mesh elements near the walls in order to accurately model the laminar boundary layer as shown in Figure 15.

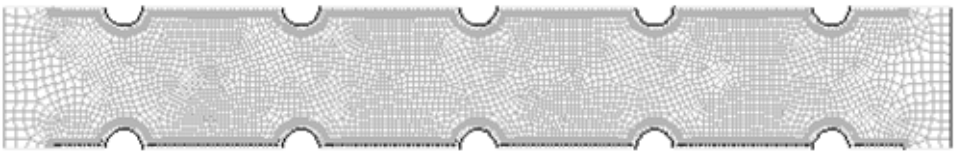

(a)

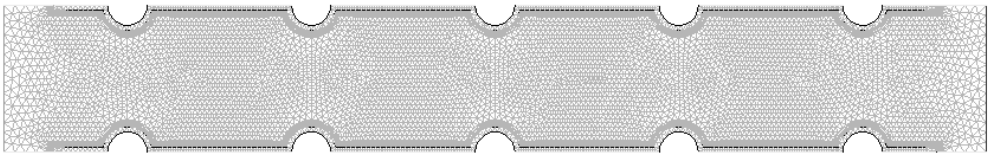

(b)

Figure 13: Mesh types; (a) Quadrilateral, (b) Triangular

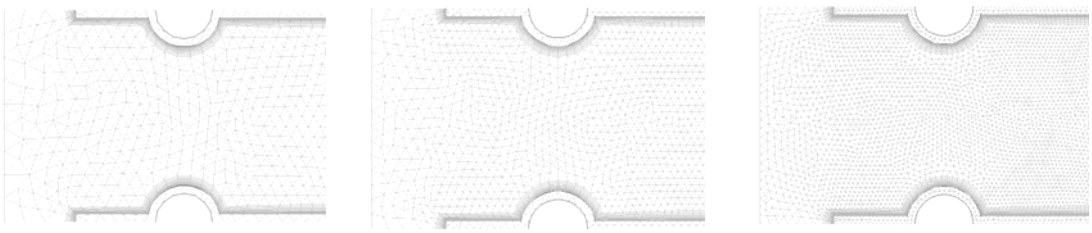

(a) Coarse (b) Baseline (c) Fine

Figure 14: Mesh resolution; (a) Coarse, (b) Baseline, (c) Fine

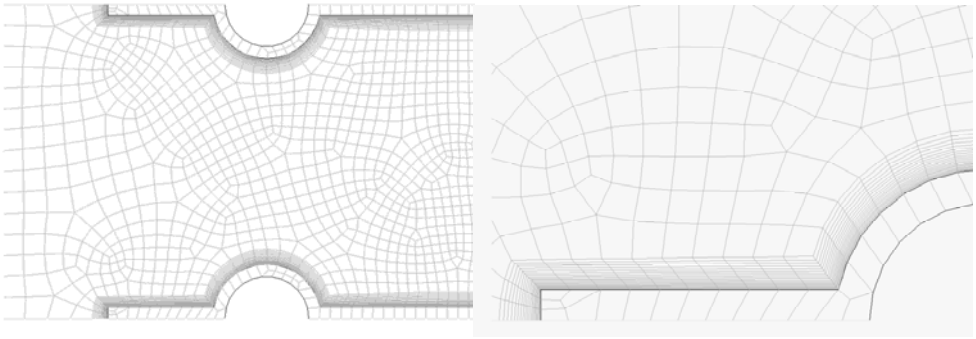

Figure 15: Inflated boundary layer mesh elements

As for the CFD simulations, PPCFD automatically generates Fluent® script files to define the problem and the appropriate solver settings. Viscous heat dissipation was accounted for in the energy equation. The no-slip boundary conditions were set for all walls and a pressure outlet condition was used for the air outlet. Symmetry was defined along the symmetry axis defined in Figure 16. Second order upwind discretization schemes were used for the governing equations and SIMPLEC (SIMPLE Consistent) (Van Doormaal and Raithby 1984) was used for the pressure coupling. The Green-Gauss Node-Based gradient evaluation was used to more accurately calculate the gradients for unstructured mesh. The solver was allowed to iterate until convergence or up to a maximum of 1000 iterations. The convergence criteria were based on maximum acceptable normalized residuals of 10^{-5} for all equations.

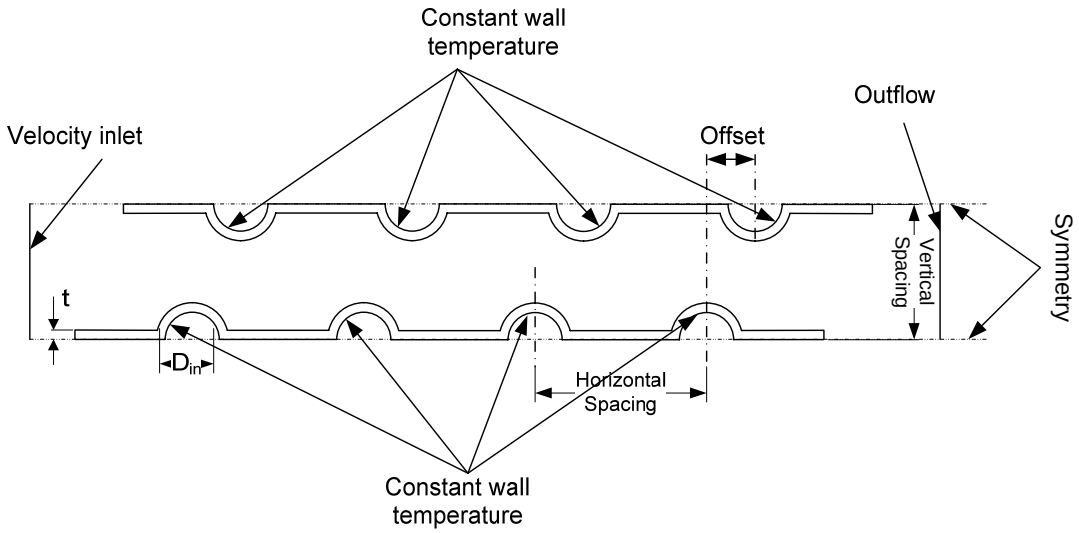

Figure 16: NGHX-13 computational domain and boundary conditions description

Post processing of CFD results was based on values of mass flow rate, pressure and temperature at the inlet and outlet boundaries and the average wall temperature and heat flux. This procedure was automated to allow for a faster processing using a code that reads the CFD output files and calculates the overall heat transfer coefficient as shown in equation (29).

$$U_{out} = \frac{q''}{\text{LMTD}} = q'' \left(\frac{T_{air,i} - T_{air,o}}{\ln\left(\frac{T_{air,i} - T_{wall,in}}{T_{air,o} - T_{wall,in}} \right)} \right)^{-1} \qquad (29)$$

4.3.2. Heat exchanger macro-analysis

The use of the new multi-scale HX simulation approach decoupled the heat transfer problem between refrigerant side "water" and the air side. The airside problem is solved using CFD simulation of a periodic element as described in the previous section. The water side performance was evaluated separately using laminar

developing flow correlations. Based on the single phase liquid flow in microtubes study presented in Appendix C, the generalized Hausen HTC correlation and the developing flow pressure drop correlations of (Shah and London 1978) were used. The generalized Hausen HTC correlation is shown in equation (30) with coefficient obtained from (Rohsenow and Choi 1961). The developing flow pressure drop was evaluated using equation (31) with the apparent friction factor evaluated as shown in equation (32). CoilDesigner (Jiang et al. 2006) was used to evaluate the outlet flow conditions, HX heat duty, volume, material, and pressure drop.

$$\mathrm{Nu} = 4.36 + 0.023\frac{\mathrm{Gz}}{1 + 0.0012\mathrm{Gz}} \tag{30}$$

$$\Delta P = \frac{\rho v^2}{2}\left(4x^+\right)\left(f_{app}\,\mathrm{Re}\right) \tag{31}$$

$$\Delta P = \frac{\rho v^2}{2}\left(4x^+\right)\left[\frac{3.44}{\sqrt{x^+}} + \frac{1.25\left(4x^+\right)^{-1} + 16 - 3.44\left(x^+\right)^{-0.5}}{1 + 0.00021\left(x^+\right)^{-2}}\right] \tag{32}$$

4.4. Results

In order to investigate the validity of the multi-scale approach described above a total of 33 designs were simulated and compared against 3D CFD simulations. These designs are based on a two level full factorial centrally augmented DOE and are summarized in Table 6. Before the implementation of the multi-scale tool for all designs, the 2D CFD simulations were verified using the approach described in section 3.2.1. This verification showed that the use of the normal mesh is acceptable with an average GCI of 1.7% for pressure drop and 1.2% for HTC. This meshing strategy was used as the baseline mesh during 3D CFD simulations.

4.4.1. Airside CFD simulation verification

The airside performance evaluation of the enhanced surface using CFD simulations was verified using the approach described in section 3.2.1. For each of the 33 cases shown in Table 6, three consecutively refined meshes, coarse, normal, and fine, were used. This grid verification study was performed with a grid refinement ratio of approximately 1.3. The observed order of convergence of the algorithm varied amongst the cases between 13.46 and 1.0 with an average of 4.69 for the pressure drop. The average GCI based on the fine mesh was 0.6% with a maximum of 2.6%. In addition, the GCI based on the normal mesh averaged at 1.8% with a maximum of 7.1%. The observed order of convergence for the HTC prediction varied amongst the cases between 13.65 and 1.0 with an average of 6.25. The average GCI based on the fine mesh was 0.4% with a maximum of 4.3%. In addition, the GCI based on the normal mesh averaged at 1.2% with a maximum of 11.3%. These results suggest that the use of the normal mesh is adequate in the analysis, especially when extending the study to cover a larger design space with larger number of cases.

4.4.2. Multi-scale approach validation

In order to judge the validity of the multi-scale simulation approach, simulation results were compared against the simulation of a single tube in cross flow using 3D CFD. The 3D CFD domain included both fluid streams: water and air. For the 3D mesh, the normal mesh generated for the 2D airside CFD simulations was extruded to the tube length for each case as specified in Table 6. The discretization along the tube length accounted for the water side developing length and was appropriately selected based on the water side Re.

Table 6: Selected Design parameters

case#	D_{in}, mm	HS, mm	VS, mm	Np	V_{air}, m/s	L_T, mm	$\dot{m}_{water}$ g/s
1	0.1	0.1875	0.25	1	1	4.15	0.0029
2	0.1	0.1875	0.25	1	3	4.15	0.0088
3	0.1	0.1875	0.25	15	1	4.21	0.0103
4	0.1	0.1875	0.25	15	3	4.21	0.0032
5	0.1	0.1875	0.5	1	1	2.94	0.0041
6	0.1	0.1875	0.5	1	3	2.94	0.0124
7	0.1	0.1875	0.5	15	1	1.4	0.0218
8	0.1	0.1875	0.5	1.5	3	1.4	0.0065
8’	0.1	0.1875	0.5	15	3	2.8	0.0065
9	0.1	0.75	0.25	1	1	4.15	0.0029
10	0.1	0.75	0.25	1	3	4.15	0.0088
11	0.1	0.75	0.25	15	1	1.4	0.0103
12	0.1	0.75	0.25	15	3	1.4	0.0032
13	0.1	0.75	0.5	1	1	2.94	0.0041
14	0.1	0.75	0.5	1	3	2.94	0.0124
15	0.1	0.75	0.5	15	1	1.4	0.0218
16	0.1	0.75	0.5	15	3	1.4	0.0065
17	0.55	2.58	2.063	8	2	22.42	0.0981
18	1	1.875	2.5	1	1	41.54	0.2923
19	1	1.875	2.5	1	3	41.54	0.8761
20	1	1.875	2.5	15	1	42.06	0.1033
21	1	1.875	2.5	15	3	42.06	0.3214
22	1	1.875	5	1	1	46.45	0.6527
23	1	1.875	5	1	3	46.45	1.9587
24	1	1.875	5	15	1	14.02	0.2181
25	1	1.875	5	15	3	14.02	0.6542
26	1	7.5	2.5	1	1	41.54	0.2923
27	1	7.5	2.5	1	3	41.54	0.8761
28	1	7.5	2.5	15	1	14.02	0.1033
29	1	7.5	2.5	15	3	14.02	0.3214
30	1	7.5	5	1	1	41.54	0.5838
31	1	7.5	5	1	3	41.54	1.7522
32	1	7.5	5	15	1	14.02	0.2181
33	1	7.5	5	15	3	14.02	0.6542

The quantities of interest for the validation study were the air and refrigerant side pressure drop and temperature change. The airside pressure drop was affected by the side wall friction for cases with small tube length to diameter ratio; 88% of the cases were simulated within ± 20% as shown in Figure 17. The remaining 12% cases had a tube length to diameter ratio of less than 20. To investigate this effect, Case 8 was repeated with twice the tube length (Case 8'). The airside pressure drop error for this case was reduced from 23.2% to 12.8%. It is also important to mention here that not all cases with small tube length to diameter ratio had higher error in estimating the airside pressure drop. This only occurred for the cases where the side wall friction was of the same order or even larger than the tube wall friction. It is expected that the actual HXs would have a tube length to diameter ratio much larger than 20; hence pressure drop results are considered to be within acceptable accuracy limits.

The water side pressure drop did not show a large deviation from the CFD simulations verifying that the use of developing flow pressure drop correlation adapted is appropriate. For all cases, the pressure drop was predicted within ± 5% as shown in Figure 18.

The airside temperature increase exhibited some errors between the multi-scale solver and the CFD simulations. Only 81.81% of the cases were predicted within ± 0.5K error bounds as shown in Figure 19. However, when the error is normalized by the temperature change based on 3D CFD simulation values, 97% of the cases were predicted within ±5% error bounds. The cases where the error in air temperature change was more than 0.5 K were characterized by low airside Re and/or uneven water outlet temperature. Cases with low airside Re exhibited large

recirculation regions near the side walls while the different port outlet water temperatures violated one of the main assumptions used in developing the multi-scale solver.

Again, the water side temperature change did not deviate significantly from the CFD simulations showing that the use of developing flow heat transfer coefficient correlation is appropriate. All cases were predicted within ± 0.5 K error bounds as shown in Figure 20.

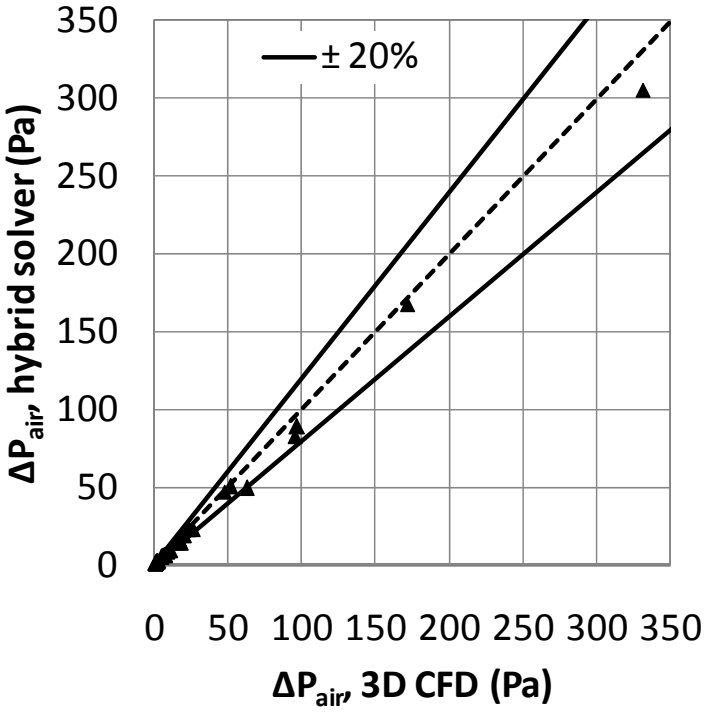

Figure 17: Airside pressure drop comparison: multi-scale solver versus CFD

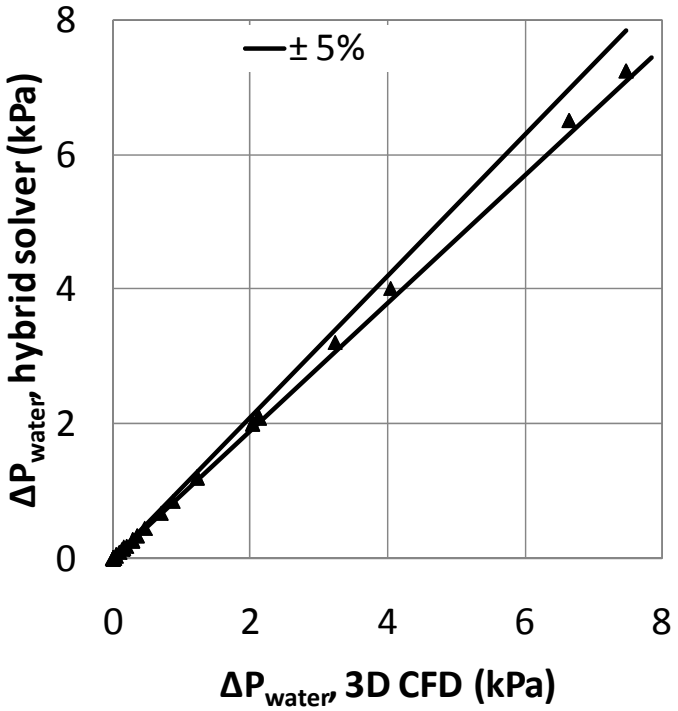

Figure 18: Water pressure drop comparison: multi-scale solver versus CFD

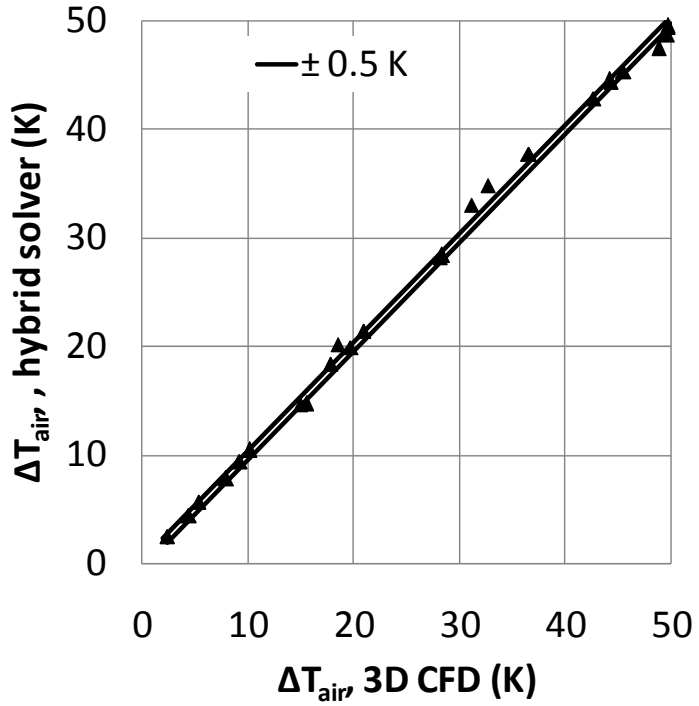

Figure 19: Airside temperature increase comparison: multi-scale solver versus CFD

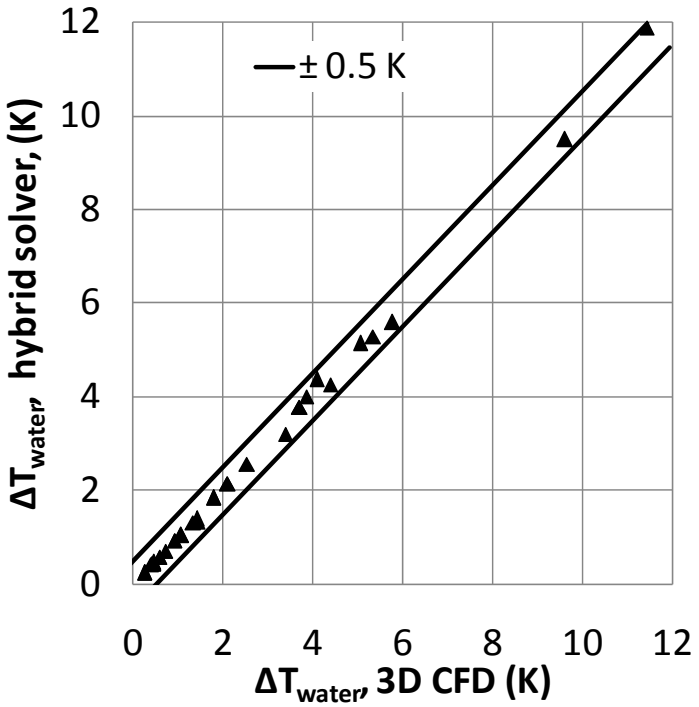

Figure 20: Water temperature drop comparison: multi-scale solver versus CFD

The simulation of case 1 took 24.5 seconds using the proposed multi-scale simulation approach and 4698 seconds using 3D CFD simulations. In this particular case the computational time was reduced by more than 190 times. The time savings depend on the tube length, the longer the tube length is the more the time savings from the proposed approach is demonstrated. For case 18, the new approach required 110 seconds whereas the 3D CFD required 13.8 hours; hence the computational time was reduced more than 450 times. The above simulations were all performed on a single processor Intel® Xeon® 3.0 GHz with 12 GB of available RAM. The validation study of the multi-scale heat exchanger simulation approach is summarized in Table 7. These results indicate that the newly developed multi-scale HX simulation approach provides acceptable accuracy given the significant time savings over CFD simulations.

Table 7: Overall multi-scale simulation approach validation results

	ΔP_{air}	ΔP_{water}	ΔT_{air}	ΔT_{water}	ΔT_{air} [K]	ΔT_{water} [K]
Max. error	– 0.8%	– 0.54%	2.27%	1.73%	0.69	0.05
Min. error	– 23.2%	– 3.38%	– 6.74%	– 6.94%	– 1.74	– 0.18
Average error	– 8.96%	– 1.91%	– 0.75%	– 1.24%	– 0.14	– 0.02
RRMSE	8.96%	1.91%	1.81%	2.01%	0.36	0.04
Std. Dev.	7.37%	0.72%	1.34%	1.33%	0.38	0.04

4.5. Summary

A new multi-scale heat exchanger simulation approach is presented and verified with CFD simulations. This approach presents an opportunity to simulate new enhanced heat transfer surfaces as part of the entire heat exchanger. This allows for evaluating the performance improvement relative to current state of the art heat exchangers. Comparison between the developed multi-scale simulation approach and the 3D CFD simulations show that the airside and water side pressure drop were under predicted by 9% and 1.9% respectively. The comparison shows no significant variations on the water side prediction with an under predicted airside temperature change of -0.14 K. These errors show that the new modeling approach had acceptable performance specially when compared with typical errors provided by publicly available heat transfer and pressure drop correlations. The GCI study shows that CFD simulations provide accurate simulations. The use of the normal level mesh maintained an acceptable computational time. Compared with tube-wise 3D CFD simulations, the simulation time was reduced by at least two orders of magnitude.

The use of a segmented heat exchanger simulation tool such as CoilDesigner, allows for more performance data to be calculated such as amount of materials, heat

exchanger packaging volume, fan power, pumping power, etc. These performance indicators can be used instead of conventional PEC to understand the improvement potential of the new heat transfer surfaces. The flexibility of the approach and the resulting computational savings enable its use in rigorous optimization studies that are tailored based on the application at hand. Optimization studies may involve multiple design objectives based on the possible performance indicators with as many constraints as dictated by the application. As such, it can provide an application niche for newly designed enhanced surfaces as shown in Chapters 7 and 8.

Further modeling accuracy can be achieved by accounting for header performance, as discussed in Chapter 5, and its impact on the flow rate maldistribution and implementing the modified ε-NTU solver, presented in Chapter 6, to account for intentional and unexpected geometrical and flow variability due to manufacturing and operating conditions limitations.

Chapter 5: Header Analysis Development

Headers play an important role in the refrigerant flow distribution in HXs. Properly designed headers result in uniform flow distribution with minimum additional volume requirements and pressure drop. In the case of novel HX design with a large number of parallel flow channels, header design becomes a challenging problem. This chapter provides an approach for fluid flow predictions in headers with multiple parallel ports based on CFD simulations. This approach applies the porous jump interior conditions in order to reduce the computational domain. The chapter starts by an introduction to the header analysis problem followed by a description of the developed modeling approach and results for different cases. The chapter concludes with design guidelines for header design based on presented results and proposes an additional header design concept and the limitations of using a simplified fluid flow resistance analogy.

5.1. Introduction

Previous advances in HX technology from tube fin HX to flat tube or microchannel designs resulted in an increase of the refrigerant header volume compared to the active heat transfer volume as shown in Figure 21. The header for tube fin HXs occupies an insignificant volume compared to the active heat transfer core; whereas for advanced HXs such as flat tube or microchannel HXs the header may occupy up to 20% of the overall HX packaging volume. This depicts that smaller flow channels tend to require larger header size in order to maintain acceptable

pressure drop and flow uniformity. However, there exists a tradeoff between increased header size to provide better refrigerant side distribution and added volume that obstruct the airside free flow area. As such it is important to design refrigerant headers that provide acceptable performance at the minimum possible volume increase. The first order studies indicated that smaller diameter tubes provide higher thermal performance. However, smaller diameter tubes lead to higher pressure drop. For laminar flow inside circular tubes, the pressure drop is inversely proportional to the square value of the diameter for the same flow velocity as shown in equation (33). Hence, when smaller diameter tubes are used, tube length and refrigerant flow velocity should be reduced in order to maintain acceptable pressure drop.

$$\Delta P = \rho \frac{fLv^2}{2D} = \rho \frac{32Lv^2}{\mathrm{Re}\, D} = \frac{32Lv\mu}{D^2} \qquad (33)$$

There is a tradeoff between better flow distribution uniformity, header pressure drop and header volume. For NGHX-13, it is suggested to use headers made with a tapered channel in order to provide static-pressure regain that improves mass flow rate distribution. Furthermore, the tapered configuration may allow inlet and outlet headers to be packaged together as shown in Figure 22. The tapered header design can not be analyzed using conventional flow resistance analogy since no pressure drop correlation exists for this type of flow configuration. Hence, in this chapter, CFD simulations are used to predict the mass flow rate distribution for different header designs.

In the configuration shown in Figure 22, the header parameters under configurations are inlet and outlet header heights ($L_{H,i}$ and $L_{H,o}$). The additional

volume occupied by the header is proportional to the overall header height ($L_{H,i}$ + $L_{H,o}$) whereas the tapered design is a function of the header size ratio ($L_{H,i}/L_{H,o}$). Hence, these 2 quantities are used to describe the header design in the following analysis.

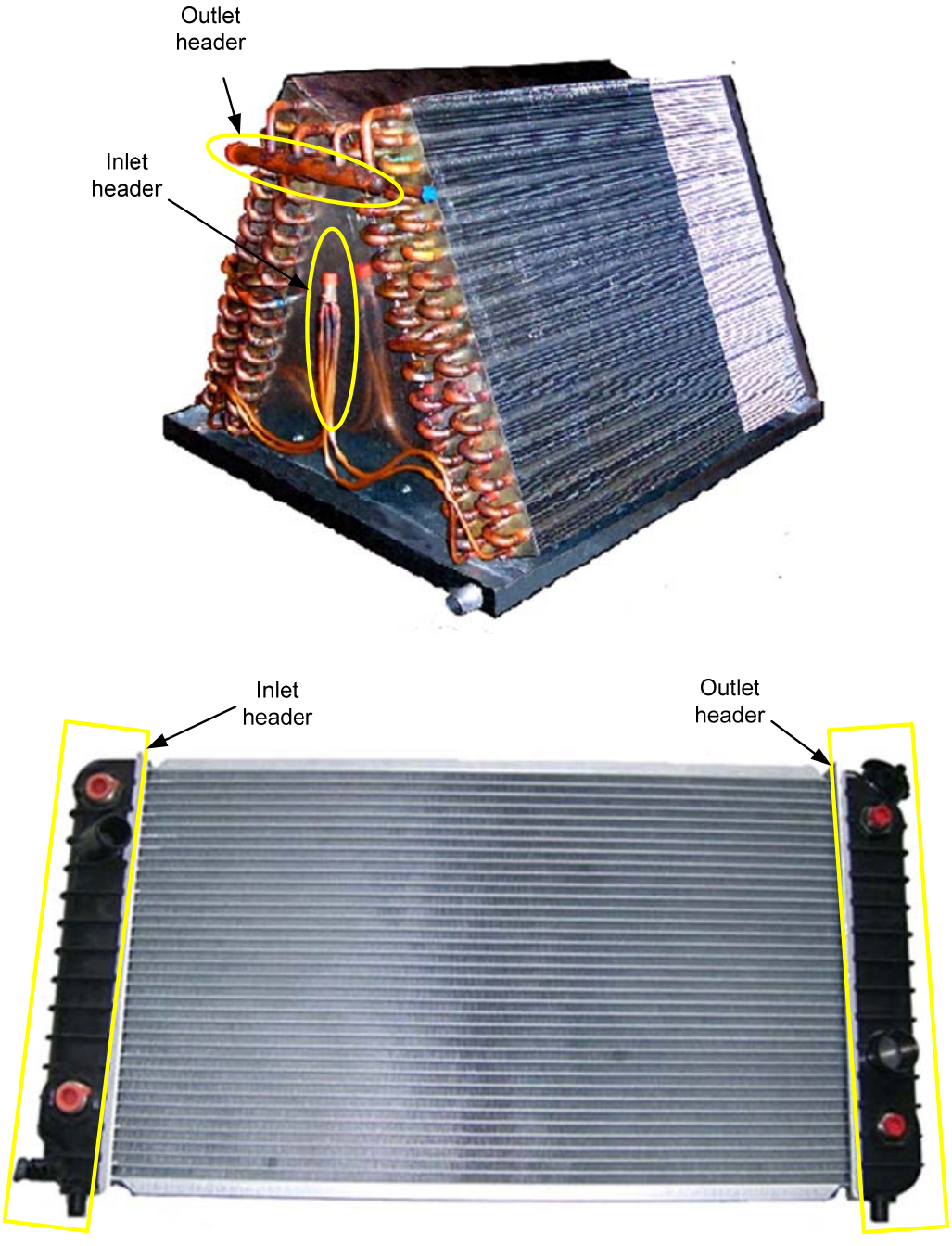

Figure 21: Increased header size from conventional to advanced designs

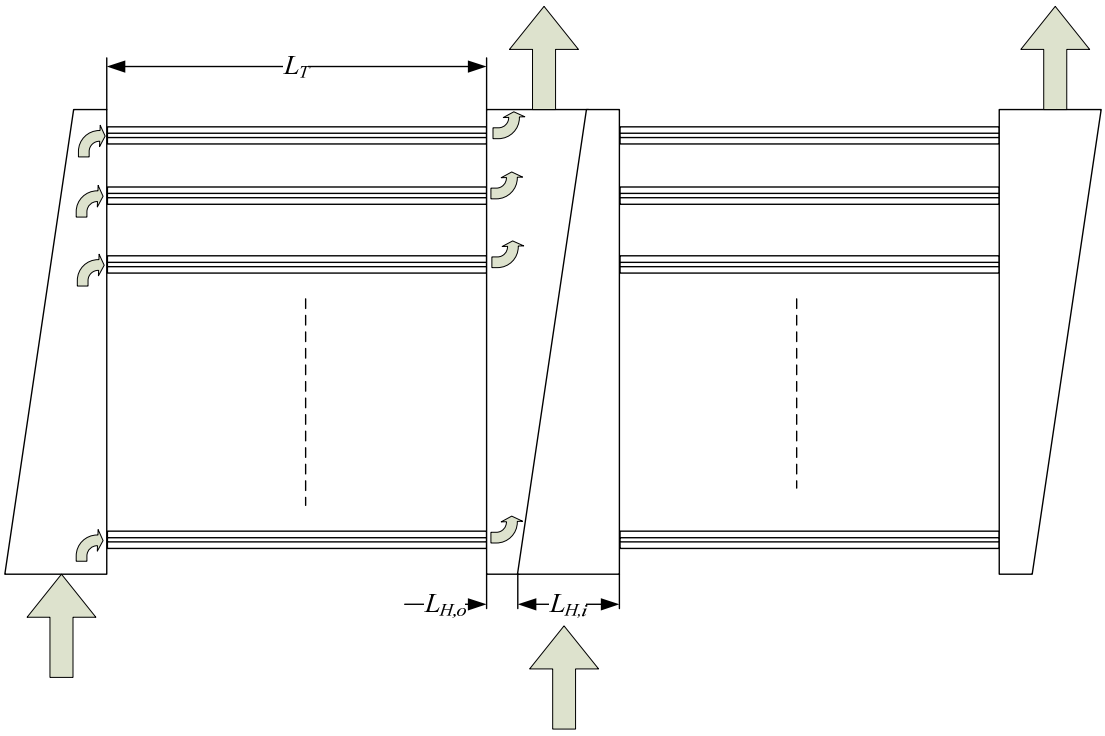

Figure 22: NGHX-13 headers configuration

5.2. Approach

Conventional CFD simulations of HX including the headers would suggest that the entire HX shown in Figure 23 be included in the computational domain. A common simplification would be to model just a periodic part of the HX assuming symmetry planes as denoted in Figure 23. This would result in a significant reduction in the computational domain; the HX shown in Figure 23 is modeled by considering 1 port per tube as shown in Figure 24. This assumption is valid only in the case of neglected side wall effects; i.e. the shear stress at the side walls is neglected such as in tubes with larger number of ports. The new approach developed here suggests the use of the porous jump interior boundary conditions to represent the tubes. Hence, the computational domain can further be reduced as shown in Figure 25. In this case, the

CFD solver, Fluent® artificially creates a pressure jump across the faces representing the tubes. This modeling approach will not be able to capture the contracta vena and the flow dynamics in the tubes; however, it will be able to account for the effect of overall pressure drop in each flow channel on the mass flow rate distribution.

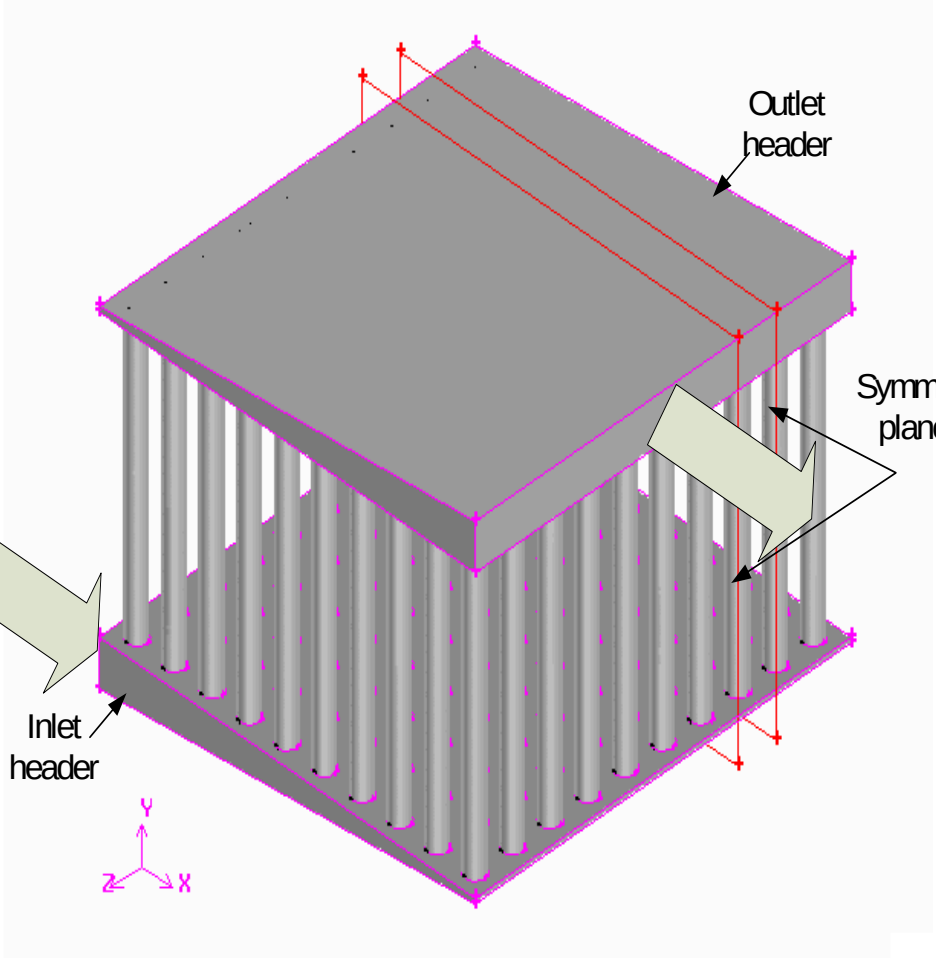

Figure 23: Computational domain for a compact HX made of 10 10-ports NGHX tubes

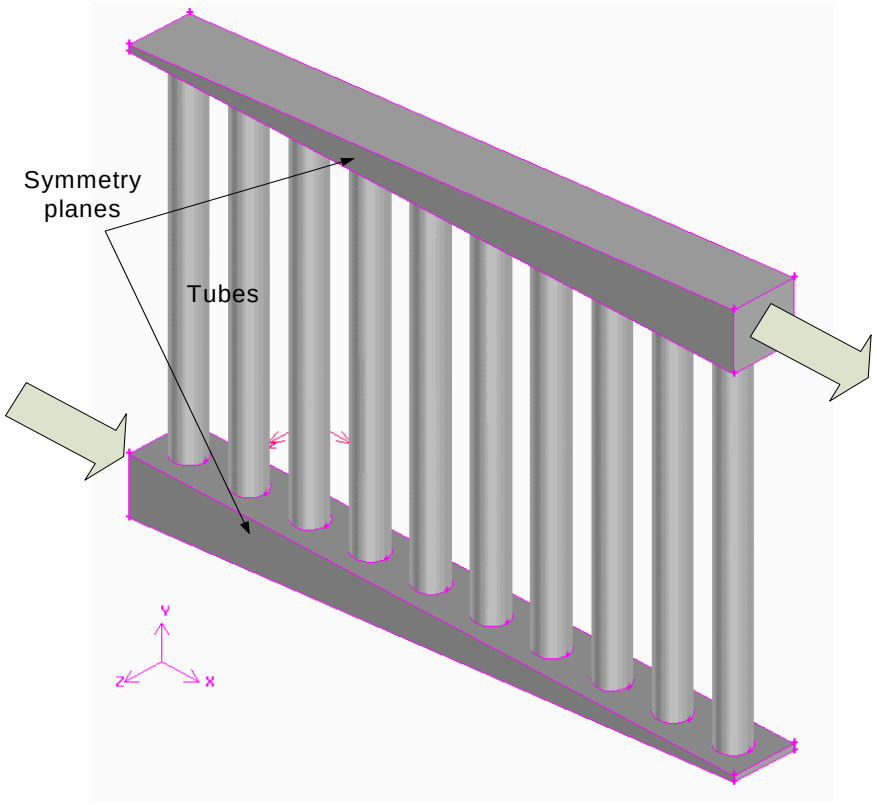

Figure 24: Conventional computational domain simplification

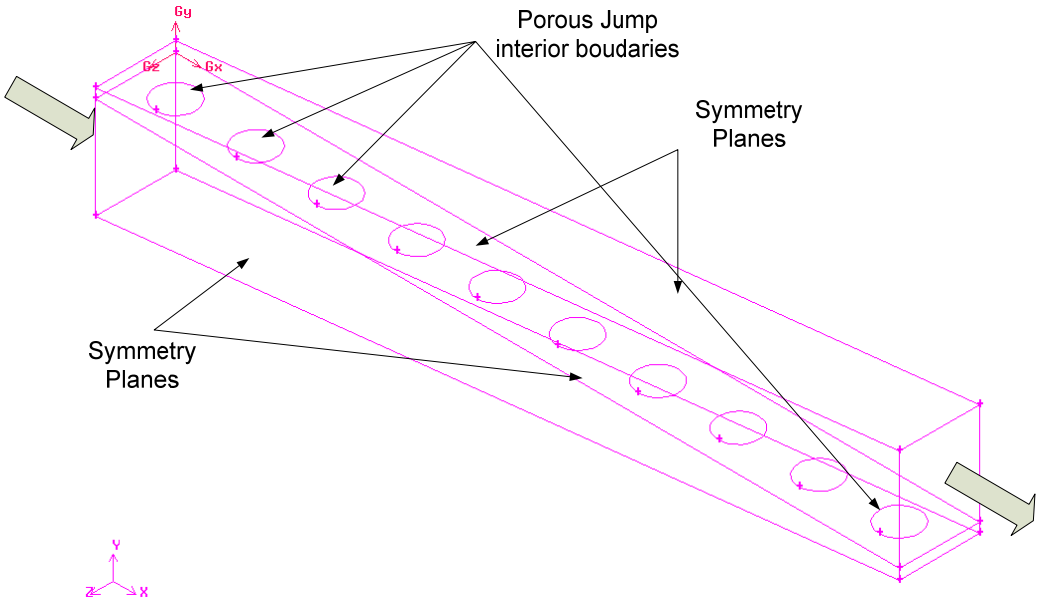

Figure 25: Computational domain simplification with porous jump interior boundaries

According to (Fluent 2007), the porous jump conditions is capable of modeling a thin porous media based on the velocity pressure-drop characteristics. The pressure drop across the porous jump conditions is correlated to the average velocity through the cell faces as shown in equation (34). In equation (34) μ is the laminar fluid viscosity, α is the permeability of the medium, C_2 is the pressure-jump coefficient, v is the velocity normal to the porous face, and Δm is the thickness of the medium. The first term represents an inertial loss term that is required for actual porous media; this term can be neglected in HX header simulations. The second term represents the pressure drop due to skin friction which is fundamental in finding the accurate mass flow rate distributions.

$$\Delta P = -\left(\frac{\mu}{\alpha} v + C_2 \frac{1}{2} \rho v^2\right) \Delta m \tag{34}$$

In order to find the value for C_2, the pressure drop correlation of interest should be considered. Based on the findings of the numerical validation of the single phase water flow in microtubes presented in Appendix C, the developing flow pressure drop correlation of (Shah and London 1978) is selected. Solving equations (34) and (32) the value of C_2 can be evaluated as shown in equation (35). This shows the dependence of C_2 on x^+ and the tube length L. x^+ is a dimensionless number representing the ratio between (L/D) and Re. Hence, C_2 vary as the flow conditions change. As such, it is required to update the value of C_2 for each port periodically while the solver is iterating. The solution procedure is developed as follows:

1. Set the solver controls, boundary conditions, and initialize the flow.

2. Use average mass flow rate per port assuming uniform flow distribution to calculate $C_{2,\,\text{initial}}$ according to equation (35) and use this value in the settings of all porous jumps in the header.
3. Set the solver to iterate for 100 iterations.
4. Re-calculate the C_2 coefficient for each port based on the current value of mass flow rate, refine the mesh based on pressure gradients and let the solver run for 20 iterations and repeat 20 times (400 iterations total).
5. Set the solver to run for 100 iterations.
6. Re-calculate the C_2 coefficient for each port based on the current value of mass flow rate, refine the mesh based on pressure gradients and let the solver run for 100 iterations and repeat 5 times (500 iterations total).

The procedure listed above provides means for Fluent® to update the pressure drop coefficient of the porous jump. This is made through the use of Scheme programming language (Dybvig 2003) which is supported within the Fluent® text command.

$$C_2 = \frac{\left(4x^+\right)}{L}\left[\frac{3.44}{\sqrt{x^+}} + \frac{1.25\left(4x^+\right)^{-1} + 16 - 3.44\left(x^+\right)^{-0.5}}{1 + 0.00021\left(x^+\right)^{-2}}\right] \qquad (35)$$

The CFD simulations were automated using the PPCFD approach described in section 3.2.2. The mesh was generated using either hexahedral or tetrahedral elements based on the design complexity. In the case of low aspect ratio headers, hexahedral mesh elements were used and the boundary layer was carefully crafted to ensure that enough elements cover the boundary layer. On the other hand, for large aspect ratios,

tetrahedral meshing was easier to produce. In the case of tetrahedral mesh generation, the mesh was further refined in Fluent® using the adapt boundary tool to split the elements near the walls. An additional mesh adaption step was introduced to the solving procedure listed above to allow Fluent® to refine the grid in areas of high pressure gradient before step 4.

As for the CFD simulations, PPCFD automatically generates Fluent® script files to define the problem and the appropriate solver settings. The CFD simulations did not consider energy equation. The no-slip boundary conditions were set for all walls and a pressure outlet condition was used for the water outlet port. Inlet velocity boundary condition was used for the water inlet header. Symmetry planes were identified as shown in Figure 25. The flow channels were simulated using the porous jump interior boundary conditions with updated pressure loss coefficient using Scheme programming language as discussed earlier. Second order upwind discretization schemes were used for the governing equations and SIMPLEC algorithm (Van Doormaal and Raithby 1984) was used for the pressure coupling. The convergence criteria were based on maximum acceptable normalized residuals of 10^{-5} for all equations.

The CFD simulations resulted in a distribution of mass flow rates across the different tubes. The relative standard deviation in mass flow rate per tube was used as a measure of flow uniformity.

5.3. Results

Two header design problems were investigated in order to understand the tradeoff in header designs and develop some design guidelines. The 2 headers are used with exactly the same NGHX-13 tube configuration listed in Table 8. The first header design considers a HX with 20 tubes in parallel (Header-20) while the second design is for 10 tubes only (Header-10). A parametric analysis was considered by changing the header size ratio ($L_{H,i}/L_{H,o}$) and overall header height ($L_{H,i} + L_{H,o}$). A total of 15 header designs were analyzed for each case. Design parameters are listed in Table 9 and Table 10 for Header-20 and Header-10 respectively. These tables also list the overall pressure drop across the HX and the relative mass flow rate standard deviation ($\sigma_{\dot{m},R}$).

Table 8: NGHX-13 tube design parameter for header analysis

Design parameter	value
Tube length	0.1 m
Port inner diameter	0.4 mm
Horizontal spacing	0.8 mm
Vertical spacing	0.8 mm
average water velocity per port	0.5 m/s

The relative mass flow rate standard deviation is plotted in Figure 26 (a) and (b) for Header-20 and Header-10 designs respectively. The same trends in mass flow rate distribution variation are experienced in both headers. The smallest header height considered for both designs shows large dependence on the header size ratio. This

scenario resulted in smaller $\sigma_{\dot{m},R}$ for larger header size ratios. The medium and large size headers provide a more uniform distribution. However, the rectangular header design (header size ratio = 1) still resulted in larger $\sigma_{\dot{m},R}$. The relative improvements between medium and large size header is marginal suggesting that the medium size header is appropriate. Furthermore, the relative improvements achieved by increasing the header size ratio tend to diminish after a header size ratio of 4. Hence it is suggested to use header size ratio of 4 for both header designs assuming that larger size ratio are more challenging to manufacture.

Table 9: Header design parameters for 20 tubes HX

	#	$L_{H,i} + L_{H,o}$ (m)	$L_{H,i} / L_{H,o}$	$V_{H,i}$ (m/s)	ΔP (Pa)	$\sigma_{\dot{m},R}$
High header velocity	1	0.002	1	1.571	4089.4	19.79%
	2	0.002	2	1.178	3470.6	10.74%
	3	0.002	4	0.982	3281.1	6.50%
	4	0.002	8	0.884	3313.8	4.95%
	5	0.002	16	0.834	3265.5	4.06%
Medium header velocity	6	0.004	1	0.785	3065.8	4.44%
	7	0.004	2	0.589	2996.8	2.84%
	8	0.004	4	0.491	2964.9	1.77%
	9	0.004	8	0.442	2931.6	1.14%
	10	0.004	16	0.417	2957.2	1.40%
Low header velocity	11	0.008	1	0.393	2911.4	1.61%
	12	0.008	2	0.295	2920.5	1.34%
	13	0.008	4	0.245	2907.2	1.20%
	14	0.008	8	0.221	2903.6	1.14%
	15	0.008	16	0.209	2893.6	1.19%

Table 10: Header design parameters for 10 tubes HX

	#	$L_{H,i} + L_{H,o}$ (m)	$L_{H,i} / L_{H,o}$	$V_{H,i}$ (m/s)	ΔP (Pa)	$\sigma_{\dot{m},R}$
High header velocity	1	0.001	1	1.571	4776.1	20.84%
	2	0.001	2	1.178	3810.2	11.46%
	3	0.001	4	0.982	3500.6	6.52%
	4	0.001	8	0.884	3358.5	3.85%
	5	0.001	16	0.834	3340.6	3.30%
Medium header velocity	6	0.002	1	0.785	3167.5	4.12%
	7	0.002	2	0.589	3026.6	2.56%
	8	0.002	4	0.491	2994.7	1.71%
	9	0.002	8	0.442	2975.3	1.31%
	10	0.002	16	0.417	2968.2	0.82%
Low header velocity	11	0.004	1	0.393	2970.5	1.39%
	12	0.004	2	0.295	2934.5	1.06%
	13	0.004	4	0.245	2906.3	0.91%
	14	0.004	8	0.221	2912.5	1.17%
	15	0.004	16	0.209	2911.0	1.20%

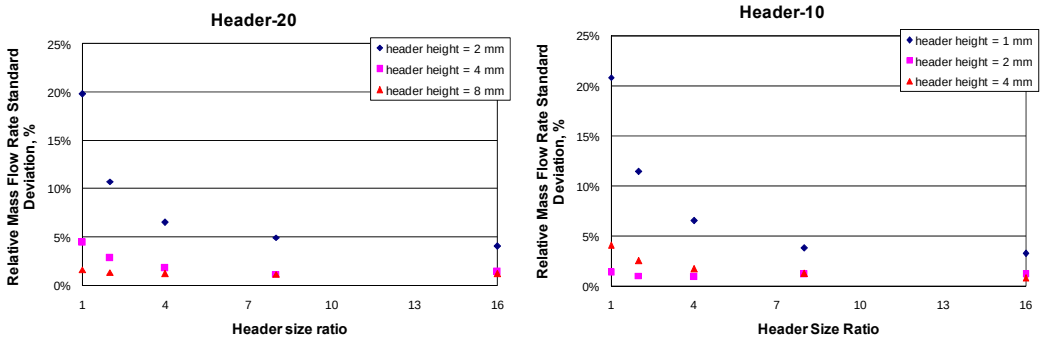

(a) (b)

Figure 26: Relative mass flow rate standard deviation:

(a) 20 tubes header, (b) 10 tubes header

Figure 27 (a) and (b) depict the effect of header size ratio and header height on the overall water size pressure drop for Header-20 and Header-10 designs

respectively. Smaller pressure drop is experienced with designs incorporating larger header size ratios and larger header height. This improvement comes at the cost of additional volume requirements and challenging manufacturing process. The findings are similar to that of the mass flow rate standard deviations. The relative improvements in pressure drop due to header size ratio and header height tend to diminish after a header size ratio of 4 and an overall header height of 4 mm for Header-20 and 2 mm for Header-10.

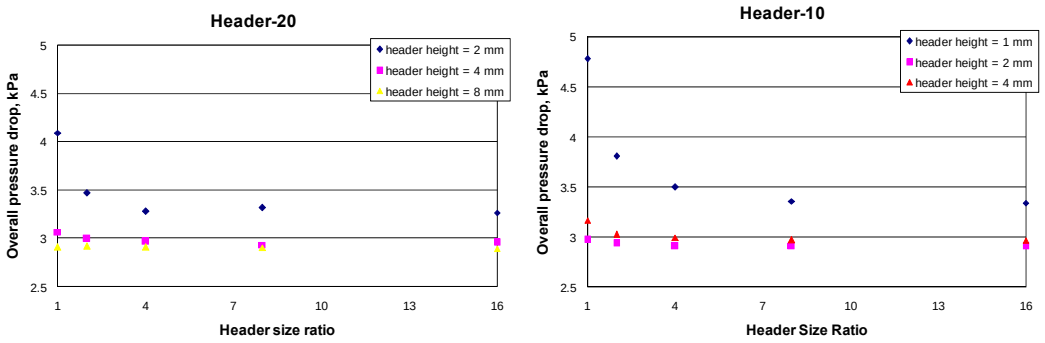

(a) (b)

Figure 27: Overall water pressure drop: (a) 20 tubes header, (b) 10 tubes header

The details of the header mass flow rate per tube for the different designs are shown in Figure 28 to Figure 30. Figure 28 (a) and (b) show the mass flow rate per tube for Header-20 and Header-10 respectively for the high header velocity scenario (smaller header height). These figures show that the mass flow rate distribution tends to become more uniform as the header size ratio increases; flow rate distribution is almost the same for both header size ratios of 8 and 16.

Figure 29 (a) and (b) show the mass flow rate per tube for Header-20 and Header-10 respectively for the medium header velocity scenario (medium header height). These figures show that the mass flow rate distribution is more uniform than

that shown in Figure 28. For the medium header velocity scenario, flow rate distribution is almost the same for header size ratios of 4 and up. Mass flow rate distribution for the lower header velocity scenario is shown in Figure 30 (a) and (b). These figures also depict that the mass flow rate is uniform for header size ratios of 4 and up. These results indicate that the findings from the relative standard deviation analysis are accurate. Hence, in future studies only mass flow rate relative standard deviation need to be considered as a minimization objective for header design optimization problems.

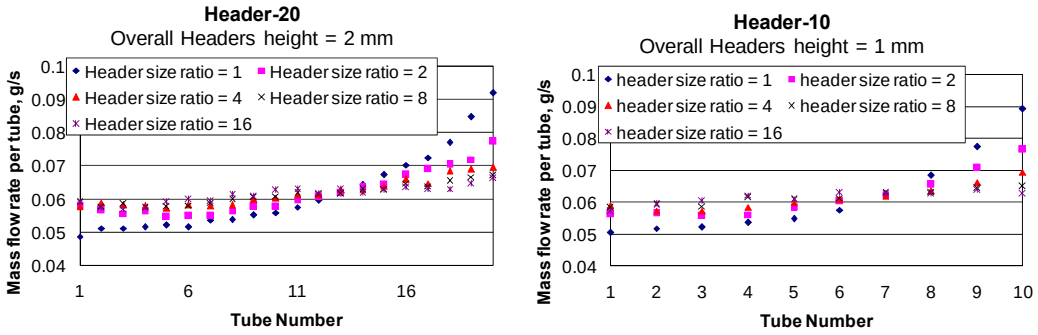

(a) (b)

Figure 28: Mass flow rate per tube for high header velocity designs: (a) 20 tubes header, (b) 10 tubes header

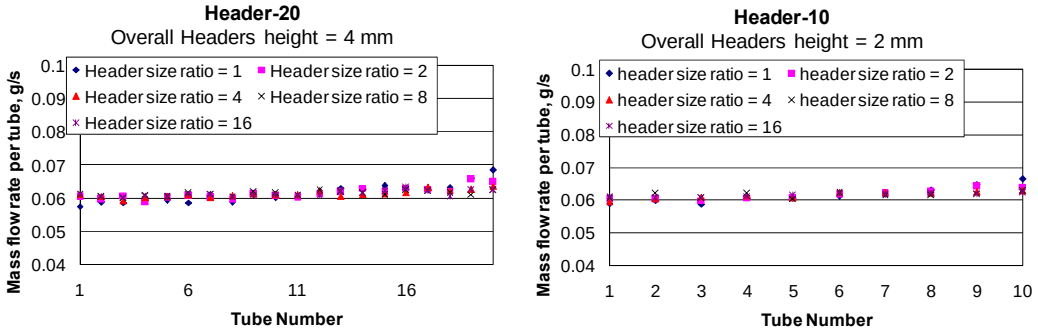

(a) (b)

Figure 29: Mass flow rate per tube for medium header velocity designs: (a) 20 tubes header, (b) 10 tubes header

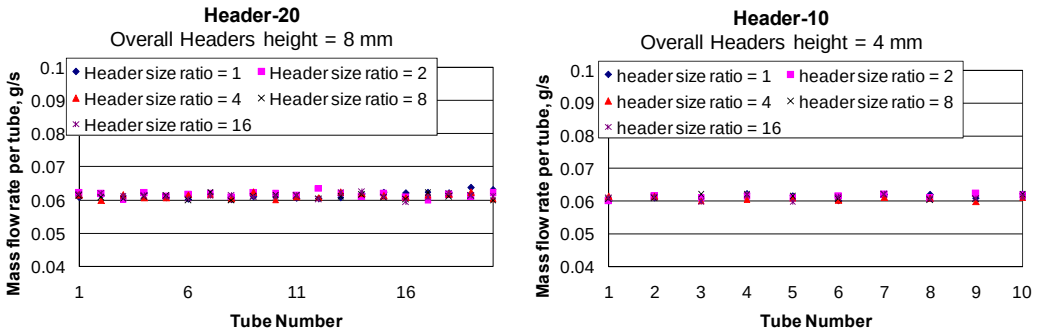

(a) (b)

Figure 30: Mass flow rate per tube for low header velocity designs: (a) 20 tubes header, (b) 10 tubes header

5.4. Design Guidelines

Based on the results presented in the previous section, it is shown that better mass flow rate distribution and lower pressure drop are achieved at lower inlet header water velocities. However, marginal improvements were experienced for cases with inlet header velocities smaller than the average port velocity (marked in red) as shown in Figure 31 and Figure 32. Except for the larger header height designs, header size ratios smaller than 4 resulted in increased overall pressure drop and poor water flow rate distribution. These findings suggest that for any header design, it is recommended to start with a header height and a header size ratio that results in an inlet velocity equal to the average port velocity. If the simulation results show poor performance, header size ratio should be increased until the desired performance is achieved. However, if the performance is still not acceptable, it is advised to go to a larger header size and start over.

Finding header height and header size ratio that result in the desired inlet velocity value represent an optimization problem with the objective of minimizing

both header height and header size ratio. The resulting Pareto optimum solutions would then present the tradeoff between smaller overall HX size and manufacturing complexity.

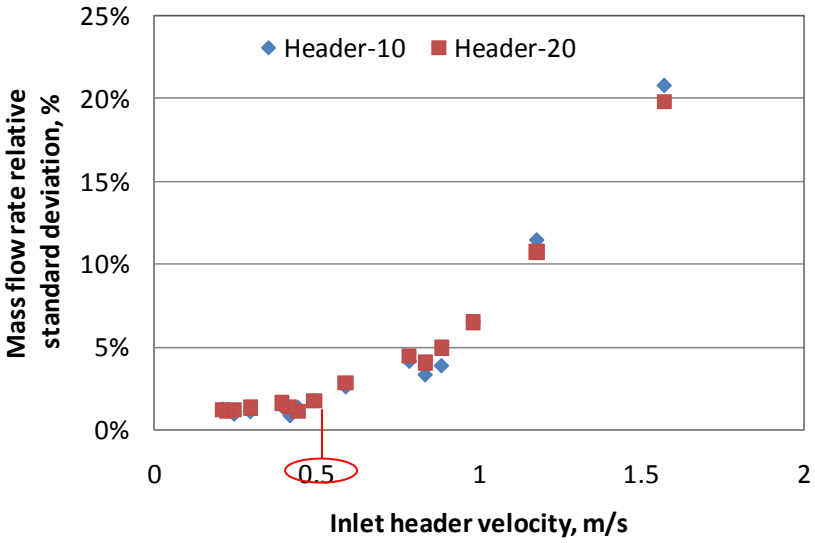

Figure 31: mass flow rate relative standard deviation versus inlet header velocity

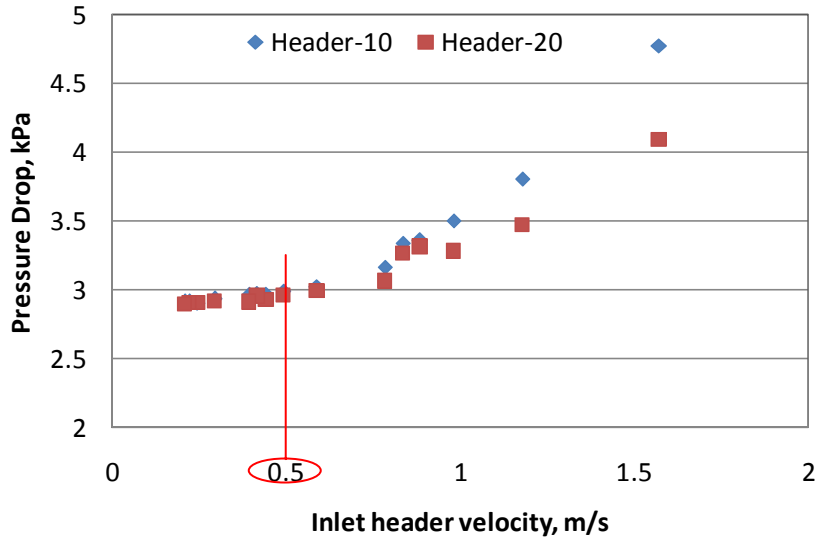

Figure 32: Overall pressure drop versus inlet header velocity

5.5. Suggested Header Design

An additional conceptual header design configuration is sought in order to provide modular HX design. The optimized tube designs are packaged in a tube bank design as shown in Figure 33. In this configuration, the inlet header is fed from both sides lateral to the tubes. Feeding the inlet header from both sides eliminate the need for static pressure regain design; hence rectangular designs might be sufficient. Furthermore, this design is not limited by the number of tubes. However, there exist an optimum value for the number of tubes per package based on the tube vertical spacing and the transition connection design. The header height for this design is a function of the number of ports per tube. Following the design guidelines suggested earlier, the header height can be calculated as shown in equation (36) assuming inlet header velocity equal to the average port velocity.

$$L_H = \frac{N_p \frac{\pi}{4} D^2}{VS} \tag{36}$$

The package unit suggested in Figure 33 can be connected in series as shown in Figure 34 to form a high aspect ratio HX or in combination of series and parallel configuration as shown in Figure 35 to provide the desired aspect ratio. This modular design can be used to design HX of the desired capacities based on a modular design.

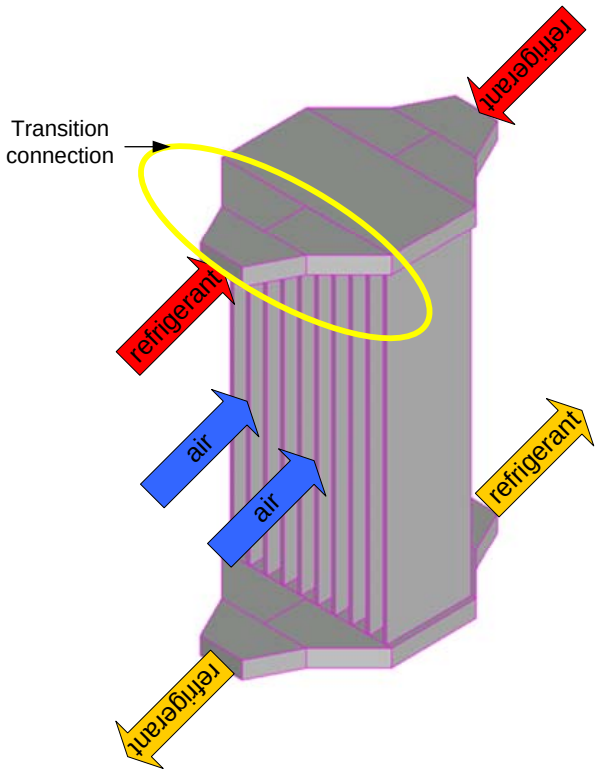

Figure 33: Alternative header design, package unit

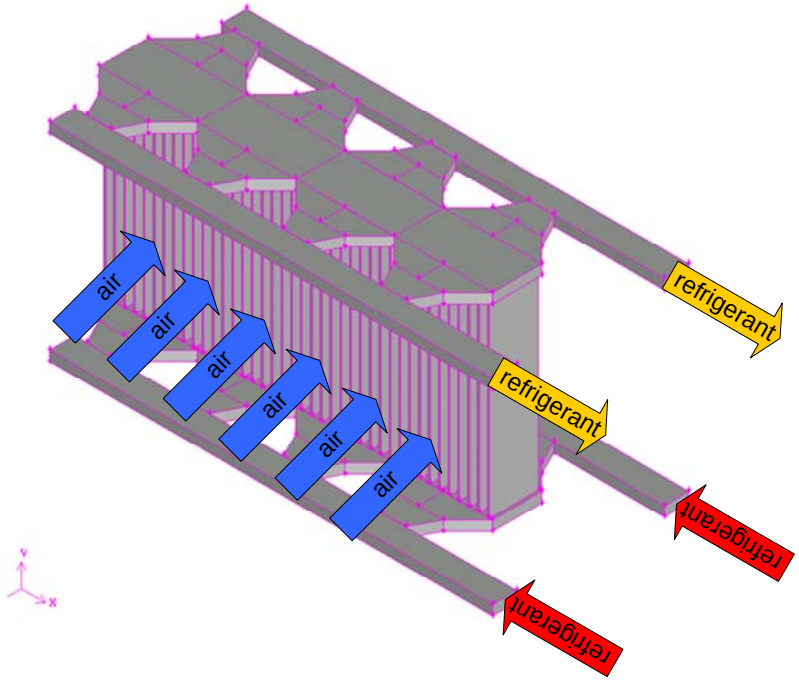

Figure 34: HX design with alternative header design using series package units

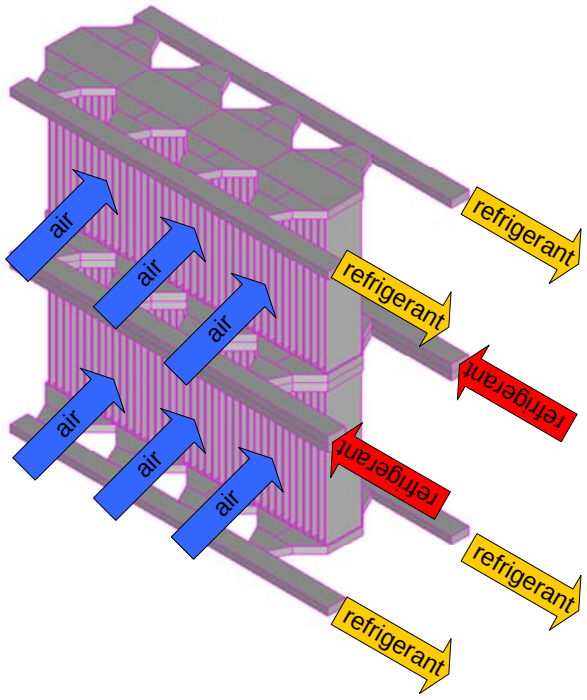

Figure 35: HX design with alternative header design using parallel and series package units

5.6. Fluid Flow Resistance Analogy Limitations

The use of fluid flow – electric resistance analogy allows for zero order approximation of the header design problem. In this analogy, the junction pressures act as flow potential while average velocity represents the flow current. In electric resistance network analysis, the potential is equal to the current multiplied by the resistance value. In the case of fluid flow network analysis, the flow potential is usually correlated to the squared value of the flow for fully developed flow and conventional connections. The header design shown in Figure 22 is unique since the connections (diverging tapered T- and converging tapered T-junctions) are not conventional and the flow inside the header through a tapered channel have not been

addressed in previous literature. There exist no correlation parameters for these flow conditions in previous literature. Furthermore, the hydraulic developing length is usually a significant portion of the tube length; hence developing flow pressure drop correlations are required to accurately model the pressure drop behavior. As such, conventional analogy can not be used. However, a system of nonlinear equations can be solved to evaluate the pressure drop per tube as shown in Appendix D.

5.7. Summary

A new approach for the CFD simulations of HX header performance is developed and applied on 2 HX designs using the porous jump interior boundary conditions. This approach applies a developing flow pressure drop correlation in order to improve the modeling accuracy. The porous-jump parameters were updated during the CFD solver iterations using the Scheme programming language. The results show that overall header height and the header size ratio affect the mass flow rate distributions and the overall pressure drop greatly for smaller header sizes. It was also found that having a header design with inlet velocity equal to the average fluid velocity per port provides good results with minimal improvement for lower header inlet velocity. Furthermore, the header size ratio had a great impact on the distribution for smaller header heights. For the 2 designs considered in this chapter, header size ratio of 4 was found to be adequate when the inlet header velocity was less than or equal to the average port velocity.

Chapter 6: Modeling Heat Exchangers Subject to Statistically Varying Geometric Parameters and Flow Conditions

Small dimensions found in modern and novel HX designs makes manufacturing very challenging. With current manufacturing techniques such products will exhibit large tolerances relative to design variables. Hence, the anticipated variation in performance is a concern. Furthermore, small flow channel dimensions are susceptible to severe fouling and even blockage resulting in uncertain flow distribution. These uncertainties in dimensions and flow distribution should be accounted for during performance evaluation of new HX geometries with focus on ultra-compact designs. This chapter presents a modification to the conventional ε-NTU HX evaluation technique to allow for such conditions. Furthermore, a new approach is developed for the random segment parameter assignment following a predefined uncertainty distribution incorporating a Monte Carlo (MC) simulation approach.

6.1. Introduction

Novel heat exchangers introduced recently rely mainly on the smaller flow channels (J Pettersen et al. 1998, Saji et al. 2001, Kasagi et al. 2003a, Kasagi et al. 2003c, Shikazono et al. 2007). However, small tubes and port dimensions lead to wobbling and less control on the vertical spacing along the tube length as shown in Figure 36 for a prototype HX manufactured using 0.4 mm outer diameter stainless steel tubes.

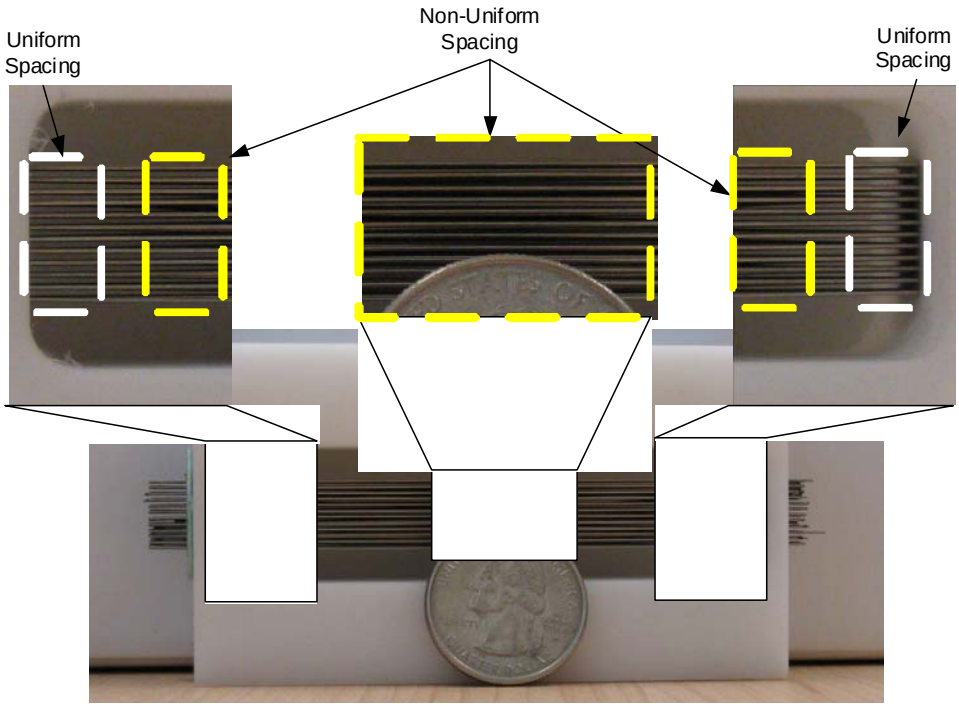

Figure 36: Geometric variability within a single HX

As depicted by Figure 36, vertical spacing can change dramatically and non-uniformly over the HX face area. As such, a statistical distribution is needed to represent the variation in HX geometry due to manufacturing tolerances and tube material structural stability effects on free flow spacing between tube rows. On the other hand; the small port diameter might lead to increased effects of flow impurities. Scales and impurities that are considered harmless in conventional flow channels (> 0.7 mm) cannot be ignored when the flow channels are reduced to the range of 0.1 mm. In microchannel applications such flow fouling can affect the refrigerant flow greatly and might lead to completely blocked tubes and hence loss of active heat transfer and refrigerant flow areas resulting in heat transfer capacity decrease and increase in refrigerant side pressure drop.

This chapter presents an effort to account for geometric and flow variability within new heat exchanger designs in order to more objectively evaluate ultra-compact designs based on current manufacturing limitations and operating conditions. The developed approach was applied to the NGX-13 geometry (Figure 2) under due consideration of water flow and vertical spacing uncertainty. A new implementation technique for ε-NTU is proposed in order to accommodate different air conditions on both sides of a given tube within the multi-scale simulation framework described in Chapter 4. A Monte Carlo simulation approach is used to estimate the HX performance distribution. This approach is applied to 3 HX designs showing the performance degradation subject to geometrical and flow distributions assuming normal distribution with different standard deviation values.

6.2. Approach

The multi-scale approach presented in Chapter 4 is modified to allow for variability in free flow spacing between the tubes. In this case, the CFD simulations were performed using pressure inlet boundary conditions instead of velocity inlet boundary condition. The model is implemented in a multi-scale approach as shown in Figure 10.

First, CFD predictions are required for all possible representative heat exchanger segments, within the HX based on the nominal design parameters and statistical distributions. Second, the geometric parameters and boundary conditions are randomly distributed amongst the entire HX. After the free flow spacing between tubes is being randomly distributed, thermal and hydraulic performance are prescribed on both sides of each tube based on the vertical spacing between

neighboring tubes. Then, water flow rate through each tube is set based on a predefined statistical distribution. Finally, for each segment, a modified ε-NTU model is implemented to estimate the outlet air and water temperatures and the information is passed to successive segments to be able to evaluate the overall HX performance. Details of this approach are discussed in more details in the following subsections.

6.2.1. Airside CFD simulations

PPCFD was used to execute CFD simulations of all possible segment arrangements for each HX based on the nominal design and the selected uncertainty distribution. This tool reads the parametric design values for all segments within the HX and automatically generates Gambit® journal files for mesh generation and Fluent® journal files for pre-processing, processing, and post-processing of the all CFD cases. For each of the CFD cases, the airside mass flow rate, pressure drop and overall HTC are stored and passed to the HX solver for overall performance evaluation.

The parameterized NGHX-13 geometry used during CFD simulations is shown in Figure 37 along with the prescribed boundary conditions. Figure 37 also depicts a sample mapped triangular mesh generated using PPCFD. The fact that there exists variability in the tube position causes variations in airside velocities between tubes. Hence, using constant airside inlet velocity as suggested in Chapter 4 will result in a variable air outlet pressure; however, in a real HX, the variable airflow resistance leads to a different velocity distribution over the HX face. As such, the total inlet pressure to the HX is kept constant at 60 Pa assuming uniform air flow after the supply fan with inlet air temperature set at 300 K. The no-slip boundary

conditions were set for all walls and a pressure outlet condition of 0 gauge was used for the air outlet. The tube inner wall temperature was set at 350 K. Symmetry was defined along the axis as shown in Figure 37. Second order upwind discretization schemes were used for the governing equations and a pressure-based coupled solver was used for improved convergence (Fluent 2007). As suggested earlier, the Green-Gauss Node-Based gradient evaluation was used. The solver was allowed to iterate until convergence or to a maximum of 4000 iterations. The convergence criteria were based on maximum acceptable normalized residuals of 10^{-5} for all equations. The inlet static pressure is recorded after each iteration. The inlet pressure changes over the last 100 iterations are checked for the cases when the maximum number of iterations is reached while not meeting the convergence criteria. The CFD results are only accepted when the standard deviation of the last 100 iterations is less that 0.5%. Out of the 75 CFD simulations performed for the 3 HX designs and the different vertical spacing only 10 cases reached the maximum number of iterations; however, the standard deviation of the inlet static pressure for the last 100 iterations were less than 0.005% for all 10 cases. The same post processing technique described in section 4.3.1 was implemented.

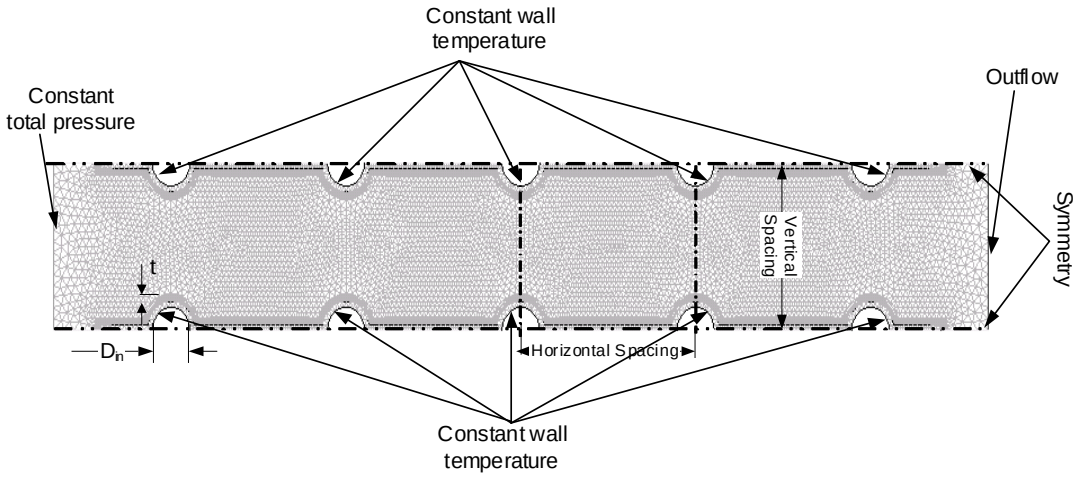

Figure 37: Discretized CFD computational domain and boundary conditions

6.2.2. Modified ε-NTU solver

CoilDesigner (Jiang et al. 2006) was used in Chapter 4 to evaluate the overall HX performance. This model applies the ε-NTU method to solve for outlet states of the two fluids for each HX segment. It can be used in cases with non uniform air flow distribution over the HX face. However, in this case the average air inlet velocity for each segment is used to find the pressure drop and HTC based on available correlations. The CFD domain presented in Figure 37, suggests that the air side performance depends on the free spacing between adjacent tubes. Vertical position uncertainty results in topside and bottom side tubes being not necessarily equally spaced from the tube under consideration as shown in Figure 38. Hence, the tube's airside performance varies from top to bottom. In order to estimate the outlet air and water conditions from each segment an overall segment capacity is calculated as shown next.

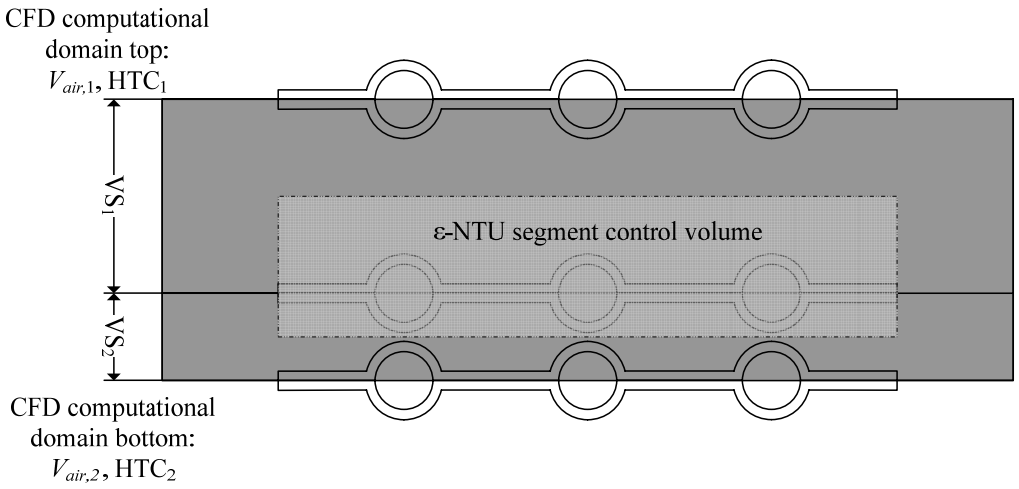

Figure 38: HX segment CFD computational domains and ε-NTU control volume

The segment modeling procedure assumes (a) no interaction between top side and bottom side neighboring tubes, (b) water flow rate is divided equally between top and bottom air sides, and (c) ideal mixing of water and air streams at the end of each segment. C_{min} for the top and bottom streams are calculated as shown in equations (37) to (40).

$$C_{water,t} = C_{water,b} = 0.5C_{water} = 0.5\dot{m}_{water}c_{water} \tag{37}$$

$$C_{air,t} = \dot{m}_{air,t}c_{p,air} \tag{38}$$

$$C_{air,b} = \dot{m}_{air,b}c_{p,air} \tag{39}$$

$$\begin{aligned} C_{\min,t} &= \min\left(C_{water,t}, C_{air,t}\right) \\ C_{\min,b} &= \min\left(C_{water,b}, C_{air,b}\right) \end{aligned} \tag{40}$$

The overall HTC is then calculated for both air streams as shown in equation (41). The area correction is required since the air to inner wall temperature overall HTC calculated using equation (29) is based on the heat flux at the primary airside heat transfer area.

$$U_{in,t} = \frac{1}{\frac{A_{in}}{A_{out}U_{out}} + \frac{1}{h_{water}}}; \quad U_{in,b} = \frac{1}{\frac{A_{in}}{A_{out}U_{out,b}} + \frac{1}{h_{water}}} \tag{41}$$

NTU is calculated for both air streams; the inner heat transfer area A_i is divided by 2 since both streams share the same inner area. ε is also calculated for each air stream using the mixed-unmixed correlations suggested by (Shah and Sekulic 2003) as shown in equation (43).

$$NTU_t = \frac{U_{i,t}\frac{A_i}{2}}{C_{\min,t}}; \quad NTU_b = \frac{U_{i,b}\frac{A_i}{2}}{C_{\min,b}} \tag{42}$$

$$\varepsilon = \begin{cases} 1 - e^{\left(-\frac{\left(1 - e^{-NTU \times C_r}\right)}{C_r} \right)} & \text{if } C_{\min} = C_{air} \\ \frac{1}{C_r}\left(1 - e^{\left(-C_r\left(1 - e^{-NTU}\right)\right)}\right) & \text{if } C_{\min} = C_{water} \end{cases} \quad (43)$$

The overall segment capacity is then calculated by means of superposition; top side and bottom side heat capacities are added as shown in equation (44). Finally, the outlet water and air temperatures are calculated based on the energy balance as shown in equations (45) and (46) respectively.

$$q = \left(\left(\varepsilon C_{\min}\right)_t + \left(\varepsilon C_{\min}\right)_b\right)\underbrace{\left(T_{water,in} - T_{air,in}\right)}_{\Delta T_{\max}} \quad (44)$$

$$T_{water,out} = T_{water,in} - \frac{q}{C_{water}} \quad (45)$$

$$T_{air,out} = T_{air,in} + \frac{q}{\left(C_{air,top} + C_{air,bottom}\right)} \quad (46)$$

The previous analysis was based on water side performance evaluation using laminar developing flow correlations as discussed in section 4.3.2.

6.3. Variability Assignment

In order to be able to simulate the performance of HX under variable geometry and flow conditions, we need first to be able to describe such variability and assign it to the HX under considerations. Standard normal distribution (Kreyszig 2006) shown in Figure 39 is suggested by (Kalpakjian 1995) to represent output results from manufacturing distribution. Hence, standard normal distribution is used to define the variability of HX geometry and flow conditions. As such, each segment

within the HX would be assigned geometric parameters that deviate from the nominal design. The refrigerant side mass flow rate through each tube would also be assigned a value deviating from the nominal average mass flow rate per tube. Geometric parameter and flow rate variability assignment methodologies are discussed in more details in the following sub-sections.

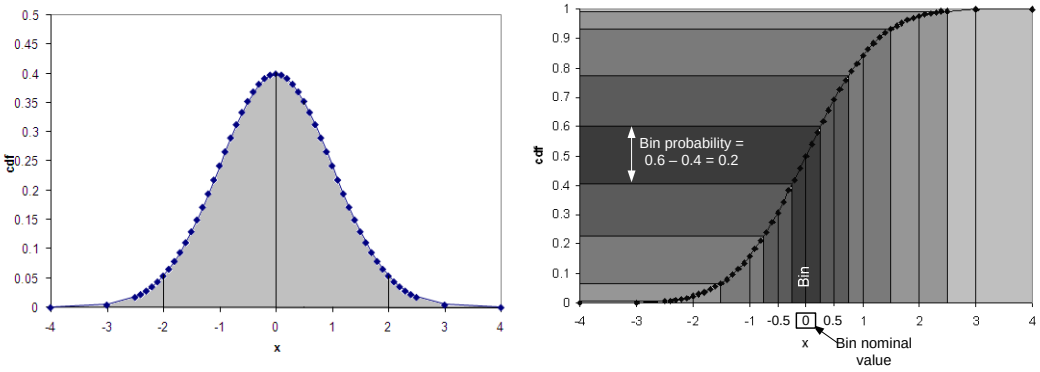

(a) (b)

Figure 39: Standard normal distribution representation: (a) probability density function (pdf), (b) cumulative density function (cdf).

6.3.1. Geometric variability distribution

Geometric variability affects the airside performance greatly. As such for each possible realization of the nominal design a CFD run would be required. With the continuous normal distribution of Figure 39, it would be required to run the CFD simulations for each segment of the HX. Thus the computational effort would depend on the number of tubes and number of segments per tube within the HX. In an effort to reduce the required number of CFD simulations, the standard normal distribution was discretized as shown in Figure 40. The discrete variability bins are set to be 0, ± 0.5 σ, ± σ, and ± 2 σ. Simulations were limited to cases with ± 2 σ since this would

roughly encompass 95.5% of the statistical distribution. For higher confidence levels (up to 99.7%) the simulations should encompass cases within ± 3 σ. For each bin, the probability is calculated such that it covers the mid points between adjacent bins (For example, $P(0) = P(-0.25\,\sigma < x < 0.25\,\sigma) = 0.2$; $P(\sigma) = P(-0.75\,\sigma < x < 1.5\,\sigma) = 0.16$. Hence, for each nominal design the number of CFD runs will be a function of the number of distribution bins.

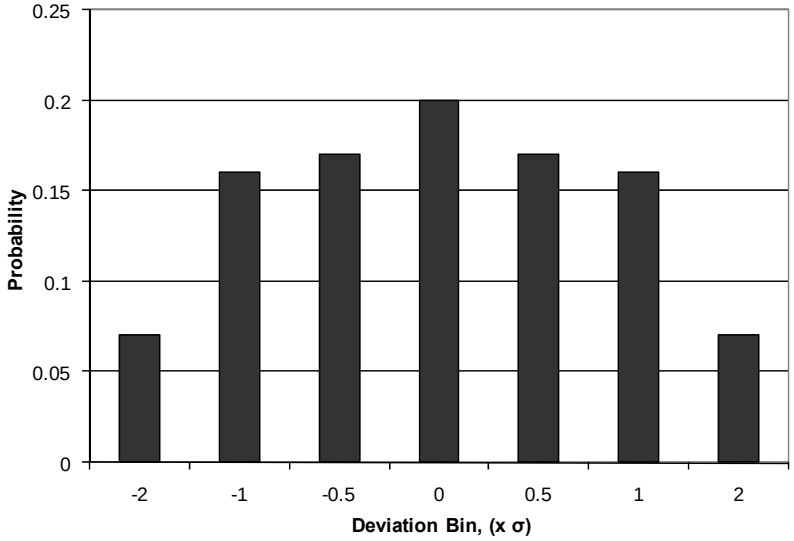

Figure 40: Discrete variability distribution

Discrete normal distribution is applied to the free flow area between NGHX-13 tubes such that for each segment of the tube-*i* the vertical position is shifted by δ_i which is subject to normal distribution with zero mean and standard deviation = $\sigma \times VS_{\text{nominal}}$ as shown in Figure 41.

A Monte Carlo simulation approach (Rubinstein and Kroese 2008) is used to randomly assign segments' position variability. In order to ensure stream wise continuity, the random distribution was constrained to pick the successive segments

along the tube length within ± 1 distribution bin. Furthermore, the distribution was constrained to have end segments within ±0.5 σ since headers are usually manufactured with finer manufacturing tolerances. For any 2 adjacent tubes (i, i + 1) the free flow spacing *FFS* is calculated as shown in equation (47).

$$FFS = \overline{FFS} - \delta_i + \delta_{i+1} \tag{47}$$

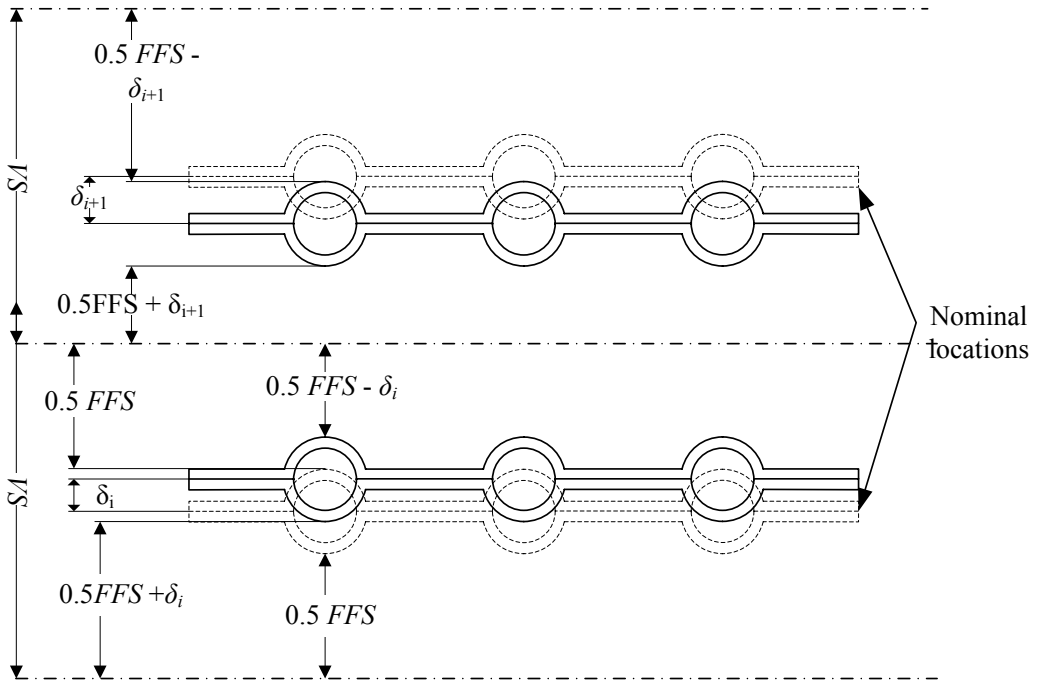

Figure 41: Geometric variability definitions

For each nominal design, CFD simulations are performed for all possible *FFS* based on discrete normal distribution bins. For the discretized normal distribution shown in Figure 40, there exist 15 different combinations for *FFS*. Hence, for each nominal design, 15 CFD runs are required to estimate the airside thermal and hydraulic performance between each pair of tubes. After the segment variability assignment, each tube is compared with neighboring tubes (top and bottom tubes) and

the top side *FFS* and bottom side *FFS* is evaluated. Finally, based on the top and bottom *FFS*, top side and bottom side HTC and air velocities are assigned.

The following numerical example is used to better describe the segment geometric assignment methodology. A nominal NGHX-13 segment design is specified as follows: D_{out} = 0.56 mm, *HS* = 2.11 mm, *VS* = 1.69 mm and number of ports = 11. This results in nominal *FFS* of 1.13 mm. Assuming that *FFS* vary according to a normal distribution with a standard deviation of 15%, each segment can be offset from its nominal vertical position by either [-30.0%, -15.0%, -7.5%, 0.0%, 7.5%, 15.0%, or 30.0%] with a probability of [7%, 16%, 17%, 20%, 17%, 16%, 7%] respectively. Such distribution results in 15 different *FFS* varying from 0.45 to 1.8 mm as summarized in Table 11 which also includes the thermal and hydraulic performance values obtained from the CFD simulations.

An example of the Monte Carlo simulation results for random geometric parameter distributions is shown in Figure 42. In this specific sample distribution, tube 11 segment 9 was assigned a variability of -30.0%, where as the neighboring segments (tube 10 segment 9 and tube 12 segment 9) were assigned *FFS* variabilities of -15.0% and +15% respectively. This results in tube 11 segment 9 having an FFS_t of 1.29 mm and FFS_b of 0.96 mm. As such, HTC_t = 71.1 W/m^{2}K with V_t = 5.1 m/s and HTC_b = 78.3 W/m^{2}K, and V_b = 4.1 m/s as shown in Table 11. Similarly, for the top and bottom tubes, the heat transfer and air velocity is determined for each segment.

6.3.2. Flow rate variability distribution

Tube wise water flow rate can be subject to distribution uncertainty due to tube fouling as well as additional pressure drop from impingement and tube buckling. Hence, the nominal water flow rate through each tube is multiplied by X subject to normal distribution of mean = 1.0 and standard deviation of either 0% (uniform water flow), 25%, or 50%. Continuous distribution can be used with this type of variability since it does not require computationally expensive CFD run. For each tube, the water mass flow rate is used to calculate the thermal and hydraulic performance based primarily on available correlations as discussed earlier.

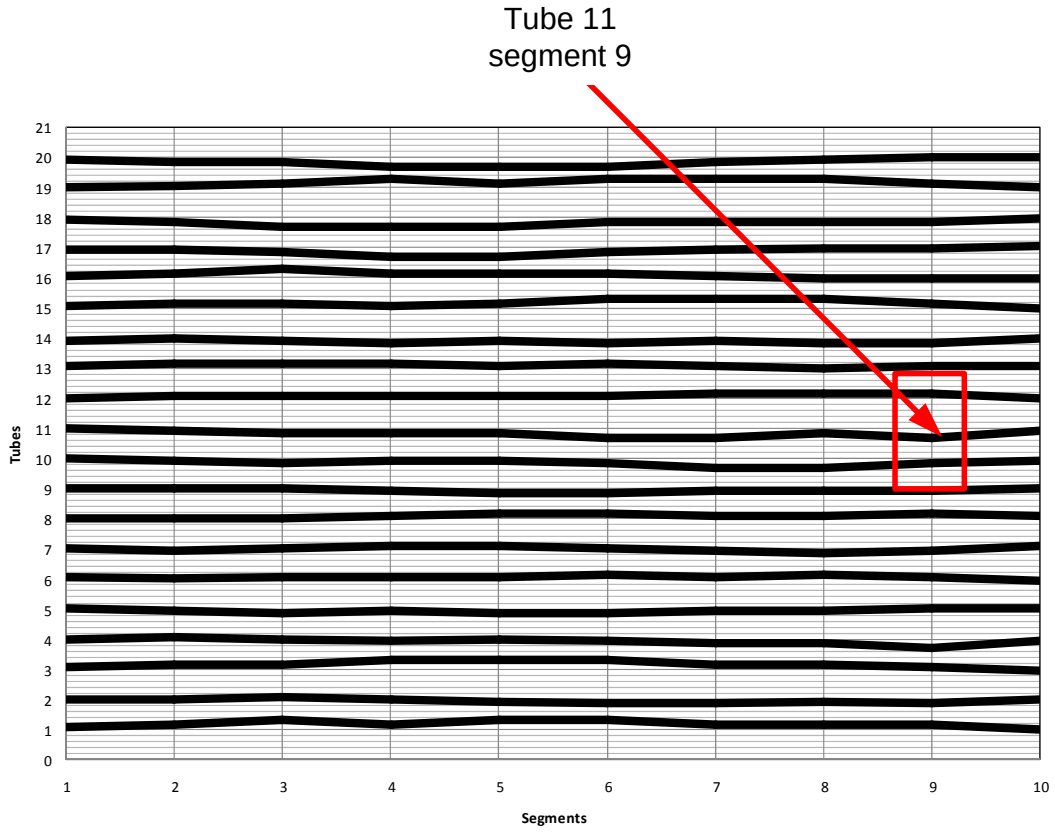

Figure 42: Heat Exchanger face, showing tube position variability for a sample random distribution

Table 11: Thermal and Hydraulic Performance of all possible FFS between tube pairs for Design HXD2

Distribution bin pairs (δ_i, δ_{i+1})	*FFS*, mm	ΔP, Pa	HTC, W/m^2K	MFR, g/ms	*V* m/s
(30.0%, -30.0%)	0.45	58.1	113.4	2.2	1.8
(30.0%, -15.0%); (15.0%, -30.0%)	0.62	55.5	96.1	3.9	2.7
(30.0%, -7.5%); (7.5%, -30.0%)	0.7	53.9	89.7	4.9	3.1
(30.0%, 0.0%); (15.0%, -15.0%); (0.0%, -30.0%)	0.79	52.5	85.3	5.8	3.5
(30.0%, 7.5%); (-7.5%, -30.0%); (15.0%, -7.5%); (7.5%, -15.0%)	0.87	51.0	81.6	6.7	3.8
(-15.0%, -30.0%); (30.0%, 15.0%); (15.0%, 0.0%); (0.0%,-15.0%); (7.5%, -7.5%)	0.96	49.4	78.3	7.7	4.1
(15.0%, 7.5%); (-7.5%, -15.0%); (7.5%, 0.0%); (0.0%, -7.5%)	1.04	48.0	76.0	8.6	4.4
For all $\delta_i = \delta_{i+1}$	1.13	46.5	73.9	9.7	4.7
(15.0%, 7.5%); (7.5%, 0.0%); (0.0%, -7.5%); (-7.5%, -15.0%)	1.21	45.2	72.4	10.6	4.9
(15.0%, 0.0%); (7.5%, -7.5%); (0.0%, -15.0%); (-15.0%, -30.0%); (30.0%, 15.0%)	1.29	43.8	71.1	11.7	5.1
(15.0%, -7.5%); (7.5%, -15.0%); (30.0%, 7.5%); (-7.5%, -30.0%)	1.38	42.6	70.0	12.6	5.3
(15.0%, -15.0%); (30.0%, 0.0%); (0.0%, -30.0%)	1.46	41.5	69.3	13.6	5.5
(30.0%, -7.5%); (7.5%, -30.0%)	1.55	40.2	68.5	14.6	5.7
(30.0%, -15.0%); (15.0%, -30.0%)	1.63	39.1	67.8	15.6	5.8
(30.0%, -30.0%)	1.8	37.0	66.8	17.6	6.1

6.4. Results and Discussions

Heat exchanger modeling with design and operating variability is applied to 3 designs denoted as HXD1, HXD2, and HXD3. HXD1 has the smallest port inner diameter (0.2 mm). HXD3 has an inner port diameter of 0.7 mm which is equal to current state of the art in microchannel HXs whereas HXD2 has an intermediate port diameter of 0.45 mm. Furthermore, those designs vary in horizontal spacing, vertical spacing, number of ports per tube, number of tubes, tube length and water flow velocity. Design parameters for designs HXD1 to HXD3 are summarized in Table 12.

Table 12: Heat Exchanger Designs

Design	D_{out}, mm	*HS*, mm	*VS*, mm	*Np*	L_{tube}, m	N_{tubes}	V_{water}, m/s
HXD1	0.25	0.375	0.5	3	0.085	40	0.3
HXD2	0.56	2.11	1.69	11	0.2	20	0.6
HXD3	0.88	5.25	3.5	19	0.3	10	1.0

For each of those designs, the discrete geometric uncertainty for the free flow spacing described hereinbefore was applied. The segment distribution procedure was carried 1000 times for each design in order to obtain a distribution of the geometric uncertainty distribution effect on the HX performance. The geometric uncertainty is based on the discretized normal distribution presented in Figure 40 with a standard deviation of 15%. Furthermore, the same distributions were used along with water flow rate uncertainty under normal distribution with a standard deviation of 25% and 50% respectively to investigate the impact on the overall performance.

The results from this study are summarized in Table 13 showing the average values and the standard deviations for the HX performance criteria for all the runs. These results suggest that the impact on the water side pressure drop is marginal and could be neglected. On the other hand, the variation in HX capacity is shown to be largely dependent on the water flow rate variability for the case of 15% geometric standard deviation.

To be able to effectively present the statistical distribution effect on the heat exchanger performance; box plots (McGill et al. 1978) are employed. To further analyze the distribution effects, box plots for capacity change are made for each of the designs and for the 3 variability scenarios: geometric variability only, geometric variability with $\sigma_{\dot{m}_{water}} = 25\%$, and geometric variability with $\sigma_{\dot{m}_{water}} = 50\%$ as shown in Figure 43. The left and right ends of each "box" represent the 25^{th} and 75^{th} percentiles of the runs. The red line inside the box represents the median of the values whereas the lines extending left and right of the box show the results extent for the rest of the values. Outliers, having values more than 1.5 times the interquartile range away from the right or left of the box, are presented as plus signs.

To better understand the box plot representation of Figure 43; the histogram for HXD3 capacity change subject to $\sigma_{\dot{m}_{water}} = 50\%$ is shown in Figure 44. The histogram shown in Figure 44 (a) shows that the capacity change follows a skewed distribution which resulted in a large number of points being represented as outliers in the box plot as described in Figure 44 (b).

Table 13: Summary of Variability impact on HX performance

Design	Case	$\dot{m}_{air}$	ΔP_{ref}	$T_{air,out}$	$T_{ref,out}$	$\dot{Q}$
		g/s	kPa	K	K	W
HXD1	$\sigma_{FFS}=0\%, \sigma_{\dot{m}_{water}}=0\%$	8.3	7.8	309.1	324.1	119.6
	$\sigma_{FFS}=15\%, \sigma_{\dot{m}_{water}}=0\%$	8.3 ± 0.03	7.8	308.9 ± 0.05	324.4 ± 0.05	118.5 ± 0.24
	$\sigma_{FFS}=15\%, \sigma_{\dot{m}_{water}}=25\%$	8.3 ± 0.03	7.8 ± 0.31	308.7 ± 0.2	324.8 ± 0.68	116.6 ± 1.66
	$\sigma_{FFS}=15\%, \sigma_{\dot{m}_{water}}=50\%$	8.3 ± 0.03	8.0 ± 0.57	308.1 ± 0.43	326.3 ± 1.08	111.9 ± 3.69
HXD2	$\sigma_{FFS}=0\%, \sigma_{\dot{m}_{water}}=0\%$	38.2	7.4	311.8	342.9	665.3
	$\sigma_{FFS}=15\%, \sigma_{\dot{m}_{water}}=0\%$	37.8 ± 0.24	7.4	311.9 ± 0.11	342.9 ± 0.02	657.6.0 ± 2.09
	$\sigma_{FFS}=15\%, \sigma_{\dot{m}_{water}}=25\%$	37.8 ± 0.24	7.4 ± 0.43	311.8 ± 0.14	343.0 ± 0.37	654.3 ± 4.29
	$\sigma_{FFS}=15\%, \sigma_{\dot{m}_{water}}=50\%$	37.8 ± 0.24	7.6 ± 0.81	311.4 ± 0.4	343.0 ± 0.62	640.0 ± 14.88
HXD3	$\sigma_{FFS}=0\%, \sigma_{\dot{m}_{water}}=0\%$	66.6	8.0	309.8	346.7	1075.1
	$\sigma_{FFS}=15\%, \sigma_{\dot{m}_{water}}=0\%$	66.8 ± 0.78	8.0	310.4 ± 0.17	346.8 ± 0.01	1059.7 ± 3.45
	$\sigma_{FFS}=15\%, \sigma_{\dot{m}_{water}}=25\%$	66.8 ± 0.78	8.1 ± 0.66	310.4 ± 0.18	346.8 ± 0.24	1057.4 ± 5.59
	$\sigma_{FFS}=15\%, \sigma_{\dot{m}_{water}}=50\%$	66.8 ± 0.79	8.4 ± 1.31	310.2 ± 0.34	346.9 ± 0.46	1045.1 ± 20.1

The average capacity loss caused by geometric uncertainty with uniform water flow rate distribution for HXD1, HXD2, and HXD3 are 0.9%, 1.15%, 1.4% respectively. When geometric variability is combined with water flow variability of a standard deviation of 25% the capacity loss is almost doubled for the smallest port design (HXD1) and had limited impact on the larger diameter port (HXD3); 2.4%,

1.7%, 1.6% for HXD1, HXD2, and HXD3 respectively. However, when water flow variability with a standard deviation of 50% is applied, i.e. higher likelihood of tubes being completely blocked; the capacity loss was significantly increased to 6.4%, 3.8%, and 2.8% for HXD1, HXD2, and HXD3 respectively. These results indicate that larger port diameters tend to increase the impact of geometric variability; whereas smaller port diameter increases the impact of water flow rate variability. This finding can be attributed to the fact that HX made with larger port diameters require less number of tubes in parallel; hence the water flow rate maldistribution will be less pronounced. Furthermore, larger port diameters results in larger *FFS* hence the absolute variation would be larger and the impact on thermal and hydraulic performance would be affected more than the case of smaller nominal values of *FFS*.

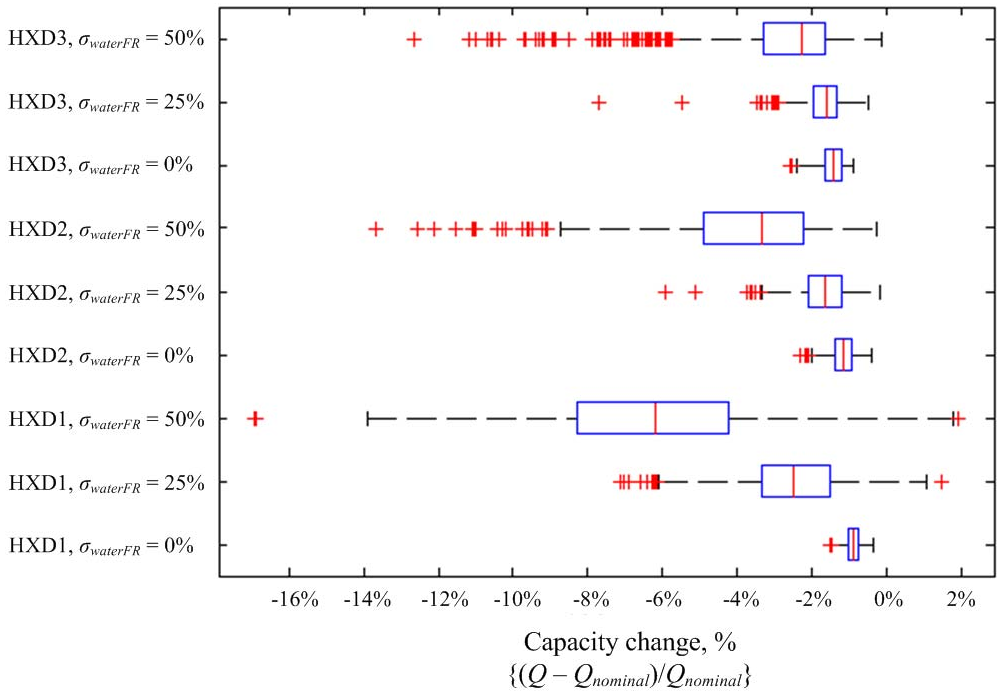

Figure 43: Box plot for the HXD1, HXD2 and HXD3 for water flow rate variability of 0%, 25%, and 50%

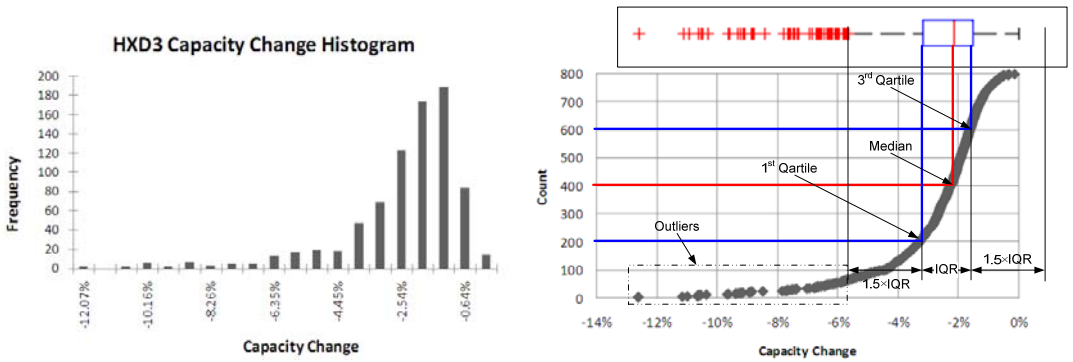

(a) (b)

Figure 44: Histogram for capacity change for HXD3 subject to $\sigma_{FFS} = 15\%$ and $\sigma_{\dot{m}_{water}} = 50\%$: (a) histogram for the capacity change, (b) box plot representation

The geometric variability impact on capacity is much smaller than its impact on the segment performance. Table 11 shows that the airside HTC varies from 67 to 113 W/m^{2}K based on the geometric variability. This corresponds to variations ranging from -10% to +53% from the nominal value. However, realizations with higher HTC experience a sharp decrease in air mass flow rate; hence the overall segment capacity changes are small as shown in Figure 45. Furthermore, the extreme cases where the capacity losses have small probability, 12%, to be realized in a HX.

HXD1 with $\sigma_{\dot{m}_{water}} = 25\%$ and $\sigma_{\dot{m}_{water}} = 50\%$ showed extreme capacity losses of -7.1% and -16.9% respectively. It also showed capacity gains of 1.5% and 2%. The capacity gains are attributed to the increased water flow rate for extreme cases; which increased the overall HTC and were able to surpass the performance degradation due to geometrical uncertainty. Extreme capacity changes for HXD2 also show severe degradation (-5.9% at $\sigma_{\dot{m}_{water}} = 25\%$ and -13.7% at $\sigma_{\dot{m}_{water}} = 50\%$) with a possible

capacity gain of only 0.11% at $\sigma_{\dot{m}_{water}} = 25\%$. The HXD3 design showed no signs of possible capacity gains and experienced extreme capacity losses of 7.7% at $\sigma_{\dot{m}_{water}} = 25\%$ and 12.6% at $\sigma_{\dot{m}_{water}} = 50\%$. This shows that for larger port diameter designs as in the case with HXD2 and HXD3 the marginal increase in water flow rate in extreme cases cannot overcome the performance degradation due to geometrical uncertainty distribution.

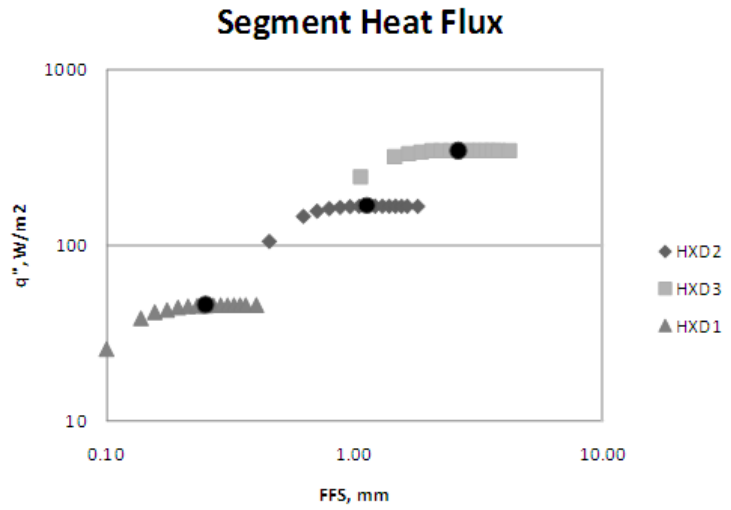

Figure 45: Segment capacity for HXD2 for different FFS – black dots represent the heat flux for the nominal design.

Additional investigation for geometric uncertainty effects were performed using HXD2. Simulations were performed under geometric variability with standard deviation of 20% and 30%. The case of 30% standard deviation in geometric variability resulted in an extreme case with airside totally blocked. A second Monte Carlo simulation was carried using 1000 runs for each case and the average heat capacity losses are summarized in Figure 46 in the form of box plots. The results

show that the impact of water flow rate variability on the HX performance becomes marginal as the standard deviation in the tubes vertical position is increased.

Results shown in Figure 46 show that the average capacity loss with the case of σ_{FFS} = 15% increased more than 3 folds from -1.2% to less than -3.8% with $\sigma_{\dot{m}_{water}} = 50\%$ whereas in the case of σ_{FFS} = 30% the average performance degradation was marginally affected by the water flow variability from -7.4% to -9.6%.

The results presented hereinbefore demonstrate the importance of accounting for manufacturing and water flow variability in the performance evaluation of heat exchangers. The results show large dependence on the standard deviation. A careful analysis of manufacturing process and tube material strength can be used to estimate the distribution parameters for the geometric uncertainty. On the other hand, tube side fluid (e.g., water or refrigerant) purity and port hydraulic diameter would be the dominant factor in determining the uncertainty distribution for the water flow rates. Further studies on geometric and flow variability are required in order determine realistic variability distributions.

The studies presented here are only valid for the case of normal (Gaussian) distribution; however, the proposed method can be applied to other statistical distributions as well. In real engineering situations, experimental data and product/prototype measurements can be used to develop the required uncertainty distribution. This would be only valid if a significant amount of data is available for statistical investigations. Future work should include a methodology that allows the

interpretation of manufacturing tolerances and flow fouling in the form of statistical distributions. Another area of future work would be the ability to investigate the performance degradation through uncertainty distribution described by closed intervals instead of a predefined statistical distribution.

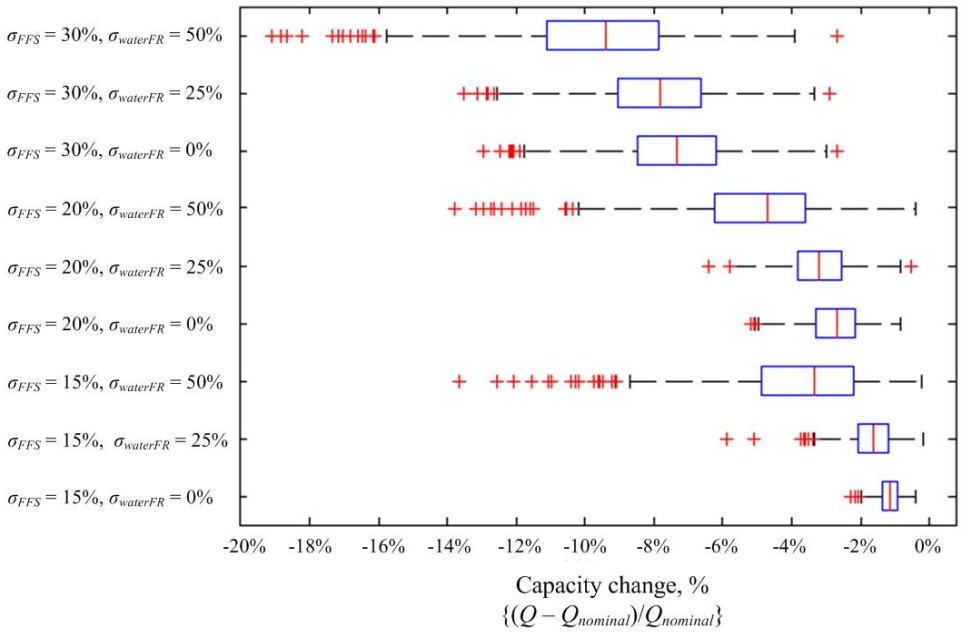

Figure 46: Capacity change for HXD2 under different geometric and water flow rate variability

6.5. Summary

A new approach for modeling novel heat exchanger designs with the ability to account for manufacturing tolerances and flow fouling conditions is introduced. This approach relies on statistical distributions of geometric parameters and water flow rates to represent manufacturing tolerances and refrigerant-side flow fouling conditions respectively. A new implementation technique is used for the segmented ε-NTU solver to allow for variable top and bottom air side conditions. The approach

was applied to NGHX-13 with uncertainty in tubes' vertical position and water flow through each tube within the HX.

Based on the results from Monte Carlo simulations the following conclusions can be drawn:

- In the case of uniform water flow, the overall loss of HX capacity is proportional to the port hydraulic diameter. Furthermore, the distribution of the change in overall HX capacity had a narrow variation interval from (-1.5% to -0.33%) for HXD1 to (-2.6% to 0.87%) for HXD3.
- Increasing the water flow rate distribution standard deviation resulted in a wider spread of expected performance change from the nominal design. Furthermore, the performance penalty trend was reversed and smaller hydraulic port experienced higher performance penalty.
- Studying the effect of geometrical uncertainty standard deviation, as in the case of HXD2, showed that increasing the σ_{FFS} for the same range of $\sigma_{\dot{m}_{water}}$ diminishes the impact of water flow rate uncertainty on the HX capacity degradation.
- For HXD1, results with $\sigma_{\dot{m}_{water}}$ of 50% showed extreme cases of improved performance since water mass flow rate through the entire HX was larger than the nominal design. For larger port sizes designs, HXD2 and HXD3, the increased water flow rate did not overcome the performance degradation due to geometrical uncertainty in any of the extreme cases.

These results suggest that a case by case analysis of possible distribution is required. The results also show that the relative impact of either of the uncertainty sources (geometric parameters or fouling conditions) affect the HX performance. The results were presented statistically using box plots as well as mean values and corresponding standard deviations; however, histogram or other statistical distribution techniques can be used to represent the resultant HX performance. Further studies on manufacturing tolerances and fouling effect on mass flow rate distribution are required to statistically represent these variabilities.

Chapter 7: Approximation Assisted Optimization: Methods and Applications to Novel Heat Exchangers

This Chapter describes a systematic approach for the use of approximation assisted optimization techniques in the design of novel HX concepts. Design optimization is performed using MOGA and higher model fidelity is achieved by applying the multi-scale heat exchanger simulation tool while the computational cost was reduced by applying approximation techniques. This technique was applied to different design problems showing that for a 1 kW heating coil with pressure drop constraints of 100 Pa on the airside and 1000 Pa on the water side there is a potential for 61% reduction in the HX volume and 84% reduction in the HX material when NGHX-13 geometry is used compared to the current state of the art technology. The proposed approximation approach resulted in significant computational savings. The approximation assisted optimization platform shows great potential to examine new and existing designs and provide a greater understanding on the design limitations.

7.1. Introduction

Over the last 25 years, new compact HX surfaces have been introduced to provide better heat transfer rates, lower flow resistance, less weight, and lower cost alternatives. Many opportunities have been overlooked in the past due to design and fabrication limitation. As such, prototypes produced were not necessarily optimized. This shows the importance of having the ability to optimize new geometries before prototype fabrication. Reliable geometry optimization requires accurate modeling

tools in order to ensure that optimization results are capable of providing the significant improvements over current state of the art.

The recent development in computational capabilities along with the improved CFD solution algorithms and increased software reliability made the CFD simulation approach more favorable in the early phase of the development cycle. Literature review presented in section 2.3 indicates that CFD simulations are appropriate for enhanced surfaces performance evaluations. Coupling HX optimization with numerical simulation tools provides an improved accuracy. Furthermore, approximation assisted optimization techniques have also been introduced to the HX design and optimization to provide computational savings. Previous work in HX optimization coupled with numerical solvers and approximation assisted HX optimization were summarized in section 2.5.

HX optimization using CFD studies in previous work focused mainly on periodic HX segment optimization; some studies went further to include a system level optimization using a simplified HX modeling tools. There has not been previous work encompassing HX segment and overall design optimization using a detailed segmented HX simulation tool. This Chapter presents a new approach in HX optimization where HX segment geometry is optimized in light of its impact on the overall HX performance. The optimization incorporates the use of multi-scale simulation approach, presented in Chapter 4. Furthermore, an adaptive DOE technique is used instead of classical DOE to be able to search the design space more efficiently allowing for fewer number of CFD simulations.

7.2. Approach

This Chapter presents a new technique to study enhanced heat transfer surfaces. This technique systematically searches for the optimum design with a higher degree of model fidelity and an acceptable computational cost. Design optimization was performed using a MOGA (Deb 2001) tool to search the design space. The higher model fidelity is achieved by applying the multi-scale heat exchanger simulation while the computational cost was reduced by applying the SFCVT adaptive approximation technique (Aute et al. 2008).

The framework incorporated in this study, which is a subset of the overall research framework adopted in this dissertation, is shown in Figure 47. HX design variables are identified, and the CFD model and meshing strategies are developed based on experience from previous studies as shown Chapter 4. Within this framework, the DOE samples the design space using the adaptive SFCVT approach; sample designs are then evaluated using PPCFD. Next, response data and sample designs are used to construct metamodels for HTC and ΔP using Kriging metamodeling techniques. The developed metamodels are then verified using a set of random designs for which PPCFD simulations provide the true response while the metamodels provide the approximated values.

If metamodels performance metrics do not meet the acceptability criteria the DOE is used to sample more designs in order to improve the metamodel performance. After the approximation step is completed, the approximated multi-scale simulation tool is established where segment performance is evaluated using metamodels instead

of CFD simulation. In this case, the multi-scale simulation is based on the coupling between segment HTC and ΔP metamodels and CoilDesigner.

MOGA is used to optimize the HX performance based on the problem definition: objectives, constraints, and design space. For each iteration during the optimization procedure, a number of HX designs are generated based on MOGA population and population replacement settings. These designs are modeled using the approximate multi-scale simulation tool. The overall HX performance criteria (e.g. heat transfer capacity, airside and refrigerant side ΔP, packaging volume, material volume/weight, etc.) are returned to the optimizer in order to sort and rank the current population and perform the required genetic operations to generate the next design generation. When the maximum number of optimization iterations is reached, Pareto optimum set is identified and stored in an optimization summary file. Optimal designs are then verified using PPCFD to ensure model accuracy. If the verification results are not satisfying, the PPCFD simulations are first investigated to check accuracy and required modeling changes. The approximation step is then revised and a new optimization study is performed.

Pareto solutions from the optimization problem results are used to demonstrate performance tradeoff and understand performance improvement mechanisms. These solutions can also be used to develop design guidelines for the new segment geometry.

7.2.1. Approximate multi-scale HX simulations

The multi-scale simulation approach provides means to accurately predict the performance of new HX segment geometries by coupling CFD simulation at the

segment level with conventional ε-NTU solver at the HX level. The flowchart for the multi-scale HX simulation approach is illustrated in Figure 48. In this approach, CFD is used to estimate the thermal and hydraulic performance of enhanced surfaces. Whereas CoilDesigner (Jiang et al. 2006) evaluates the performance of the entire HX using segment performance evaluation from CFD simulations. Additional computational savings can be achieved by introducing approximation techniques to replace the most computationally expensive part, CFD simulations. An adaptive approximation technique is used to develop accurate metamodels over the entire design space for the thermal and hydraulic performance of the new airside geometries based on CFD simulations. These metamodels can be used for all new HX designs; hence no further CFD simulations will be required except for verification purposes. Developing globally accurate metamodels, offline approximation, require more sample designs. However, these metamodels can be used for any optimization problem incorporating the new design.

7.2.2. Adaptive DOE

The use of adaptive DOE technique ensures efficient use of expensive function evaluations. The SFCVT adaptive DOE technique (Aute et al. 2008, Aute 2008) is used within the framework described in Figure 47. In SFCVT, new samples are selected based on the tradeoff between space-filling criterion and metamodel performance. This tradeoff is solved through multi-objective optimization formulation.

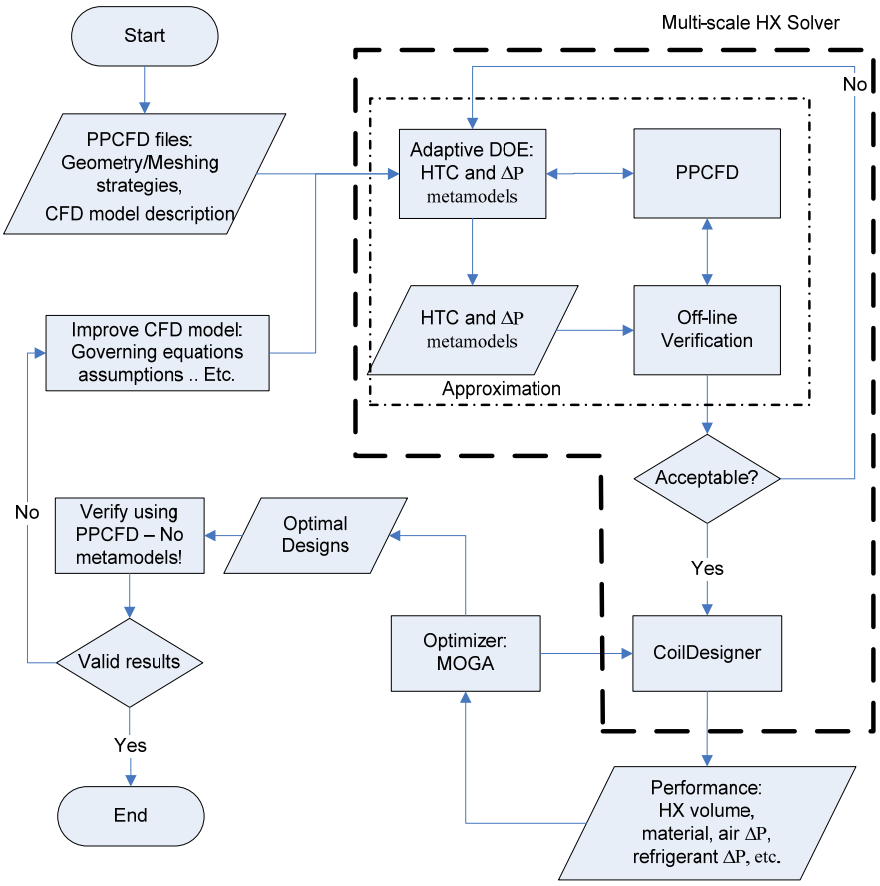

Figure 47: Approximation assisted HX optimization framework

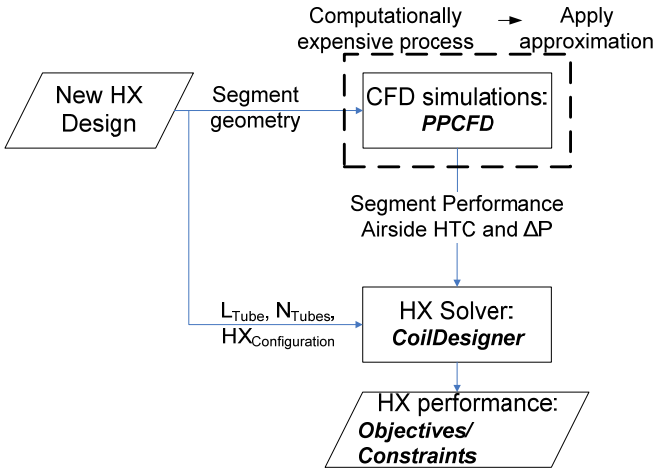

Figure 48: Multi-Scale HX simulation approach

In a multi-response problem such as finding the airside heat transfer coefficient and pressure drop of the new geometry, new sample points are selected from the Pareto solution set (tradeoff) of the performance of the metamodels for individual responses while maintaining the required space filling criterion. In the present work, MED is used to initially sample the design space while the multiresponse SFCVT approach is used to sample the design space for HTC and ΔP simultaneously. The DOE steps are summarized as follows:

1. Use MED to generate an initial design to explore the entire design space.
2. Calculate the leave one out error (e_{LOO}) (Li et al. 2009) for all initial design points and build a Kriging metamodel for e_{LOO}.
3. Solve the optimization problem of equation (48) to find the tradeoff of missed information for the different responses. For NGHX-13, $M = 2$ ($j = 1$ for the pressure drop and $j = 2$ for the heat transfer coefficient). S is the space filling criterion (Aute et al. 2008) and D is the design space.
4. Select the number of desired points from the Pareto solution set: in the current approach 3 points are selected at each sampling stage: the 2 extremes (points corresponding to maximum $\hat{e}_{LOO}$ for pressure drop and heat transfer coefficient) and one point that is closest to the utopian or best point (Deb 2001) according to both objectives.
5. Evaluate the true response of the new sample points.
6. If the number of samples selected in D equals to the required (maximum allowable) sample size; then stop. Otherwise continue to step 2.

$$\begin{aligned} \max_{x} \quad & e_{LOO}^{j} \quad j = 1,..,M \\ \text{subject to} \quad & \\ & \left\| x - x_k \right\|_2 > S \\ & x_k \in D \end{aligned} \tag{48}$$

7.2.3. Metamodeling

Metamodels are used to correlate the response of a new design based on available response from the DOE. The current framework applies the Kriging metamodeling techniques since it does not require a functional form and provides a metamodel performance variance.

Kriging can be viewed as a predictor that estimates the unobserved response for a design based on known responses and the distance of that design from the observed design points. Kriging treats the deterministic response y as a realization of the stochastic process Y:

$$Y = \mu + Z(x) \tag{49}$$

Where Y is the unobserved response, μ is a constant representing known responses (e.g., mean of all known responses) and $Z(x)$ is a stochastic process with zero mean. The current study employed the DACE toolbox (Lophaven et al. 2002) within MATLAB® for the development of the different metamodels.

7.2.4. Metamodel performance metrics: errors verification

The metamodel performance evaluation metrics discussed in section 3.3.3 are used to assess the performance of the metamodels developed prior to the optimization study. The available response data are fitted using Kriging with different regression

models and correlation functions in order to find the best performing metamodel. The pressure drop metamodel showed superior performance when the metamodel was developed based on the natural log of the response data.

7.3. Problem Description

The HX approximation assisted optimization approach described above was used to design air-to-water HXs for 2 different applications: car radiator and room air heating. The HX design is based on NGHX-13 segment design shown in Figure 2. NGHX-13 segment can be geometrically defined based on the port inner diameter, horizontal and vertical spacing, number of ports per tube, tube stagger offset and port thickness. In the current optimization study, the segment HTC and air-side pressure drop (ΔP_{air}) were correlated to the port inner diameter, horizontal spacing, vertical spacing, number of ports per tube, the inlet air velocity, and stagger offset as shown in Figure 49. The design space is summarized in Table 14. The port thickness was kept constant at 10% of the D_{out}.

7.3.1. Car radiator design optimization

The work of (Kelly et al. 2002) presented an optimized novel HX concept geometry for a car radiator application. In their work, the optimized micro crossflow HX designs were compared against conventional tube-fin and flat-tube HXs designs from literature. The current study follows the same optimization problem definition for HXs built using NGHX-13 segments. Pareto optimum designs were compared to optimized designs from (Kelly et al. 2002) and conventional designs.

This design problem assumes water and air inlet temperatures of 368.15 K and 293.15 K respectively. The airside and refrigerant side pressure drop were constrained by a maximum value of 175 Pa and 5 kPa respectively. The water temperature drop through the heat exchanger was also constrained between 5 and 10 K. An additional constraint was used for NGHX-13 to maintain a HX aspect ratio (tube length to HX height ratio) between 0.25 and 4.0. The objective of this study was to maximize heat transfer per unit of HX face area, HX volume, and HX material weight. This problem can be summarized as shown in equation (50)

$$
\begin{aligned}
&\underset{x}{\text{maximize}} && Q / A_{\text{face}} \\
&\underset{x}{\text{maximize}} && Q / V_{\text{HX}} \\
&\underset{x}{\text{maximize}} && Q / M_{\text{material}} \\
&\text{subject to:} && \Delta P_{air} \le 175\,\text{Pa} \\
& && \Delta P_{water} \le 5\,\text{kPa} \\
& && 5\,\text{K} \le T_{water,in} - T_{water,out} \le 10\,\text{K} \\
& && 0.25 \le \frac{L}{N_t \times VS} \le 4
\end{aligned}
\tag{50}
$$

7.3.2. Room heating coil design optimization

The second HX optimization problem involved a 1 kW heating coil design. Water inlet temperature was assumed to be 350 K with a mass flow rate of 0.025 kg/s whereas the air inlet temperature was assumed at 300 K at air mass flow rate of 0.035 kg/s. The baseline HX design (Huang 2008) used for comparison in this study is a microchannel HX with 22 port per tube and 18 louver fins per inch.

Both Aluminum and polymers were sought as possible materials to manufacture NGHX-13 tubes. The objective of this study was to minimize the airside

pressure drop (reducing fan power and running costs) while maximizing the heat transfer per unit HX volume. In this optimization study, the airside pressure drop was constrained to 100 Pa whereas the water side pressure drop was constrained to a maximum value of 1 kPa. In addition, the HX heat duty was constrained between 1000 and 1050 kW, the HX volume was constrained by a maximum value of 240 cm^3 (baseline HX volume) and the HX aspect ratio was constrained between 0.25 and 4.0. This optimization problem can be summarized as shown in equation (51).

$$\begin{aligned} &\underset{x}{\text{minimize}} && \Delta P_{air} \\ &\underset{x}{\text{maximize}} && Q / V_{\text{HX}} \\ &\text{subject to:} && \Delta P_{air} \le 100\,\text{Pa} \\ & && \Delta P_{water} \le 1\,\text{kPa} \\ & && 0.25 \le \frac{L}{N_t \times VS} \le 4 \\ & && 1000\,\text{W} \le Q \le 1050\,\text{W} \\ & && V_{\text{HX}} \le 240\ \text{cm}^3 \end{aligned} \tag{51}$$

Table 14: Enhanced HX segment design space

Parameter	*Range*	*Unit*
D_{in}	0.2 – 0.7	mm
Horizontal Spacing	1.5 – 6.0	D_{out}
Vertical Spacing	2.0 – 4.0	D_{out}
Number of Ports	3 – 19	-
Air velocity	0.5 – 3	m/s
Offset	0 – 1	HS

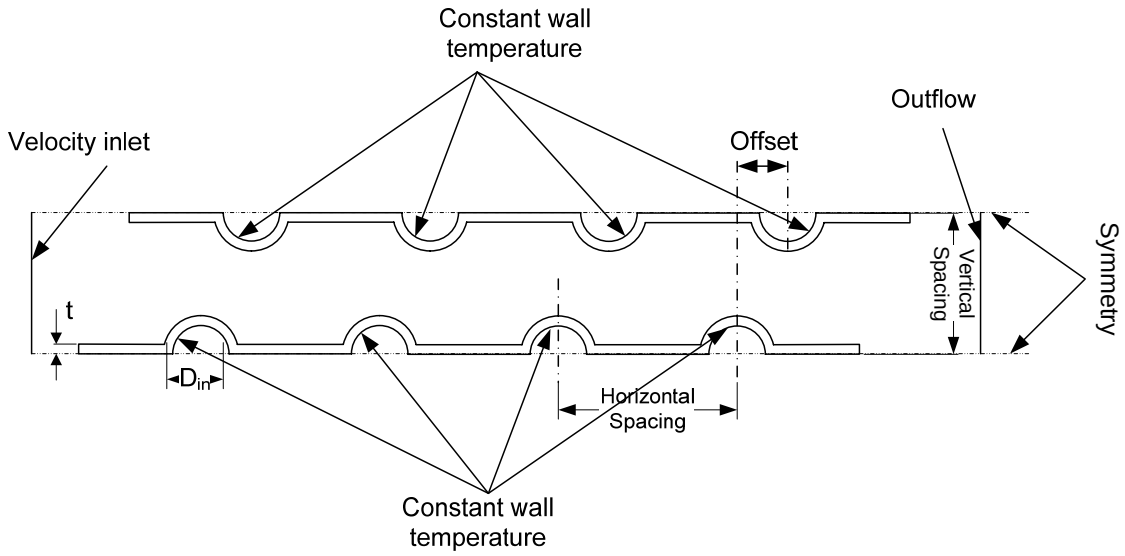

Figure 49: HX segment computational domain showing boundary conditions and geometrical parameters

7.4. Results

In order to develop HTC and ΔP_{air} metamodels, the approximation approach was employed to sample the design space. The DOE designs were based on 200 initial designs using MED and an additional 201 designs using multiresponse SFCVT for HTC and ΔP_{air}. The PPCFD simulation tool described in section 4.3.1 was used to evaluate the heat transfer and pressure drop for those 401 DOE designs as well as an additional 500 random designs for verification purposes. The ΔP_{air} metamodel for the aluminum heat coil and the car radiator design problems showed poor performance when compared against the random sample. Hence an additional 100 sample where generated using the single response SFCVT approach with 1 point at a time. The developed metamodels for airside HTC and ΔP_{air} were then used along with the macro-scale HX simulation tool described in section 4.3.2 to model the performance

of the entire HX (i.e. to evaluate the outlet flow conditions, HX heat duty, volume, material, and pressure drop).

7.4.1. Approximation results

Prior to any optimization study, the airside HTC and ΔP_{air} metamodels need to be verified. As such the predictions from the metamodels generated using the DOE designs were compared against the function evaluations for the 500 random designs. The following subsections summarize the metamodel parameters and verification results for each of the 2 design problems mentioned earlier.

For the car radiator design, HTC and ΔP_{air} metamodels for the NGHX-13 geometry were developed based on 501 sample points: 200 initial MED samples, 201 MSFCVT samples, and 100 additional SFCVT samples based on ΔP_{air}. Metamodels were generated using Kriging with a second order polynomial regression and an exponential correlation function. HTC and ΔP_{air} metamodels for the aluminum heating coil design problem were also developed using 501 sample points with similar DOE to that of the car radiator problem. The aluminum heating coil metamodels were generated using Kriging with a second order polynomial regression and an exponential correlation function. Finally, the HTC and ΔP_{air} metamodels for the polymer heating coil design problem were developed based on 401 sample points: 200 initial MED samples and 201 MSFCVT samples. The polymer heating coil metamodels were generated using Kriging with a first order polynomial regression and an exponential correlation function. The metamodel performance metrics for the 3 cases are summarized in Table 15 and Table 16 for ΔP_{air} and HTC respectively.

Table 15: Airside pressure drop metamodels performance summary

Design Problem	RMSE (Pa)	MAE (Pa)	RRMSE	RMAE	MAS
Aluminum heating coil	0.69	5.50	4.0%	22.0%	98.4
Polymer heating coil	1.08	9.30	5.4%	23.8%	94.8
Car radiator	0.71	5.55	4.1%	17.8%	98.8

Table 16: Airside heat transfer coefficient metamodels performance summary

Design Problem	RMSE (W/m^2K)	MAE (W/m^2K)	RRMSE	RMAE	MAS
Aluminum heating coil	2.29	12.09	2.4%	13.1%	99.6
Polymer heating coil	1.79	10.24	2.9%	13.9%	99.4
Car radiator	2.73	18.58	2.8%	14.8%	99

7.4.2. Multi-objective optimization results

The optimization results for the design problems mentioned above are presented in forms of Pareto solution sets. For each of the design problems, the baseline is identified for comparison and relative performance improvement is identified.

Car radiator design optimization results

The car radiator design optimization results showed a tradeoff between heat transfer per unit HX face area and heat transfer per unit volume and mass as shown in Figure 50 and Figure 51 respectively. NGHX-13 optimum designs dominate all conventional designs (tube fin 1 row, 2 rows and flat tube designs) as well as the poly methyl methacrylate (PMMA) micro crossflow design of (Kelly et al. 2002). However, aluminum and ceramic optimized micro crossflow HX designs of (Kelly et al. 2002) provided higher heat transfer density but at a much lower heat transfer per

unit face area. Hence, these designs did not dominate any of the NGHX-13 Pareto designs. At heat transfer per unit face area values of 23.4 W/cm^2, optimized NGHX-13 design yielded heat transfer density of 19.4 W/cm^3; more than 10 folds increase compared to 1.5 W/cm^3 for conventional designs.

The tradeoff in heat transfer per unit material weight shown in Figure 51 depict that Pareto solution from the optimization study dominates all baseline designs including the polymer micro crossflow design of (Kelly et al. 2002). It is also important to notice that there was no conflict between maximizing heat transfer per unit volume and maximizing heat transfer per unit material mass for NGHX-13. NGHX-13 optimized design for a heat transfer per unit area of 23.4 W/cm^2 has a heat transfer per unit material weight of 58 W/g providing more that 17 times the heat transfer per unit material weight of conventional designs. NGHX-13 optimization did not result in any designs with Q/A_{face} less than 11.75 W/cm^2. However, even at larger Q/A_{face}, NGHX-13 yielded higher performance than all micro crossflow HX designs in terms of heat transfer per unit material weight.

Designs corresponding to extreme Pareto solutions for NGHX-13 and all baseline designs discussed earlier are summarized in Table 17. The optimum solution corresponding to maximum heat transfer per unit volume and material weight required a modest pressure drop (38 Pa) to drive the air across the heat exchanger and comparable water pressure drop of 3.5 kPa. The design corresponding to the maximum heat transfer per unit face area resulted in a higher airside pressure drop of 169 Pa; however, this value is less than the pressure drop exhibited in baseline designs. the water side pressure drop for both cases (3.5 kPa and 3.8 kPa) is less than

the pressure drop of the designs by (Kelly et al. 2002); yet higher than other conventional baseline designs.

Aluminum heating coil design optimization results

The aluminum heating coil design optimization problem results in tradeoff between airside pressure drop and heat exchanger volume as shown in Figure 52. All Pareto optimum solutions dominated the baseline design. For the same airside pressure drop of the baseline design, NGHX-13 provides a design with 61% HX volume reduction and 84% material volume reduction compared to the baseline HX. The other extreme of the Pareto solution performance resulted in a 95% reduction in airside pressure drop with 69% reduction in material volume. This extreme provides modest volume reduction of only 5%. All Pareto optimum results had an inner port diameter ranging from 0.367 to 0.433 mm (minimum port diameter is 0.2 mm) with a horizontal port spacing ranging from 0.69 to 1.29 mm and vertical tube spacing ranging from 0.92 to 1.33 mm. Pareto solutions had a wide variation in inlet air velocity from 0.84 to 2.88 m/s. The HX volume minimization objective forced the results towards the smallest possible vertical spacing that satisfies the airside pressure drop constraint.

Polymer heating coil design optimization results

The polymer heating coil design optimization problem results in tradeoff between airside pressure drop and heat exchanger volume as shown in Figure 53. All Pareto optimum solutions dominated the baseline design. Based on these optimization results, polymer NGHX-13 tubes can result in designs that provide 48% HX volume reduction with a 79% material volume reduction for the same airside pressure drop compared to the baseline HX performance. The reduction in HX material weight is

92% due to the difference in material density of polymer and Aluminum (baseline). The other extreme of the Pareto solution resulted in a 76% reduction on the airside pressure drop with a 70% reduction in material volume (89% reduction in material weight) with only 7% reduction in HX volume. All Pareto optimum results had an inner port diameter ranging from 0.333 to 0.4 mm with a horizontal port spacing ranging from 0.625 to 1.02 mm. As for the aluminum heating coil optimization results, the vertical spacing was limited by the HX minimization objective and varied only between 0.92 and 1.12 mm. The inlet air velocity varied from 1.6 to 2.81 m/s which is a smaller variation interval compared to the aluminum heating coil optimization results since higher HTC is required to overcome the higher conduction heat transfer resistance due to the low thermal conductivity of the polymer material specified.

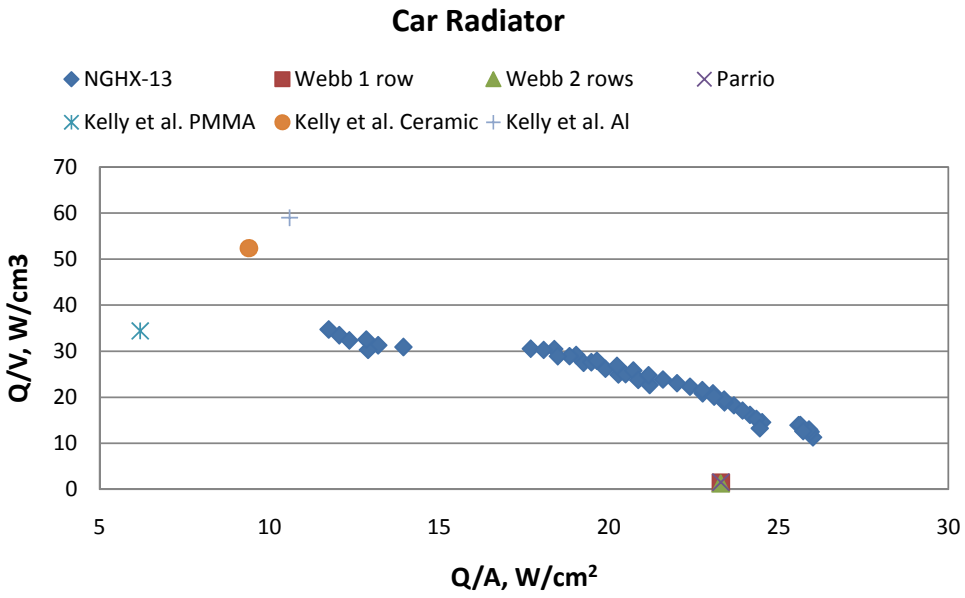

Figure 50: Tradeoff between heat transfer per unit volume and heat transfer per unit HX face area

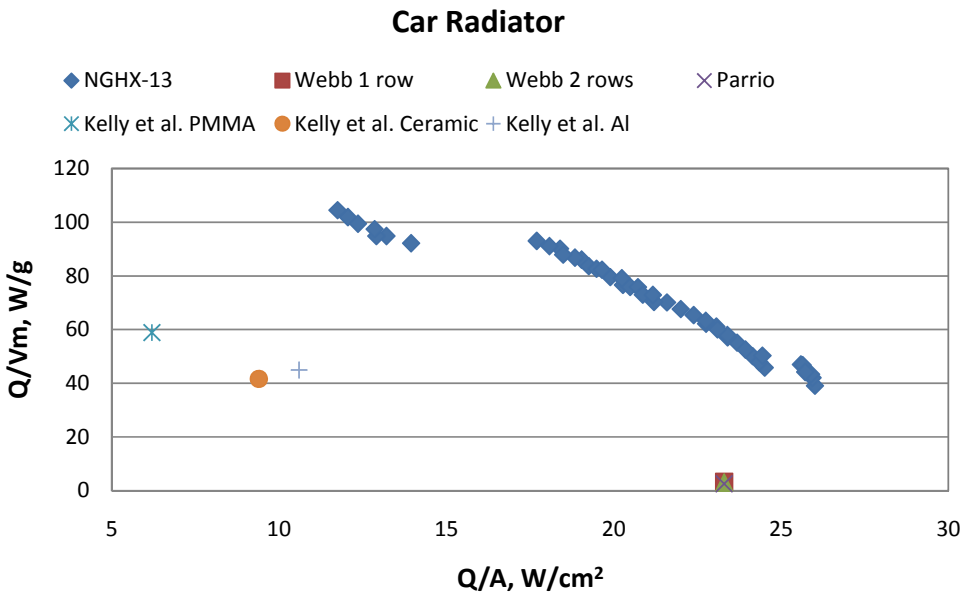

Figure 51: Tradeoff between heat transfer per unit material mass and heat transfer per unit HX face area

Table 17: Extreme optimization results performance comparison with baseline designs

HX design	Q/V, W/cm^3	Q/A, W/cm^2	Q/m, W/g	ΔP_{air}, Pa	ΔP_{water}, Pa
Webb 1 row	1.41	23.3	3.29	179	1.65
Webb 2 rows	1.26	23.3	2.93	204	7.45
Parrio	1.53	23.3	2.55	179	2.5
Kelly et al. PMMA	34.4	6.2	58.9	175	5
Kelly et al. Ceramic	52.4	9.4	41.6	175	5
Kelly et al. Al	59	10.6	44.9	175	5
NGHX-13 max Q/A	11.3	26.0	39.1	169.2	3.8
NGHX-13 max Q/V, max Q/m	34.7	11.8	104.4	34.8	3.5

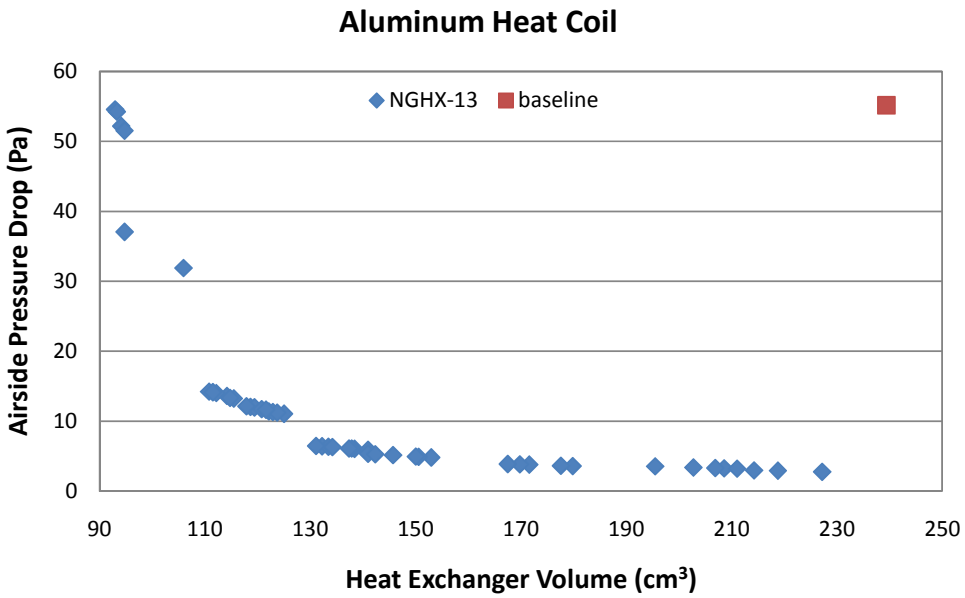

Figure 52: Tradeoff between airside pressure drop and heat exchanger volume for the Aluminum heating coil design optimization problem

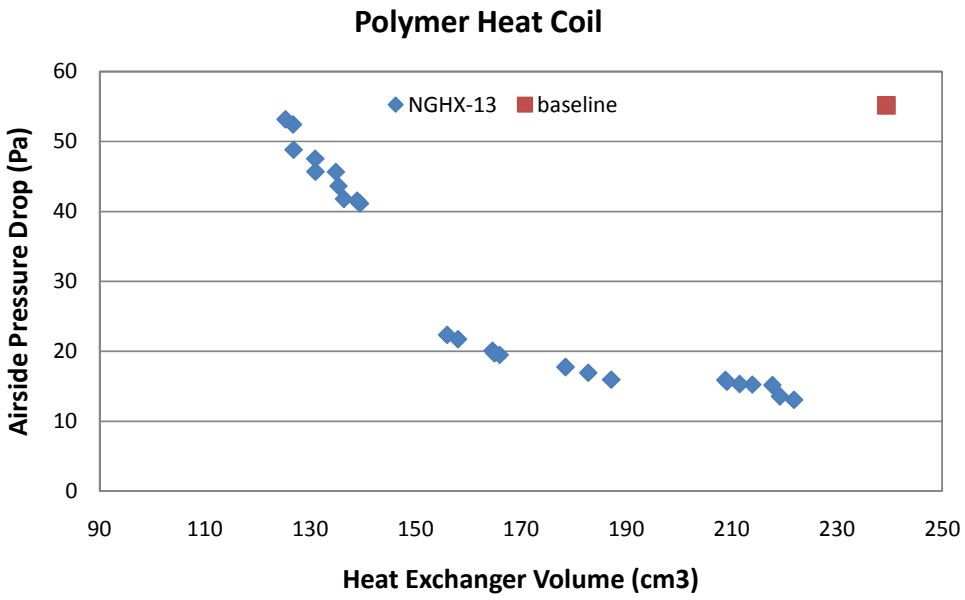

Figure 53: Tradeoff between airside pressure drop and heat exchanger volume for the Polymer heating coil design optimization problem

7.4.3. Pareto solutions verification

To further verify the accuracy of the proposed approach, all Pareto solutions were verified with CFD simulations for segment airside thermal and hydraulic performance. The overall HX performance was then re-calculated. The resulting percentage errors in the predicted air side pressure drop and heat transfer coefficients are summarized in Table 18. These results suggest the metamodel performance was adequate for the optimization studies. The low pressure drop metamodel performance in the case of the car radiator design problem is due to the fact that the optimization routine tends to push the solution towards a larger air velocity range. In these cases, the metamodel yield an over predicted pressure drop compared to CFD simulations as shown in Figure 54 where the solid lines represent a ± 10% error bounds.

Table 18: Pareto optimal designs verification results

		RMSE	MAE	RRMSE	RMAE	MAS
Aluminum heating coil	ΔP_{air}	0.66	1.44	5.02%	9.68%	100
	HTC	2.49	4.01	2.15%	3.22%	100
Polymer heating coil	ΔP_{air}	1.73	4.28	4.79%	8.80%	100
	HTC	2.08	3.36	2.25%	3.50%	100
Car radiator	ΔP_{air}	8.82	19.18	10.38%	16.67%	54.3478
	HTC	7.5	9.97	4.10%	5.44%	100

The use of CFD based HTC values to estimate the heat load from the Pareto optimal designs yielded marginal errors. In the case of the car radiator designs the errors were between -0.14% and 2.7%. The errors in the aluminum heating coil

design varied between -0.4% and 1.7% whereas the errors in the heat load prediction for the Pareto solutions of the polymer heating coil ranged from -1.01% an 1.7%. These marginal errors in heat transfer prediction suggest that the metamodels provided an acceptable performance during the optimization studies.

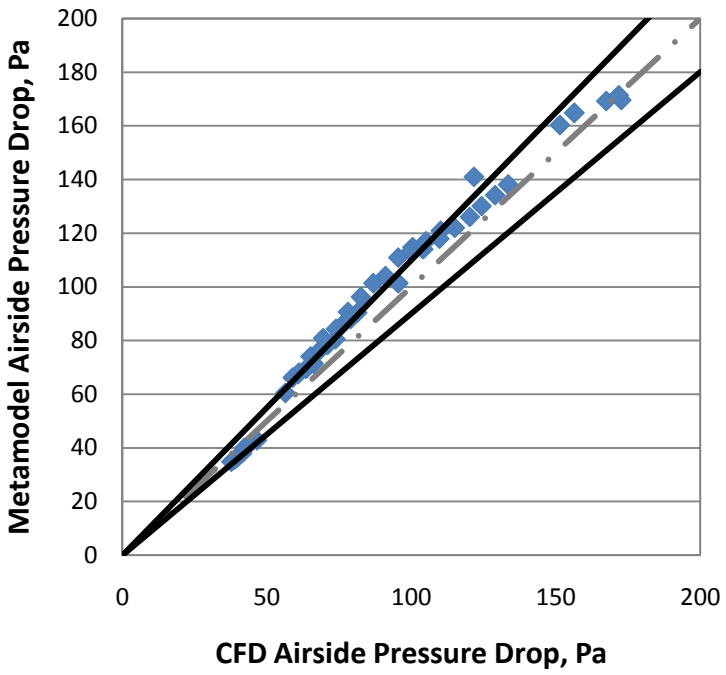

Figure 54: Comparison between CFD and metamodel prediction for the airside pressure drop for the Pareto solution set of the car radiator problem

7.5. Design Considerations

The following design guidelines are developed based on the results from NGHX-13 design and optimization studies presented hereinbefore:

- Port inner diameter selection is largely dependent on the refrigerant-side pressure drop constraint.

- In the car radiator design problem, the pressure drop constraints of 5 kPa resulted in Pareto optimum solutions having small variations in port inner diameter from 0.233 to 0.3 mm.
- In the heating coil optimization problem, the pressure drop constraint of 1 kPa which resulted in Pareto optimum solutions having port inner diameters varying from 0.37 to 0.43 mm. This indicates that the optimization routine was not able to find feasible solutions for smaller port diameter tubes which are of superior thermal performance.

- Heat transfer surface augmentation is proportional to the value of the horizontal spacing. Although larger horizontal spacing results in boundary layer restarting, the heat transfer is only enhanced from the boundary layer restarting point onwards. This resulted in an overall reduction in heat transfer coefficient.
  - Optimum solutions tend to use small horizontal spacing
  - Slightly higher horizontal spacing is required for cases with lower airside pressure drop. In these cases, the horizontal spacing is used to provide additional heat transfer surface due to larger vertical spacing and lower velocities.
- Higher pressure drop is experienced in cases with of high velocity, long horizontal spacing and small vertical spacing.
- The number of ports for each of the designs is dictated by the energy balance. The designs with lower HTC cannot accommodate larger number of ports due

to the balance between the airside and water side flow rates. For these designs more tubes with longer length are required to fulfill the same heat duty.

7.6. Summary

A new approach for novel HX concepts approximation assisted optimization is presented. This approach integrates the SFCVT adaptive DOE technique, along with multi-scale heat exchanger simulation approach to optimize new heat exchanger geometry. The approximation technique resulted in a significant reduction in computational time compared to conventional optimization techniques: for the car radiator design problem 501 CFD simulations were required for metamodel development, 500 CFD simulations were used for metamodel verification and 47 CFD simulations were used for Pareto solutions verification compared to 25500 function evaluation required during optimization (1048 CFD simulation versus 25500 function evaluation without approximation ~ 95.9% reduction). The metamodel verification study showed acceptable performance which was also demonstrated through the verification of the Pareto solutions.

The heating coil optimization study using both aluminum and polymer as the materials for NGHX-13 tubes resulted in a significant performance improvement over the baseline design. The extremes of the Pareto solutions for both HXs are presented in Table 20 below.

Table 19: Heating coil Pareto extreme designs performance improvement over baseline design

	% volume reduction	% ΔP_{air} reduction	% material weight reduction
Aluminum Heating coil, maximum Q/V	– 61%	– 1%	– 84%
Aluminum Heating coil, minimum ADP	– 5%	– 95%	– 69%
Polymer Heating coil, maximum Q/V	– 48%	– 4%	– 92%
Polymer Heating coil, minimum ADP	– 7%	– 76%	– 89%

The findings presented hereinbefore suggest that approximation assisted optimization of heat exchangers using multi-scale simulation approach is an efficient way to investigate new geometries. The tool presented in this chapter can help in streamlined evaluation of new geometries and identifying their application potential. The optimized designs can be prototyped and tested in wind tunnels to prove the improvement potential. Such an effort is presented in Chapter 9.

Chapter 8: Approximation Assisted Optimization for A-Type Heat Exchangers

A-Type heat exchangers are used to meet required heat load with minimum duct dimensions in air-conditioning applications. This greatly reduces the air-conditioning system footprint in residential and commercial applications. This chapter presents an effort to minimize the material costs and the enclosure volume of A-type HXs. This optimization problem requires accurate prediction of heat transfer and pressure drop of A-type HXs. Existing air side heat transfer and pressure drop correlations may not be applicable for A-type heat exchangers due to non-uniform air velocity profile and temperature distribution at the HX inlet. As such the approximation assisted optimization technique incorporating the multi-scale simulation tool is implemented as discussed in Chapter 7. This chapter starts by an introduction about the relevance of A-type HXs and the need for the approximation assisted optimization techniques followed by the details of the modeling approach and the definition of the design optimization problem. The chapter concludes with a summary of the main findings.

8.1. Introduction

Most residential air conditioning applications employ an A-type HX (A-coil) for indoor air conditioning. This coil serves as an evaporator in air conditioning mode and a condenser in heat pumping mode. Currently, the air-to-water HX industry is still lagging in the development compared to electronics cooling due to challenges imposed by the air side. However, sustainable development requires designing HX

with improved efficiency and reduced material utilization. Design optimization presents an effective technique to address these challenges; only if accurate models exist with adequate computational expenses.

Available heat exchanger models employ an air velocity/flow profile at the coil face, and assume it is propagated through the coil, perpendicular to tube banks, e.g., (Domanski 1991, Liang et al. 2001, Liu et al. 2004, Jiang et al. 2006, Oliet et al. 2007, Singh et al. 2008). Simulation of A-type HXs presents a unique challenge as air inlet through the duct is not perpendicular to the coil face. Early air flow visualization experiments for various coil slab configurations and angles (Chwalowski et al. 1989) indicated that the air velocity is predominantly perpendicular to the coil face. This key result has been widely used as a fundamental assumption in several validated heat exchanger simulation tools. However, recent particle image velocimetry studies (Domanski and Yashar 2007) demonstrated air flow maldistribution inside the coil. The air maldistribution affects the coil performance greatly; hence accurate models are crucial for reliable optimization. To accurately model A-type HXs, CFD simulations are required to estimate the air inlet velocity profile as well as the air flow propagation within the HX.

The complexity of the A-type HX simulation warrants the use of advanced simulation tools such as the multi-scale HX simulation tool suggested in Chapter 4. Fins play an important role in the determination of the air flow dynamics. Hence, the periodic computational domain should include the fins as well as the tubes. As such, the computational domain can not be reduced to 2D CFD simulations. This results in a prohibitive computational expense for an optimization study. The use of

approximation assisted optimization, as discussed in Chapter 7, provides a solution for computational savings and allows for the use of accurate simulations during the optimization study.

8.2. Modeling Approach

Accurate evaluation of A-type HX performance requires the knowledge of the inlet air profile and the air flow propagation patterns within the HX. These profiles depend on the coil inclination angle as well as tube vertical and horizontal spacing. Furthermore, the airflow propagation through the coil is not normal to the face area as in conventional heat exchanger designs, which means that the airside heat transfer coefficient correlations for airflow across a tube bank might not be valid. Nevertheless, the inclination of the coil and the top plate position, shown in Figure 55, could lead to a recirculation region that penalizes some of the top tubes' performance for a down flow configuration.

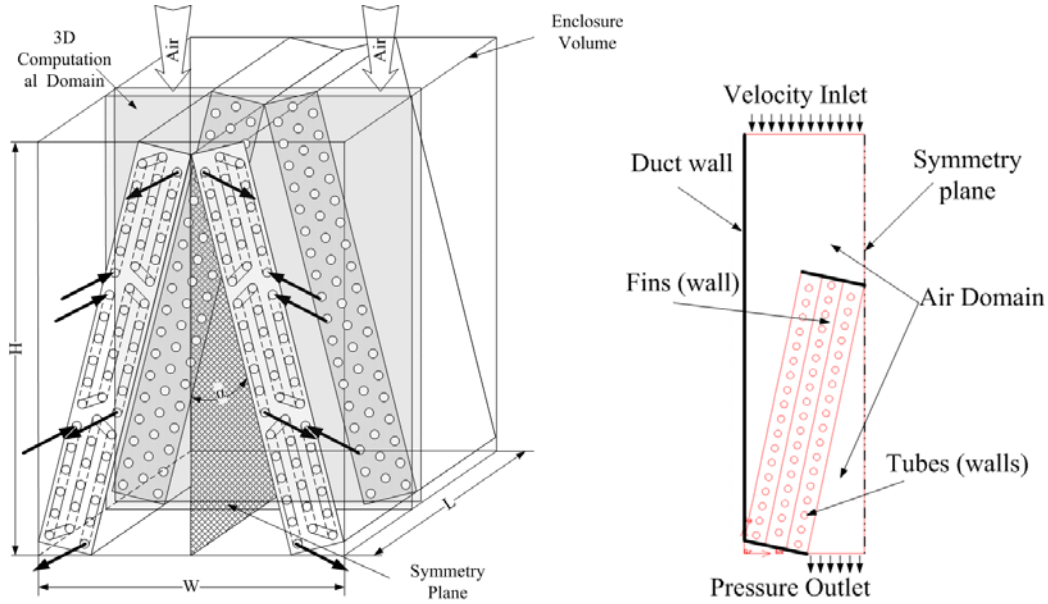

Figure 55: A-type HX configuration and computational domain

CFD simulations were used to more accurately evaluate the airside velocity distribution and heat transfer coefficients for each tube. The approach implemented here follows the same framework presented in Figure 47 except for the use of MED DOE techniques instead of adaptive techniques. The multi-scale simulation implementation is based on the flow chart presented in Figure 48. Mesh generation, CFD simulations and post processing were automated using PPCFD. Details of mesh generation and CFD simulations are discussed in the following sections. The macro-scale HX simulation is based on the work of (Jiang et al. 2006). The approximation assisted optimization follows the same approach presented in Chapter 7 except for the DOE step which was performed using only MED.

8.2.1. Geometry and mesh generation

Following the PPCFD approach, a code was developed to generate Gambit® journal file based on initial MED designs. The geometry was generated as a function of the values of α, HS and VS and the fin spacing. Triangular pave mesh was used to mesh the fin area first, and then the triangular mesh was extruded in Z direction to discretize the air flow domain on both sides of the fin. A sample mesh using the automatically generated Gambit® journal file is shown in Figure 56 depicting the fine mesh near the walls and the quadrilateral inflated mesh in the vicinity of tubes. The boundary conditions listed in Figure 55 are used to define all computational domain boundaries as well as the different wall interfaces within the computational domain.

8.2.2. CFD simulations and post processing

The automated Fluent® script generator was developed such that it accounts for the design variables in assigning the inlet air velocities. The inlet velocity for each

case is calculated as shown in equation (52) taking into account the coil dimensions. The inlet air temperature was kept constant for all cases at 294.15 K. Tubes' wall temperatures were set to the saturation temperature (317.15 K) based on the inlet refrigerant pressure. Preliminary investigations indicated that the RNG k-ε model provides the highest stability and best convergence. Therefore, it was used for the turbulent closure equations. The Fluent® built in two-layer model with enhanced wall treatment was enabled including the pressure gradient and thermal effects in the boundary layer for improved solution of the viscosity affected region. The Green-Gauss Node-Based gradient evaluation was used for a better representation of the unstructured mesh solution. Second order discretization scheme was used for pressure, momentum and energy equations while first order upwind scheme was used for the k and ε equations. The air properties are evaluated using REFPROP 8 (Lemmon et al. 2007). The solver was allowed to iterate up to 1000 iterations or until a convergence was achieved. Convergence criteria were based on minimum acceptable residuals of 10^{-3} for all equations except the energy equation which was set to 10^{-6}.

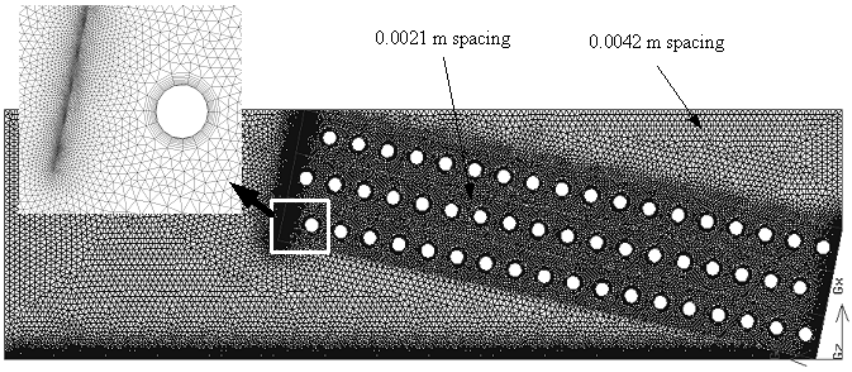

Figure 56: Sample mesh from automated mesh generation scripts

$$V = \frac{0.284}{L \times \left[18.5VS \sin(\alpha) + 3HS \cos(\alpha) \right]} \tag{52}$$

Post processing CFD simulations required the values of mass flow rate, inlet temperature, outlet temperature, and total heat transfer rate for each tube. Hence, these values were written to a temporary file for each tube control volume. The inlet velocity profile is estimated based on the mass flow rate distribution at the coil face. On the other hand, for each tube, the heat transfer coefficient is calculated based on the total tube heat transfer rate, log mean temperature difference and the velocity profile at the coil face. The use of velocity profile at the coil face eliminated the need to track the air flow propagation within the HX since HTC is developed using the same value that is used by the macro-scale ε-NTU solver.

8.2.3. Approximation

The approximation for the problem at hand required the development of 54 HTC metamodels for each tube, 18 metamodels for the inlet velocity profile and a metamodel for the overall pressure drop. This results in a total of 73 metamodel. Adaptive DOE techniques would be prohibitive due to the large number of response data. As such, the classical maximum entropy designs technique was used. For the problem at hand, 182 initial designs were generated using MED. For each design, the 73 responses were evaluated using CFD simulations as discussed earlier. Response data from these designs were then used to develop Kriging metamodels for HTC for each of the 54 tubes, pressure drop and the inlet velocity profile. Metamodels verification involved 48 random designs evaluation using CFD simulations and the developed metamodels.

8.3. Problem Description

The HX design optimization under consideration is for an A-type 10 kW R410A condensing unit application. The baseline design is similar to a conventional A-type HX used in commercially available 10 kW air conditioning systems (Wang 2008) with flat fins instead of louver fins for simplified CFD simulations. The baseline design has a packaging volume of 0.095322 m^3 and provides a heat transfer capacity of 9821.6 W for the boundary conditions shown in Table 20. For these flow conditions, the airside pressure drop is 81 Pa and the refrigerant side pressure drop is 1872.6 Pa.

Table 20: Baseline A-coil boundary conditions

Inlet air flow rate per slab	0.284	m3/s
Inlet air temperature	294.15	K
Inlet air relative humidity	43.46	%
Inlet refrigerant flow rate	0.0212	kg/s
Inlet refrigerant pressure	2.6525	MPa
Inlet refrigerant temperature	345.55	K

The problem at hand is to minimize material cost and packaging volume. The first objective reflects potential savings in final product costs while the second objective reflects the savings in the real-estate footprint of the air conditioning equipment in a typical residential application. Airside pressure drop, heat load and volume constraints are imposed on the optimization problem in order to identify feasible HX designs. The airside pressure drop is constrained to be less than 100 Pa. In order to find heat exchangers with smaller packaging volume than the baseline system, designs with larger packaging volumes are considered infeasible. Finally, all

designs must provide the same heat load as the baseline system, hence only a ± 5% difference from the baseline heat load was allowed.

The optimization variables included in this study are: tube length, slab inclination angle, number of fins per inch, tube horizontal spacing and tube vertical spacing. These variables are defined as continuous variables in the MOGA routine with a bit-length of 4 (16 values) for each variable. Baseline values, range and precision of these variables are shown in Table 21. The MOGA population size was set to 150 with a replacement of 33%, and it was set to run for 200 iterations. This resulted in a total of 10300 function evaluations out of a possible 1048576 (16^5) design combination. During optimization some of the design aspects were kept unchanged (design parameters). The design parameters for the problem at hand are summarized in Table 22. This optimization problem can be summarized as shown in equation (53).

$$
\begin{aligned}
&\underset{HX}{\text{minimze}} \quad Packaging\ Volume \\
&\underset{HX}{\text{minimze}} \quad Material\ Cost \\
&\text{Subject to} \\
&\qquad 0.95Q_{BL} \le Q(HX) \le 1.05Q_{BL} \\
&\qquad Packaging\ Volume(HX) \le Packaging\ Volume_{BL} \\
&\qquad air\ side\ pressure\ drop \le 100\ \text{Pa} \\
&\qquad HX \equiv \left[L \quad \alpha \quad HS \quad VS \quad FPI \right]^T
\end{aligned}
\tag{53}
$$

Table 21: Optimization Variables

Variable	Baseline value	Range	Precision	Unit
Tube Length	0.46	0.3174 - 0.736	0.028	m
Inclination angle (α)	18.5	10 - 40	2	°
FPI	14	9 – 24	1	(–)
HS	0.0205	0.0173 - 0.0346	0.00116	m
VS	0.0265	0.0159 - 0.0448	0.00193	m

Table 22: HX design parameters

Parameter	Baseline value	Unit
Inner tube diameter	0.0094	m
Outer tube diameter	0.0105	m
Tube banks	3	
Number of tube per bank	18	
Fin thickness	0.001	m

8.4. Results

The developed metamodels were verified against 48 random designs in order to ensure accurate modeling during the optimization study. The HTC MAS is shown in Figure 57 assuming acceptable error bound of ± 20%. Lower metamodel performance is experienced in the recirculation regions (tubes: 16 – 18; 33 – 36; 51 – 54). The lower HTC metamodel performance for these tubes did not affect the overall HX modeling accuracy since tubes inside the recirculation region have negligible contribution towards the overall HX capacity. These metamodels can be selectively improved using adaptive techniques or by increasing the number of MED designs. RRMSE and RMAE for the 54 HTC metamodels are illustrated in Figure 58 and Figure 59 respectively. These figures indicate large errors in the recirculation region (near the top of the HX) and poor HTC metamodel performance for the second tube bank.

The pressure drop metamodel shows an RRMSE less than 15% with as RMAE of 35% this is considered an acceptable metamodel since conventional correlations are usually bounded by ± 20% error. The inlet velocity profile metamodels verifications showed that except for the top 2 tubes the RRMSE was less

than 20% while the RMAE was less than 30% for the first 14 tubes. The inlet air velocities at the top tubes are usually very small due to the recirculation region. Hence, their lower metamodel performance will not affect the overall HX performance prediction accuracy.

The MOGA study was conducted based on materials cost per kg based on December 23rd 2008 quotes: 3 $/kg for copper[1] and 1.5$/kg for aluminum[2]. The feasible designs and Pareto optimum set resulting from the approximation assisted optimization are shown in Figure 62. This figure shows that the conflict in the optimization objectives: material cost and packaging volume was limited. Only two designs dominated the entire feasible solutions representing the extremes in either cost savings or packaging volume reductions.

The design parameters and the performance improvements over baseline design are summarized in Table 23. Both optimum designs have a slab inclination angle of 40° and the minimum possible HS of 17.3 mm. Both designs have smaller tube length, HS, VS, and FPI compared to the baseline. The smaller packaging volume design has the shorter tube length and slightly larger VS and FPI compared to the lowest cost design. The increase in FPI is to provide additional heat transfer area to account for the reduction in tube length. The increase in VS was to compensate for the smaller duct size; larger VS allows for large free flow area for the same tube length. This would result in moderate air flow velocity that results in airside pressure drop less than 100 Pa.

[1] http://www.metalprices.com/FreeSite/metals/cu/cu.asp#
[2] http://www.metalprices.com/FreeSite/metals/al/al.asp#

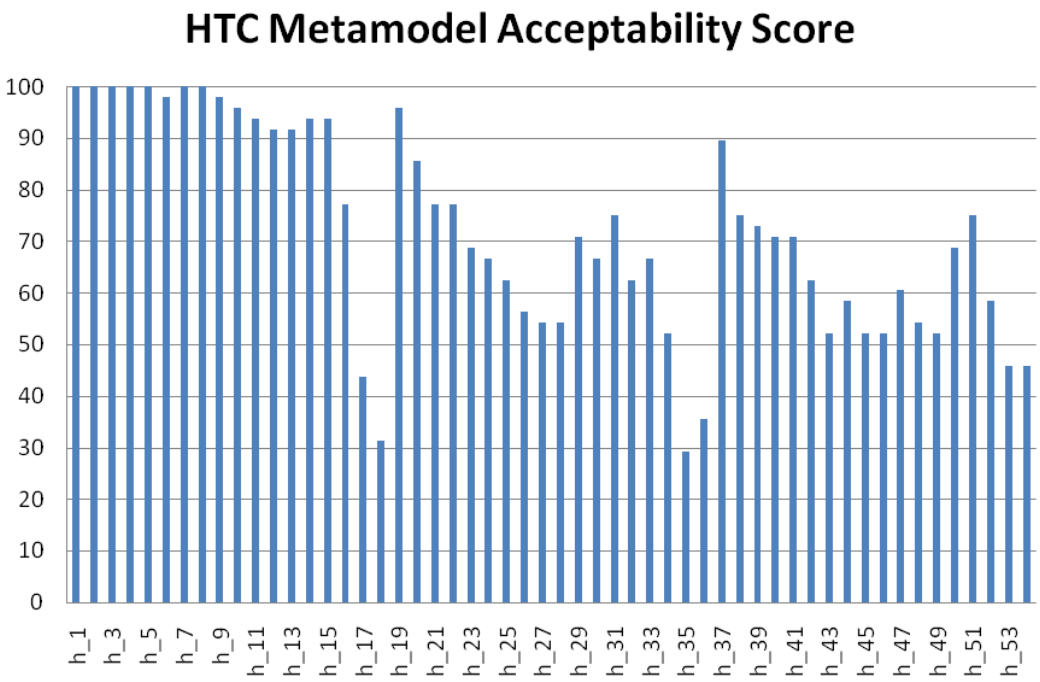

Figure 57: HTC MAS

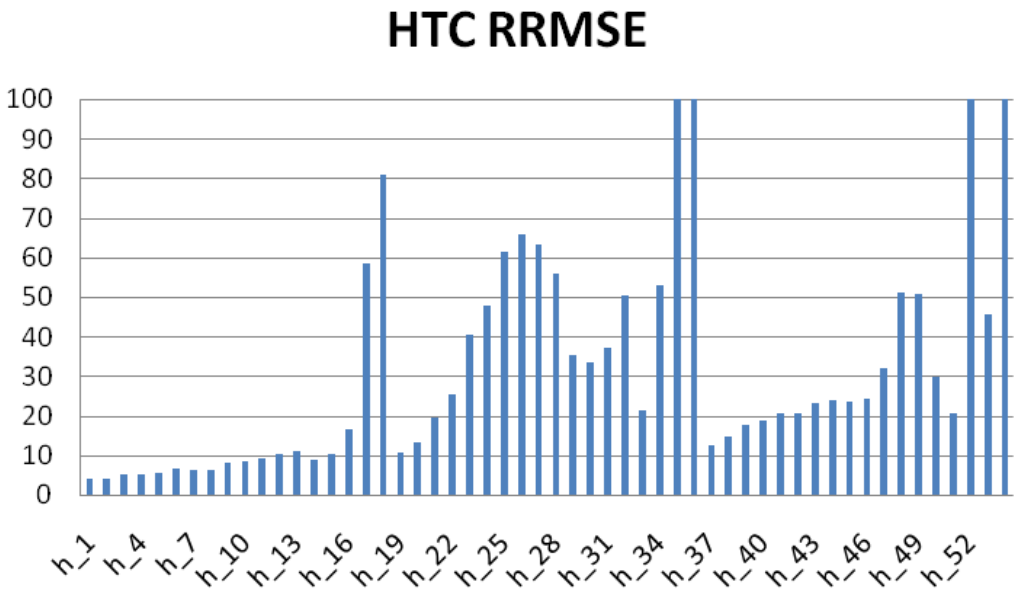

Figure 58: HTC metamodels RRMSE

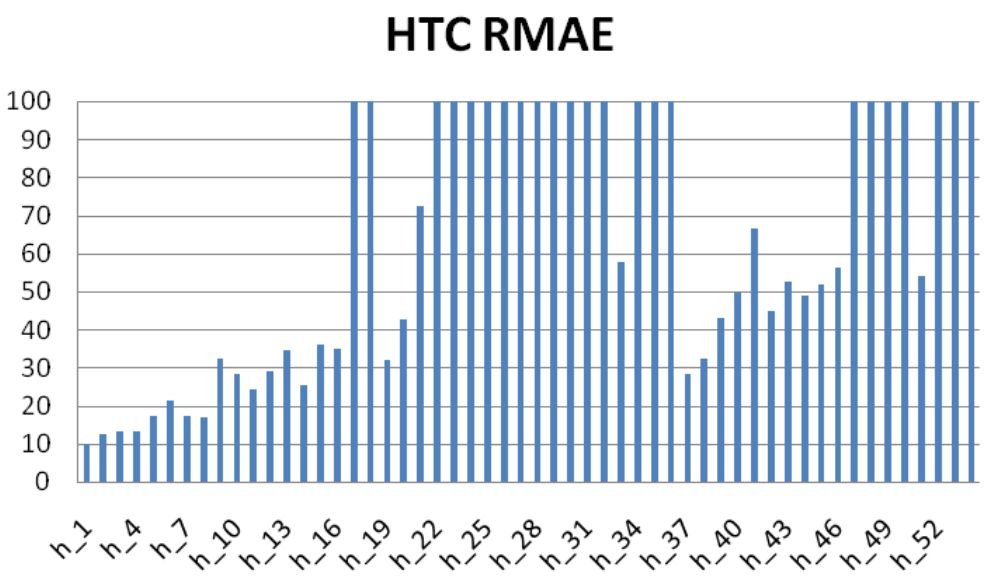

Figure 59: HTC metamodels RMAE

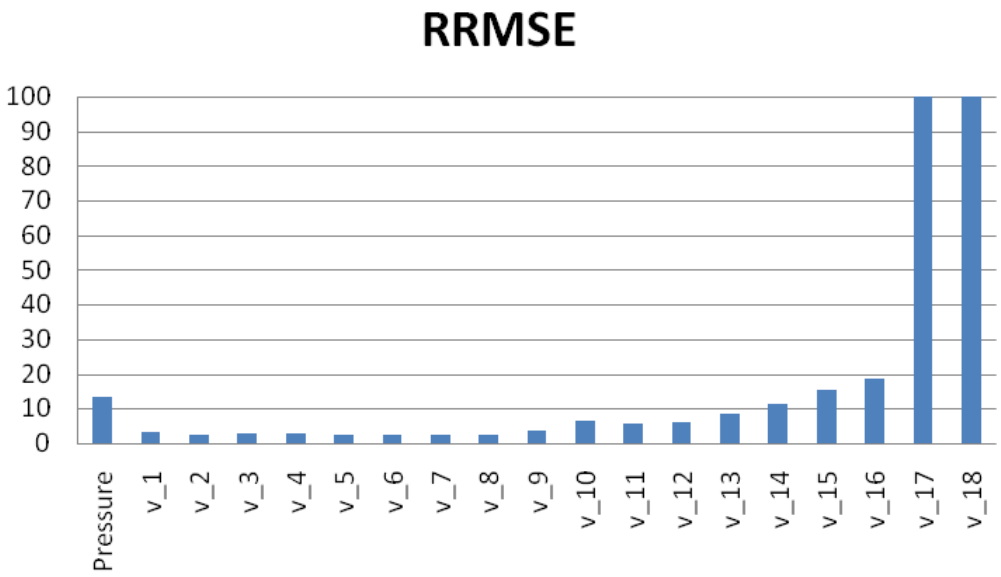

Figure 60: Pressure drop and inlet velocities metamodels RRMSE

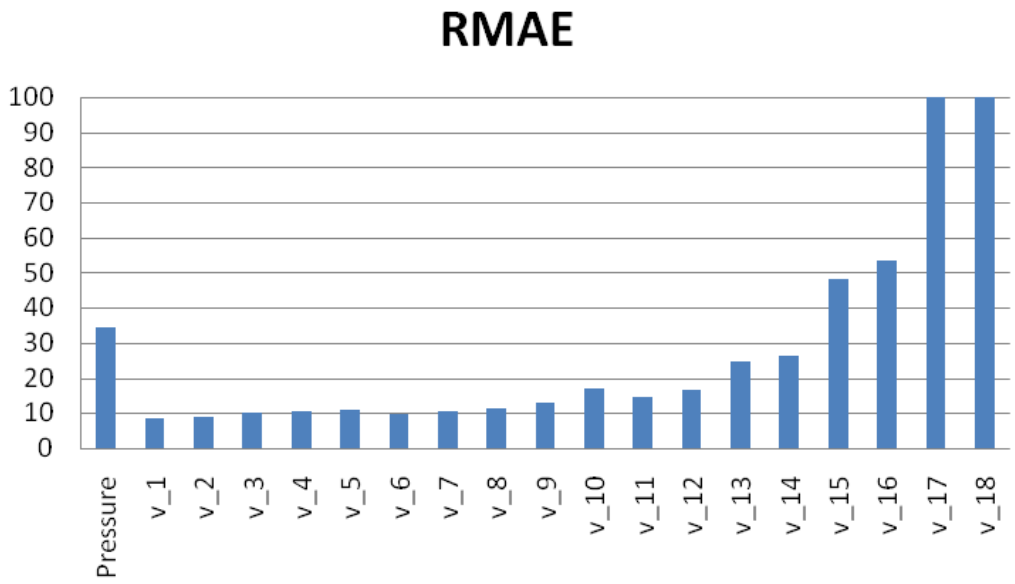

Figure 61: Pressure drop and inlet velocities metamodels RMAE

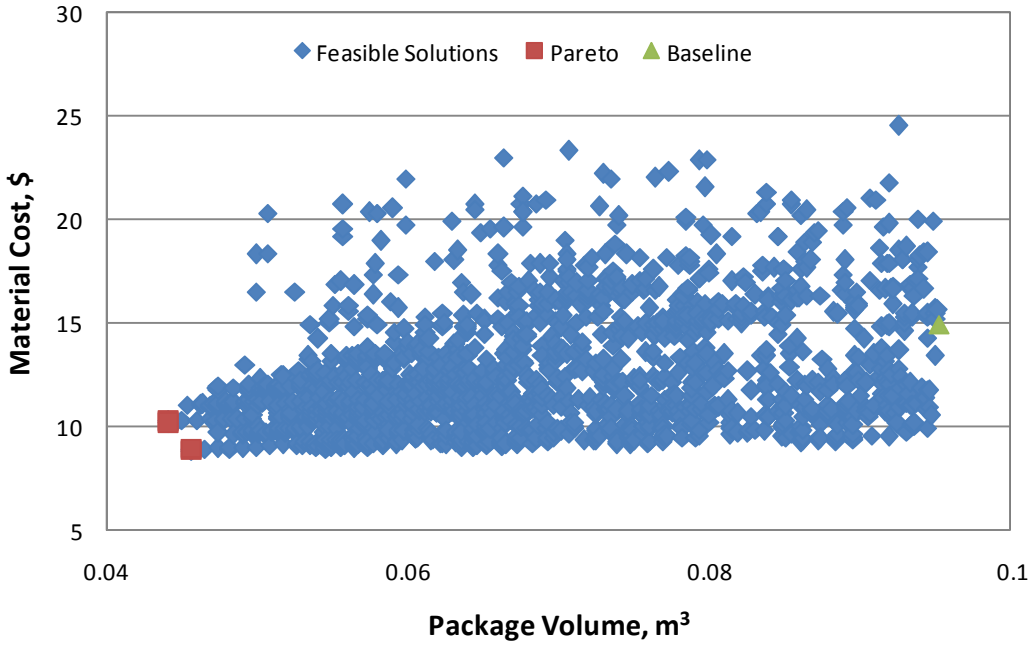

Figure 62: MOGA results for December 23rd 2008 material price quotes

Table 23: Pareto optimum solutions comparison with baseline

Coil No.	α [°]	*HS* [mm]	*VS* [mm]	*L* [mm]	FPI [-]	Volume Savings [%]	Cost Savings [%]
Baseline	18.5	20.5	26.5	460	14	0	0
1	40	17.3	17.8	317.4	11	52.07	29.62
2	40	17.3	15.9	373.2	10	53.66	38.93

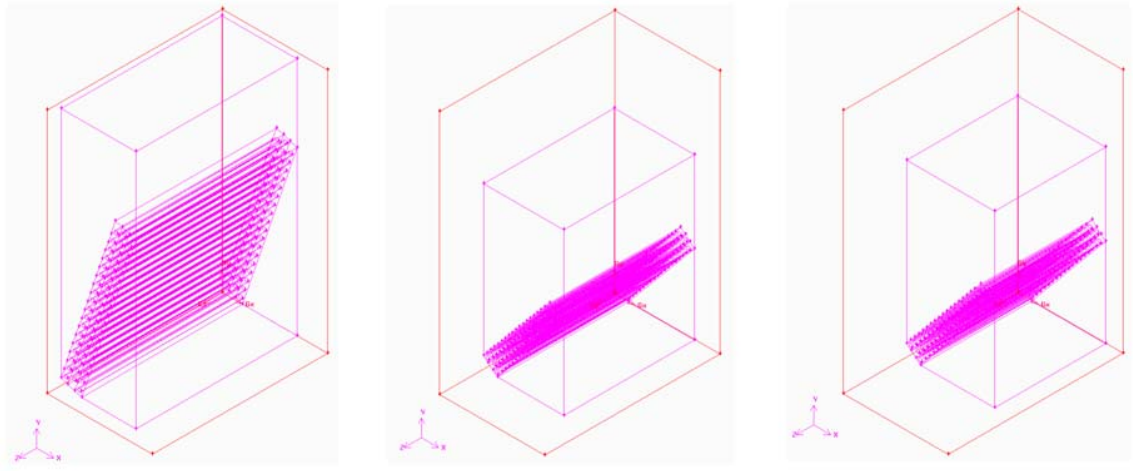

Figure 63: Optimum HX designs compared to the baseline: (a) baseline, (b) lowest material cost design, (c) lower packaging volume design

Another MOGA optimization study was conducted with the updated material prices based on June 24th 2009 quotes: 4.89 $/kg for copper[3] and 1.6$/kg for aluminum[4]. The feasible designs and Pareto optimum set resulting from the approximation assisted optimization are shown in Figure 64. This figure shows that the conflict in the optimization objectives: material cost and packaging volume was more pronounced then in the case of December 23rd 2008 quotes. The Pareto optimum resulting from this study included 7 designs.

[3] http://www.metalprices.com/FreeSite/metals/cu/cu.asp#
[4] http://www.metalprices.com/FreeSite/metals/al/al.asp#

The design parameters and the performance improvements over baseline design for all Pareto solutions based on the June 24th 2009 quotes are summarized in Table 24. These solutions are different than the solution based on December 23rd 2008 quotes. Lowest cost design provided reduction of volume and cost of 22.5% and 35.2% respectively. Smallest volume design provided 48.1% volume savings but at with 22.3% higher material cost. Optimum designs have slab inclination angle varying from 18° to 40° with higher volume savings for smaller slab angle. The *HS* varied from the minimum value of 17.3 mm to 30.01 mm; both design extremes had *HS* equal to the minimum value of 17.3. *VS* varied from the minimum value of 15.9 mm to 23.6 mm. lowest cost design required larger *VS* than smallest volume design in order to maintain an acceptable free flow area. FPI varied from 9 to 17; smallest volume design required larger FPI than the lowest cost designs.

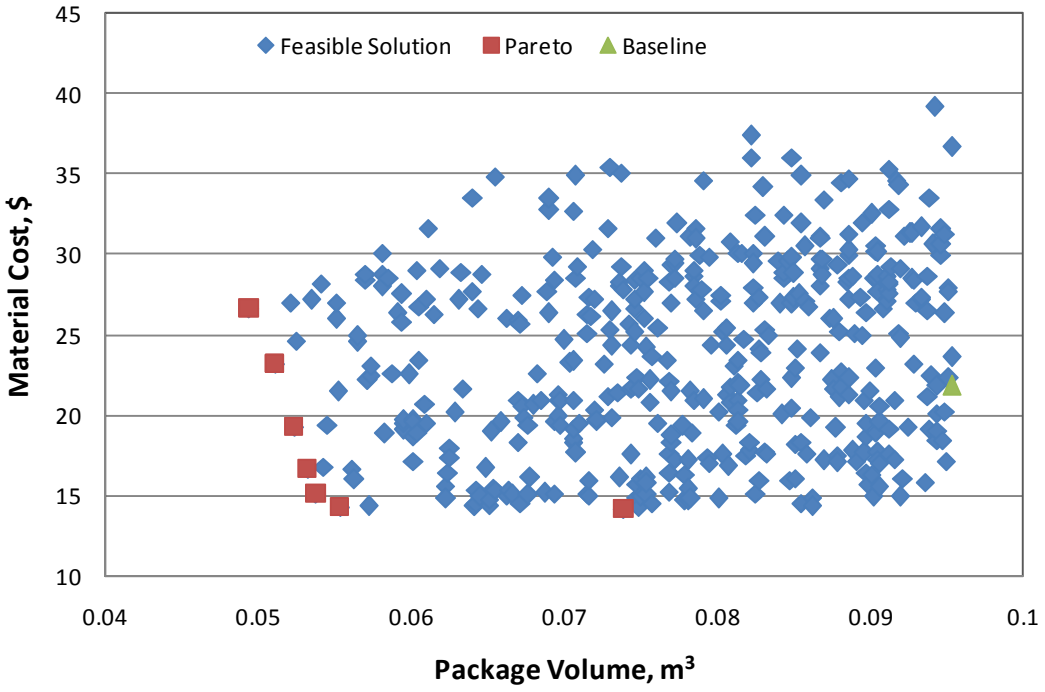

Figure 64: MOGA results for June 24th 2009 material price quotes

Table 24: Pareto optimum solutions based on June 24th 2009 quotes comparison with baseline

Coil No.	α [°]	*HS* [mm]	*VS* [mm]	*L* [mm]	FPI [-]	Volume savings [%]	Cost Savings [%]
Baseline	18.5	20.50	26.50	460.0	14	-	-
1	38	17.28	23.60	317.4	11	22.46	35.17
2	40	30.01	17.83	317.4	9	41.90	34.73
3	38	23.07	17.83	345.3	9	43.56	30.62
4	34	19.60	17.83	373.2	13	44.08	23.69
5	26	17.28	17.83	429.0	16	45.09	11.57
6	18	17.28	17.83	512.7	17	46.37	-6.35
7	18	17.28	15.90	596.5	17	48.10	-22.29

8.5. Summary

The approximation assisted optimization technique was applied to the A-type HX design optimization to minimize enclosure volume and material cost. This technique resulted in significant computational savings; MOGA required only 10300 function evaluations compared to 16^5 for exhaustive search. Furthermore, the approximation technique resulted in 98% reduction in CFD simulations required. The Pareto optimal set based on the December 23rd 2008 material price quotes contained only 2 designs indicating that both objectives selected for this study were not strongly conflicting. The tradeoff between volume and material cost minimization can be summarized as follows:

- Minimum volume design: 54% reduction in volume at 30% cost reduction

- Minimum material cost design: 52% reduction in volume at 39% cost reduction

When material prices were updated for the June 24th material prices quotes, a tradeoff in material cost versus enclosure volume was more pronounced. The Pareto optimum set had 7 designs. Optimization tradeoff showed that 48.1% volume savings could be achieved at 22.3% material cost increase. The other optimization extreme showed that minimum material cost with a cost savings of 35.2% can be achieved with 22.5% volume reduction.

The impact of material prices on the optimization results show that there is a need for robust optimization that is capable of yielding optimum designs that are less sensitive to price variability. The use of the developed approximation assisted optimization technique proved to be very useful since no CFD simulations were required when the material prices were updated. The same metamodels developed for the earlier optimization were used resulting in a significant computational savings.

The results presented in this chapter suggest that current state of the art conventional designs were not fully optimized. This can be seen as an opportunity for HX improvements without major technological innovations. The results show that systematic optimization techniques coupled with accurate HX models are able to provide significant design improvements. The approach presented in this chapter can be further implemented in the optimization of the C-type HXs which are widely used in split air-conditioning systems. Furthermore, it can be used to eventually find the optimum HX structural configuration based on the current technological standards and limitations.

Chapter 9: Experimental Validation

The previous modeling and optimization analyses were verified numerically using systematic techniques adopted from literature. However, such verifications cannot eliminate the need for experimental investigations to validate the developed model. In addition, such an experimental investigation is required to test the optimization results as described in the unified framework presented in Figure 1. The experimental investigation introduces a working prototype and demonstrates potential heat exchanger development. This chapter discusses prototype production, HX test setup and testing procedure, experimental results and a validation for the multi-scale simulation tool.

9.1. HX Prototype Production

A candidate HX prototype was selected from the Pareto optimum set of the heating coil optimization study. This design had 12 ports per tube with port inner diameter of 0.3 mm, *HS* of 0.61 mm and *VS* of 0.915 mm. Several efforts were made to find manufacturing techniques to produce NGHX-13 tubes based on the selected design. For the selected design, port thickness was 0.0375 mm and connecting fins between ports were 0.075 mm. These small material thicknesses pose a great challenge on available manufacturing techniques. Hence it was decided to eliminate the fins that connect the ports especially that the HS was small suggesting no boundary layer restarting along the fin. Furthermore, the bare tube design resulted in only 29.5% reduction in heat transfer area compared to NGHX-13. This loss of heat transfer area does not affect the overall performance greatly as a great portion of the

fin surface of NGHX-13 is accompanied by a recirculation region. Hence, the bare tube design would have a small impact on the HX performance.

Commercially available stainless steel tubing was used with dimensions matching the target design. The closest match were stainless steel tubes with average 0.26035 mm inner diameter and 0.41275 mm outer diameter (27TW 304). Stainless steel tubes were selected since they have higher strength which is important in the initial investigations. Cutting the tubes to the required length was challenging. After several trials with different cutting techniques, it was found that the best approach is to use wire inserts of roughly the same inner diameter and use a fast cutting tool (such as grinding wheel) to cut the tube to the required length. This approach resulted in tubes with burr-free cuts. Cut tubes were examined using 10X magnification lens to control the cut quality. The second step was to manufacture a frame and a header as shown in Figure 65. Afterwards, tubes were carefully inserted through the top pressure plate and a rubber sheet to the HX frame shown in Figure 66. After all 144 tubes are inserted; the pressure plate is screwed to the HX frame to provide a pressure on the rubber sheet in order to seal the tubes at the inlet header connection. No sealing was required at the outlet header since tube were discharging to the free flow tubing. The assembled prototype heat exchanger is shown in Figure 68 before header assembly. The final prototype as used in the experiment is shown in Figure 69.

9.2. HX Test Setup

Testing this prototype HX design requires a wind tunnel like setting in order to ensure proper air inlet stream conditions. The main goal for this experimental investigation is to measure the heat capacity. Hence, the experiment was instrumented

with water and air mass flow meters as well as inlet and outlet air and water temperature measurements. In order to provide controlled boundary conditions, the water was supplied from a NESLAB HX-150 water conditioning unit that maintains the inlet water temperature at the desired value. The whole wind tunnel is then put in an environmental chamber to control the ambient air conditions. The experimental test setup design is shown in Figure 70 showing the installed instruments. The test setup as build is shown in Figure 71 showing installed instruments and data acquisition system. The water flush valve is installed to allow for water supply line flushing before testing in order to ensure clean water supply to the prototype HX.

The water mass flow rate was measured using a Coriolis type mass flow meter, Micro Motion® Elite® model # DS012S100SU. This mass flow meter was calibrated for flow rates between 0.5 and 3 g/s. Typical measurement accuracy for this type of flow meters are ±0.1% for flow rates above 1.1 g/s. The water inlet and outlet temperatures were measured using instream Omega® PT100 Resistance Temperature Detectors (RTD).

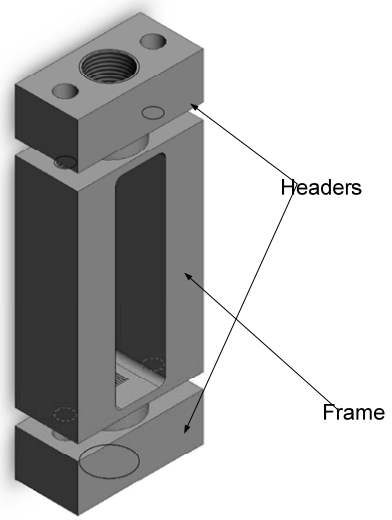

Figure 65: Prototype HX frame and header assembly

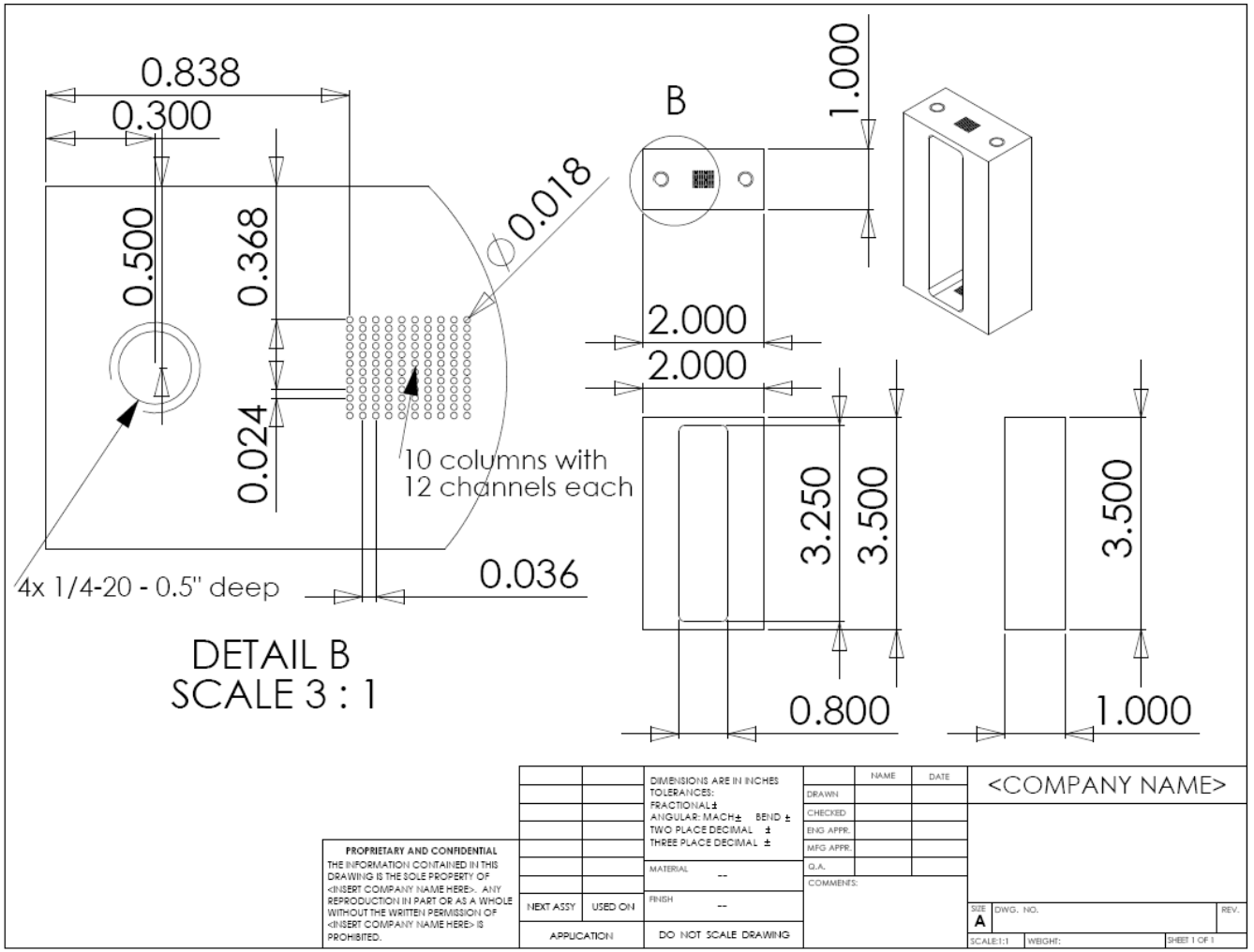

Figure 66: Detailed prototype HX frame design, dimensions in inch

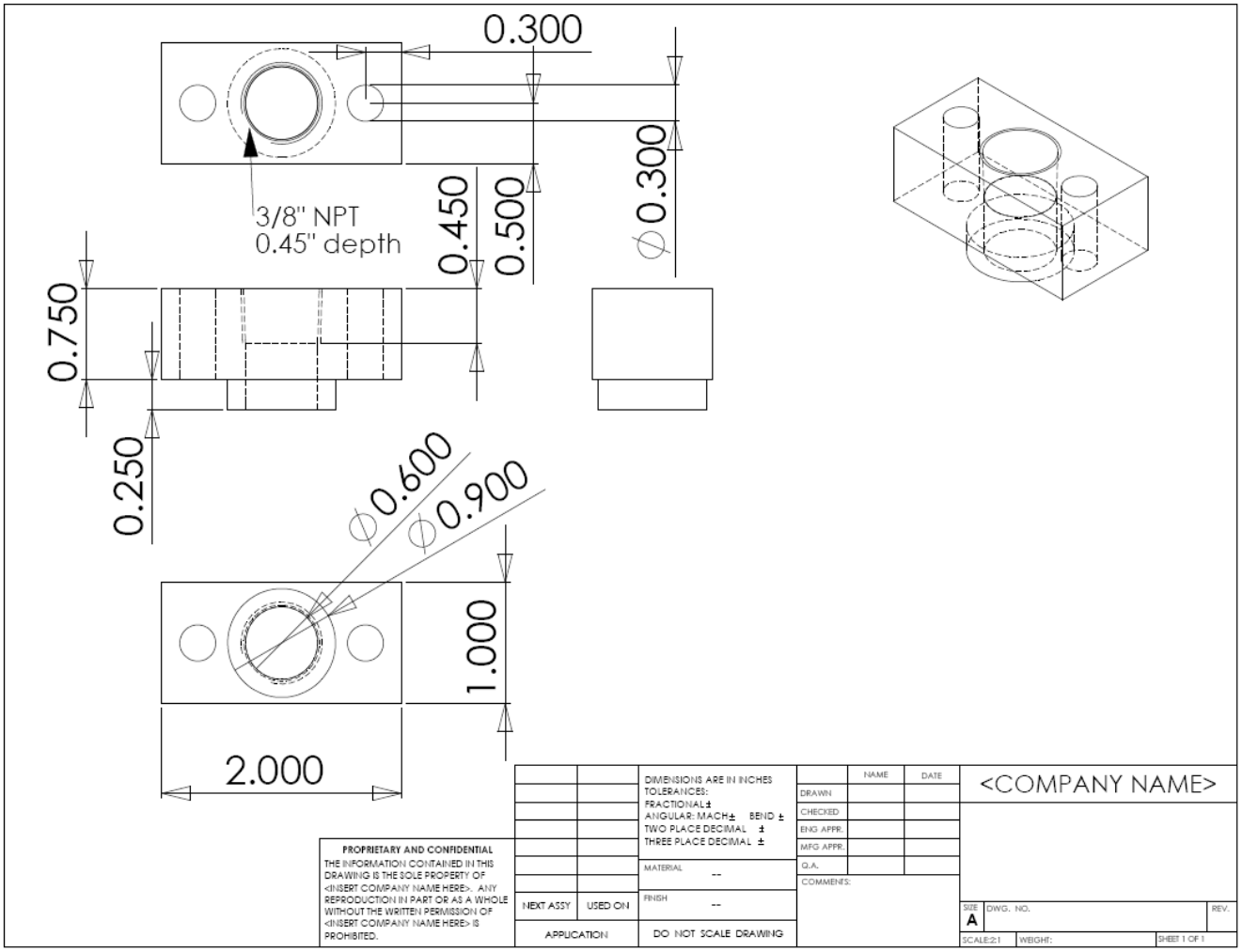

Figure 67: Detailed prototype HX header design, dimensions in inch

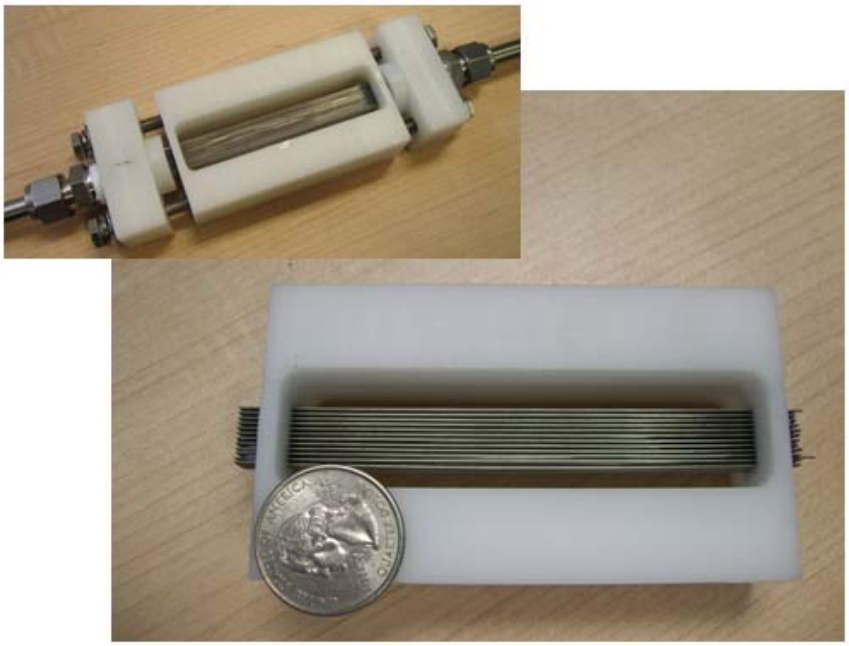

Figure 68: Assembled NGHX prototype

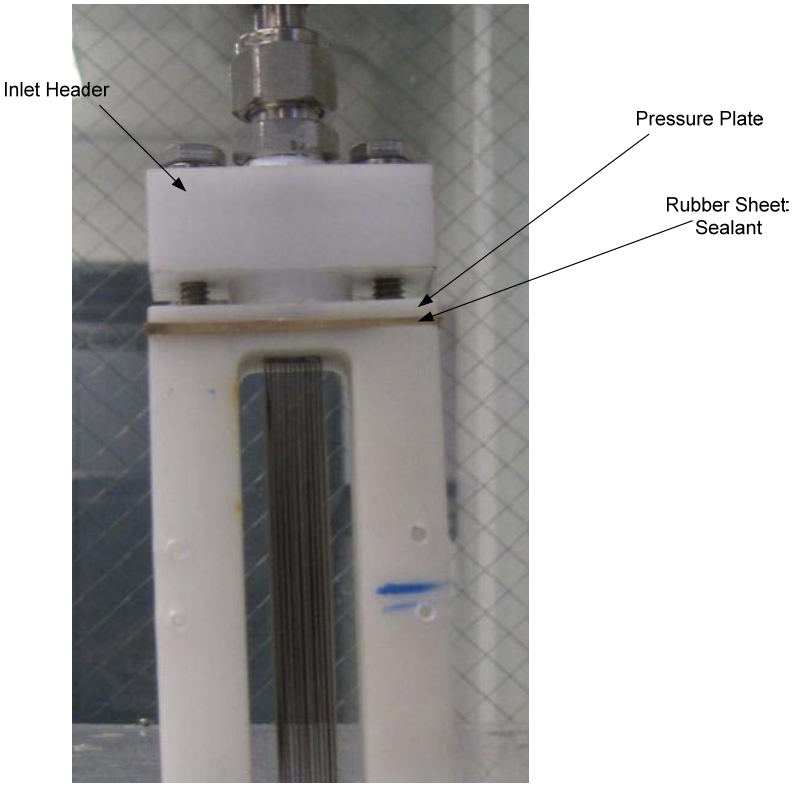

Figure 69: Assembled prototype HX with header sealing details

The air flow rate was measured with a rotameter, omega® model # FL4513. This rotameter has a range from 0 to 8 SCFM on 127 mm scale giving higher reading precision. In addition, the data sheet indicates 3.5% measurement accuracy. The air side inlet and outlet temperatures were measured using a mesh of T-type thermocouples. On each side, the mesh is formed of 9 thermocouple junctions in a 3 × 3 configuration. Every 3 thermocouple junctions are connected together; such settings results in separate temperature measurements at the top, middle and bottom of the HX.

Measurement uncertainties of the instruments used in the experimental investigations are summarized in Table 25. These instruments were connected to a National Instruments® data acquisition system except for the air flow rate which required a manual input. Online experiment monitoring and data logging was made using a developed LabVIEW® program.

Table 25: Measurement instruments summary

Measured value	Instrument range	Accuracy	Units
Water mass flow rate	0 – 3	0.1% for flow rates > 1.1 g/s and 0.0005 g/s otherwise	g/s
Air volume flow rate	0.8 – 8	3.5%	SCFM
Water instream temperature	-200 – 260	0.2 K	°C
Air temperature	-250 – 350	0.5	°C

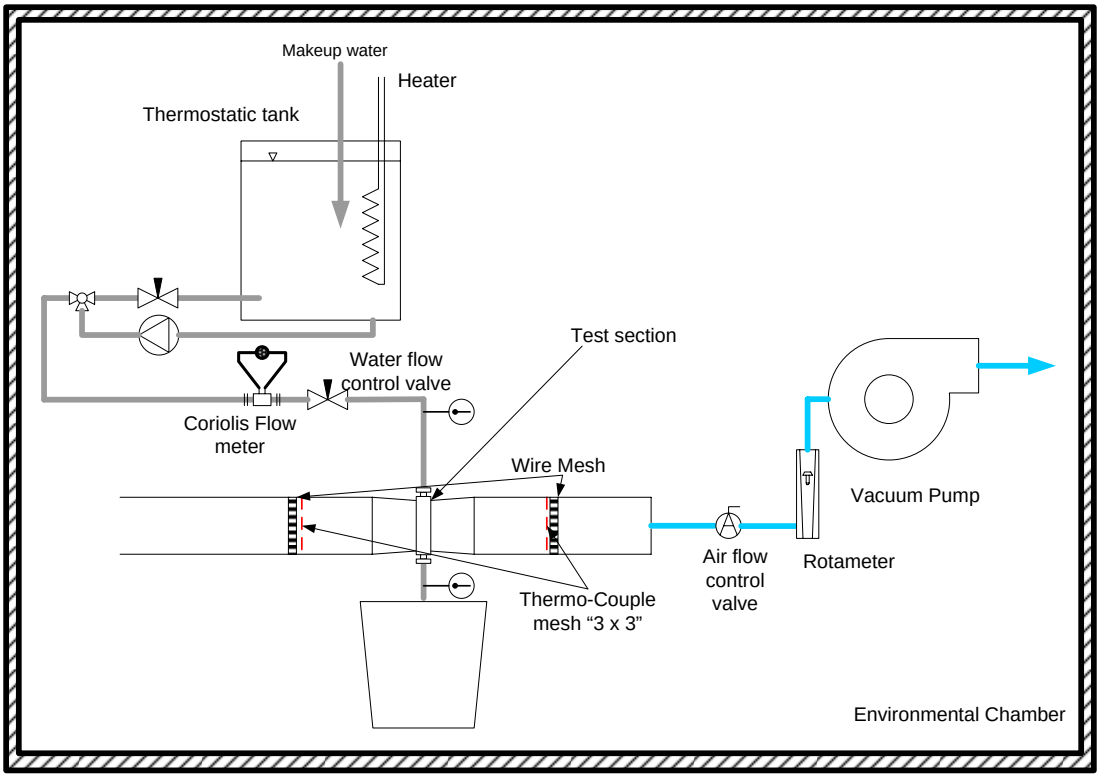

Figure 70: Experimental test setup

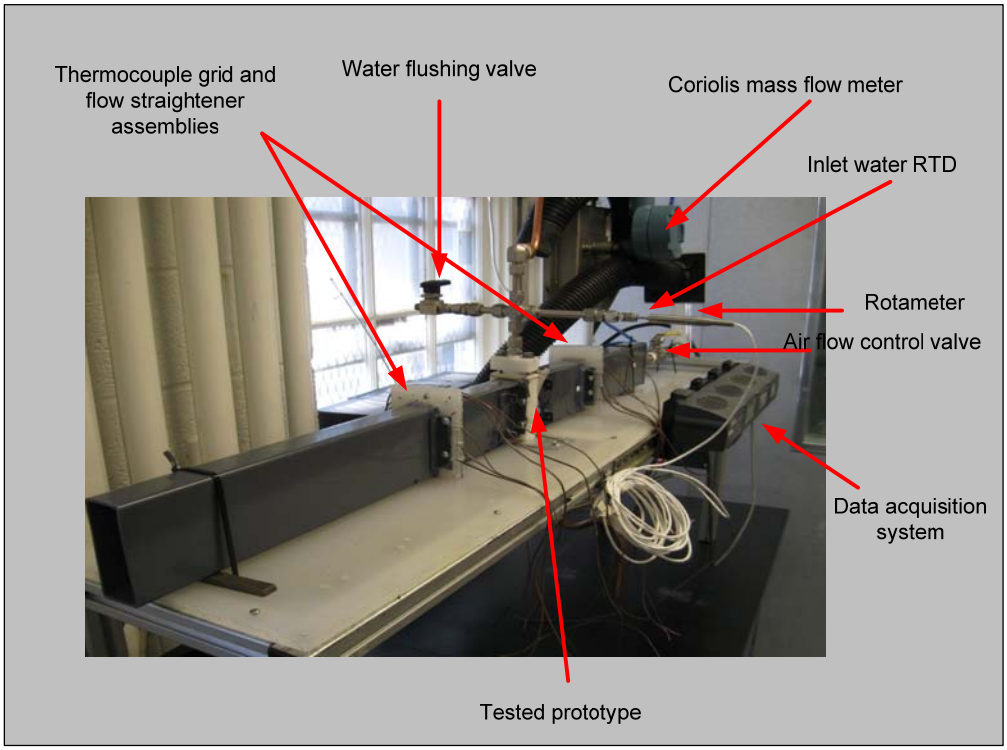

Figure 71: Experimental HX test facility as built

9.3. Test Procedure

Generating the required data to investigate the performance of the developed prototype HX design requires varying both water and air side conditions. HX performance depends on the air and water flow rates as well as the approach temperatures. The experiment was designed to test 3 levels of water flow rates, air flow rates and approach temperature resulting in a combination of 27 test points. The NESLAB HX-150 water conditioning unit is limited to a maximum temperature of 35 °C. However, the large water line tubing from the water conditioning unit to the heat exchanger inlet resulted in heat loss to the environment. Hence the inlet water temperature varied between 34.76 for higher water flow rates to 30.61 for low water flow rates. Hence, the approach temperature was mainly varied by adjusting the environmental chamber temperature to 5, 15 and 25 °C resulting in design approach temperatures of 30, 20 and 10 K.

A test procedure was developed in order to ensure systematic measurements and allow for easier data collection. This testing procedure is based on the fact that the air flow rate provides the smallest stiffness. Hence, it was easy to measure the performance for different air flow rates in one day. However, changing the water flow rates and the approach temperatures required more time for the system to reach steady state. The main test procedure steps are indicating below:

1. Adjust the environmental chamber temperature to the required set point (5, 15, or 25 °C).
2. Set the water cooled recirculating chiller to 35°C.

3. Allow the chamber and the water conditioning unit to stabilize (2 hours roughly).
4. Record the mass flow meter zero flow rate reading signal and update the correlation function (to minimize zero drift).
5. Let the water flow through the heat exchanger at the desired flow rates (0.5, 1, 2, or 3 g/s) and allow for the water line to reach steady state (30 minutes to 2 hours depending on the water flow rate).
6. Measure the water heat capacity at zero air flow rate (to account for heat transfer loss in the energy balance).
7. Run the Fan and adjust the air flow rate to the desired value (2.4, 5, or 7.6 SCFM) and allow the HX to reach steady state (this is judged by the change in capacity reading over time).
8. After the HX reaches steady state, record measurement data for 5 min with 5 second interval.

9.4. Experimental Results

A total of 29 points were measured (the 27 combination and 2 additional points) according to the procedure described in section 9.3. For each of these conditions, the 5 minutes average value of the measured quantities (water flow rate, air flow rate, inlet and outlet air and water temperatures) were used to determine the water side and airside heat transfer and the energy balance. In addition, standard deviations were used along with the instruments accuracies in order to analyze the measurement uncertainties and develop error bars for relevant quantities.

Post processing the experimental data was performed using EES® (http://www.fchart.com/) since it provides fluid properties as well as automated uncertainty propagation analysis. The air side mass flow rate is calculated as shown in equation(54). Airside capacity is then calculated as shown in equation (55), where the air specific heat is evaluated at the average inlet and outlet air temperatures.

$$\dot{m}_{air} = \rho_{air,out} \dot{V}_{air} \tag{54}$$

$$\dot{Q}_{air} = \dot{m}_{air} cp_{air} \left(T_{air,out} - T_{air,in} \right) \tag{55}$$

The water side heat transfer is calculated as shown in equation (56) with water specific heat evaluated at the average water temperature. The last term in equation (56) accounts for the heat loss to the chamber when no air is flowing through the heat exchanger. This value accounts for the heat loss from the headers and connection pipes to the HX since the instream thermocouples are located just before and after the inlet and outlet headers respectively.

$$\dot{Q}_{water} = \dot{m}_{water} cp_{water} \left(T_{water,in} - T_{water,out} \right) - \dot{Q}_{water,\dot{m}_{air}=0.0} \tag{56}$$

Finally, for each test point, the energy balance between the airside and the refrigerant side heat transfer is calculated as shown in equation (57) assuming that water side measurements are more accurate (Coriolis mass flow and RTDs versus rotameter and thermocouples). The energy balance errors are plotted in Figure 72. Energy balance error varied from -22% to 11% with 60% of the points within ±10%. However, 83% of the measurement points have the 0% energy balance error passing through the measurement error bars. These results indicate that acceptable energy balance performance especially at the challenging flow conditions specified.

$$\text{Energy Balance Error} = \frac{\dot{Q}_{water} - \dot{Q}_{air}}{\dot{Q}_{water}} \times 100\% \qquad (57)$$

In order to investigate the correlation between the experimental parameters and the heat transfer rates, the measured airside heat transfer is plotted against the air and water mass flow rates as shown in Figure 73 and Figure 74 respectively for the different approach temperatures. These figures suggest that the heat transfer rate is mainly correlated to the air flow rate and approach temperature with limited impact of the water flow rate. This indicates that the air flow velocity affects the overall HX conductance the most. As such, for the remainder of the experimental analysis, air flow velocity is used as the dependent variable. Furthermore, the baseline heat exchanger (Huang 2008) performance was simulated for the same inlet conditions in order establish comparison criteria.

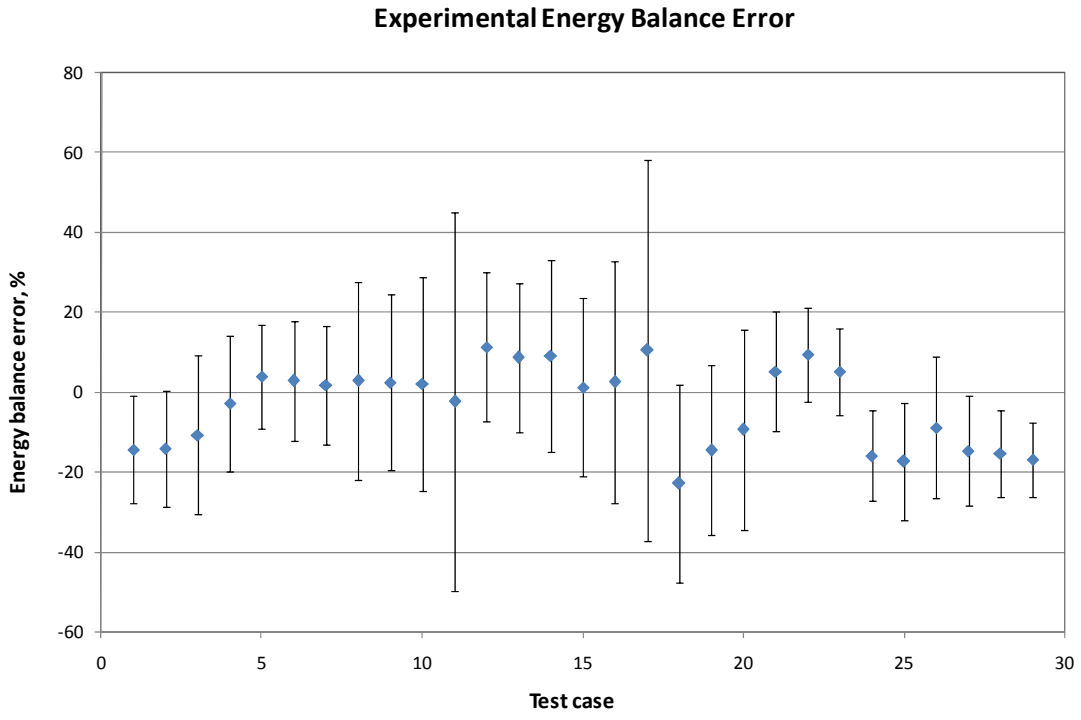

Figure 72: Experimental energy balance error, %

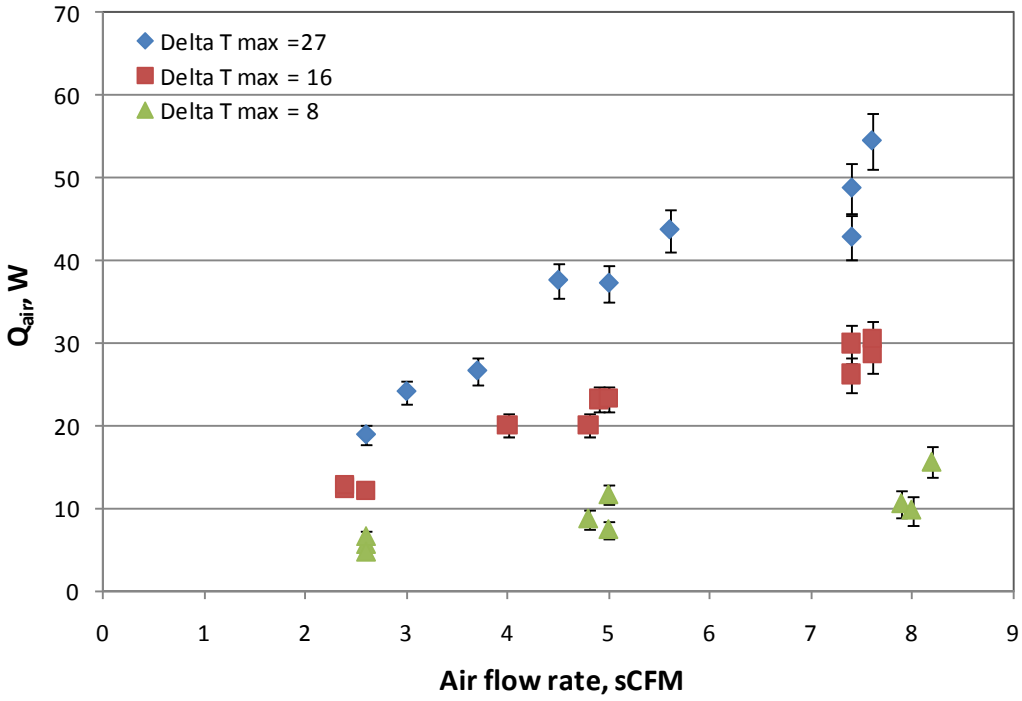

Figure 73: Heat capacity variations with air flow rates

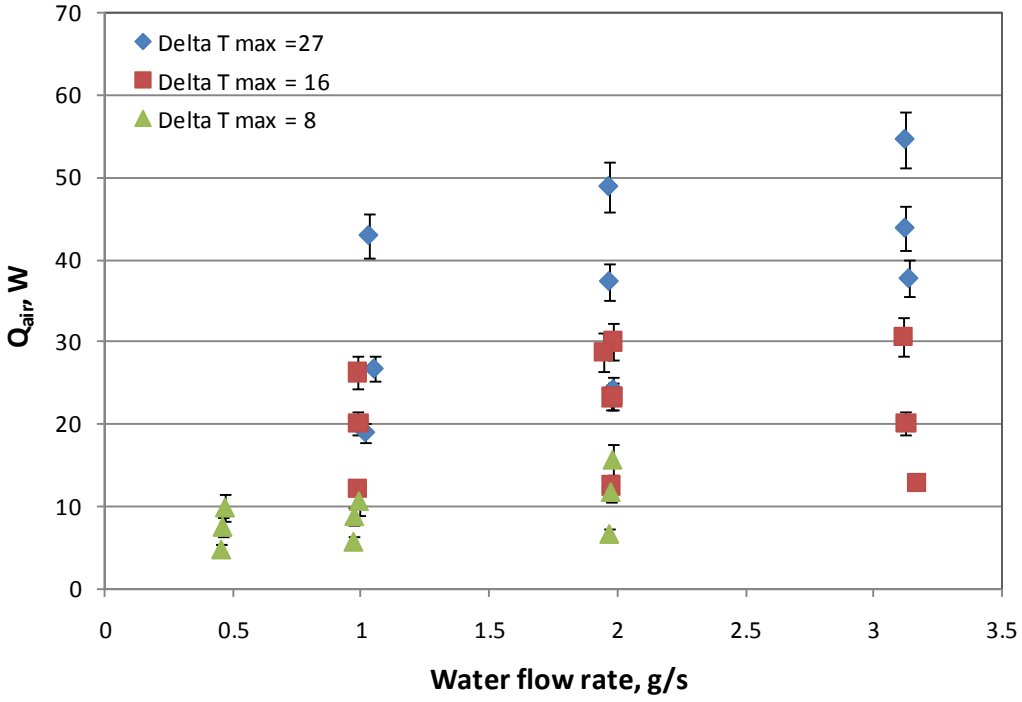

Figure 74: Heat capacity variations with water flow rates

Prototype HX was compared against the baseline in terms of heat transfer per unit material volume, HX compactness and overall HX conductance per unit HX volume. Heat transfer per unit material volume was calculated for all test points as well as the baseline. The results are plotted against the air inlet velocity as shown in Figure 75 for the prototype and baseline designs. The average performance improvement of the prototype HX over the baseline HX is a factor of 6; that is the new design can transfer 6 times greater heat transfer compared to the baseline design.

The HX compactness was also calculated for all test points. The comparison between the prototype and the baseline performance is summarized in Figure 76. The prototype design provides a superior compactness over the baseline design. The average performance improvement factor is 2.6 (260% higher compactness). However, this higher improvement may be potentially hindered by the added volume of the required distribution headers when the HX is scaled to larger capacities.

Finally, the comparison of the overall HX conductance (*UA*) per unit HX core volume between the prototype and baseline HXs revealed average performance improvement of 183%. This comparison criteria accounts for the fact that the log mean temperature difference is different for the 2 designs since the water flow rate was kept constant for the baseline HX. *UA* per unit volume is plotted for the 29 test points in Figure 77 for the tested prototype and simulated MCHX. Figure 77 clearly indicates the strong correlation between the overall conductance and the air flow velocity. This correlation is not as strong in the case of the baseline design.

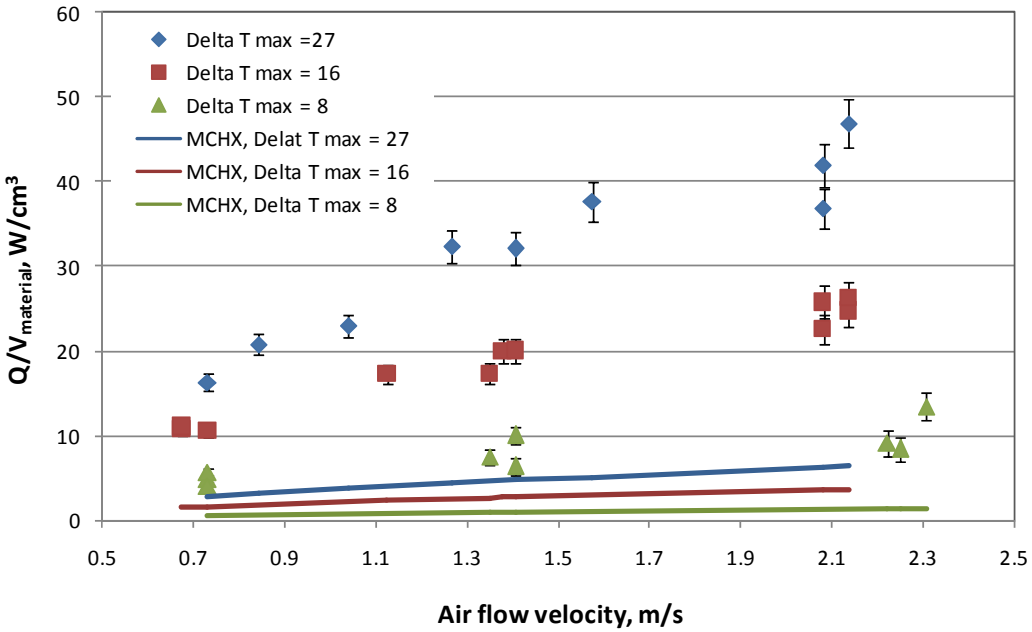

Figure 75: Heat transfer per unit HX material volume

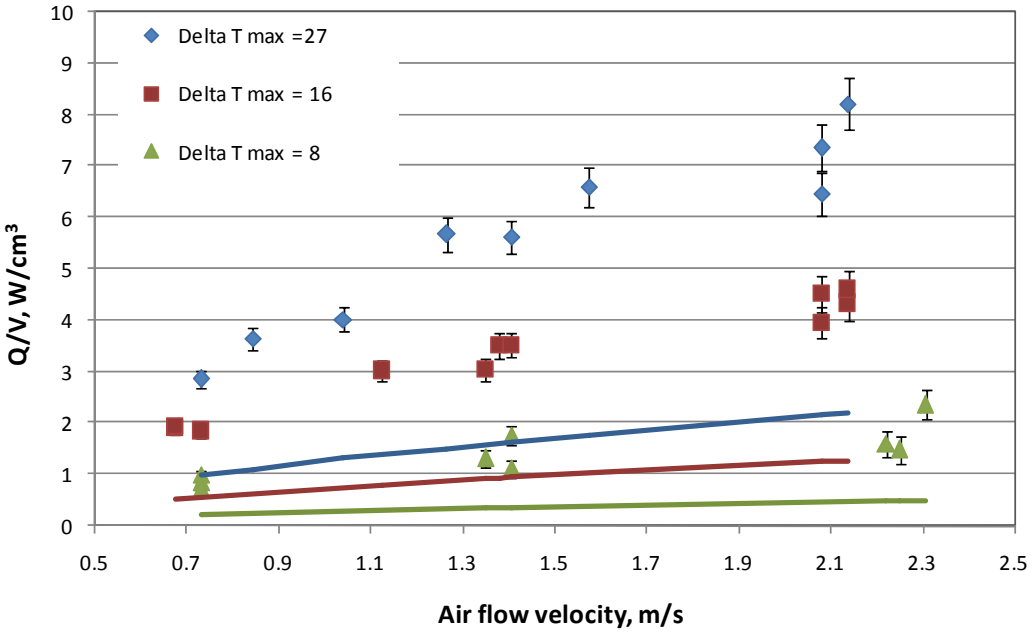

Figure 76: Heat transfer per unit HX core volume

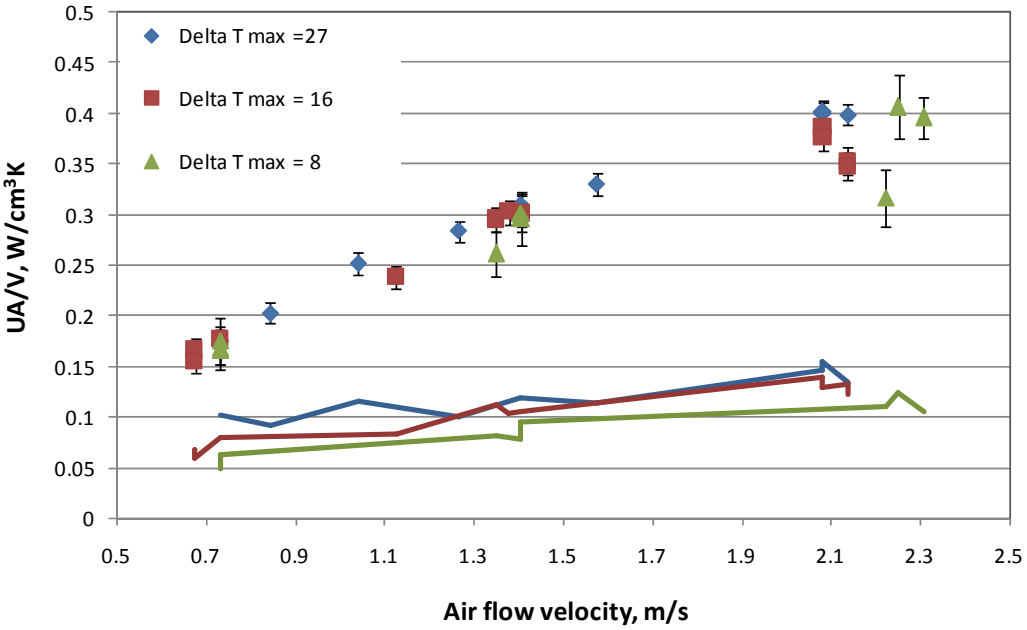

Figure 77: Overall HX conductance per unit HX core volume

Results presented in Figure 75 to Figure 77 suggest that the tested prototype HX design provides a superior performance over the baseline design. The indicated performance improvements are in the same order of magnitude with the approximation assisted optimization results. This suggests that the developed framework provide physically sound designs that outperform the current state of the art. However, a detailed validation of the multi-scale simulation tool is required using the available experimental data as discussed in the next section.

9.5. Validation of the Multi-Scale Simulation Tool

The multi-scale simulation tool described in Chapter 4 has been numerically verified and validated earlier against 3D CFD simulations. These efforts cannot eliminate the need to validate the simulation approach experimentally in order to ensure the accuracy and fidelity. This validation study requires the development of

multi-scale simulation tool for the prototype design. This tool is then used to model the performance of the prototype HX for the same set of inlet and boundary conditions.

Initial efforts to develop the multi-scale simulation capabilities for the prototype HX reduced the computational domain to a 2-D simulation of a single tube row in cross flow. The discretized computational domain is shown in Figure 78. A zoomed in view of the mesh around the tubes is shown in Figure 79. A single mesh file is used to run all the cases for the validation since the HX design parameters were kept constant (testing a single design). For this simplified computational domain, a velocity inlet boundary condition was prescribed on the left side of the computational domain. A 0 gage pressure outlet boundary condition was prescribed on the right end of the computational domain. The top and bottom axes were set as symmetry boundaries. Finally, inner tube walls were set to constant wall temperature boundary conditions.

For each of the experimental test cases, the airside velocity is calculated from the standard airflow rate measurement; the inlet air temperature is set according to the measured values while the wall temperature was set to be equal to the average water inlet and outlet temperatures. Second order upwind discretization scheme was used for momentum and energy equations with second order pressure discretization. The Fluent® coupled solver was used for pressure velocity coupling in order to reach higher convergence.

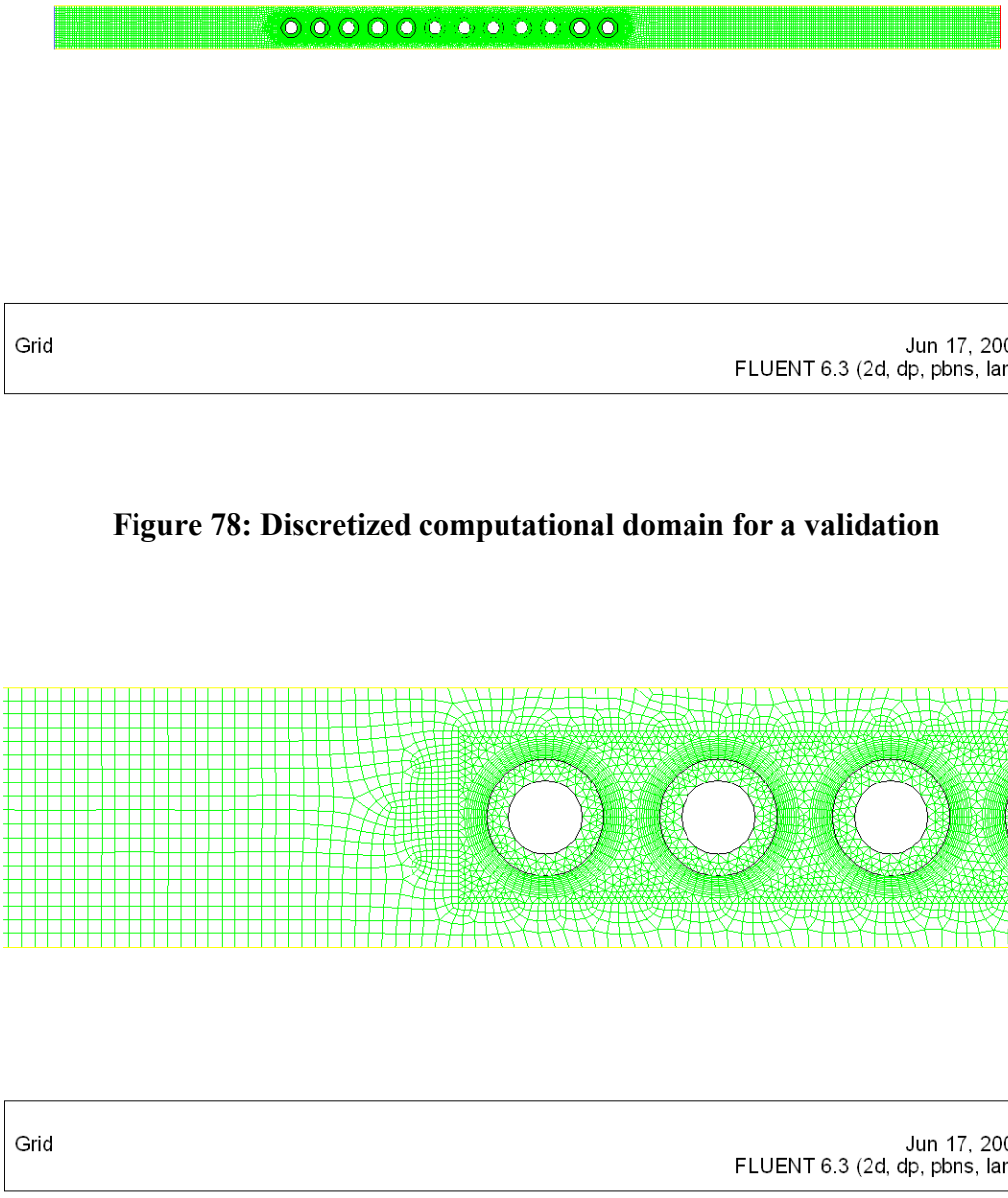

Figure 78: Discretized computational domain for a validation

Figure 79: Zoomed view of the mesh details around the tubes

Sample results for pressure and temperature contours are presented in Figure 80 and Figure 81 respectively and velocity vectors are presented in Figure 82 for the 10^{th} test point. The CFD simulation results were post processed to obtain an overall airside heat transfer coefficient as described in section 4.3.1. The segmented HX

solver was then used to evaluate the performance using the HTC from the CFD results. This simulation studies showed large discrepancies between modeled performance and experimental measurements (between -7.44% and + 55%). The problem was further investigated and it was found that the HX frame design resulted in side gaps larger than the vertical spacing between tubes. This configuration alters the periodicity assumption used in the computational domain simplification.

As such, the entire tube bank was modeled using 2D CFD simulations. The new computational domain is shown in Figure 83. This computational domain accounts for the side gaps and their impact on the thermal and hydraulic performance.

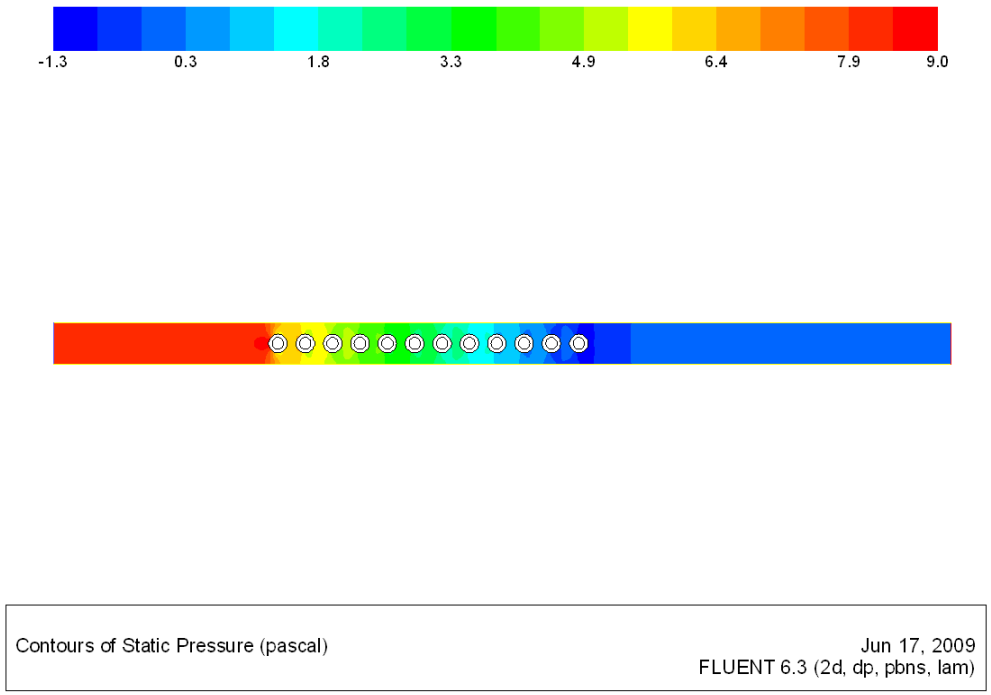

Figure 80: Pressure contours for experimental test conditions #10

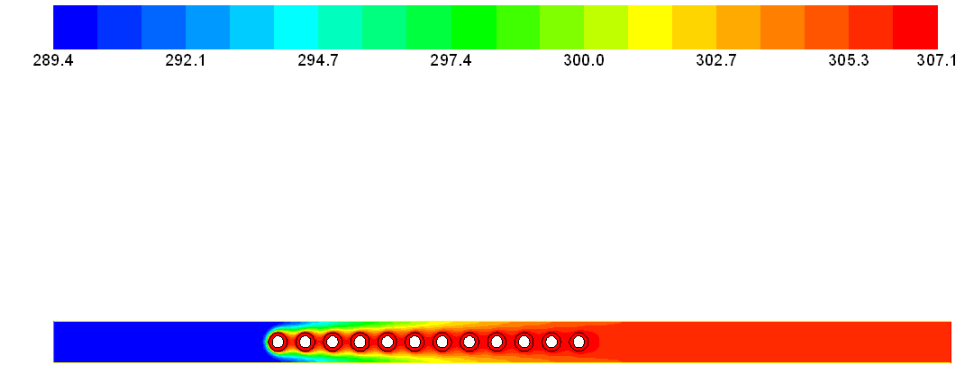

Figure 81: Temperature contours for experimental test conditions #10

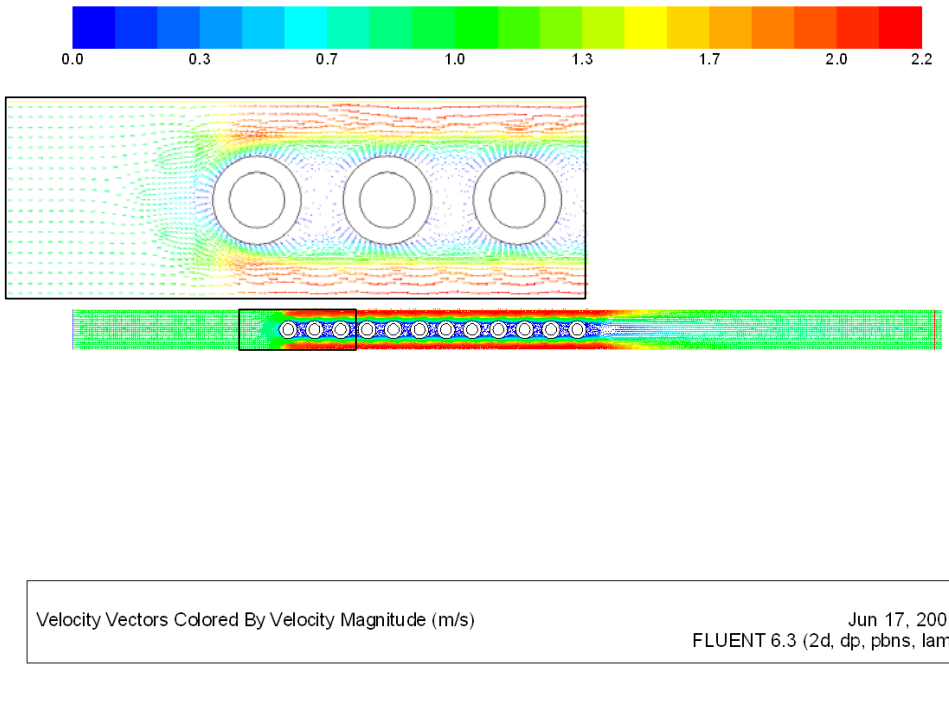

Figure 82: Velocity vectors for experimental test conditions #10

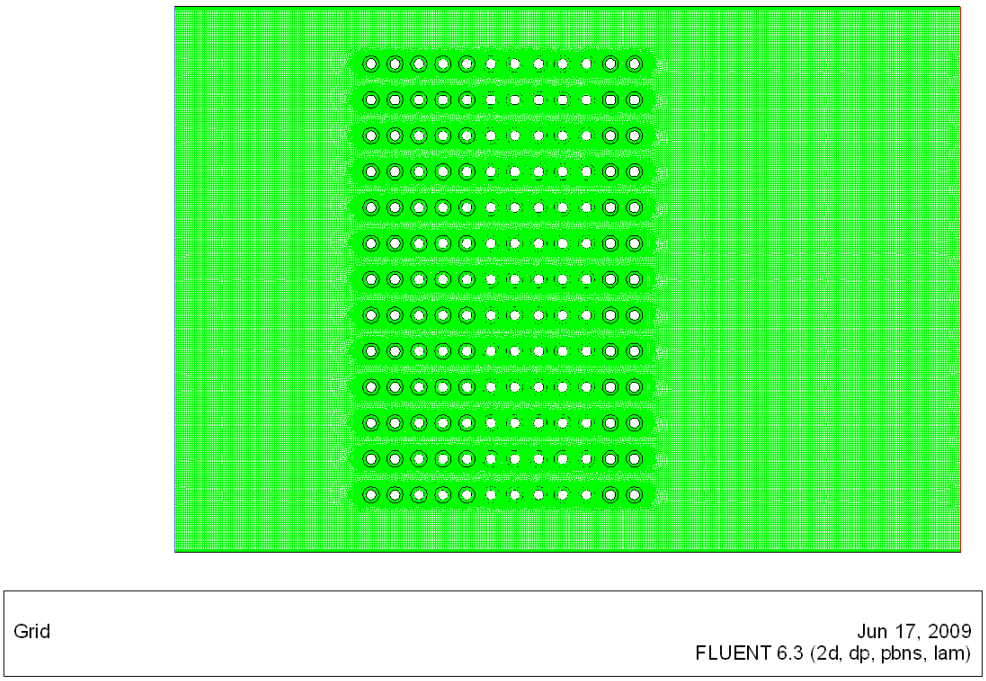

Figure 83: Computational domain for the entire tube bank

The same boundary conditions and solver details were used to process the 29 CFD cases using the entire 2D computational domain. Sample results for the case corresponding to the 10th test point are presented in Figure 84, Figure 85, and Figure 86 for pressure, temperature contours and velocity vectors respectively. Velocity vectors shown in Figure 86 depict the impact of the wide side gaps on the air flow profile. This gap resulted in a large portion of airflow being bypassed resulting in lower airflow rate through the tube bank. Simulation results based on CFD simulations of the new computational domain were in good agreement with experimental measurements as shown in Figure 87. The multi-scale simulation results varied from -8% to 21.4% from the experimentally measured values with an average absolute error of 8%. Figure 87 also shows that for 18 out of the 29 test cases, the

multi-scale simulation results are within the error bars of the experimentally measured heat transfer.

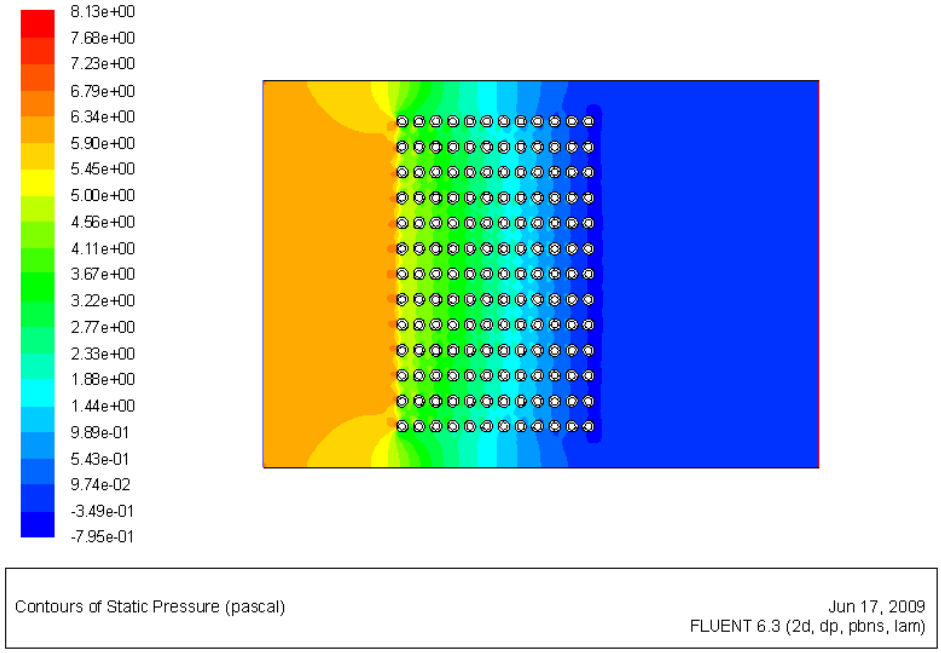

Figure 84: Pressure contours for test conditions #10 for the entire tube bank

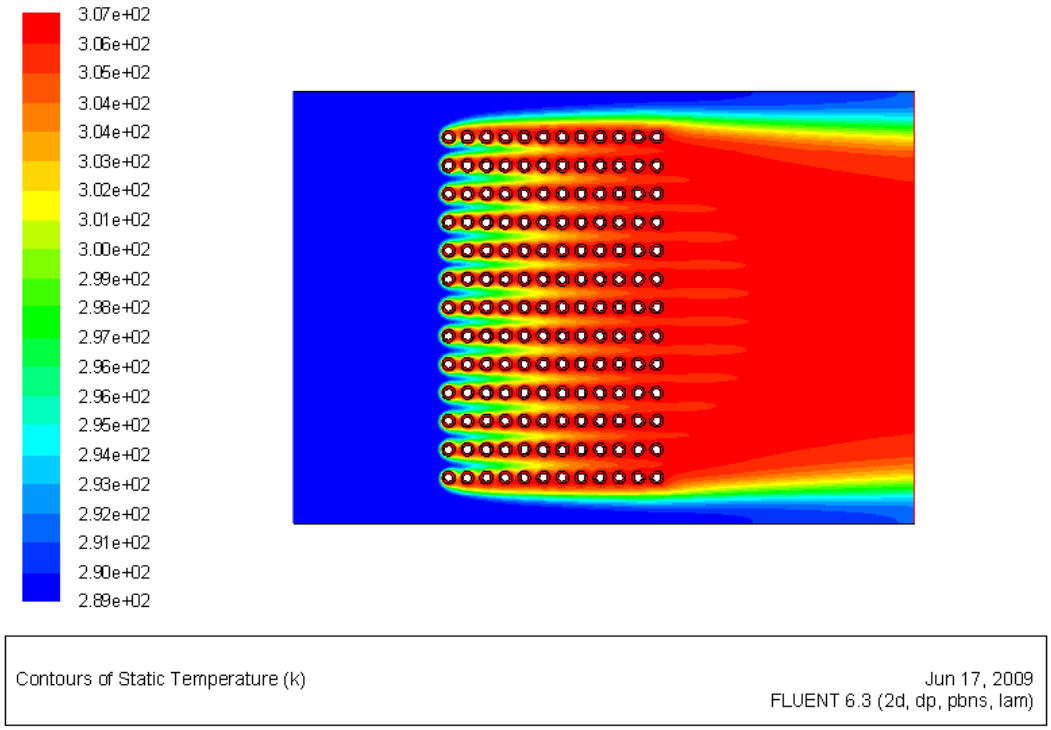

Figure 85: Temperature contours for test conditions #10 for the entire tube bank

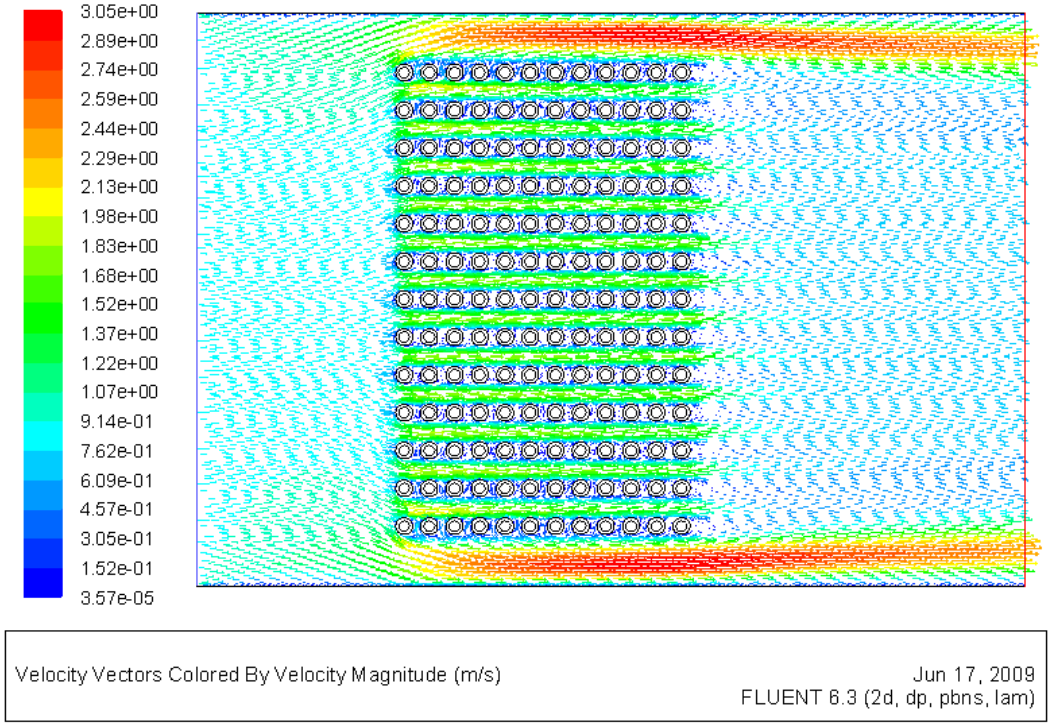

Figure 86: Velocity vectors for test conditions #10 for the entire tube bank

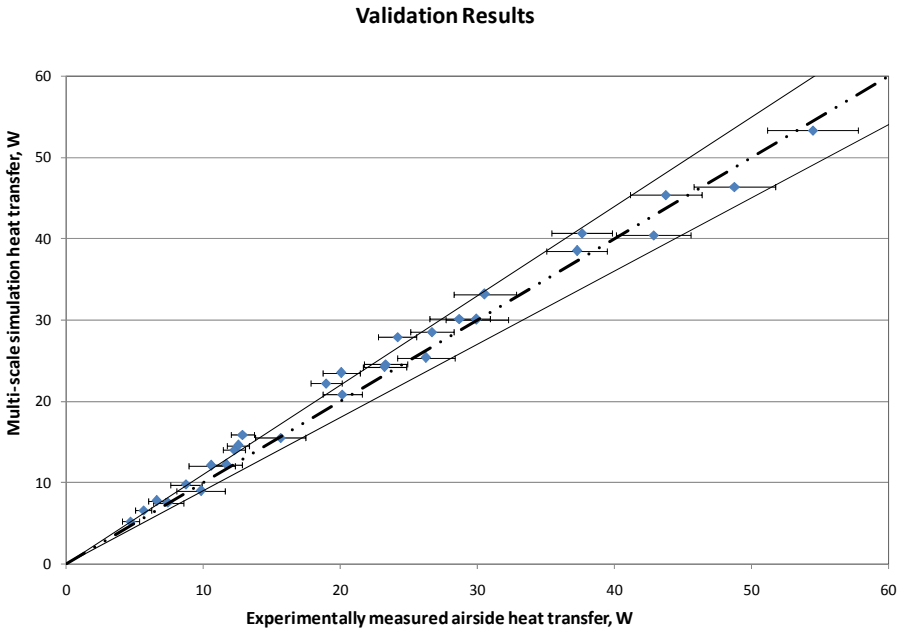

Figure 87: Overall multi-scale simulation validation results

9.6. Summary and Conclusions

The experimental investigations presented in this chapter provided a sound proof of concept. The proposed prototype HX was successfully manufactured using commercially available stainless steel tubing. The required cutting and assembly technologies were developed. Experimental results showed some degree of high energy balance errors due to the challenges with water temperature measurements. Future investigations should incorporate higher accuracy RTD (0.01 K errors) in order to accurately measure the small temperature change on the water side. Furthermore, RTDs should be located inside the header in order to reduce the errors associated with heat loss to the ambient.

The experimental results showed high performance improvements as suggested from the multi-objective optimization results. This indicates that smaller tube diameters can indeed be used to design the next generation of ultra-compact HXs. The average and standard deviation in performance improvements of the tested prototype over the modeled baseline design are summarized in Table 26 below.

Table 26: Prototype performance improvements over baseline

	Heat transfer per unit material volume, $W/m^3_{material}$	Heat transfer per unit volume, W/m^3	Overall HX conductance per unit volume, W/m^3K
Average improvement, %	600%	260%	183%
Standard deviation, %	94%	48%	45%

The validation results of the multi-scale simulation tool suggest that the tool is of adequate fidelity. However, this study indicated the high impact of the

computational domain reduction assumption on the overall results. For an ideal HX case, modeling a single row of tubes would have been sufficient. However, the manufactured frame resulted in side gaps that allowed between 6.3 to 10% of the air flow to bypass the coil; hence it was required to model the entire tube bank. Multi-scale simulation results validation incorporating CFD simulations resulted in RMSE of 9.5% with a MAE of 19%. These results suggest that the modeling approach is valid.

Chapter 10: Conclusions

Work presented in this dissertation demonstrates great potential of heat transfer performance improvement for air-to-water heat exchangers based on heat exchanger design concept innovation and optimization. The research pursued followed a newly developed framework that introduced and integrated novel simulation techniques and incorporated latest developments in approximation assisted optimization. The developed simulation techniques were verified numerically and validated using measurements. This chapter emphasizes the key contributions and performance improvement and summarizes the main design considerations.

10.1. Novel HX Simulation Tools

Work presented in this dissertation resulted in successful development and implementation of a multi-scale heat exchanger simulation tool. This tool can analyze the performance of novel heat exchanger geometries. Furthermore, it can be applied to conventional designs with challenging airflow patterns such as A-coils. The multi-scale heat exchanger simulation tool was successfully implemented for the design and optimization of NGHX-13 segment geometry, conventional A-coil geometry and bare micro tube banks geometry. The tool was verified and validated numerically and experimentally. Validation results indicated acceptable levels of accuracy.

Additional simulation flexibility was developed to accommodate heat exchanger designs having variability in geometric design parameters. This tool required modification to the conventional ε-NTU technique to allow for simulation of tubes with heat transfer coefficient and mass flow rate variability. In support of this

effort, another tool was developed to assemble a heat exchanger based on statistical distributions of geometric parameter variability using Monte Carlo Simulation approach. Furthermore, the tube side mass flow rate was assigned randomly based on an imposed statistical distribution. This tool was successfully implemented for the analysis of NGHX-13 in order to analyze the impact of different geometric and flow rate variability scenarios on the overall performance.

In addition to the multi-scale simulation tools developed earlier; a new simulation tool for the refrigerant header analysis was developed. This tool is used for the design of refrigerant headers for heat exchangers with a large number of parallel microchannel ports. The tool can be used to design headers that provide adequate mass flow distributions at the minimum possible refrigerant pressure drop and additional volume.

Finally, the multi-scale simulation tool was successfully coupled with a recently developed approximation assisted optimization technique. The approximation assisted optimization coupled with the multi-scale simulation tool was used for the design optimization of a car radiator, aluminum heating coil, polymer heating coil, and R410-A A-coil condenser.

10.2. Promising Results

Searching for improved heat exchanger design following the framework described in this dissertation provided sound results that were verified experimentally. One of the designs was selected from the Pareto optimum set of the heating coil optimization study presented in Chapter 7. For this design, a simplified

prototype was manufactured and experimentally tested as shown in Chapter 8. The validation of the multi-scale simulation tool showed errors ranging from -8% to 21.4% in heat capacity with average absolute error of 8%. The tested prototype showed average performance improvements of 600% for heat transfer rate per unit material volume, 260% for heat transfer rate per unit volume and 183% for overall conductance over the current state of the art heat exchanger technology.

The validation results suggest that the optimum solutions for the 3 different design optimization studies presented in Chapter 7 are sound and can indeed provide an unprecedented level of compactness at no additional pressure drop penalties. Such designs may be able to provide the next generation of air-to-refrigerant heat exchangers.

Furthermore, the approximation assisted optimization framework was applied in the optimization of a conventional heat exchanger, A-coil. The optimization results showed a tradeoff between heat exchanger packaging volume reduction and material cost reduction. Two optimum designs were identified with potential for 52% savings in packaging volume at 39% material cost savings or 54% savings in packaging volume at 30% material cost savings. The approximation assisted optimization techniques resulted in 97.7% reduction in computational time compared to the multi-scale simulation coupled with periodic CFD simulations.

10.3. Computational Time Savings

The multi-scale simulation approach presented in Chapter 4 provided 2 orders of magnitude savings in computational time compared with conventional 3D CFD

simulations. These computational savings were at the cost of modest accuracy loss as shown in section 4.4.2. Hence this approach can be used in extensive parametric analysis and optimization studies.

Further computational savings were achieved by replacing CFD simulation in the multi-scale simulations with metamodels developed using adaptive approximation techniques. The additional computational savings stems from the fact that CFD simulations are only performed during the metamodel development stage and the verification of the final Pareto solutions. For the car radiator design optimization problem a total of 1048 CFD simulations were performed and the metamodels were run for 25,500 function evaluations resulting in 95.89% savings in required CFD simulations if the optimization was coupled directly with the multi-scale simulation approach. For the aluminum water heating coil, a total of 1049 CFD simulations were required to develop, verify the metamodel and verify Pareto simulations while the optimization study required 100,500 function evaluations (i.e. computational savings ~ 98.96%). For the polymer heating coil design problem a total of 926 CFD simulations were performed while the optimization study required 112,500 function evaluations (i.e. computational savings ~ 99.177%).

10.4. Design Considerations

Optimization and parametric analysis studies presented in this dissertation were analyzed to develop design guidelines for compact air-to-water heat exchanger as per the developed research framework. The developed design guidelines can be divided into segment design guidelines, header design guidelines and consideration

for design under varying geometric and flow conditions. These general guidelines are summarized in the following subsections.

10.4.1. Segment design

First order heat transfer analysis provided general guidelines for improved thermal performance of compact heat exchangers. Smaller flow channel dimensions result in increased compactness (heat transfer area per unit volume). Conventional fin designs can not be used to augment the heat transfer area when the channel port diameter is smaller than 0.3 mm. NGHX-13 design does require heat transfer area augmentation and is capable of providing larger heat transfer area per unit volume than microchannel heat exchangers for port hydraulic diameters less than 0.3 mm. Furthermore, the first order analysis indicated that the impact of the tube thermal conductivity on the overall heat transfer coefficient diminishes when smaller material thickness is used. This finding indicates flexibility in material selection for compact heat exchanger designs. This finding was confirmed further based on the results of the structural analysis study. Detailed design guidelines for NGHX-13 segment designs are summarized below based on the results from the different studies presented in this dissertation:

- Port inner diameter selection is largely dependent on the refrigerant-side pressure drop constraint. Smaller port diameters provide enhanced heat transfer performance at the cost of higher refrigerant side pressure drop per unit tube length.
- Horizontal spacing affects the heat exchanger packaging volume greatly; hence for ultra-compact designs, smaller horizontal spacing should be used.

- Airside pressure drop minimization requires heat exchanger designs with lower airside velocities and larger vertical spacing. In this case; slightly larger horizontal spacing is required to provide adequate heat transfer area augmentation.
- The number of ports for each of the designs is dictated by the air-to-refrigerant thermal capacity ratio.

10.4.2. Header design

The header design problem can be formulated as a design optimization problem where overall header height and header size ratio are minimized subject to a constraint of maximum allowable refrigerant pressure drop and mass flow rate maldistribution. The mass flow rate maldistribution can be quantified by the relative standard deviation in the mass flow rate per tube. The resulting Pareto optimum solutions presenting the tradeoff between smaller overall heat exchanger size and manufacturing complexity can be analyzed and the most suitable design can be selected based on the application at hand. The general conclusions from the parametric studies of the 2 header design problems indicated that better mass flow rate distribution and lower pressure drop are achieved at lower inlet header water velocities. The results also indicated that header size ratio of 4 resulted in good performance with diminishing performance improvements at header size ratios higher than 4.

10.4.3. Design under varying geometric parameters and flow conditions

Heat exchanger modeling under uncertainty revealed the impact of the geometric and flow variability on the heat transfer. For uniform water flow conditions, the overall loss of heat exchanger capacity is proportional to the port hydraulic diameter. Furthermore, the distribution of the change in overall HX capacity ranged a narrow interval from (-1.5% to -0.33%) for HXD1 to (-2.6% to 0.87%) for HXD3. However, the superposition of the water flow variability resulted in wider spread of the expected heat exchanger performance. This uncertainty analysis study suggests that a case by case analysis of possible distribution is required.

10.4.4. Manufacturing Challenges

The design guidelines presented in the previous sections were developed without considering manufacturability. These guidelines present an effort to extend conventional design space in order to investigate the potential improvement that can be achieved if novel manufacturing techniques can be developed. A prototype HX was successfully manufactured using commercially available stainless steel microtubes; however, there is a need to develop new extrusion capabilities that can produce tubes with new configurations and small material thickness.

Investigations performed on the NGHX-13 design resulted in an unprecedented performance improvement in material utilization and airside pressure drop minimization. These results present a new challenge to the machining and manufacturing community to be able to provide the required technology to produce

the next generation of heat exchangers to support the sustainability cause. The potential performance improvements warrant aggressive investment in research and development of the required machining techniques that would enable such novel heat exchanger design to compete with current state of the art in heat exchanger technologies.

10.5. Closure

This dissertation presents engineering contributions to advance the state of the art in air to refrigerant heat exchanger technologies. These contributions ranged from development of specific simulation capabilities to the development of design guidelines for next generation heat exchangers. However, most importantly this dissertation presented an effort to systematically integrate available tools and provide required modifications in order to increase productivity. The developed framework addressed several challenges and gaps in previous literature and was successfully implemented to optimize a novel heat exchanger segment geometry for different design problems. The framework was also applied to a conventional heat exchanger design, A-type heat exchangers, with a design optimization targeting cost and size reduction. The latter implementation demonstrates the usefulness and flexibility of the developed approach.

Chapter 11: Recommendation for Future Work

The work presented in this dissertation focused mainly on the development of novel HX simulation capabilities with implementation to a sample novel design (NGHX-13). The multi-scale simulation tool was also applied to conventional A-coil design as another proof of concept. However, these tools can be implemented on a variety of other HX segment design with possible extension to gas-to-gas HXs. Future work may be extended to encompass tube shape optimization. This can be achieved by the use of NURBS to define the outer tube profile. Furthermore, this framework can be used to define new tube design placement that is capable of improving the performance of conventional HX with geometrical constraints such as in A-coil design and the new generation indoor coils of unitary split air conditioning systems (C-coil). It is also envisioned that this tool can be ultimately used to design new tube configuration based on the HX placement constraints.

This study did not go into the details of refrigerant circuitry optimization. However, there is a room for improvement for the conventional circuitry design and optimization. Adding circuitry optimization to the framework presented in this dissertation would result in designs that account for the refrigerant header performance and its impact on the airside free flow area, refrigerant pressure drop and refrigerant flow distribution. Coupling the header performance to the HX simulation tool during optimization would ensure technical feasibility. Modular tube bundle designs can be used to assemble HXs of various capacities. As such, more work is required in analyzing new conceptual header designs suited for modular assembly. Furthermore, additional work is required to provide a simplified header design and

analysis tools based on refrigerant flow circuitry. These tools require the development of new pressure drop correlations for new fittings designs accommodating microscale dimensions which provide ultra-compact HX designs.

HX modeling under varying geometric parameters and flow conditions as presented in Chapter 6 suggests that there is a need for better statistical representation of the geometric and flow variabilities. Geometric parameters variability would require analysis of manufacturing techniques and evaluation of sample products in order to establish statistical distributions. On the other hand, the refrigerant flow variability would require evaluation of various fouling conditions and structural impact on the flow behavior. The tool presented in Chapter 6 was limited to the free flow spacing and the water flow rate variability. However, it can further be extended to include additional geometric variability such as for the horizontal spacing and the inner port diameter.

The A-coil optimization study presented in Chapter 8 indicated the impact of material prices on the optimized solutions. This indicate the need to introduce robust optimization techniques into the HX industry in order to provide designs that are less sensitive to parameter variability. Robust optimization should consider material prices, geometrical parameters, fouling and part load performance.

Finally, there is a need to extend the current analysis to investigate additional refrigerant side fluids including sea water and 2-phase refrigerants. In the case of sea water analysis, further studies on the corrosion effects should be introduced. On the other hand, 2-phase refrigerant flow requires additional work to ensure correlation validity for the flow conditions of interest.

Chapter 12: Appendices

12.1. Appendix A: First Order Analysis for NGHX-13

The preliminary CFD simulations of NGHX-13 showed heat transfer performance improvement over state of the art Micro-Channel HXs (MCHX). The higher heat transfer performance stems from:

- higher water side heat transfer coefficient due to smaller port diameter,
- better air side heat transfer coefficient due to boundary layer restarting in cases of larger horizontal spacing; as illustrated in Figure 88, and
- higher heat transfer per unit volume/material.

Furthermore, the number of ports within each tube was investigated. The larger the number of ports is, the higher the possibility that the segment becomes pinched; i.e. the air side temperature approaches the wall temperature. This would lead to part of the heat transfer area being inactive resulting in a poor HTC.

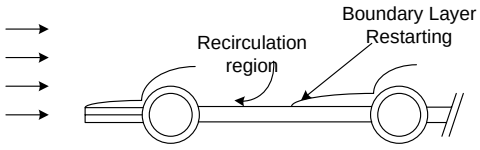

Figure 88: NGHX-13 Boundary layer restarting

Based on the above observations, a series of first order analyses were performed to investigate the potential length scale and benefits of NGHX-13. These analyses are divided into investigations of heat transfer area per unit volume/material for bare tubes, for NGHX-13 (with comparison to microchannel HX), and the impact

of the length scale on heat transfer performance penalty using lower thermal conductivity materials.

12.1.1. Length scale impact

As HX design optimization incorporates compactness; a first order analysis is performed to investigate heat transfer area augmentation assuming no gain in HTC. In the case of bare circular tubes, the heat transfer area per unit volume is inversely proportional to the tube outer diameter. Assuming equal horizontal and vertical spacings that are twice the outer diameter, the area to volume ratio can be described as in equation (58). The heat transfer area per unit tube material volume can be expressed by equation assuming tube thickness to be 10% of D_o.

$$\frac{A}{V} = \frac{\pi D_o L}{HS \times VS \times L} = \frac{\pi}{4 \times D_o} = \frac{0.7854}{D_o} \tag{58}$$

$$\frac{A}{V_{\text{material}}} = \frac{\pi D_o L}{\frac{\pi}{4}\left(D_o^2 - D_i^2\right) L} = \frac{4}{D_o\left(1 - 0.64\right)} = \frac{11.11}{D_o} \tag{59}$$

These heat transfer area per unit volume and per unit material volume are plotted in Figure 89 for the range of outer tube diameter from conventional HX technology down to 2 orders of magnitude smaller dimensions. This simplified analysis shows the potential of gain in compactness just by incorporating smaller tubes. However, smaller tubes would lead to a larger refrigerant side pressure drop; and may lead to issues regarding the flow distribution in headers.

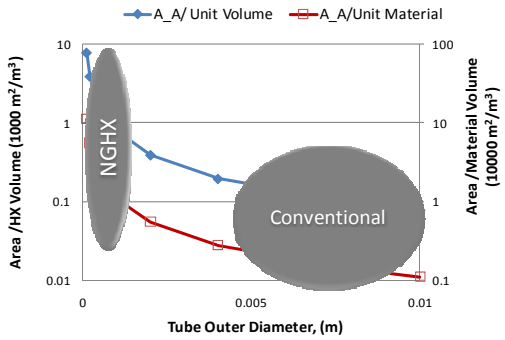

Figure 89: First order analysis of diameter effect on heat transfer area augmentation

12.1.2. NGHX-13 versus MCHX

In order to further analyze the potential for NGHX geometry over state of the art MCHX another geometric analysis is performed. In this study, heat transfer area per unit volume/material volume is compared for the same hydraulic diameter. The MCHX was assumed to have 10 square ports with material thickness as defined in Figure 90 and 20 FPI. The NGHX-13 geometry shown in Figure 2 was used with circular, square and diamond shaped ports, Figure 91. for circular and diamond shaped ports, the number of ports was calculated based on the same hydraulic diameter and flow area as for the square MCHX in order to maintain the same refrigerant side pressure drop. NGHX-13 with circular ports provide larger area per unit HX volume (compactness) for port size less than 0.3 mm, as shown in Figure 92, and larger area per unit HX material volume (material utilization) for port size less than 1 mm, as shown in Figure 93. This is mainly caused by the smaller fin surface area contribution at smaller port sizes. For MCHX, the finned area is larger than 50% of the total airside HT area for a D_h of 1 mm and less than 10% of the total airside HT area for a D_h of 0.1 mm. Further studies on the NGHX-13 port shapes showed that

diamond shaped ports are best in compactness followed by square while the later provided superior material utilization. Compactness is shown in Figure 94 and Figure 95 for rectangular and diamond shaped ports respectively. Material utilization is shown in Figure 96 and Figure 97 for rectangular and diamond shaped ports respectively. The benefit of using square or diamond shaped ports might be outweighed by the increase in airside pressure drop. Hence circular ports are used in the pilot investigations performed in this dissertation.

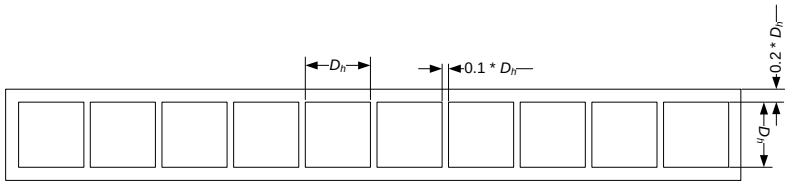

Figure 90: Microchannel tube configuration

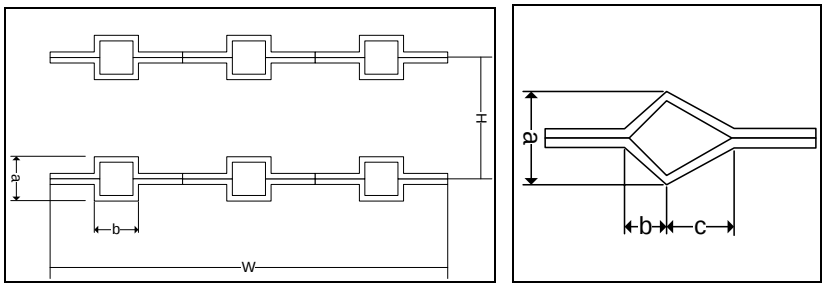

(a) (b)

Figure 91: Alternative NGHX-13 port shapes: (a) square, (b) diamond

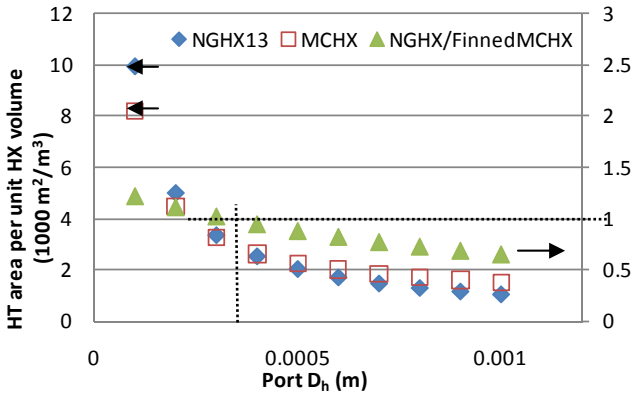

Figure 92: Heat transfer area per unit HX volume

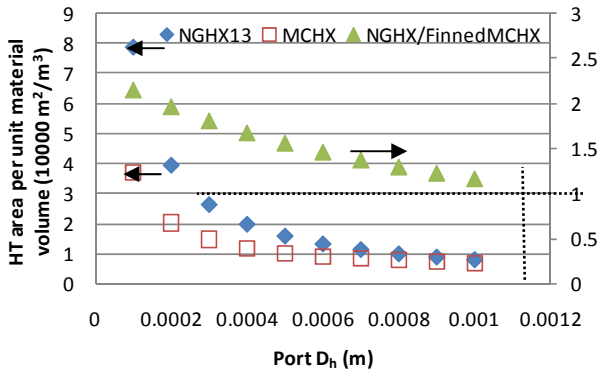

Figure 93: Heat transfer area per unit HX material volume

It is shown that the rectangular port with an aspect ratio of 1 (square) provide higher HT area per unit volume with similar material utilization to the circular ports. The diamond shaped ports provided better compactness than the square ports, however at the cost of inferior material utilization. Circular ports were seen as better candidates in terms of initial investigations due to easier manufacturing techniques. Furthermore, the benefit of using square or diamond shaped ports could be outweighed by the increase in airside pressure drop.

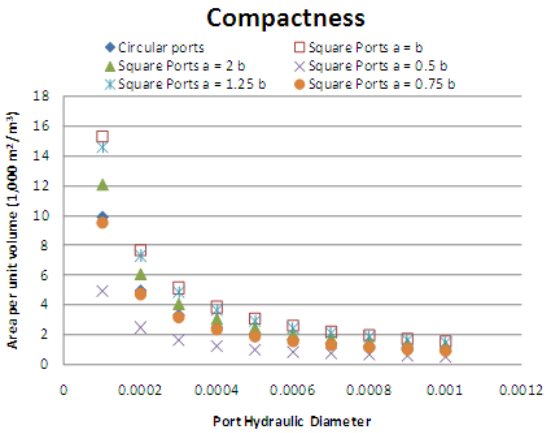

Figure 94: NGHX-13 compactness for rectangular ports with different aspect ratios

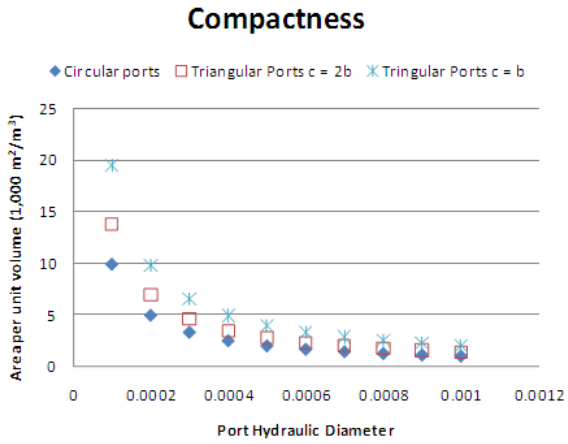

Figure 95: NGHX-13 compactness for diamond ports

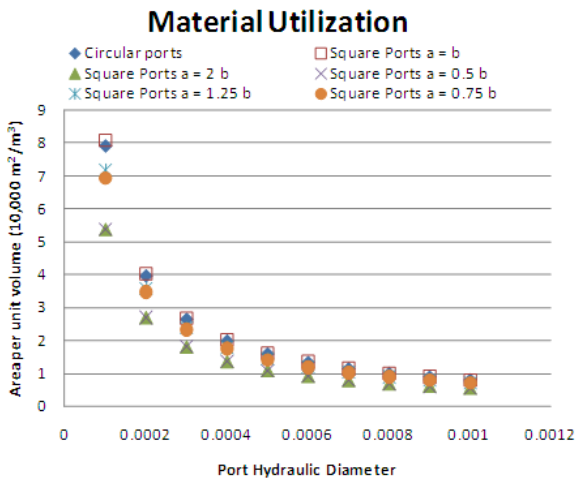

Figure 96: NGHX-13 HT area per unit HX material volume for rectangular ports

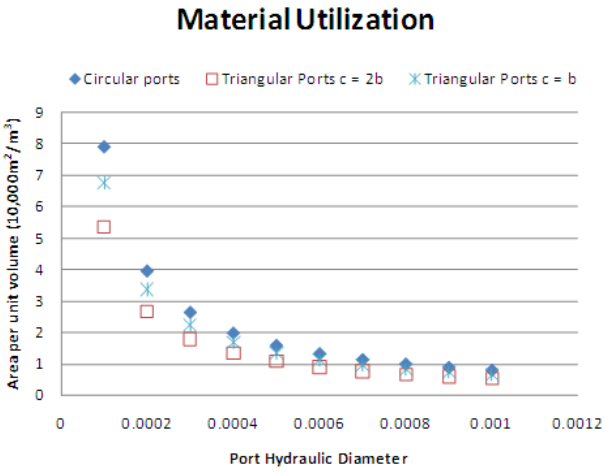

Figure 97: NGHX-13 HT area per unit HX material volume for diamond ports

12.1.3. Impact of thermal conductivity on overall heat transfer coefficient

Smaller tube diameters are promising due to their potential to increase compactness and material utilization. Furthermore, smaller tube diameters lead to smaller material thickness; hence the conduction heat transfer resistance diminishes.

In order to investigate the impact of tube material thermal conductivity on the overall heat transfer coefficient the change in overall heat transfer coefficient was studied for different tube diameters at different tube thickness ratios. This study is based on the following assumptions:

- Plain tubes with different thickness ratios (t/D_{out}) from 5 to 20 %.
- Tube diameters varying from 0.1 to 10 mm.
- Airside HTC using Hilpert Correlation (Incropera and DeWitt 1996).
- Waterside HTC based on laminar fully developed flow: $Nu_D = 4.36$.
- Liquid water inside tube and air on the outside with constant fluid properties as summarized in Table 27.

The overall HTC based on the internal surface area is calculated as shown in equation (60). This equation is valid for the tubes with different material thicknesses assuming 1-D heat conduction.

Table 27: Fluid Properties for tube material thermal conductivity study

Inner Fluid "Water"			Outer Fluid "air"	
ρ	977		ρ	1.177
k	0.665		k	0.02622
μ	0.000393		μ	1.86E-05
cp	4191.1		cp	1006.6
			Pr	0.714064

$$U_i = \frac{1}{\frac{1}{h_i} + \frac{r_{in}}{k_{tube}} \ln\left(\frac{D_{out}}{D_{in}}\right) + \frac{D_{in}}{h_{out} D_{out}}} \qquad (60)$$

The percentage change in overall HTC due to tube material thermal conductivity reduction form 200 to 0.2 W/mK is then calculated as shown in equation (61). The results are shown in Figure 98 for different tube thicknesses (5% to 20% of D_o) for D_i ranging from 0.1 to 10 mm.

$$\%\ \text{Overall HTC change} = \frac{U_{i,k_{tube}=0.2} - U_{i,k_{tube}=200}}{U_{i,k_{tube}=200}} * 100\% \qquad (61)$$

The results shown in Figure 98 depict that the conduction thermal resistance contribution to the overall HTC reduces greatly as the channel dimension or tube material thickness are reduced. In this case, using low thermal conductivity material such as polymers for NGHX-13 with a tube thickness of 20% of D_o reduces the performance by less than 10% for tubes with port diameter smaller than 0.7 mm.

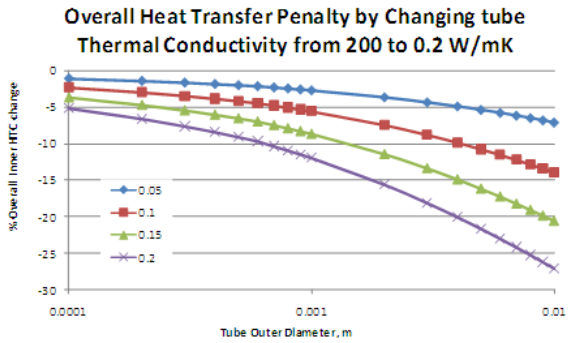

Figure 98: Percentage Change in U_i

12.2. Appendix B: Structural Analysis of NGHX-13

New concept geometries come with the challenge of structural integrity. In order to ensure the ability of the proposed structure to withstand the fluids' operating pressures as well as other loading requirements, a parametric FEM needs to be conducted covering the range of design conditions. In the current study, FEM is only used to investigate the ability of the flow channels to contain refrigerant's operating pressures. As such a parametric FEM study for NGHX-13 tube structure was conducted. The problem was formulated for a tube with 3 circular ports using the Design Explorer (DX) tool within the ANSYS Workbench®. The geometry was parameterized as shown in Figure 99 incorporating tube diameter, tube wall thickness and tube material. Refrigerant's operating pressure was assumed to be 2.5 MPa and tube ends were assumed as fixed supports. The FEM results of interest were the maximum equivalent stresses and the minimum factor of safety.

NGHX-13 geometry was generated using the outer diameter and the tube thickness ratio as the only input parameters using ANSYS DesignModeler®. The FEM analysis settings were also automated in order for the DX to evaluate the equivalent stresses and factor of safety for different designs. The parametric runs included 4 values for D_o (0.125, 0.47, 0.94, and 1.25 mm), 4 values for thickness ratio (0.05, 0.1, 0.15, and 0.2) and 3 tube materials (Stainless steel, Aluminum alloy, and Polyethylene). A sample solid mesh is shown in Figure 100 and a sample equivalent stresses and factor of safety distribution in a stainless steel tube are shown in Figure 101 and Figure 102 respectively. Tube diameter did not affect the structural integrity for the same material and thickness ratio which is intuitive since the major factor in

the structural analysis is the thickness to diameter ratio and the yield strength. The minimum factor of safety is plotted against the tube thickness ratio for the 3 materials in Figure 103. The results indicate that higher yield strength materials could be used with the smallest thickness ratio while for reduced yield strength (polymer materials); higher thickness ratio (0.15 or 0.2) is required to have an appropriate factor of safety.

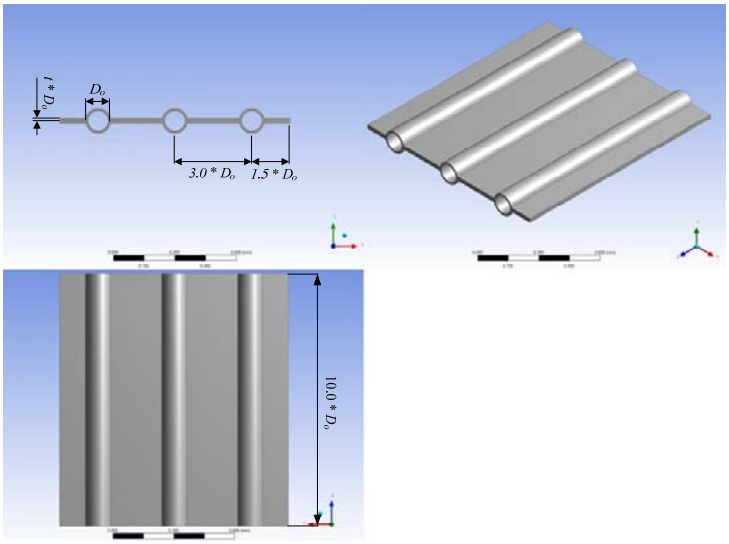

Figure 99: NGHX-13 geometrical parameters used in structural analysis

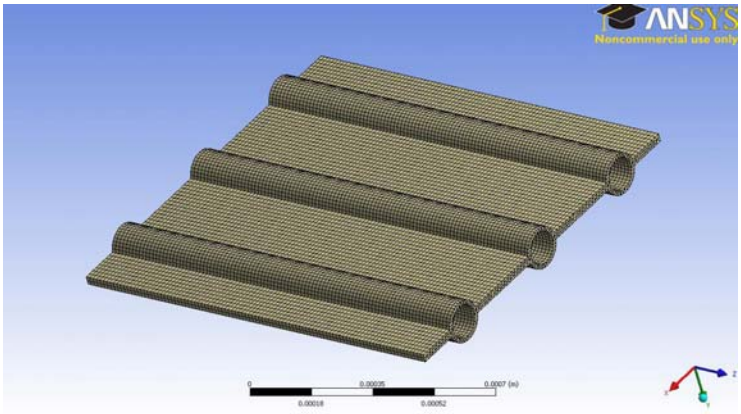

Figure 100: Sample NGHX-13 solid structural mesh

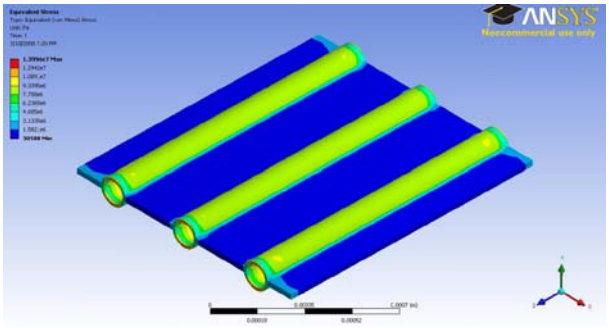

Figure 101: Equivalent stresses subject to internal pressure of 2.5 MPa – SS tubes

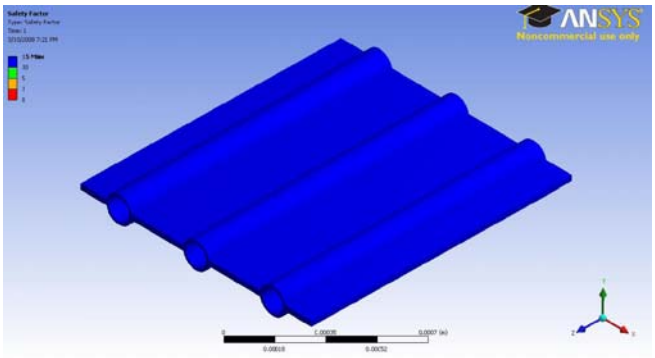

Figure 102: Factor of safety subject to internal pressure of 2.5 MPa – SS tubes

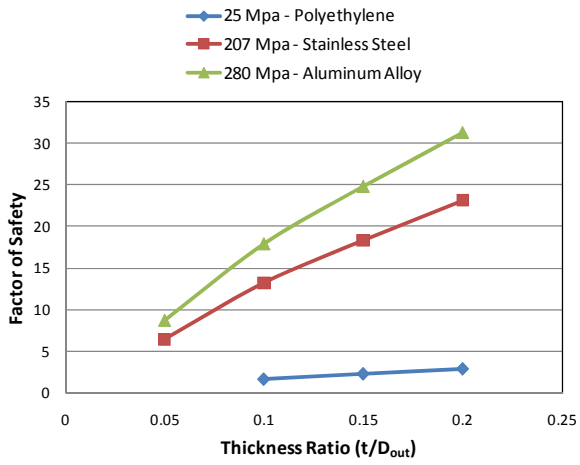

Figure 103: Minimum Factor of Safety for NGHX-13 with different thickness ratio and different materials

12.3. *Appendix C: Water Flow in Microtubes Numerical Validation*

The objective of this investigation is to test the conventional correlations validity for water flow through microtubes. This is an important step before the multi-scale HX simulation, Chapter Chapter 4:, can be devised. In this study, correlation validity is investigated numerically for sub-millimeter hydraulic diameter and low Re. The general body of literature agrees now that conventional heat transfer and pressure drop correlations are valid for tube diameters as low as 100 μm (Guo and Li 2003, Morini 2004, Lee et al. 2005, Shen et al. 2004, Steinke and Kandlikar 2005). However, all studies showed higher uncertainty at lower Re and smaller tube diameters. Furthermore, the thermal entry length effect is yet to be clearly defined. Numerical simulations using the commercial CFD package FLUENT ® are used as higher fidelity tool to investigate the lower end of Re in the laminar flow region. CFD can be seen as a reliable tool especially when measurement uncertainties are prohibitively high such as in the case of lower Re laminar flow. Systematic verification and validation of the CFD results are presented to build confidence in the numerical results.

12.3.1. Approach

Water flow in microtubes with inner diameters ranging from 100 to 1000 μm is modeled using CFD simulations. The tubes considered had a length to diameter ratio of 500 to ensure that the developing length is captured and fully developed flow is exiting the tube. These simulations were performed using FLUENT® 6.3.26 commercial CFD packages. The computational mesh was generated using Gambit® 2.3.16. For the validation cases, tubes are made similar to those reported in the

experimental setups from literature. The effect of simulation domain configuration, water properties and mesh convergence are studied in order to ensure reliable simulations. FLUENT® 3-D double precision segregated solver is used to sequentially solve the governing equations. Second order upwind scheme was used for the governing equations discretization. The solver starts by updating the fluid properties (if there is a dependence of flow variables), then the discretized momentum equations are solved to update the flow field velocities. These updated velocity fields are then used in the pressure-velocity coupling equation in order to satisfy the continuity equation and update the pressure and mass flow rates in the solution domain. For faster convergence, SMPLEC algorithm (Van Doormaal and Raithby 1984) was used for the pressure velocity coupling. Finally, all scalar equations (like the energy equation) are solved to update their values in the solution domain. This process is repeated until convergence is achieved.

12.3.2. Model accuracy

Considering the number of parametric runs required in the study, modeling the full tube would be computationally expensive. Simplification can be achieved by either assuming 2 planes of symmetry and thus modeling one fourth of the tube (Quad Tube configuration (Lee et al. 2005) or employ the axisymmetric 2D assumptions (Lelea et al. 2004). To check the effect of these assumptions on the simulation results, a 100 mm long tube with 0.5 mm inner diameter and 0.7 mm outer diameter steel tube was simulated using the 3 configurations: full 3D, 3D Quad Tube and 2D axisymmetric simulations. Figure 104 and Figure 105 show the mesh details for the 2D and 3D configuration respectively.

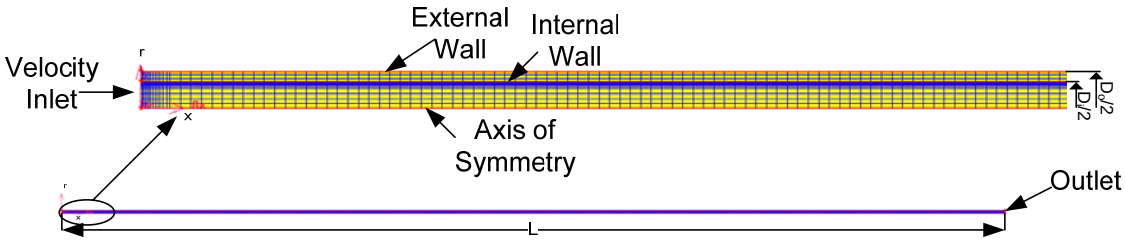

Figure 104: 2D axisymmetric mesh details showing fine mesh near the wall boundary

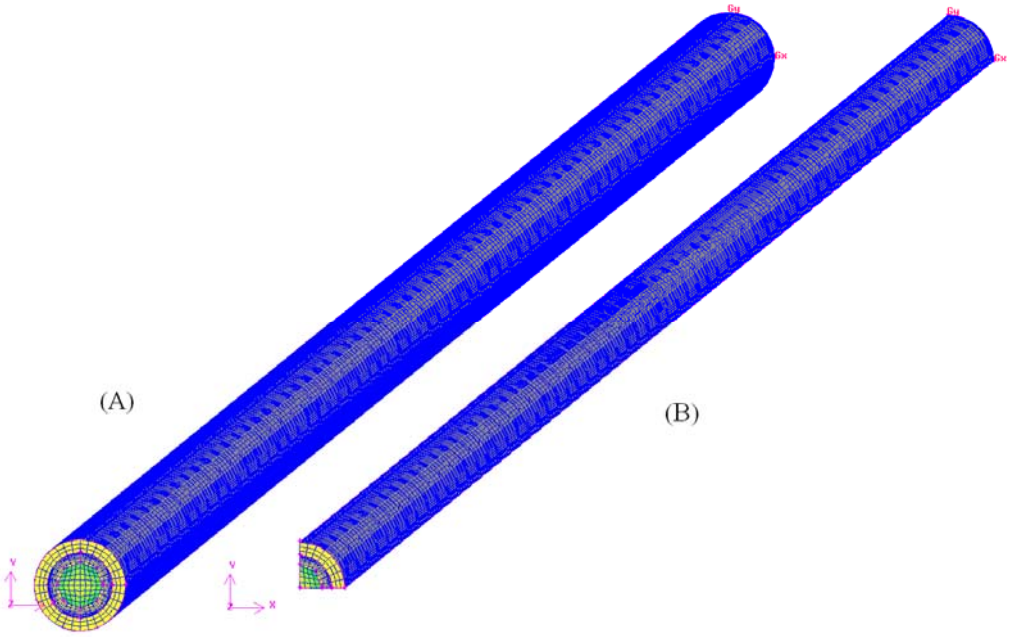

Figure 105: 3D mesh details, (A) full, (B) Quad Tube

The mesh was generated with the same spacing and boundary layer inflation for the 3 geometries, the same initial and boundary conditions were applied as well as the same solver details. The inlet water velocity was set to be uniform at 0.5 m/s, while the outer tube wall was subject to a heat flux of 75 kW/m^2. Results are summarized in Table 28, depicting that axisymmetric simulation under predicts values for heat transfer and pressure drop. The use of symmetry planes to reduce the

problem to just simulating one fourth of the tube produced results that are within the numerical accuracy. Based on the savings in computational time using the "Quad Tube" configuration, was further used in the following analysis.

Table 28: Simplified model results

	Full 3D	Quad Tube 3D	2D axisymmetric
Pressure drop (Pa)	5658.1016	5658.1367	5532.5488
Error %	0	6.2e-4%	2.219%
ΔT_{water}	40.89713	40.89706	40.43494
Error %	0	-1.7e-4%	-1.13%

Another important factor in the accuracy of the model is the impact of temperature dependent fluid properties. REFPROP 8.0 (Lemmon et al. 2007) shows that water viscosity exhibits a large dependence on temperature. Water viscosity is 853.81 μPa-s at 300 K and 368.81 μPa-s at 350 K, which is a 56.8% reduction for 50 K temperature increase. To account for such temperature dependence during CFD simulations, data between 300 K and 360 K were fitted in a cubic form as shown in equation (62). The coefficients of this equation are used to define the water viscosity in Fluent®. Other properties like density, thermal conductivity and specific heat capacities did not exhibit a considerable difference for a 50 K temperature rise. As such, water properties, other than viscosity, were evaluated at 300 K throughout the study.

$$\mu = 6.304491\times10^{-2} - 5.164042\times10^{-4}\times T + 1.42941\times10^{-6}\times T^2 - 1.3303\times10^{-9}\times T^3 \quad (62)$$

The same problem defined earlier is used to evaluate pressure drop and temperature to compare between variable and constant viscosity for the same heating mode. The fact that the viscosity is variable now during the simulation makes the choice of the viscosity value used in calculating the Po, given by equation (63) an open question. One option is to calculate the viscosity based on the average wall temperature along the tube, another option is to use the average of inlet and outlet viscosity, as suggested in (Judy et al. 2002), or report it based on the inlet viscosity. In addition, 3 values of outer wall heat fluxes were used to estimate the effect of heat flux on the temperature dependent viscosity evaluation. The CFD simulation results are summarized in Table 29.

$$\mathrm{Po} = f \times \mathrm{Re} = \frac{2\Delta P D_h^2}{L \mu v} \tag{63}$$

Table 29: Summary results for variable viscosity study

Case	1	2	3	4	5	6
Heat Flux (kW/m^2)	75	75	37.5	37.5	18.75	18.75
Viscosity	Variable	Constant	Variable	Constant	Variable	Constant
Pressure Drop (Pa)	3454	5658	4284	5658	4881	5658
T_{out} (K)	340.87	340.9	320.44	320.45	310.22	310.22
T_{wall} (K)	337.59	338.83	318.93	319.14	309.51	309.56
$\mu@(T_{in})$ (μPa-s)	852.11	853.82	852.28	853.82	852.36	853.82
$\mu@(T_{wall})$	455.08	853.82	596.86	853.82	705.45	853.82
$\mu@((T_{in} + T_{out})/2)$	635.91	853.82	712.53	853.82	772.18	853.82
$Po@(T_{in})$	40.53	66.27	50.26	66.27	57.27	66.27
$Po@(T_{wall})$	75.90	66.27	71.77	66.27	69.19	66.27
$Po@((T_{in} + T_{out})/2)$	54.31	66.27	60.12	66.27	63.21	66.27

For the constant viscosity cases, the Po number was constant for the 3 heat fluxes. The value of 66.27 is slightly higher than the theoretical value of 64.0 due to developing length. Results presented in Table 29 show that Po number approaches that of constant viscosity as the heat flux is reduced. Furthermore, it is shown that the choice of viscosity value to be used is very important. In the case of using inlet or average inlet and outlet viscosities, the Po is less than theoretical value and tends to increase with decreasing the heat rate. In the case of using the viscosity at the average wall temperature, the Po is larger than the theoretical value and decreases with the decrease in heat rate. Furthermore, if the viscosity is taken to be the average between average inlet and outlet viscosity and average wall viscosity Po was found to be 63.2, 65.43 and 66.07 for the 75, 37.5, and 18.75 kW/m^2 heat flux respectively. These values are well within the conventional values. On the other hand, it is clear that the effect of temperature dependent viscosity on heat transfer is very minimal and could be neglected. In order to have data that is not controversial, constant viscosity values were used. Furthermore, if a pressure drop or heat transfer correlation is implemented in a segmented heat exchanger model, the fluid temperature rise per segment will be relatively small and hence these effects could be neglected.

In addition to the flow modeling checks performed above, systematic numerical verification is used to identify the GCI and the estimated error in the simulations. Following the approach described in section 3.2.1, the estimated error was found to be less than 1% for the heat transfer coefficient calculations and less than 0.5% for pressure drop calculations. These results suggest that the second mesh used in this analysis is adequate and provide accurate simulation results.

Table 30: Verification summary

	Pressure Drop	Temperature difference	Heat transfer coefficient
ϕ	$P_{in} - P_{out}$	$T_{in} - T_{out}$	$U = q/(A_i \Delta T)$
r_{21}	1.212		
r_{32}	1.307		
ϕ_1	29941.45	3.9372	3459.531
ϕ_2	29928.19	3.9299	3446.025
ϕ_3	29796.297	3.9888	3467.083
p	8.149	8.107	1.866
ϕ_{ext}^{21}	29944.9414	3.93913	3490.8270
e_a^{21}	0.04427%	0.1852%	0.39%
e_{ext}^{21}	0.01167%	0.04929%	0.9%
GCI_{fine}^{21}	0.01459%	0.06164%	1.13%

In addition to the verification analysis performed above, a series of validation tests were preformed. CFD predictions were compared against experimental data from (Lelea et al. 2004). The experimental data was for water flow in stainless steel tubes heated by the joule heating effect. For the validation purposes, the "Quad Tube" configuration was used. CFD results showed no significant effect of the heat flux on the local Nu or Po. However, in the experimental data, Po for the 125.4 μm tube was around 60 while CFD prediction showed it to be at an average of 65. Furthermore, CFD prediction were able to account for the effect of developing length as seen in Figure 106 where for the 125.4 and 300 μm tubes the longer the developing length is (lower end of L/L_e) the higher the apparent Po becomes. For the heat transfer validations, the CFD under-predicted the experimental values in the thermally developing region but the same trends were captured. Furthermore, the heat flux was shown to have no effect on Nu. The local heat transfer along the tube length is

illustrated in Figure 107 to Figure 109 for the 3 tube diameters under considerations at different Re.

These results suggest that CFD simulations are capable of capturing the underlying physics in the microscale heat transfer if the proper mesh is generated. Furthermore, CFD prediction allows us to probe the fluid flow details anywhere in the solution domain. In addition, statistical approaches like area-weighted-average and mass-weighted-average can be used to accurately determine the properties of interest.

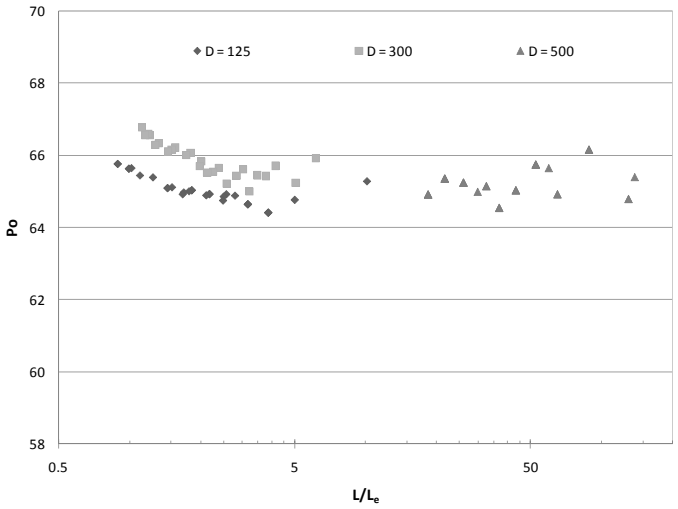

Figure 106: Entry length effect on Po

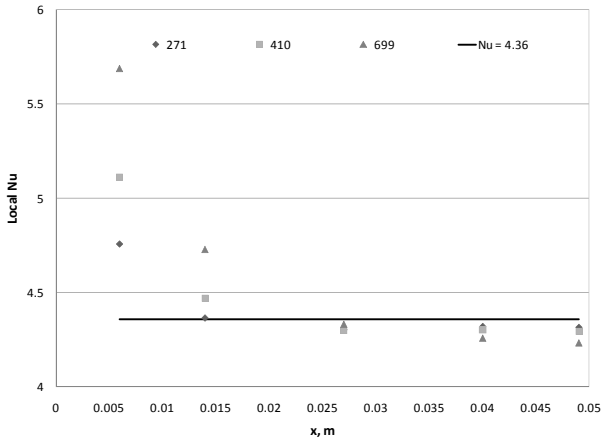

Figure 107: Local Nu along the tube length, D_i = 125 µm for different Re

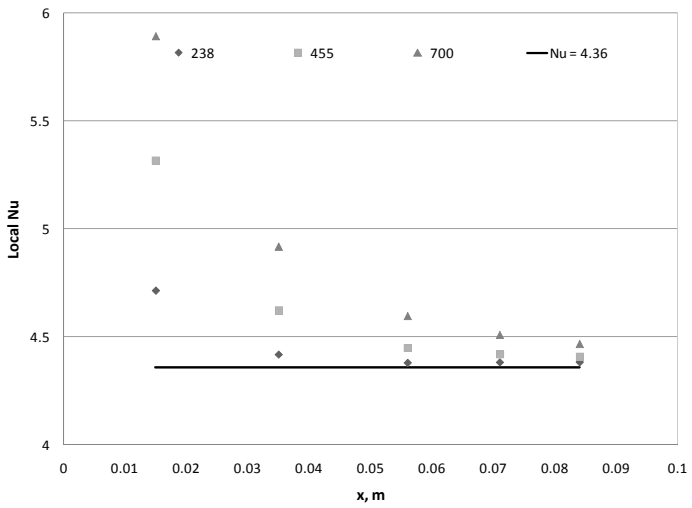

Figure 108: Local Nu along the tube length, D_i = 300 µm for different Re

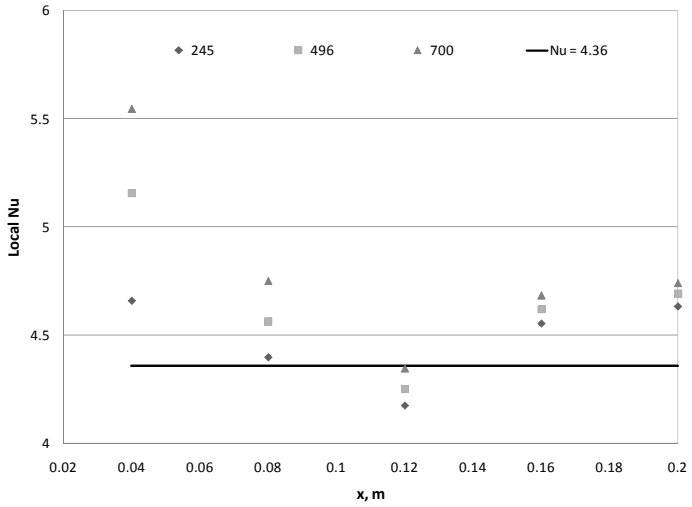

Figure 109: Local Nu along the tube length, D_i = 500 µm for different Re

12.3.3. Results

The same CFD solver details described earlier were used to investigate the simultaneously developing heat transfer and fluid flow in microtubes. A parametric study was performed on 6 tubes with internal diameters of 100, 200, 400, 600, 800 and 1000 µm. The Re was varied from 10 to 500. All tubes had the same D_o/D_i ratio

of 1.25 and L/D_i ratio of 500. In this analysis, a cooling process was assumed where heat is rejected from the hot water flowing through the microtube. This process is relevant for the case of microscale air to single-phase refrigerant heat exchangers.

The parametric study was performed using a mesh consisting of 705705 finite volumes in the fluid domain and 300300 finite volumes in the solid domain for the "Quad Tube" configuration shown in Figure 105. CFD simulations were performed assuming constant water properties. The external wall boundary was treated as a convective boundary with a heat transfer coefficient of 300 W/m^2-K and ambient temperature of 300 K. Uniform inlet water velocity was used while the outlet was set to be a pressure outlet.

Microscale laminar pressure drop is highly affected by the developing length as discussed hereinbefore. In this flow developing region, pressure drop is highly non-linear due the increased wall shear stress imposed by the radial velocity profile. In this regards, it is required to compare the hydrodynamic developing length to conventional theory. The developing length is the length required for the flow to become self similar; this can be characterized by constant centerline velocity for a constant area pipe. According to (Suryanarayana 1995) the hydrodynamic entrance length in a simultaneously developing flow can be calculated from equation (64). To estimate the entrance length from CFD prediction, values of centerline velocity was compared against the fully developed velocity. The criterion of developing length was based on having the centerline velocity within 1% of the fully developed centerline velocity.

$$L_e = 0.0565 \,\mathrm{Re}\, D_i \tag{64}$$

The difference between the CFD predicted and theoretical entrance length is shown in Figure 110. It is clear that for lower Re, the entrance length is less accurately captured by the conventional correlation. The difference is more than 20% for Re less than 100. The entrance length effect on the apparent pressure drop can be seen in Figure 111 which shows the difference between the apparent and fully developed Po for different L/L_e ratios. It is shown that for L/L_e larger than 200 the apparent and fully developed Po values coincide.

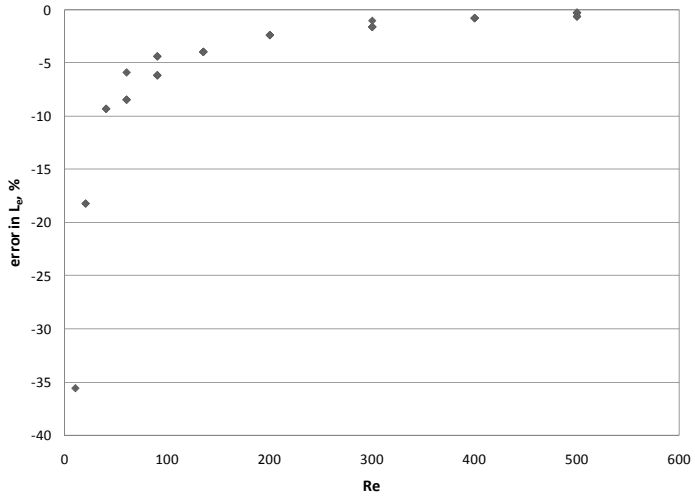

Figure 110: Difference between Theoretical and CFD-predicted entrance length

Based on the results presented, the fully developed Po number is within ± 0.5% of the theoretical value of 64 excluding cases with low Re and larger inner diameters (Re less than 60 with D_i larger than 400μm). For these cases, the difference between the apparent and fully developed Po was minimal. These CFD results suggest that the use of conventional laminar pressure drop correlation is valid if the developing length is less than 0.5% of the tube length. If the entrance length is larger, a developing length pressure drop correlation such as that of Shah and London (1978)

should be used. Furthermore, the entrance length at smaller Re should be further investigated as conventional entrance length correlations failed below a Re of 100.

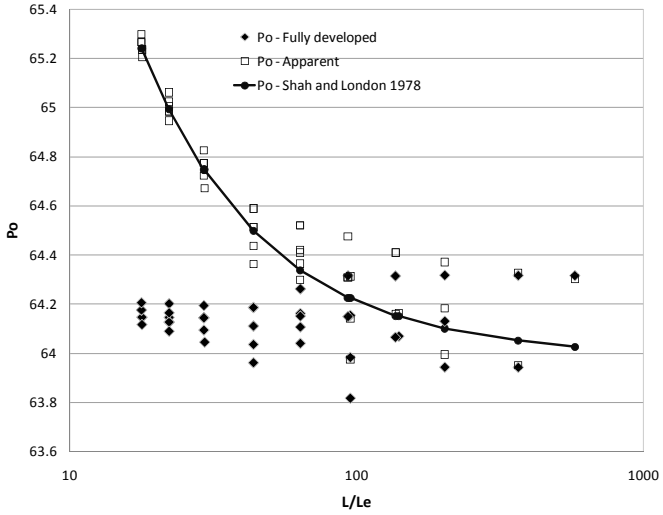

Figure 111: Fully developed and apparent Po for different L/L_e

Thermal entrance length is characterized by increased local Nu. This entrance length depends on Pe. If thermal entrance length is comparable to the tube length, its contribution to heat transfer enhancement becomes significant; which can be seen as an opportunity for heat transfer augmentation. Theoretical entry length can be calculated from equation (65) (Suryanarayana 1995).

$$L_{e,th} = \begin{cases} 0.037\,\mathrm{Re}\,\mathrm{Pr}\,D_i, & \text{Constant wall temperature} \\ 0.053\,\mathrm{Re}\,\mathrm{Pr}\,D_i, & \text{Constant wall heat flux} \end{cases} \quad (65)$$

For the CFD prediction, the thermal entry length is defined as the length required for the flow to reach a value within 5% of the fully developed local Nu, (Kays et al. 2005). The fully developed Nu is based on the average local Nu between 80% and 90% of the total tube length. Based on CFD results, the slope of equation (65) was found to be 0.044924 with an R^2 value of 0.997867 as seen in Figure 112.

This is 15% less than the theoretical value of 0.053. However, when the criterion for the thermal entry length based on fully developed Nu was changed from 1 to 10% the slope of the curve varied from 0.074447 to 0.032004 as shown in Table 31. This suggests that the theoretical thermal entry length agrees well with the CFD prediction in the microscale. The percentage difference between CFD-predicted and theoretical thermal entry length is plotted in Figure 113. The error is higher in the case of Pe less than 150; larger Pe showed differences within ±20%.

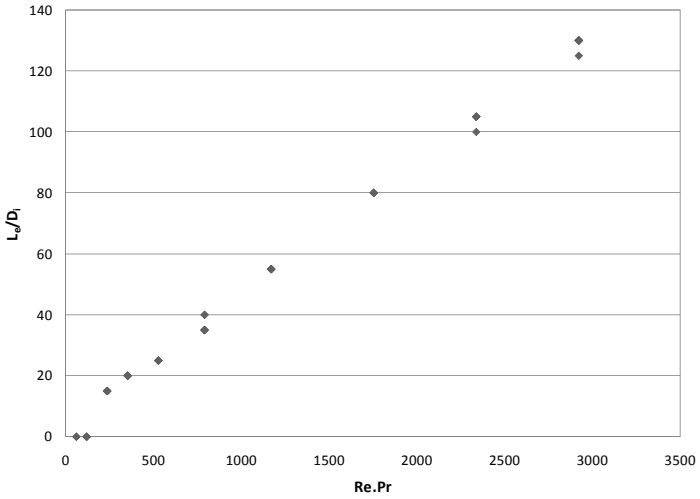

Figure 112: Thermal entrance length versus Pe - all cases

The local Nu for all points was plotted against Gz number to check for correlation validity. The CFD predicted data was compared against Shah and London (1978), Stefan (1959), Sider and Tate (1936), as well as the generalized Hausen correlations as suggested by (Morini 2004). The coefficients of the generalized Hausen correlations are taken from (Rohsenow and Choi 1961). Comparison between correlations and CFD-predicted local Nu are shown in Figure 114. These results suggest that the generalized Hausen correlation provide the best fit over the entire range of data.

The local Nu prediction for the fully developed portion of the water flow agrees well with the conventional value of 4.36. The average local Nu at 90% of the tube length was 4.33 with a standard deviation of 5%.

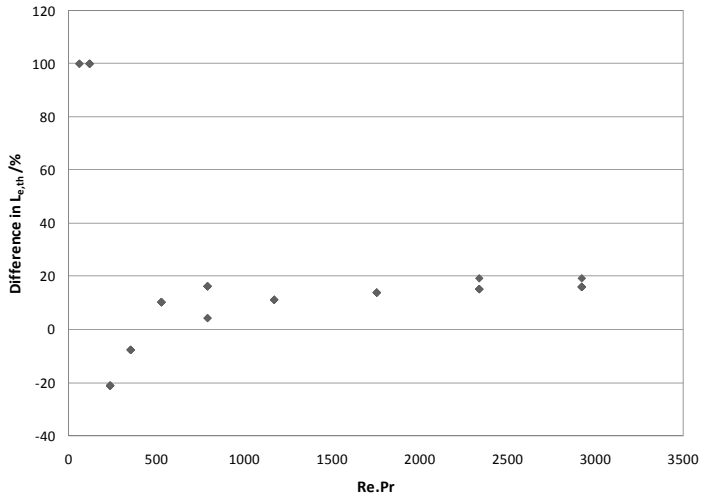

Figure 113: Difference between CFD-predicted and theoretical thermal entry length

Table 31: Curve fitting for the thermal entry length

Criteria, % of Nu	m	R^2
1	0.074447	0.998614
2	0.062028	0.998649
4	0.048759	0.998199
6	0.041351	0.996995
8	0.036302	0.998343
10	0.032004	0.996783

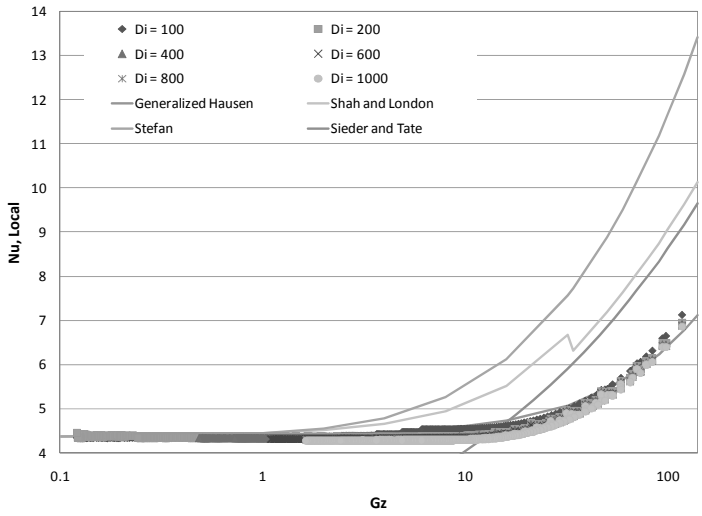

Figure 114: Local Nu for different Gz - all cases

12.3.4. Summary

CFD simulations were used for the study of single phase liquid heat transfer and pressure drop in microtubes of internal diameters ranging from 100 to 1000 μm. Verification and validation showed that the errors are far less than the experimental error. A systematic CFD uncertainty analysis was used and showed errors to be less than 2% with high observed convergence index. It was also shown that the use of 2D axisymmetric assumption simulations under-predicts the heat transfer and pressure drop due to the missing diffusion term in the governing equations. In order to reduce the computational cost, only 1 quadrant of the tube was simulated assuming 2 symmetry planes. Comparisons with the full tube simulations showed errors to be within the numerical precision error. Also, the temperature dependent viscosity effect was studied showing that it has an impact on the pressure drop. However, the Po number did not change if the accurate averaging for the viscosity was used.

The results for the single-phase heat rejection assuming convective boundary conditions showed that the fully developed values are the same as those for

conventional correlations for the constant wall heat flux values. Predicted Po was well within the theoretical value of 64; the hydraulic entrance length was also well represented by the theoretical entrance length equation for Re above 100. The results show that more studies are needed for the case where Re less than 100. This range of Re would be of importance for air to refrigerant microchannel heat exchangers. As for the heat transfer, the local Nu was well predicted with the generalized Hausen correlation. However, the thermal entry length was within ± 20% of the theoretical correlations based on the fully developed criteria. For Pe_D less than 150, CFD simulations showed very small thermal entry length compared to theoretical correlations showing close to 100% deviation.

12.4. Appendix D: First Order Header Analysis Problem Definition

Using the flow resistance analogy, the mass flow distribution and pressure drop in a heat exchanger problem can be presented as shown in Figure 115. This figure highlights the different flow resistances and the key Pressure nodes locations. The total number of unknowns in such a circuit is a function of the number of parallel flow channels, $5n-2$. The breakdown of the number of unknowns is as follows:

- Inlet header pressures: n – 1
- Outlet header pressures: n
- Port velocities: n
- Inlet header velocities: n – 1
- Outlet header velocities: n

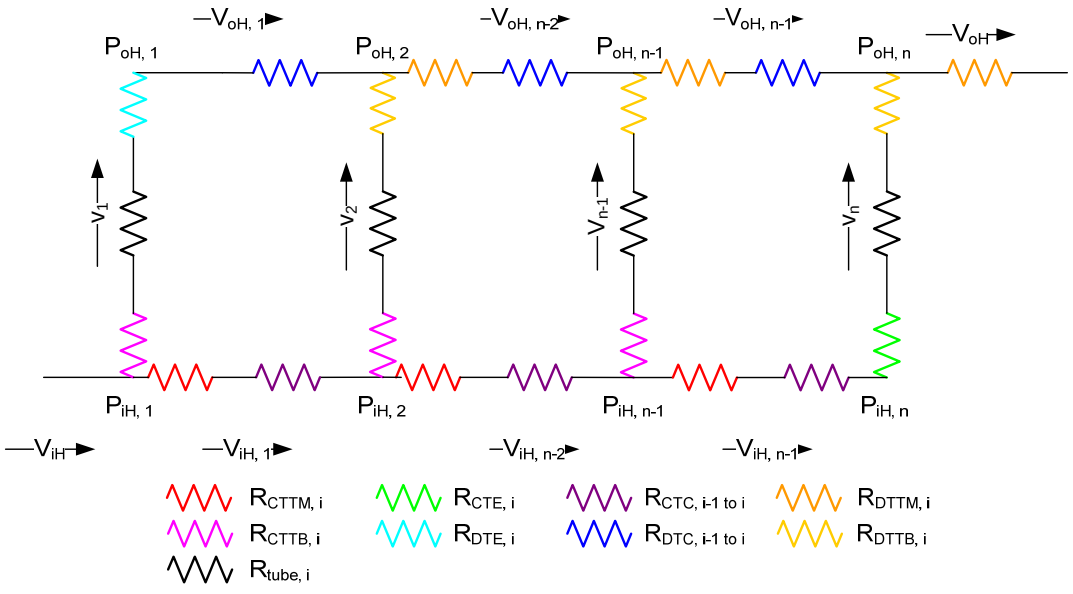

Figure 115: refrigerant flow circuitry

The refrigerant flow circuit presented in Figure 115 can be analyzed by solving the following equations (66) through (74) simultaneously. Note that equations (67) and (68) are repeated for i = 2 to n (n – 1 equations), equation (70) is repeated for i = 3 to n (n – 2 equations), and equations (71) and (72) are repeated for i = 1 to n – 1 (n – 1 equations). These equations result in a system of $5n-2$ nonlinear equations. Further complication arises from the fact that the pressure drop coefficients have some sort of dependence on the flow velocity; hence additional system of equation is solved simultaneously to obtain the required pressure drop coefficients.

$$P_{oH,1} = P_{iH,1} - \frac{1}{2}\rho\left[K_{CTTB,1} + K_{tube,1} + K_{DTE,1}\right]v_1^2 \tag{66}$$

$$P_{oH,i} = P_{iH,i-1} - \frac{1}{2}\rho\left[K_{CTTB,i} + K_{tube,i} + K_{DTTB,i}\right]v_1^2 \tag{67}$$

$$P_{iH,i} = P_{iH,i-1} - \frac{1}{2}\rho\left[K_{CTTM,i}v_{iH,i-1}^2 + K_{CTC,i-1\text{ to }i}v_{iH,i}^2\right] \tag{68}$$

$$P_{oH,2} = P_{oH,1} - \frac{1}{2}\rho\left[K_{DTC,i-1\text{ to }i}v_{oH,i}^2\right] \tag{69}$$

$$P_{oH,i} = P_{oH,i-1} - \frac{1}{2}\rho\left[K_{DTTM,i}v_{oH,i-1}^2 + K_{DTC,i-1\text{ to }i}v_{oH,i}^2\right] \tag{70}$$

$$v_{iH,i} = \frac{v_{iH,i-1}A_{iH,i-1} - v_i A_p}{A_{iH,i}} \tag{71}$$

$$v_{oH,i} = \frac{v_{oH,i-1}A_{oH,i-1} + v_i A_p}{A_{oH,i}} \tag{72}$$

$$v_{oH} = v_{iH} \tag{73}$$

$$v_{iH} = \sum_1^n v_i \tag{74}$$

Where

- K_{CTC} = Pressure drop coefficient for converging tapered channel (accounting for static pressure loss)
- K_{DTC} = Pressure drop coefficient for diverging tapered channel (accounting for static pressure regain)
- K_{tube} = Pressure drop coefficient for developing flow in circular tubes (accounting for developing length)
- K_{CTTM} = Pressure drop coefficient for converging tapered tee to the main flow
- K_{CTTB} = Pressure drop coefficient for converging tapered tee to the branch flow
- K_{DTTM} = Pressure drop coefficient for diverging tapered tee from the main flow
- K_{DTTB} = Pressure drop coefficient for diverging tapered tee from the branch flow
- K_{CTE} = Pressure drop coefficient for converging tapered elbow
- K_{DTE} = Pressure drop coefficient for diverging tapered elbow
- $v_{iH,\,i}$ = average flow velocity at the inlet header between tube i and tube i + 1
- $v_{oH,\,i}$ = average flow velocity at the outlet header between tube i and tube i + 1
- v_i = average flow velocity at tube

Bibliography

Abdelaziz, O., Aute, V. and Radermacher, R. (2007) 'Compact mini-channel heat exchanger', PS-2007-116),

American Institute of Aeronautics and Astronautics. (1998) *AIAA guide for the verification and validation of computational fluid dynamics simulations,* Reston, Va.: American Institute of Aeronautics and Astronautics.

Androulakis, I. P. and Venkatasubramanian, V. (1991) 'Genetic algorithmic framework for process design and optimization', *Computers and Chemical Engineering,* 15(4), 217-228.

'ANSYS CFX', (2006)

Aute, V. (2008) *Single and Multiresponse Adaptive Design of Experiments with Application to Design Optimization of Novel Heat Exchangers*, Working Dissertation, University of Maryland, College Park, MD, June 20th 2008.

Aute, V., Abdelaziz, O., Azarm, S. and Radermacher, R. (2008) *Cross-validation based single response adaptive design of experiments,* translated by Victoria, British Columbia, Canada: AIAA, AIAA-2008-6067: 1- 23.

Babu, B. V. and Munawar, S. A. (2007) 'Differential evolution strategies for optimal design of shell-and-tube heat exchangers', *Chemical Engineering Science,* 62(14), 3720-3739.

Babuska, I. and Oden, J. T. (2004) 'Verification and validation in computational engineering and science: Basic concepts', *Computer Methods in Applied Mechanics and Engineering,* 193(36-38), 4057-4066.

Badar, M. A., Zubair, S. M. and Sheikh, A. K. (1993) 'Uncertainty analysis of heat-exchanger thermal designs using the Monte Carlo simulation technique', *Energy,* 18(8), 859-866.

Bennett, I. J. D., Besant, R. W., Schoenau, G. J. and Johnson, A. B. (1994) *Procedure for optimizing coils in a run-around heat exchanger system,* 1 ed.*,* translated by New Orleans, LA, USA: ASHRAE, 442-451.

Bergles, A. E. (1997) 'Heat transfer enhancement - the maturing of second-generation heat transfer technology', *Heat Transfer Engineering,* 18(1), 47-55.

Bergles, A. E. (2002) 'ExHFT for fourth generation heat transfer technology', *Experimental Thermal and Fluid Science,* 26(2-4), 335-344.

Bernard, P. S. and Wallace, J. M. (2002) *Turbulent flow : analysis, measurement, and prediction,* Hoboken, N.J.: Wiley.

Bernier, M. A. and Dinse, D. R. (2002) *Uncertainty in the design length calculation for vertical ground heat exchangers,* translated by Atlantic City, NJ, United states: Amer. Soc. Heating, Ref. Air-Conditoning Eng. Inc., 939-944.

Brutin, D. and Tadrist, L. (2003) 'Experimental friction factor of a liquid flow in microtubes', *Physics of Fluids,* 15(3), 653-661.

Cadafalch, J., Perez-Segarra, C. D., Consul, R. and Oliva, A. (2002) 'Verification of finite volume computations on steady-state fluid flow and heat transfer', *ASME Journal of Fluids Engineering,* 124(1), 11-21.

Campbell, L. A. and Kandlikar, S. (2004) *Effect of entrance condition on frictional losses and transition to turbulence in minichannel flows,* translated by Rochester, NY, United states: American Society of Mechanical Engineers, 229-235.

Celata, G., Cumo, M., Guglielmi, M. and Zummo, G. (2002) 'Experimental investigation of hydraulic and single-phase heat transfer in 0.130-mm capillary tube', *Microscale Thermophysical Engineering,* 6(2), 85-97.

Celata, G. P. (2004) 'Single Phase Fluid Flow' in Celata, G. P., Guo, Z.-Y., Li, Z.-X. and Zummo, G., eds., *Heat Transfer and Fluid Flow in Microchannels*, Wallingford, U.K.: Begell House, Inc., 3-29.

Celata, G. P., Cumo, M., McPhail, S. J. and Zummo, G. (2007) 'Single-phase laminar and turbulent heat transfer in smooth and rough microtubes', *Microfluidics and Nanofluidics,* 3(6), 697-707.

Celik, I. and Zhang, W.-M. (1995) 'Calculation of numerical uncertainty using Richardson extrapolation: application to some simple turbulent flow calculations', *ASME Journal of Fluids Engineering,* 117(3), 439-435.

Cervone, G., Kaufman, K. K. and Michalski, R. S. (2000) *Experimental validations of the learnable evolution model,* translated by California, CA, USA: IEEE, 1064-1071.

Chaudhuri, P. D., Diwekar, U. M. and Logsdon, J. S. (1997) 'An automated approach for the optimal design of heat exchangers', *Industrial and Engineering Chemistry Research,* 36(9), 3685-3693.

Cho, S. M. (1987) 'Uncertainty analysis of heat exchanger thermal-hydraulic designs', *Heat Transfer Engineering,* 8(2), 63-74.

Chudnovsky, Y. and Kozlov, A. (2006) *Development and Field Trial of Dimpled-Tube Technology for Chemical Industry Process Heaters*, Final Report.

Chwalowski, M., Didion, D. A. and Domanski, P. A. (1989) 'Verification of evaporator computer models and analysis of performance of an evaporator coil', *ASHRAE Transactions,* 95(1), 1229-1236.

Clarke, D. D., Vasquez, V. R., Whiting, W. B. and Greiner, M. (2001) 'Sensitivity and uncertainty analysis of heat-exchanger designs to physical properties estimation', *Applied Thermal Engineering,* 21(10), 993-1017.

Cressie, N. A. C. (1993) *Statistics for spatial data,* Rev. ed., New York: J. Wiley.

De Losier, C. R., Subramanian, S., Ponyavin, V., Chen, Y., Hechanova, A. E. and Peterson, P. F. (2007) 'The parametric study of an innovative offset strip-fin heat exchanger', *ASME Journal of Heat Transfer,* 129(10), 1453-1458.

Deb, K. (2001) *Multi-objective optimization using evolutionary algorithms,* 1st ed., Chichester ; New York: John Wiley & Sons.

Domanski, P. A. (1991) *Simulation of an evaporator with nonuniform one-dimensional air distribution,* pt 1 ed., translated by New York, NY, USA: Publ by ASHRAE, 793-802.

Domanski, P. A. and Yashar, D. (2007) 'Application of an evolution program for refrigerant circuitry optimization', in *Challenges to Sustainability, ACRECONF 2007*, Delhi, India, 7 - 8 December,

Domanski, P. A., Yashar, D., Kaufman, K. A. and Michalski, R. S. (2004) 'An optimized design of finned-tube evaporators using the learnable evolution model', *HVAC and R Research,* 10(2), 201-211.

Dybvig, R. K. (2003) *The scheme programming language,* 3rd ed., Cambridge, Mass.: MIT Press.

Fabbri, G. (1997) 'A genetic algorithm for fin profile optimization', *International Journal of Heat and Mass Transfer,* 40(9), 2165-2172.

Fang, K., Lin, D., Winker, P. and Zhang, Y. (2000) 'Uniform design: Theory and application', *TECHNOMETRICS,* 42(3), 237-248.

Farin, G. E. (1999) *NURBS : from projective geometry to practical use,* 2nd ed., Natick, Mass.: A.K. Peters.

Fax, D. H. and Mills, J. R. R. (1957) 'Generalized optimal heat-exchanger design', *American Society of Mechanical Engineers - Transactions,* 79(3), 653-658.

Fluent (2007) 'User's Guide', 6.3(

Foli, K., Okabe, T., Olhofer, M., Jin, Y. and Sendhoff, B. (2006) 'Optimization of micro heat exchanger: CFD, analytical approach and multi-objective evolutionary algorithms', *International Journal of Heat and Mass Transfer,* 49(5-6), 1090-1099.

Freitas, C. J. (2002) 'The issue of numerical uncertainty', *Applied Mathematical Modelling,* 26(2), 237-248.

Freitas, C. J., Ghia, U., Celik, I., Roache, P. and Raad, P. (2003) *ASME'S Quest to Quantify Numerical Uncertainty,* translated by Reno, Nevada: American Institute of Aeronautics and Astronautics, 1-7.

Giunta, A. A., Wojtkiewicz, S. F. and and Eldred, M. S. (2003) *Overview of modern design of experiments methods for computational simulations,* translated by Reno, NV: AIAA, 1-17.

Gnielinski, V. (1976) 'New equations for heat and mass-transfer in turbulent pipe and channel flow', *International Chemical Engineering,* 16(2), 359-368.

Goldstein, R., Eckert, E., Ibele, W., Patankar, S., Simon, T., Kuehn, T., Strykowski, P., Tamma, K., Bar-Cohen, A., Heberlein, J., Davidson, J., Bischof, J., Kulacki, F., Kortshagen, U. and Garrick, S. (2002) 'Heat transfer - a review of 2000 literature', *International Journal of Heat and Mass Transfer,* 45(14), 2853-2957.

Goldstein, R., Ibele, W., Patankar, S., Simon, T., Kuehn, T., Strykowski, P., Tamma, K., Heberlein, J., Davidson, J., Bischof, J., Kulacki, F., Kortshagen, U., Garrick, S. and Srinivasan, V. (2006) 'Heat transfer - A review of 2003 literature', *International Journal of Heat and Mass Transfer,* 49(3-4), 451-534.

Grohmann, S. (2005) 'Measurement and modeling of single-phase and flow-boiling heat transfer in microtubes', *International Journal of Heat and Mass Transfer,* 48(19-20), 4073-4089.

Gruss, J., Bouzon, C. and Thonon, B. (2005) 'Extruded microchannel-structured heat exchangers', *Heat Transfer Engineering,* 26(3), 56-63.

Guessous, L. and Maddipatla, S. (2002) *Improving radiator design through shape optimization,* 6 ed., translated by New Orleans, LA, United states: American Society of Mechanical Engineers, 233-239.

Guo, Z.-Y. and Li, Z.-X. (2003) 'Size effect on microscale single-phase flow and heat transfer', *International Journal of Heat and Mass Transfer,* 46(1), 149-159.

Guo, Z. Y., Li, D. Y. and Wang, B. X. (1998) 'A novel concept for convective heat transfer enhancement', *International Journal of Heat and Mass Transfer,* 41(14), 2221-2225.

Halbritter, A., Schygulla, U., Wenka, A. and Schubert, K. (2004) *Comparison of numerical simulation and experimental results for crossflow and counterflow microchannel heat exchangers,* translated by Rochester, NY, United states: American Society of Mechanical Engineers, 967-976.

Hamad, H. (2006) 'A new metric for measuring metamodels quality-of-fit for deterministic simulations', in *Proceedings of the 38th conference on Winter simulation*, Monterey, California, Winter Simulation Conference,

Harris, C., Despa, M. and Kelly, K. (2000) 'Design and fabrication of a cross flow micro heat exchanger', *Journal of Microelectromechanical Systems,* 9(4), 502-508.

Harris, C., Kelly, K., Wang, T., McCandless, A. and Motakef, S. (2002) 'Fabrication, modeling, and testing of micro-cross-flow heat exchangers', *Journal of Microelectromechanical Systems,* 11(6), 726-735.

Harris, R. L., Godines, C. R., Rangel, L. A., Herrera, E. C. and Manteufel, R. D. (2002) 'Use of probabilistic methods in design of fluidic systems', *Collection of Technical Papers - AIAA/ASME/ASCE/AHS/ASC Structures, Structural Dynamics and Materials Conference,* 1, 554-558.

Haseler, L. E., Owen, R. G. and Sardesai, R. G. (1983) 'Sensitivity of heat exchanger calculations to uncertainties in the physical properties of the process fluids', *Proceedings of the Institution of Mechanical Engineers, Part A: Journal of Power and Energy,* 197, 171-178.

Hedderich, C. P., Kellher, M. D. and Vanderplaats, G. N. (1982) 'Design and optimization of air-cooled heat exchangers', *ASME Journal of Heat Transfer,* 104(4), 683-690.

Hilbert, R., Janiga, G., Baron, R. and Thevenin, D. (2006) 'Multi-objective shape optimization of a heat exchanger using parallel genetic algorithms', *International Journal of Heat and Mass Transfer,* 49(15-16), 2567-2577.

(2008) *State of the art heat exchanger design* available: [accessed].

Hwang, Y. W. and Kim, M. S. (2006) 'The pressure drop in microtubes and the correlation development', *International Journal of Heat and Mass Transfer,* 49(11-12), 1804-1812.

Incropera, F. P. and DeWitt, D. P. (1996) *Fundamentals of heat and mass transfer,* 4th ed.*,* New York: Wiley.

Jacobi, A. M. and Shah, R. K. (1995) 'Heat transfer surface enhancement through the use of longitudinal vortices: a review of recent progress', *Experimental Thermal and Fluid Science,* 11(3), 295-309.

Jacobi, A. M. and Shah, R. K. (1998) 'Air-side flow and heat transfer in compact heat exchangers: a discussion of enhancement mechanisms', *Heat Transfer Engineering,* 19(4), 29-41.

James, C. A., Taylor, R. P. and Hodge, B. K. (1995) 'Application of uncertainty analysis to cross-flow heat exchanger performance predictions', *Heat Transfer Engineering,* 16(4), 50-62.

Jiang, H. B., Aute, V. and Radermacher, R. (2006) 'CoilDesigner: a general-purpose simulation and design tool for air-to-refrigerant heat exchangers', *International Journal of Refrigeration-Revue Internationale Du Froid,* 29(4), 601-610.

Jin, R., Chen, W. and Sudjianto, A. (2002) *On sequential sampling for global metamodeling in engineering design,* translated by Montreal, Que., Canada: American Society of Mechanical Engineers, 539-548.

Jing, W., Jianbing, W., Liuyang, G., Suili, W. and Dayong, H. (2005) *CFD optimization application on airside plate fins of condenser coil of gravity-assisted heat pipe,* translated by San Francisco, CA, United states: American Society of Mechanical Engineers, 779-785.

Johnson, M., Moore, L. and Ylvisaker, D. (1990) 'Minimax and maximin distance designs', *Journal of Statistical Planning and Inference,* 26(2), 131-148.

Judy, J., Maynes, D. and Webb, B. W. (2002) 'Characterization of frictional pressure drop for liquid flows through microchannels', *International Journal of Heat and Mass Transfer,* 45(17), 3477-3489.

Kalagnanam, J. and Diwekar, U. (1997) 'An efficient sampling technique for off-line quality control', *Technometrics,* 39(3), 308-319.

Kalpakjian, S. (1995) *Manufacturing engineering and technology,* 3rd ed.*,* Reading, Mass.: Addison-Wesley.

Kandlikar, S. G., Joshi, S. and Tian, S. (2003) 'Effect of surface roughness on heat transfer and fluid flow characteristics at low Reynolds numbers in small diameter tubes', *Heat Transfer Engineering,* 24(3), 4-16.

Kasagi, N., Shikazono, N., Suzuki, Y. and and Oku, T. (2003a) *Assessment of High-Performance Compact Micro Bare-Tube Heat Exchangers for Electronics Equipment Cooling,* translated by University of Newcastle upon Tyne: 1-6.

Kasagi, N., Shikazono, N., Suzuki, Y. and Oku, T. (2003b) *Assessment of high-performance compact micro bare-tube heat exchangers for electronics equipment cooling,* translated by University of Newcastle upon Tyne, UK: 1-6.

Kasagi, N., Suzuki, Y., Shikazono, N. and and Oku, T. (2003c) *Optimal design and assessment of high performance micro bare-tube heat exchangers,* translated by Crete: 241-246.

Kays, W. M., Crawford, M. E. and Weigand, B. (2005) *Convective heat and mass transfer,* 4th ed.*,* Boston: McGraw-Hill Higher Education.

Kays, W. M. and London, A. L. (1998) *Compact heat exchangers,* Third ed.*,* Malabar, Florida: Krieger Publishing Company.

Kelly, K. W., Harris, C. R. and Despa, M. S. (2002) *Crossflow Micro Heat Exchanger*, US 6415860 B1.

Kim, S. Y., Paek, J. W. and Kang, B. H. (2000) 'Flow and heat transfer correlations for porous fin in a plate-fin heat exchanger', *Journal of Heat Transfer,* 122(3), 572-578.

Knetsch, T. and Hauptmanns, U. (2005) 'Integration of stochastic effects and data uncertainties into the design of process equipment', *Risk Analysis,* 25(1), 189-198.

Koo, J. and Kleinstreuer, C. (2003) 'Liquid flow in microchannels: Experimental observations and computational analyses of microfluidics effects', *Journal of Micromechanics and Microengineering,* 13(5), 568-579.

Koo, J. and Kleinstreuer, C. (2004) 'Viscous dissipation effects in microtubes and microchannels', *International Journal of Heat and Mass Transfer,* 47(14-16), 3159-3169.

Kreyszig, E. (2006) *Advanced engineering mathematics,* 9th ed.*,* Hoboken, NJ: John Wiley.

Lee, K.-S., Kim, W.-S. and Si, J.-M. (2001) 'Optimal shape and arrangement of staggered pins in the channel of a plate heat exchanger', *International Journal of Heat and Mass Transfer,* 44(17), 3223-3231.

Lee, P.-S., Garimella, S. V. and Liu, D. (2005) 'Investigation of heat transfer in rectangular microchannels', *International Journal of Heat and Mass Transfer,* 48(9), 1688-1704.

Lee, S. Y. and Dimenna, R. A. (2005) *FLUENT test and verification document*, Aiken, SC 29808.

Lelea, D., Nishio, S. and Takano, K. (2004) 'The experimental research on microtube heat transfer and fluid flow of distilled water', *International Journal of Heat and Mass Transfer,* 47(12-13), 2817-2830.

Lemmon, E. W., Huber, M. L. and McLinden, M. O. (2007) *NIST standard reference database 23: reference fluid thermodynamic and transport properties-REFPROP*, Gaithersburg, MD, USA.

Li, G., Aute, V. and Azarm, S. (2009) 'An accumulative error based adaptive design of experiments for offline metamodeling', *Structural and Multidisciplinary Optimization*, 1-19.

Li, Z., Davidson, J. and Mantell, S. (2004) 'Heat transfer enhancement using shaped polymer tubes: Fin analysis', *ASME Journal of Heat Transfer,* 126(2), 211-218.

Li, Z., Davidson, J. H. and Mantell, S. C. (2006) 'Numerical simulation of flow field and heat transfer of streamlined cylinders in cross flow', *ASME Journal of Heat Transfer,* 128(6), 564-570.

Li, Z., Du, D. and Guo, Z. (2003) 'Experimental study on flow characteristics of liquid in circular microtubes', *Microscale Thermophysical Engineering,* 7(3), 253-265.

Li, Z., He, Y.-L., Tang, G.-H. and Tao, W.-Q. (2007) 'Experimental and numerical studies of liquid flow and heat transfer in microtubes', *International Journal of Heat and Mass Transfer,* 50(17-18), 3447-3460.

Liang, S. Y., Wong, T. N. and Nathan, G. K. (2001) 'Numerical and experimental studies of refrigerant circuitry of evaporator coils', *International Journal of Refrigeration,* 24(8), 823-833.

Ligrani, P. M., Oliveira, M. M. and Blaskovich, T. (2003) 'Comparison of heat transfer augmentation techniques', *AIAA Journal,* 41(3), 337-362.

Lin, T.-Y. and Yang, C.-Y. (2007) 'An experimental investigation on forced convection heat transfer performance in micro tubes by the method of liquid crystal thermography', *International Journal of Heat and Mass Transfer,* 50(23-24), 4736-4742.

Litinetski, V. V. and Abramzon, B. M. (1998) 'Mars - a multistart adaptive random search method for global constrained optimization in engineering applications', *Engineering Optimization,* 30(2), 125-154.

Liu, J., Wei, W., Ding, G., Zhang, C., Fukaya, M., Wang, K. and Inagaki, T. (2004) 'A general steady state mathematical model for fin-and-tube heat exchanger based on graph theory', *International Journal of Refrigeration,* 27(8), 965-973.

Lophaven, S. N., Nielsen, H. B. and Sondergaard, J. (2002) *Aspects of the MATLAB toolbox DACE*, Kongens Lyngby, Denmark: Technical University of Denmark.

Mackay, F. J., Apostolakis, G. E. and Hejzlar, P. (2008) 'Incorporating reliability analysis into the design of passive cooling systems with an application to a gas-cooled reactor', *Nuclear Engineering and Design,* 238(1), 217-228.

Mala, G. and Li, D. (1999) 'Flow characteristics of water in microtubes', *International Journal of Heat and Fluid Flow,* 20(2), 142-148.

Malapure, V. P., Mitra, S. K. and Bhattacharya, A. (2007) 'Numerical investigation of fluid flow and heat transfer over louvered fins in compact heat exchanger', *International Journal of Thermal Sciences,* 46(2), 199-211.

Manglik, R. M. and Bergles, A. E. (2004) 'Enhanced heat and mass transfer in the new millennium: A review of the 2001 literature', *Journal of Enhanced Heat Transfer,* 11(2), 87-118.

Manzan, M., Micheli, D. and Pieri, S. (2006) *Automatic integration in the design of a microturbine compact recuperator,* translated by Barcelona, Spain: American Society of Mechanical Engineers, 333-341.

Maranzana, G., Perry, I. and Maillet, D. (2004) 'Mini- and micro-channels: Influence of axial conduction in the walls', *International Journal of Heat and Mass Transfer,* 47(17-18), 3993-4004.

Martin, J. D. and Simpson, T. W. (2005) 'Use of kriging models to approximate deterministic computer models', *AIAA Journal,* 43(4), 853-863.

McGill, R., Tukey, J. W. and Larsen, W. A. (1978) 'Variations of Box Plots', *The American Statistician,* 32(No. 1), 12-16.

McKay, M. D., Beckman, R. J. and Conover, W. J. (1979) 'A Comparison of Three Methods for Selecting Values of Input Variables in the Analysis of Response from a Computer Code', *Technometrics,* 21, 239-245.

Mehta, U. B. (1996) 'Guide to credible computer simulations of fluid flows', *Journal of Propulsion and Power,* 12(5), 940-948.

Michalski, R. S. and Kaufman, K. A. (2006) 'Intelligent evolutionary design: A new approach to optimizing complex engineering systems and its application to designing heat exchangers', *International Journal of Intelligent Systems,* 21(12), 1217-1248.

Micheli, D., Pediroda, V. and Pieri, S. (2008) 'Multi-objective optimization of a microturbine compact recuperator', *Journal of Engineering for Gas Turbines and Power,* 130(3).

Morini, G. L. (2004) 'Single-phase convective heat transfer in microchannels: A review of experimental results', *International Journal of Thermal Sciences,* 43(7), 631-651.

Myers, R. H. and Montgomery, D. C. (2002) *Response surface methodology : process and product optimization using designed experiments,* 2nd ed.*,* New York: J. Wiley.

Nithiarasu, P. (2005) *Role of Numerical Modeling in Compact Heat Exchanger Analysis,* translated by NJ, USA: 180-191.

Nobile, E., Pinto, F. and Rizzetto, G. (2005) *Multiobjective shape optimization of convective wavy channels,* translated by San Francisco, CA, United states: American Society of Mechanical Engineers, 829-838.

Nobile, E., Pinto, F. and Rizzetto, G. (2006) 'Geometric parameterization and multiobjective shape optimization of convective periodic channels', *Numerical Heat Transfer, Part B: Fundamentals,* 50(5), 425-453.

O'Brien, J. E. and Sohal, M. S. (2005) 'Heat transfer enchancement for finned-tube heat exchangers with winglets', *Journal of Heat Transfer,* 127(2), 171-178.

O'Brien, J. E., Sohal, M. S. and Wallstedt, P. C. (2004) 'Local heat transfer and pressure drop for finned-tube heat exchangers using oval tubes and vortex generators', *Journal of Heat Transfer,* 126(5), 826-835.

Oberkampf, W. and Blottner, F. (1998) 'Issues in computational fluid dynamics code verification and validation', *AIAA Journal,* 36(5), 687-695.

Oliet, C., Perez-Segarra, C. D., Danov, S. and Oliva, A. (2007) 'Numerical simulation of dehumidifying fin-and-tube heat exchangers: Semi-analytical modelling and experimental comparison', *International Journal of Refrigeration,* 30(7), 1266-1277.

Owen, A. (1992) 'Orthogonal arrays for computer experiments, integration and visualization', *Statistica Sinica,* 2(2), 439-452.

Owhaib, W. and Palm, B. (2004) 'Experimental investigation of single-phase convective heat transfer in circular microchannels', *Experimental Thermal and Fluid Science,* 28(2-3), 105-110.

Pagani, L. P., Apostolakis, G. E. and Hejzlar, P. (2005) 'The impact of uncertainties on the performance of passive systems', *Nuclear Technology,* 149(2), 129-140.

Palm, B. and Peng, X.-F. (2004) 'Single-Phase Convective Heat Transfer' in Celata, G. P., ed. *Heat Transfer and Fluid Flow in Microchannels*, New York: Begell House, Inc., 31-52.

Park, K. and Moon, S. (2005) 'Optimal design of heat exchangers using the progressive quadratic response surface model', *International Journal of Heat and Mass Transfer,* 48(11), 2126-2139.

Park, K., Oh, P.-K. and Lim, H.-J. (2006) 'The application of the CFD and Kriging method to an optimization of heat sink', *International Journal of Heat and Mass Transfer,* 49(19-20), 3439-3447.

Patankar, S. V. (1980) *Numerical heat transfer and fluid flow,* Washington
New York: Hemisphere Pub. Corp. ;
McGraw-Hill.

Peng, H. and Ling, X. (2008) 'Optimal design approach for the plate-fin heat exchangers using neural networks cooperated with genetic algorithms', *Applied Thermal Engineering,* 28(5-6), 642-650.

Pettersen, J., Hafner, A., Skaugen, G. and Rekstad, H. (1998) 'Development of compact heat exchangers for CO2 air-conditioning systems', *INTERNATIONAL JOURNAL OF REFRIGERATION-REVUE INTERNATIONALE DU FROID,* 21(3), 180-193.

Pettersen, J., Hafner, A., Skaugen, G. and Rekstad, H. (1998) 'Development of compact heat exchangers for CO2 air-conditioning systems', *International Journal of Refrigeration,* 21(3), 180-193.

Prasad, R. C., Karmeshu and Bharadwaj, K. K. (2002) 'Stochastic modeling of heat exchanger response to data uncertainties', *Applied Mathematical Modelling,* 26(6), 715-726.

Queipo, N., Devarakonda, R. and Humphrey, J. A. C. (1994) 'Genetic algorithms for thermosciences research: Application to the optimized cooling of electronic components', *International Journal of Heat and Mass Transfer,* 37(6), 893-908.

Queipo, N. V., Arevalo, C. J. and Pintos, S. (2005) 'The integration of design of experiments, surrogate modeling and optimization for thermoscience research', *Engineering with Computers,* 20(4), 309-315.

Radermacher, R., Azarm, S., O., A. and Aute, V. (2007) *Next Generation Heat Exchangers Workshop*, College Park, MD.

Reneaume, J. M. and Niclout, N. (2003) 'MINLP optimization of plate fin heat exchangers', *Chemical and Biochemical Engineering Quarterly,* 17(1), 65-76.

Roache, P. (1998) 'Verification of codes and calculations', *AIAA Journal,* 36(5), 696-702.

Roache, P. J. (1997) 'Quantification of uncertainty in computational fluid dynamics' in, 29 ed., 123-123.

Rohsenow, W. M. and Choi, H. Y. (1961) *Heat, mass, and momentum transfer,* Englewood Cliffs, N.J.,: Prentice-Hall.

Romero-Méndez, R., Sen, M., Yang, K. T. and McClain, R. (2000) 'Effect of fin spacing on convection in a plate fin and tube heat exchanger', *International Journal of Heat and Mass Transfer,* 43(1), 39-51.

Rosenblueth, E. (1981) 'Two-point estimates in probabilities', *Applied Mathematical Modeling,* 5(5), 329-335.

Rubinstein, R. Y. and Kroese, D. P. (2008) *Simulation and the monte carlo method,* 2nd ed., Hoboken, N.J.: John Wiley & Sons.

Sacks, J., Welch, W. J., Toby, J. M. and Wynn, H. P. (1989) 'Design and Analysis of Computer Experiments', *Statistical Science,* 4(4), 409-423.

Saji, N., Nagai, S., Tsuchiya, K., Asakura, H. and Obata, M. (2001) 'Development of a compact laminar flow heat exchanger with stainless steel micro-tubes', *PHYSICA C,* 354(1-4), 148-151.

Schmit, T. S., Dhingra, A. K., Landis, F. and Kojasoy, G. (1996) 'Genetic algorithm optimization technique for compact high intensity cooler design', *Journal of Enhanced Heat Transfer,* 3(4), 281-290.

Shah, R. K. (2006) 'Advances in science and technology of compact heat exchangers', *Heat Transfer Engineering,* 27(5), 3-22.

Shah, R. K. and London, A. L. (1978) *Laminar flow forced convection in ducts : a source book for compact heat exchanger analytical data,* New York: Academic Press.

Shah, R. K. and Sekulic, D. P. (2003) *Fundamentals of heat exchanger design,* Hoboken, NJ: John Wiley & Sons.

Shen, P., Aliabadi, S. K. and Abedi, J. (2004) *A review of single-phase liquid flow and heat transfer in microchannels,* translated by Rochester, NY, United states: American Society of Mechanical Engineers, 213-220.

Shewry, M. C. and Wynn, H. P. (1987) 'Maximum entropy sampling', *Journal of Applied Statistics,* 14(2), 165 – 170.

Shikazono, N., Okawa, D., Kobayashi, M., Kasagi, N., Waki, T., Kandori, I. and Hataya, S. (2007) *Research and Development of High-Perfromance Compact Finless Heat Exchanger,* translated by Potsdam, Germany: 1-7.

Silber-Li, Z.-H. and Cui, H.-H. (2005) *The effects of viscous heating and the pressure-dependent viscosity on liquid flow in microtubes,* translated by Toronto, ON, Canada: American Society of Mechanical Engineers, 225-231.

Simpson, T. W., Peplinski, J. D., Koch, P. N. and Allen, J. K. (2001) 'Metamodels for computer-based engineering design: Survey and recommendations', *Engineering with Computers,* 17(2), 129-150.

Singh, V., Aute, V. and Radermacher, R. (2008) 'Numerical approach for modeling air-to-refrigerant fin-and-tube heat exchanger with tube-to-tube heat transfer', *International Journal of Refrigeration,* 31(8), 1414-1425.

Steinke, M. E. and Kandlikar, S. G. (2004) 'Review of single-phase heat transfer enhancement techniques for application in microchannels, minichannels and microdevices', *International Journal of Heat and Technology,* 22(2), 3-11.

Steinke, M. E. and Kandlikar, S. G. (2005) *Single-phase liquid heat transfer in microchannels,* translated by Toronto, ON, Canada: American Society of Mechanical Engineers, 667-678.

Stern, F., Wilson, R., Coleman, H. and Paterson, E. (2001) 'Comprehensive approach to verification and validation of CFD simulations - Part 1: Methodology and procedures', *ASME Journal of Fluids Engineering,* 123(4), 793-802.

Sunden, B. (2007) 'Computational fluid dynamics in research and design of heat exchangers', *Heat Transfer Engineering,* 28(11), 898-910.

Suram, S., Ashlock, D. A. and Bryden, K. M. (2006) *Graph based evolutionary algorithms for heat exchanger fin shape optimization,* translated by Portsmouth, VA, United states: American Institute of Aeronautics and Astronautics Inc., 647-657.

Suryanarayana, N. V. (1995) *Engineering heat transfer,* Minneapolis/St. Paul: West Pub. Co.

Taguchi, G. B. (1987) *System of experimental design : engineering methods to optimize quality and minimize costs,* White Plains, N.Y.
Dearborn, Mich.: UNIPUB/Kraus International Publications ;
American Supplier Institute.

Tao, W.-Q., Guo, Z.-Y. and Wang, B.-X. (2002) 'Field synergy principle for enhancing convective heat transfer - Its extension and numerical verifications', *International Journal of Heat and Mass Transfer,* 45(18), 3849-3856.

Tayal, M. C., Fu, Y. and Diwekar, U. M. (1999) 'Optimal design of heat exchangers: A genetic algorithm framework', *Industrial and Engineering Chemistry Research,* 38(2), 456-467.

Van Der Vyver, H., Dirker, J. and Meyer, J. P. (2003) *Validation of A CFD Model of a Three-Dimensional Tube-in-Tube Heat Exchanger,* translated by Melbourne, Australia: 235-240.

Van Doormaal, J. P. and Raithby, G. D. (1984) 'Enhancement of the SIMPLE Method for Predicting Incompressible Fluid Flows', *Numerical Heat Transfer,* 7(2), 147-163.

Versteeg, H. K. and Malalasekera, W. (1995) *An introduction to computational fluid dynamics : the finite volume method,* Harlow, Essex, England Longman Scientific & Technical ;: New York : Wiley.

Wang, G. G. and Shan, S. (2007) 'Review of metamodeling techniques in support of engineering design optimization', *Journal of Mechanical Design, Transactions of the ASME,* 129(4), 370-380.

Wang, Q., Liang, H., Xie, G., Zeng, M., Luo, L. and Feng, Z. (2007) 'Genetic algorithm optimization for primary surfaces recuperator of microturbine', *ASME Journal of Engineering for Gas Turbines and Power,* 129(2), 436-442.

Wang, X. (2008) *Performance Investigation of Two Stage Heat Pump System with Vapor Injected Scroll Compressor*, unpublished thesis University of Maryland.

Webb, R. and Kim, N. H. (2005) 'Principles of Enhanced Heat transfer',

Westphalen, D., Roth, K. W. and Brodrick, J. (2006) 'Heat transfer enhancement', *ASHRAE Journal,* 48(4), 68-71.

Wu, J. M. and Tao, W. Q. (2007) 'Investigation on laminar convection heat transfer in fin-and-tube heat exchanger in aligned arrangement with longitudinal vortex generator from the viewpoint of field synergy principle', *Applied Thermal Engineering,* 27(14-15), 2609-2617.

Wu, Z., Ding, G., Wang, K. and Fukaya, M. (2008) 'Knowledge-based evolution method for optimizing refrigerant circuitry of fin-and-tube heat exchangers', *HVAC and R Research,* 14(3), 435-452.

Xiong, Y., Moscinski, M., Frontera, M., Yin, S., Dede, M. and Paradis, M. (2005) 'Multidisciplinary design optimization of aircraft combustor structure: An industry application', *AIAA Journal,* 43(9), 2008-2014.

Yang, C. Y. and Lin, T. Y. (2007) 'Heat transfer characteristics of water flow in microtubes', *Experimental Thermal and Fluid Science,* 32(2), 432-439.